A Millimeter-Wave Radar Microfabrication Technique and Its Application in Detection of Concealed Objects

by

Mehrnoosh Vahidpour

A dissertation submitted in partial fulfillment

of the requirements for the degree of

Doctor of Philosophy

(Electrical Engineering)

in The University of Michigan

2012

Doctoral Committee:

Professor Kamal Sarabandi, Chair
Professor Mark A. Burns
Professor Mahta Moghaddam
Associate Professor Anthony Grbic
Research Scientist Jack R. East

To my parents,
for their unconditional belief in me

ACKNOWLEDGEMENTS

This work could not have been completed without the contribution of the souls and hands many of whom I cannot mention individually. Most importantly, I would like to acknowledge my research advisor Prof. Kamal Sarabandi for giving me the opportunity to work with him. He has been a great source of motivation for me. I learnt a great deal of knowledge from him, have been always impressed by his passion towards science and deeply respect and admire him as a role model. I also thank Prof. Mahta Moghaddam, Prof. Anthony Grbic and Prof. Mark Burns for their precious time serving as my dissertation committee members. Many sincere thanks are given to Dr. Jack East for his continuous assistance, support and encouragement throughout the radar project.

I would like to specifically thank Meysam Moallem, for his valuable friendship especially in the many moments of frustration during the work and for his helps and fruitful discussions especially during the measurements.

Experimental research could not be completed without the assistance of many colleagues. I would like to acknowledge all the staff and users in the Lurie nanofabrication facility (LNF), most importantly Edward Tang who was my mentor in the early stages of microfabrication, Leslie George, Greg Allion, Brian VanDerElzen, Matt Oonk, David Yates, Russ Clifford, Robert Hower, Sanrine Matrin, Pilar Herrera-fierro, Nadine Wang, Katharine Beach, Ali Besharatian and Behzad Sadat for all their

Table of Contents

LIST OF FIGURES

LIST OF TABLES

LIST OF ABBREVIATIONS

MMW	Millimeter-wave
SMMW	Submillimeter-wave
PO/IPO	Physical Optics/Iterative Physical Optics
RCS	Radar Cross Section
DRIE	Deep Reactive Ion Etching
GO	Geometrical Optics
FMCW	Frequency Modulate Continuous Wave
CBCPW	Cavity-Backed CoPlanar Waveguide
ONO	Oxide Nitride Oxide

ABSTRACT

A Millimeter-Wave Radar Microfabrication Technique and Its Application in Detection of Concealed Objects

by

Mehrnoosh Vahidpour

Chair: Kamal Sarabandi

Millimeter-wave (MMW) radars are envisioned for a number of safety and security applications such as collision-avoidance, navigation and standoff target detection in all weather conditions. This work focuses on two MMW radar applications: (1) phenomenology of radar backscatter from the human body for the purpose of identification and detection of concealed objects on the body (2) microfabrication of advanced MMW radar to achieve compact and low-cost systems for autonomous navigation.

In MMW band, the wavelength (1 mm ~ 1 cm) is long enough to allow signal penetration through cluttered atmosphere and clothing with little attenuation and short enough to allow for fabrication of small-size radar systems. Hence, this frequency band is

well suited for the design of small sensors capable of obstacle detection and navigation in heavily cluttered environment and detecting hidden objects carried by individuals. For this purpose, a novel non-imaging approach is developed for distinction of walking human body and concealed carried object using polarimetric backscatter Doppler spectrum. This approach does not need radiometric calibration of the radar and preparation of the subject for radar interrogation. It is shown that a coherent polarimetric radar at W-band (95 GHz) or higher frequencies can be used for standoff detection of concealed carried objects.

Motivated by these results, the thesis also includes an investigation on developing a technology for compact MMW radar systems. A micromachined, high-resolution, compact and low-power imaging MMW radar operating at 240 GHz intended for obstacle detection in complex environment is introduced. A frequency scanning antenna array micromachined from three layers of stacked silicon wafers is designed to provide 2^0 beamwidth in azimuth and 8^0 in elevation with azimuthal beam scanning range of $\pm 25^0$. The frequency beam scanning is enabled by a meander rectangular waveguide with a slot array on its broad wall to feed linear microstrip patch antennas microfabricated on a suspended Parylene membrane. This technique offers high fabrication precision; provide easy fabrication and integration with active devices. The performances of the passive components of the radar system are verified using a WR-3 S-parameter and a near-field measurement systems.

Chapter I

Introduction

The millimeter wave (MMW) spectrum is a range of electromagnetic band between 30 GHz and 300 GHz corresponding to wavelengths form 10mm to 1mm, between microwave and THz/optical region. The current interest in MMW band arises from the understanding of the limitations with the adjacent frequency bands [1]. In the microwave region, atmospheric loss is significantly low and excellent penetration through many obstacles such as walls, clothing, vegetation, fog and dust can be realized. In addition, the technology for radars operating at microwave band has matured significantly. This includes high-power transmitters, low power electronics, data collection and storage as well as signal processing techniques for noise reduction and enhanced target detection. However, for applications where very high resolution is required, utilization of radars operating at low frequencies is impractical due to the required large aperture and very wide fractional bandwidth. Moreover, the microwave band is small, overcrowded and protected for wireless telecommunication networks, long-range military, weather and traffic control radars. Alternatively, optical range of spectrum requires small apertures and provides high resolution and the phenomenology of wave interaction is well understood and interpreted. Nevertheless, the physical dimension of the objects under detection are large compared to the wavelength which brings up the necessity of either using computers with significant amount of memory and fast processors for analysis or applying asymptotic methods of analysis. Also, lack of technology in developing

coherent sources, sensors and detectors in optical range makes many potential applications unfeasible. Furthermore, due to the high atmospheric attenuation, most obstacles such as dust and smoke are no longer transparent at this range.

The main advantages of the MMW range are:

Short wavelength: the component sizes are reduced compared to those in the microwave band. This makes them suitable for mobile platforms such as aircrafts, helicopters, cars or even small robotic platforms. It is also possible to achieve lower beamwidth ($\frac{\lambda}{l}$) which results in better resolution.

Wide bandwidth: Investigating atmospheric absorption for horizontal propagation over 400 GHz of bandwidth including the MMW band (Figure 1. 1) represents that the principal windows exist at 35, 94, 140 and 220 GHz with extremely large available bandwidths around each. This has a number of advantages:

- High data rate for communication systems,

- High resistance to jamming since wide bandwidth is available,

- Very high range resolution for tracking and target detection,

- Increased recognition capability of slowly moving target due to the high Doppler frequency

Low sensitivity to environmental characteristics Atmospheric absorption and attenuation due to inclement weather condition such as fog, dust or smoke are much lower compared to optical and IR frequencies [3].

2
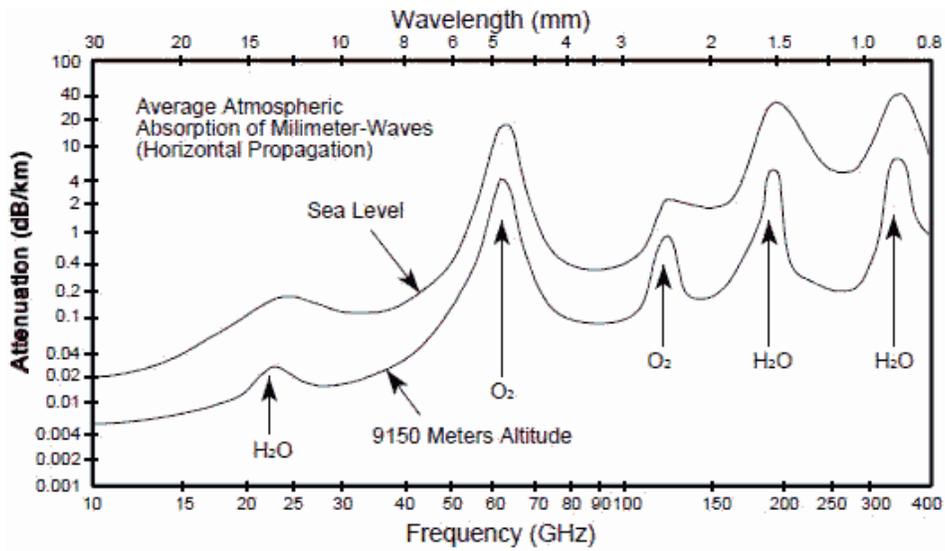
Figure 1. 1. Atmospheric absorption of millimeter wave [2]. Principal windows exist at 35, 94, 140 and 220 GHz with extremely large available bandwidths around each.
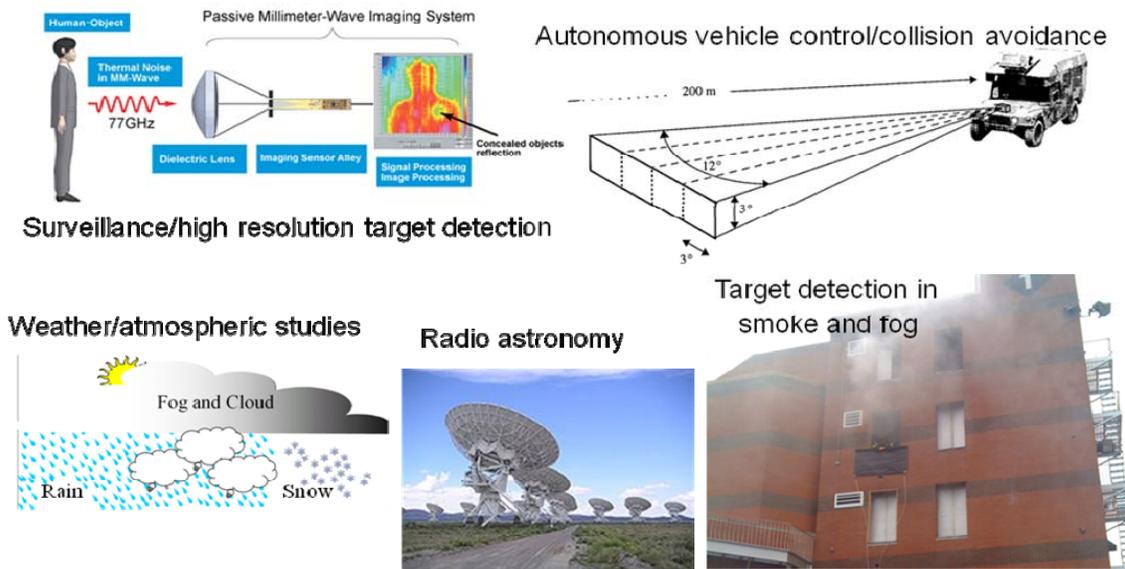
Figure 1. 2. MMW radar applications in surveillance, autonomous vehicle control, weather studies, radio astronomy and target detection in smoke and fog.

1.1.   Radar Phenomenology in the MMW Band

With the increased potential applications in the areas of wireless communication systems, imaging systems, atmospheric studies, remote sensing of the environment,

3

surveillance, navigation, autonomous vehicle control, radio astronomy, high resolution target detection, perimeter security, etc (Figure 1. 2), the MMW part of electromagnetics spectrum has received extensive attention over the past two decades. One of the main applications of MMW radars is in the area of surveillance, perimeter security and detection of pedestrians and hidden objects carried by individuals in heavy-cluttered environment. Detection and identification of human beings in highly scattering radar scenes such as urban and indoor environments is rather challenging. Traditional detection systems include metal detectors and X-ray systems. The latter has hazardous health effects for human, while the former detects metal by measuring magnetic field generated by eddy current and can only be used in situ and is incapable of distinguishing harmless small personal objects [4]. More elaborate systems employ imaging techniques to identify the targets [5] - [9]. MMW imagers offer high resolution for a compact system while providing see-through-clothing and day-and-night operation capabilities. Furthermore, unlike X-rays, MMW radiation is non-ionizing, leading to minimal health risks. These make the MMW band ideally suited for surveillance of individuals for many applications ranging from identification of the human body itself to detection of concealed weapons.

Both active (reflecting) and passive (radiometric) MMW imaging systems have been investigated for these purposes. Passive systems are based on electromagnetic emission and apparent temperature variations of human body and concealed objects. Such imagers operate on the principle that a metallic weapon will reflect the temperature of the ambient surroundings at a different degree compared to the human body. This contrast is then detected by the radiometer and weapons can be recognized if the radiometer has sufficient spatial resolution [10]. Figure 1. 3 shows an image obtained from such a system

4

that clearly shows two handguns hidden beneath a person's sweater. On the other hand, active MMW radars illuminate the targets and build the images based on the reflected signal. Some of these systems use combined MMW-IR or MMW-Optical sensors in order to take advantage of both MMW penetration through clothing and very high resolution of the IR/optical range [11]. Focal plane arrays, pupil plane array and phased arrays have been extensively used in the detection of explosives concealed beneath the clothing [11], [12]. These arrays are large for moving platforms and costly since they use complex circuitry.
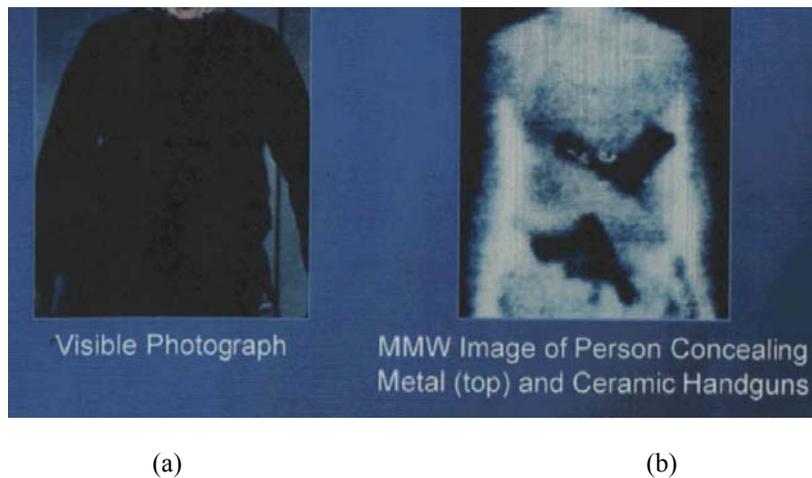
(a)   (b)
Figure 1. 3. 94 GHz radiometric image of a person concealing two handguns beneath a heavy sweater [10].

Identification of moving targets –such as walking or jogging human or animals - can be accomplished from the analysis of their backscatter Doppler spectrum. Due to the wideband spectrum compared to microwave frequencies, more details of human motion can be detected. This feature, in addition to the high-resolution capability of MMW radars, makes such radars more attractive for identification of walking bodies. The proposed methods for detection of human body and carried objects [13] rely on the

5

absolute value of the response which requires radiometric calibration of the radar and the knowledge of RCS of the human body at all incident angles. This of course is not practical due to the fact that the RCS of different human subjects are very different. There is a very large RCS variability as a function of aspect angle, and if the subject is partially illuminated or if it is not in the far-field region of radar system, its RCS becomes a function of radar range and radar beam. To circumvent these difficulties to some extent the application of polarimetric radars is proposed for which narrow beams with footprints commensurate to human body can be generated. Also using radar polarimetry, radiometric calibration will not be required. However, at lower microwave frequencies, the human body can depolarize the backscatter signal considerably and therefore cross-polarized signature cannot effectively be used. In addition, for narrow beamwidths, very large antennas are required. At high MMW frequencies, the amount of co-polarized backscatter response is dominant for smooth targets and cross-polarized response represents the level of roughness and asymmetry of the target. Uneven and asymmetric targets generate greater cross-polarized response. The geometries of common concealed objects carried by individuals are highly irregular and, once placed near human body, can indeed increase the level of cross-polarized backscatter observed by MMW radars. Therefore, at higher MMW frequencies, a significant increase in the cross-polarized response can be an indication of an external irregular object and can be used for detection. For detection of external irregular objects, the overall radar backscatter response of human body is decomposed into components associated with the body parts using time-frequency analysis. Isolating the torso response and noting that the presence of irregular objects on or around the torso increase cross- to co-polarized backscatter

6

ratio, it is shown that a coherent polarimetric radar at W-band or higher frequencies can be used for standoff detection of concealed objects.

A part of this thesis is focused on utilizing the backscatter Doppler spectrum at MMW frequencies to identify walking human bodies from other stationary and moving objects and using radar polarimetry in conjunction with time-frequency analysis for detecting concealed objects on a walking human subject.

1.2.   Radar Technology in the MMW band

The first generations of MMW radars were large in size mainly due to the utilization of tube oscillators and amplifiers and bulky antennas. Moreover, beam scanning was performed mechanically which required high mechanical accelerations in order to achieve high speed scanning or tracking. Recent advances in RFIC and MMIC technologies have made the fabrication of light-weight and less costly VCO and amplifier chips more feasible. Figure 1. 4 represents the MMIC chip sizes versus cost, yield and packing density for a high-yield MESFET process using ion-implantation. It shows that for smaller chips, cost decreases while the yield and density increases. This provides a major incentive to employ MMIC for MMW radar fabrication. Also, understanding the advantages of frequency modulated continuous wave (FMCW) radars which are fully compatible with these technologies, and the need for smaller, lighter, cheaper and low power systems, have focused the attentions on the realization of the on-chip fully integrated FMCW systems. At 24, 77, and 94 GHz, on-chip systems have been fabricated for automotive applications such as autonomous vehicle control and sensors for industrial robots and for range detection and target identification [13] - [19]. These designs are

using waveguides or MMIC consisting of mechanically or electrically tunable voltage-controlled oscillators (VCO), couplers, low noise amplifier, high electron-mobility (HEMT) transistors, mixers, circulators (for single transmit-receive antenna) etc. The solid state designs use a wide variety of different substrates from GaAs [15] to LTCC [18], [20] and silicon [21]. Recently, silicon germanium has been widely used at frequencies above 100 GHz to increase operating speed, reduce electronic noise, lower power consumption, support higher levels of integration, and, thus, enables the design of more functional components on a chip. However, in most of these systems, the antenna is a separate module which is connected to the MMIC via a transition. This makes the structure bulky and large while the transition adds additional loss to the system, whereas antenna integration enhances system loss, weight and compactness. However, most of the integrated systems employ simple antennas with limited performance such as patches with fixed and wide beams.
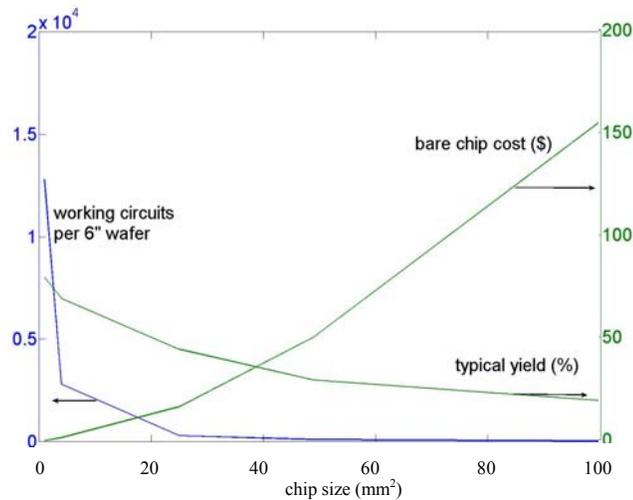
Figure 1. 4. MMIC chip sizes versus cost, yield and packing density for a high-yield MESFET process using ion-implantation. It shows as the chip size increases less chips are obtained from the wafer and hence lower yield and high cost are resulted.

8
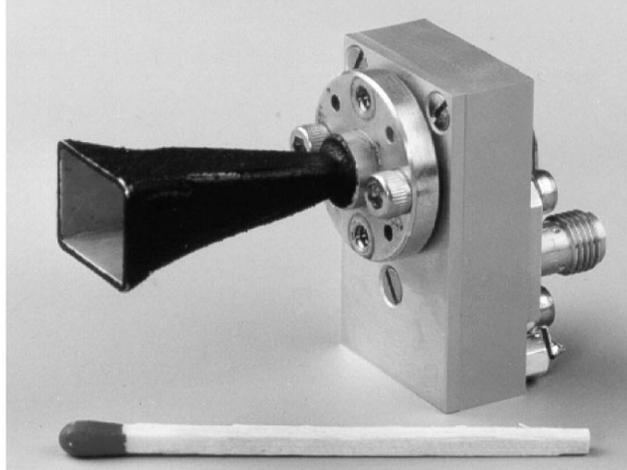
Figure 1. 5. 94-GHz FMCW radar using a horn antenna and microstrip hexaferrite circulator [15].

In an attempt to make a fully-integrated radar system suitable for applications in navigation and target detection, a new generation of radars at Y-band (240 GHz) with integrated frequency scanning antenna is presented in this thesis. The RF front-end of the radar system including the antenna, waveguide transitions and filters is designed using low-loss rectangular waveguides and fabricated using novel silicon micromachining technology. This technique offers easy fabrication of complex devices and easy integration with active devices.

1.3. Contributions of the Dissertation

The current MMW detection systems such as airport MMW scanners take a full-body image that has raised privacy concerns. In fact to detect hazardous objects on human body one does not need high resolution image of the entire body. The current MMW scanners require close proximity to the subject in isolation and preparation of the subject

by requiring removal of all coats and jackets. The method proposed in this dissertation does not image the body and does not require the individual to be isolated from its surrounding, so the radar does not need to be radiometrically calibrated. It relies only on the ratio of cross- to co-polarized response of measured backscatter. As shown in Figure 1. 6, the time domain polarimetric response of the walking body is processed using the Fourier transform and time-frequency analysis to derive a means for identification and detection.
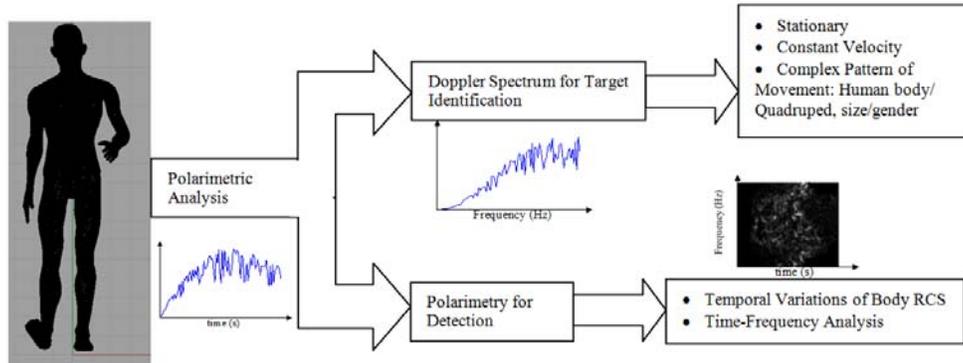
Figure 1. 6. Procedures used for target discrimination and detection. The time domain polarimetric response of the walking body undergoes processes such as Fourier transform and time-frequency analysis to derive a means for identifying human body and detecting concealed objects.

The Y-band radar proposed for target detection is suitable for operation in conditions limited by smoke, dust, haze or darkness and the goal is to provide beam scanning in the field of view $\pm 25^0$ with overall weight below 5 g. The active components of the radar are realized on CMOS and InP, while the passive components are realized on low-loss hollow rectangular waveguides to reduce weight and loss. Novel designs for various parts of the radar system are investigated such as multi-step CPW to rectangular waveguide transition and multi-step patch substrate to make the structure compatible with

microfabrication techniques. The designed structures have features aligned with Cartesian coordinates, do not incorporate dielectric materials and can be easily integrated. Novel microfabrication processes are used for the fabrication of passive components which include multi-step DRIE process, gold thermocompression bonding, controlled metallization on the sidewalls and realization of very large membranes using Parylene transfer method. The performance of the system is verified using assembled WR-3 measurement setups for S-parameter and near-field measurements.

1.3.1.   Overview of the Dissertation

This dissertation discusses the application of MMW radars in identification of walking human body and detection of concealed carried objects on human body in complex highly cluttered scene, and microfabrication of advanced MMW radars to achieve compact and low-cost systems for autonomous navigation.

Chapter II describes an efficient method for the radar backscatter analysis of human bodies in the high MMW band - Physical Optics (PO) and Iterative Physical Optics (IPO). Realistic body models including human bodies with different sizes and genders, dog and handgun are generated using laser scan and reference photographs of real targets. The body motion models are generated using a motion capture system. The simulated Radar Cross-Sections (RCS) of these targets at W-band are then calculated and the feasibility of target identification is discussed.

Chapter III discusses the radar backscatter analysis of walking bodies at W-band (Figure 1. 7). The Doppler spectra of human body and a dog models are derived from the

calculated backscatter signal in the time domain. The polarimetric responses of the walking bodies are then studied and the feasibility of detecting body-attached irregular objects by decomposing the overall backscatter response from different body parts is investigated. Based on the results, a novel method on the detection of external carried objects is developed and discussed. Experimental results of human body RCS measurement with/without carrying a handgun with the University of Michigan W-band radar system are presented to verify the carried object detection algorithm.
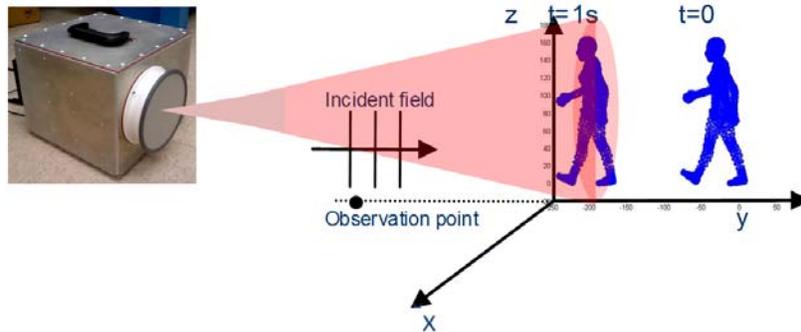
Figure 1. 7.   The University of Michigan W-band polarimetric radar is used for human body RCS measurement.

Human Doppler analysis at Y-band is performed using the same method. Y-band compared to W-band is underutilized and the available bandwidth is much higher and Y-band radars require technological advances to be well-suited for navigation and obstacle detection. These motivate the development of a Y-band radar which can be later enhanced for polarimetric applications and concealed target detection.

Chapter IV introduces a new generation of MMW radars at Y- band. The radar is low-profile and low-cost with high range resolution for navigation and obstacle detection. It is ultra-light weight and compact compared to the state of the art systems with components

fabricated on MMIC and assembled eventually on the antenna substrate. The radar antenna is a frequency scanning array with $\pm 25^0$ steering capability with narrow (2^0) beamwidth. The radar components and specifications as well as and the antenna characteristics are presented and discussed. The motivations behind suggesting the antenna structure and the radar assembly with low-cost micromachining techniques are presented.
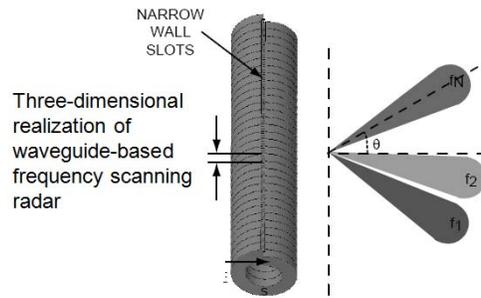
Figure 1. 8. Waveguide-based helical slot antenna.

The design details of a two-dimensional micromachined meander-line frequency scanning antenna array are presented in Chapter V. The antenna is designed using hollow rectangular waveguide with the slots cut on the broad wall of the waveguide as the radiating elements. This structure makes a narrow beam one-dimensional array therefore to confine the beam in the other direction slot-coupled patch arrays are used. Some of the design parameters are eventually modified throughout the fabrication process to be adapted to micromachining limitations.

Chapter VI presents the methods and components developed for radar integration. The antenna structure is excited with frequency multipliers which are fabricated on planar

transmission lines. Therefore, waveguide transitions to such transmission lines are required. In addition, a new method is developed to integrate the external chips of frequency multipliers and VCO with the antenna substrate. Waveguide bandpass filters are also designed to be incorporated with the system mainly in order to remove the unwanted components of the signal received by the antenna. The components and integration techniques are developed in a manner to be compatible with micromachining processes used to fabricate the antenna substrate.

Chapter VII discusses the details of microfabrication processes of the structure. The antenna is fabricated with a Deep Reactive Ion Etching (DRIE) method using silicon as the structural material. The process is performed on three silicon wafers each of which include a part of the antenna and other passive devices which are bonded together at the final step. Various microfabrication procedures such as silicon DRIE, gold sputtering, gold evaporation, multi-step mask deposition, silicon-oxide deposition, low-stress silicon-oxide/silicon nitride deposition, XeF_2 silicon etching, gold thermocompression bonding, topside and backside wafer alignment, polymer deposition and polymer bonding are employed and optimized for the fabrication of the radar components.

Chapter VIII presents the measurement setup for the Y-band system and discusses the on-wafer measurement process, calibration and antenna pattern measurement approach. The measurement results are presented and discussed.

This thesis concludes with a summary of its contributions and future work on this research topic in Chapter IX.

Chapter II

Electromagnetics Scattering Analysis of Human Body

The MMW region of electromagnetic spectrum offers certain unique features that can be utilized in detection and identification of individuals from their surroundings. In this region, the wavelength is short enough to allow fabrication of compact radars and achieve higher resolution. Yet, at the same time, the wavelength is long enough to allow signal penetration through non-conductive objects, clothing, smoke and fog with little or no attenuation. These make the MMW band ideally suited for surveillance of individuals for many applications ranging from the identification of the human body itself to the detection of concealed weapons ([8], [9]). Specifically, higher MMW bands can be used for radar backscatter analysis of human body since:

- Human motion has a unique pattern which is captured more easily at higher MMW band due to the higher recognition capability of Doppler at higher frequencies.

- The response of human-like targets is mostly co-polarized at high MMW frequencies. This is due to the fact that the radii of the curvatures of the body are much larger than the wavelength. This feature can be utilized to detect external carried objects by human body when a high cross-polarized response is received.

- Smaller size antennas can provide narrow beams with footprints commensurate to human body.

- The penetration depth is much smaller than the wavelength. Therefore, the target can be considered as a surface and there is no need to model the internal organs.

At W-band and higher MMW frequencies, dimensions of a typical human body are very large compared to the wavelength and therefore methods based on full-wave analysis are not practical for present computers. However, the radii of curvature on human body are much larger than the wavelength which makes it a suitable candidate for high frequency methods. In addition, as will be shown later, the human skin at MMW frequencies is very lossy. Thus a homogenous dielectric can be assumed and the equivalent induced electric and magnetic currents on the surface of the body can be approximated using the physical optics (PO) model. The PO model for human body should perform well as the penetration depth is small and as a result the multipath within the dielectric body can be ignored. However, the PO approach does not account for the interactions between different body parts and, therefore, does not guarantee the accuracy of the cross-polarized response. To account for the interactions and to enhance the accuracy, the iterative physical optics (IPO) method is employed and utilized for radar backscatter analysis of human body to calculate the total scattered field and the scattering matrix of the human target.

In this chapter, first the characteristics of human body models such as the surface body models and skin dielectric constant are discussed. The PO/IPO methods along with Geometrical Optics (GO) method are introduced and their formulations are presented. Since the IPO method is very time/memory intensive, some simplifying methods are presented to reduce analysis time. Then the results of radar backscatter analysis with these methods for human bodies with different sizes/genders are presented and the feasibility of human body identification based on the radar backscatter response is discussed.

16

2.1. Characteristics of the Human Body Models

2.1.1. Dielectric constant of skin

In order to simulate the radar response of the human body at W-band and higher frequencies, it can be modeled as homogeneous dielectric material since the skin depth of the targets is less than 1 mm. The electric permittivity of the skin at MMW frequencies obtained from the Debye equation is:

$$\varepsilon_r(\omega) = \varepsilon_r'(\omega) - j\varepsilon_r''(\omega) = \varepsilon_\infty + \frac{\varepsilon_s - \varepsilon_\infty}{1 + j\omega\tau} + \frac{\sigma}{j\omega\varepsilon_\infty} \qquad (1)$$

Where $\varepsilon_\infty = 4.0, \varepsilon_s = 42.0, \tau = 6.9 \times 10^{-12}\,\text{s}, \varepsilon_0 = 8.85 \times 10^{-12}\,\text{F/m}$, and $\sigma = 1.4\,\text{S/m}$. These parameters were obtained experimentally and have been shown to provide an adequate representation of the complex dielectric constant of human skin at microwave frequencies [22]. In [23] the complex permittivity of ex-vivo sample of human skin fixed in formaldehyde was measured over the band of 60 to 100 GHz using a quasi-optical method which shows deviation from the predicted Debye model. Table I lists a number of models which present electric permittivity of the human skin. Considering the fact that human skin is very lossy at MMW frequencies, a set of in-vivo measurements have been conducted using open-ended rectangular waveguide aperture radiating into skin which is considered as a homogeneous dielectric sample with relative complex dielectric constant. In this set of measurements, a calibrated open-ended WR-10 waveguide being tightly in contact with a finger's skin was used as shown in Figure 2.1 and the S_{11} is measured. By analyzing this structure with Ansoft HFSS and tuning the value of the dielectric constant to fit the measured S_{11}, we can find the relative permittivity and loss tangent of the skin.

17

It is noticed that even for a specific person, depending on the location, the skin dielectric constant can change considerably. This variability depends on the moisture, cleanness, skin thickness, etc. The table shows some sample measurements showing this variability and a comparison with the proposed models. The Fresnel reflection coefficient at normal incidence for each value of dielectric constant is also presented. This comparison is made to indicate that the surface reflectivity is not much affected by the small variations by different models and measured values. Besides, by taking the ratio of cross- to co-polarized response - which is needed in the detection algorithm as will be shown later - this effect is even less important.

Figure 2.1. The setup for in-vivo measurement of the skin dielectric constant.

		Relative permittivity (95 GHz)	Loss tangent (95 GHz)	Reflection coefficient at normal incidence (magnitude)
Debye model [22]		6.11	1.42	0.4333
Four term Cole-Cole expression (Walters [24])		5.8	1.3	0.4218
Four term Cole-Cole expression (Gabriel [25])		7.51	1.156	0.4691
Measurement with open-ended waveguide	Sample 1	5.7	1.12	0.4163
	Sample 2	6	1.05	0.4254

Table I . The dielectric constant of human skin predicted by analytical models and measurement. The results show that the value of the reflection coefficient undergoes only maximum of 6% deviation. By taking the ratio of cross- to co-polarized response, the effect of the dielectric constant is even less important.

The University of Michigan polarimetric W-band radar system works at 95 GHz and at this frequency, skin dielectric constant (Debye model) is $6.1154 - j8.7127$. For such a medium the penetration depth is:

$$\frac{\delta}{\lambda_0} = \frac{1}{\pi}\sqrt{\frac{1}{2\,\mathrm{Im}(\varepsilon_r)}} = 0.0763 \tag{2}$$

Since the penetration depth is much smaller and radii of human body's curvature is much larger than the wavelength, and also since the skin is lossy, we can make use of PO method and model the body as a homogeneous dielectric material by equivalent surface currents. Thus a homogenous dielectric can be assumed and the equivalent induced electric and magnetic currents on the surface of the body can be approximated using the PO model.

It is worth mentioning here that most clothings appear mainly transparent at MMW frequencies. This fact is used nowadays in most prevalent MMW imaging systems installed at airports. Even for thicker clothing where attenuation can be slightly higher than the usual, the clothing alone does not increase the ratio of cross- to co-polarized ratio which is the metric we use for detection of relatively large concealed objects.

2.1.2.   Surface Human Body Models

In order to be able to analyze the radar backscatter of human body with the PO method, surface human models are required. The creation of a humanoid character suitable for use with these experiments went through several stages which consisted of: modeling,

19

rigging, animation (to model walking), subdivision, and exportation performed at the University of Michigan 3D Animation Laboratory.

The initial humanoid models were created in Autodesk's 3D Studio Max, a popular modeling and animation software package, using reference photographs of real individuals to ensure the proportions of the character were correct. 3D models are ultimately comprised of many individual triangles which are placed side-by-side to construct a surface. Using photographs these triangles were placed in strategic locations to generate the appearance of a woman. Another set of models with different size/gender made use of the MakeHuman [26] open source software package which allows for easy creation of characters at differing ages, weights, and ethnicities. We have also been provided by 3D laser radar scans of human body. However, due to instability of the laser platform, the surface models are not clean and uniform. They have holes and irregularities in different areas. To clean up, fix and convert these raw scanned data to facet surfaces, 3Matics from Materialize was used to repair scan data from the CAESAR [27] database by filling holes and fixing surface irregularities. 3D Studio Max was then used to pose, segment, and export the final dataset in a format recognized by the code. Once the preferred characteristics were set the models are exported.

A requirement of the project was to create convincing animations of a character walking for future Doppler analysis. Traditionally, these animations are done manually by talented artists who pose the body multiple times. When these poses are played back in sequence the illusion of motion is created. To ensure the highest quality with the motion, a motion capture system was used to capture the movements of a live performer which was then directly applied to the digital character. This process involved outfitting a

performer with special reflective markers, which is a lycra suit equipped with small, ball-shaped reflectors. Each reflector consists of special retroflective tape from 3M wrapped in a ball and strategically placed on the subject as shown in Figure 2.2 (a). A set of eight cameras then track these reflectors as the subject moves about with each camera having its own "view" of the captured volume. A computer communicates with each camera and cross references what the cameras "see" to calculate the position of each marker in space. Connections are made between these markers to build up a skeleton which determines the proportions of the character. Then a digital model is created based on those proportions to generate human body shape. The surfaces were created by hand using the photographs for measurements. Figure 2.2 (b) represents the reflector points captured by one camera which build a skeleton. Through this process one can animate the skeleton (a few simple objects) and have the complex humanoid mesh deform according to the position and orientation of the individual bones. This greatly simplifies the animation process as one does not need to animate each individual vertex or point in the mesh and allows for easier use of motion capture data.

The process of binding a mesh to the skeletal structure (also known as skinning) can be a lengthy task as one needs to assign each vertex/point of the mesh to the appropriate bone. In areas such as the shoulder or hips one specific points need to receive influence from multiple bones to create a smooth deformed surface, which can add to the processing time. Once the mesh has been bound to the underlying skeleton it is free to animate. For this project, the motion capture data was applied to the character and trimmed to a looping walk cycle that was 30 frames (~1 second) in length.
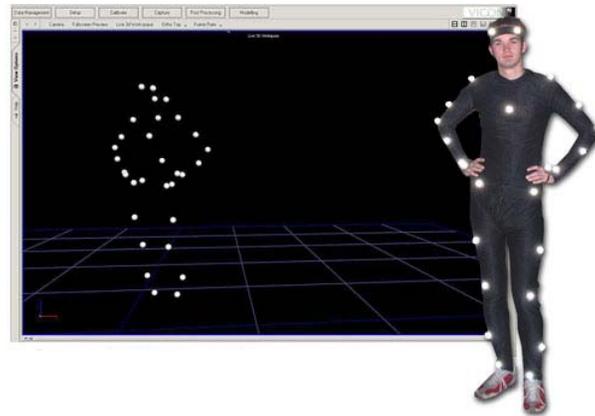
(a)
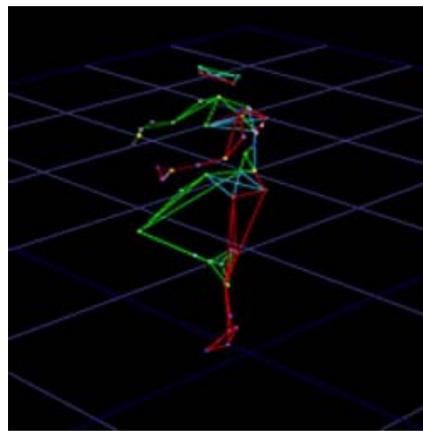
(b)

Figure 2.2. (a) A person wears the lycra suit equipped with reflectors. The captured positions of these reflectors from one of the cameras are shown in the right inset. (b) The captured positions of the reflectors estimate a skeleton.

Identifying the key parts of the mesh was a critical component of the project. As such, the model was broken into fifteen discreet parts (e.g. head, chest, abdomen, left bicep, right bicep, etc.) which were then adjusted and fitted to the same skeleton used to deform the mesh. Through an internal process the parts followed the already deforming mesh with little extra effort and were ready for further processing. Since the skinning of a character is a computationally expensive process, we could not complete the process if the mesh was at the targeted mesh density. Thus, skinning was done on a lower resolution model which was then subdivided to generate the density needed for the current experiments. Subdivision of a mesh is a fully automatic process that includes taking each

existing polygon (often limited to a quadrilateral) and dividing it into four parts. Once the individual meshes representing the various sections of the body were animated and set to the proper resolution, they were exported to the STL (stereolithography) format using a custom script written for 3D Studio Max. The developed script analyzes the existing scene and exports the mesh at each time step. Due to the complexity of the dataset, each time step often took several minutes to be written to file. This file contains the coordinates of flat facets with non-uniform sizes on the surface of human body, along with their normal vectors [28]. The total number of triangular facets varies depending on the model size and posture. The facets sizes are non-uniform, large in areas like arms and legs, middle-sized in torso, and very small in hands, toes and some parts in face as shown in Figure 2.3. Figure 2.4 represents the area of the facets in different body parts. It is noticeable that meshing is adaptive and large facets belong to legs, arms and torso areas.

However, the number of the exported frames is not enough for monitoring the motion at 95 GHz. Since the model walks around 1.8 m in one second on average, the distance between frames is approximately around 6 cm, which is much larger than the wavelength at 95 GHz. To calculate the number of frames required for the analysis, we must have information about the velocity of the fastest component of the body. Suppose we do not have any moving particle faster than v_{max}, the Doppler shift we end up with for this particle is: $2k_0 v_{max} t$. To have the minimum required samples of this function (Nyquist rate), $2k_0 v_{max} t$ must be sampled each π times. Hence we have

$$2k_0 v_{max} t_1 - 2k_0 v_{max} t_2 \leq \pi \Rightarrow 2k_0 v_{max} \Delta t \leq \pi \ \Rightarrow \ 4\pi / \lambda_0 v_{max} \Delta t \leq \pi \ \Rightarrow \ \Delta t \leq \ \lambda_0 /(4v_{max})$$

and the number of samples is:

$$n = \frac{1}{\Delta t} \geq \frac{4v_{max}}{\lambda_0} \qquad (3)$$
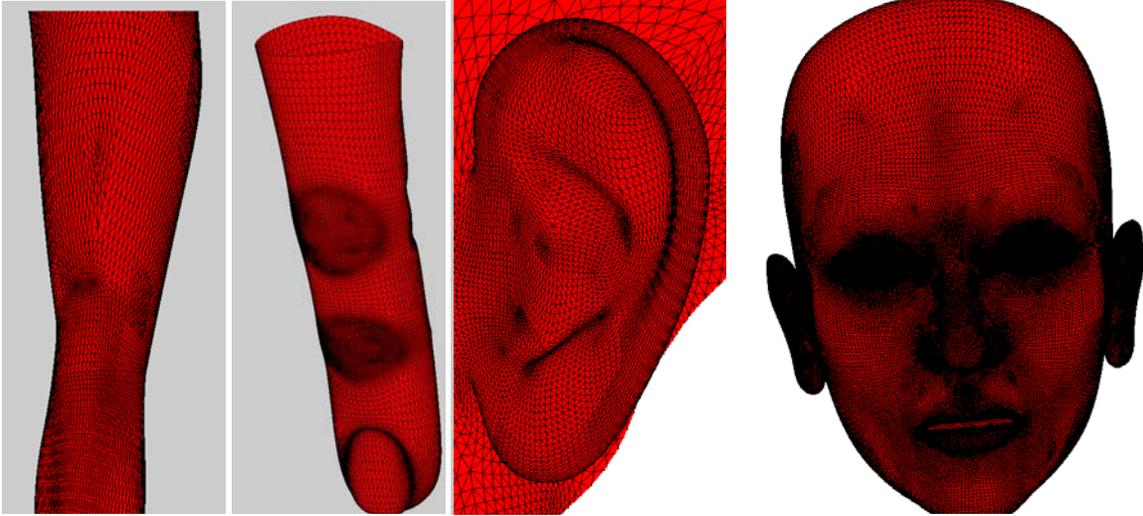
Figure 2.3.   Facet distribution in the ear, thigh, finger and face. The non-uniform descretization involves the smaller parts have finer facets (fingers and ears) while larger parts have larger facets (thighs).
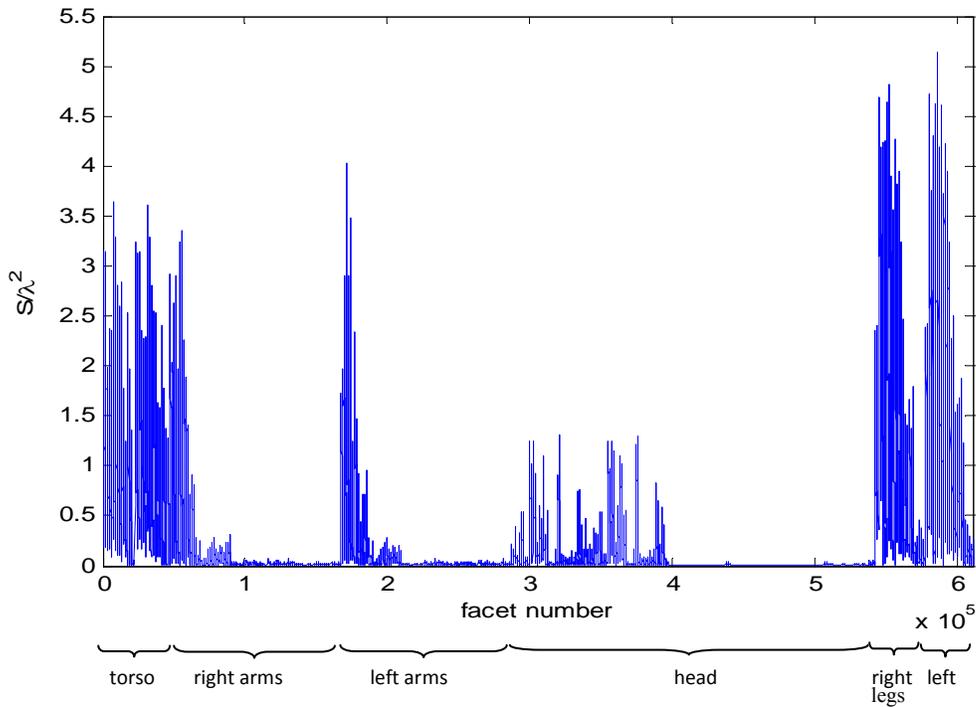
Figure 2.4. Area of 612,224 facets comprising a human body surface. The non-uniform division has led to the facet sizes distribution from $5.4\,\lambda^2$ in leg to $10^{-4}\lambda^2$ in head

Assuming v_{max}=5.5m, $n \geq 7000$. It will be proven later that the maximum velocity of any body part cannot exceed this number for our present human models. However, the process of exporting data for this large number of frames is extremely time- and memory-intensive. To resolve this issue the idea of "tweening" is used. It is the creation of intermediate frames be*tween* two key points. Here the estimation of the information of the required frames in between each two frames is performed by linear interpolation. For the human body example, if we can extract 250 frames between every two frames, a total number of 7500 frames is achieved which satisfies the Nyquist rate. The linear interpolation procedure is illustrated in Figure 2.5 for two identical facets from two adjacent sequences. The coordinates of the vertices and the normal vectors for 249 facets in between is derived as

$$A_i = A_0 + i \frac{A_1 - A_0}{250} \tag{4}$$

where $A_i = \begin{pmatrix} x_i & y_i & z_i \end{pmatrix}$. Having determined the coordinates of all the facets of the 7500 frames, the backscattering response for each facet can be calculated using PO method and the total electric field of a frame by superposing all the responses: $\vec{E}_s = \sum_{n=1}^{N} \vec{E}_s^n$ where N is the number of facets. The scattering parameters for frames can then make a sequence as follows

$$S_{xx} = \begin{pmatrix} S_{xx}^1 & S_{xx}^2 & \dots & S_{xx}^{7500} \end{pmatrix} \tag{5}$$
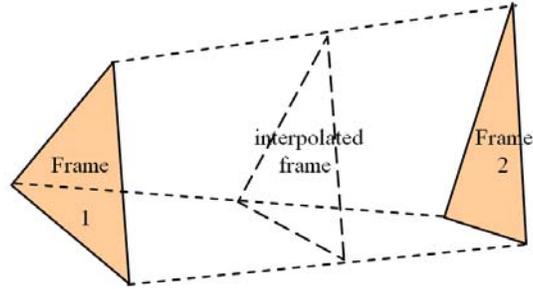
Figure 2.5. Linear interpolation is performed between each two adjacent facets from each frame in order to estimate the "in-between" frames.

where S_{xx}^i is the backscattering response of the xx component, of the ith frame. This sequence of the backscattering response generates a time domain signal which is Fourier transformed to derive the Doppler spectrum for each polarization.

In addition to analyzing different bodies with different size/genders, a walking quadruped model is also analyzed. In this analysis, a real dog (a short-haired Labrador) along with its anatomy information is used as a reference to model and animate the walking dog. The same procedure is performed and thirty frames per second in one step of walking are modeled. Then the surface of the body in each frame is discretized to triangular facets. Figure 2.6 shows the dog model and facet discretization. The same idea of tweening used here as well to compute all the required frames. The only difference is that since dog has smaller range of movements, a smaller number of frames is required to model the walking at W-band (95 GHz).

To analyze the polarimetric radar backscatter response of the individual who carries a handgun, a generic model of a handgun is also needed. For this purpose, 3D laser radar scans of a real handgun are taken. The data undergoes a similar process as above to render the surface model for a handgun as well. The model is shown in Figure 2.7.

26
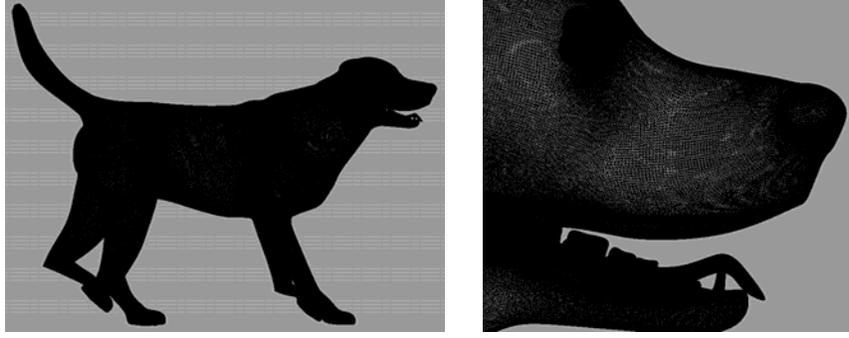
Figure 2.6. Dog model and facet distribution
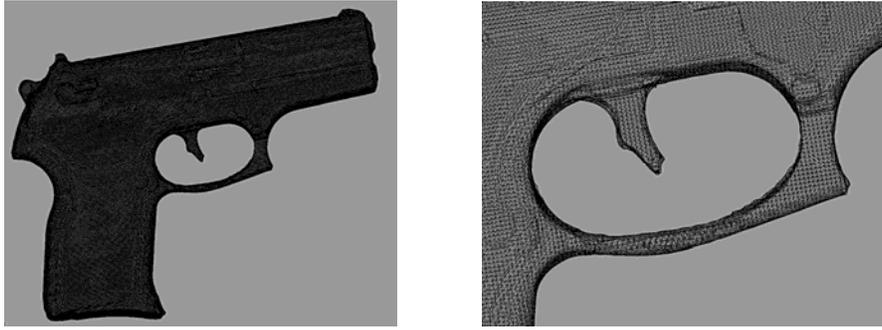
Figure 2.7. Handgun model and facet distribution

2.2.   Physical Optics / Iterative Physical Optics Approach

2.2.1.   Physical Optics

For the models consisting of flat facets, the current distribution and scattered field for each facet are modeled first. When an incident field impinges upon a flat surface, we can determine the induced currents on the surface from tangential components of fields:

$$\vec{J}_s(\vec{r}) = \hat{n} \times \vec{H}_i(\vec{r}) + \hat{n} \times \vec{H}_s(\vec{r})$$
$$\vec{M}_s(\vec{r}) = -\hat{n} \times \vec{E}_i(\vec{r}) - \hat{n} \times \vec{E}_s(\vec{r})$$

(6)

Where, $\vec{J}_s$ and $\vec{M}_s$ are induced surface currents, $\vec{H}_i, \vec{E}_i$ are magnetic and electric incident fields, while $\vec{H}_i(\vec{r}) = \vec{H}_0 e^{jk_0 \hat{k}_i \cdot \vec{r}}$, $\vec{E}_i(\vec{r}) = \vec{E}_0 e^{jk_0 \hat{k}_i \cdot \vec{r}}$ and $\vec{H}_s, \vec{E}_s$ are magnetic and

27

electric scattered fields. Taking advantage of the PO approach, one can approximate the scattered fields with reflected ones. Since the reflected fields in each surface can be calculated using Fresnel coefficients, the problem of determining induced surface currents gets much simpler using this approximation.

By assigning $\hat{t} = (\hat{k}_i \times \hat{n}) / \left| \hat{k}_i \times \hat{n} \right|$, incident and reflected fields can be written as sum of two vectors parallel and perpendicular to $\hat{t}$, as follows:

$$\vec{E}_i(\vec{r}) = (A(\hat{k}_i \times \hat{t}) + B\hat{t})e^{jk_0\hat{k}_i.\vec{r}}$$

$$\vec{H}_i(\vec{r}) = \frac{1}{Z_0}(B(\hat{k}_i \times \hat{t}) - A\hat{t})e^{jk_0\hat{k}_i.\vec{r}}$$

$$\vec{E}_r(\vec{r}) = (AR_{TM}(\hat{k}_r \times \hat{t}) + BR_{TE}\hat{t})e^{jk_0\hat{k}_i.\vec{r}}$$

$$\vec{H}_r(\vec{r}) = \frac{1}{Z_0}(BR_{TE}(\hat{k}_r \times \hat{t}) - AR_{TM}\hat{t})e^{jk_0\hat{k}_i.\vec{r}}$$

(7)

Where $\hat{n}$ is the surface normal vector, Z_0 is characteristic impedance of free space (377 Ohm), R_{TE} and R_{TM} are the Fresnel's reflection coefficients for TE and TM polarizations obtained by the following relations (ε_r is the relative electric permittivity of the surface and θ_1 is the angle of incident field relative to the surface):

$$R_{TE} = \frac{\cos\theta_1 - \sqrt{\varepsilon_r - \sin^2\theta_1}}{\cos\theta_1 + \sqrt{\varepsilon_r - \sin^2\theta_1}}$$

$$R_{TM} = \frac{\varepsilon_r \cos\theta_1 - \sqrt{\varepsilon_r - \sin^2\theta_1}}{\varepsilon_r \cos\theta_1 + \sqrt{\varepsilon_r - \sin^2\theta_1}}$$

(8)

Substituting the fields (7) into (6) and using vector algebra to simplify, we get to the following relation for surface currents [29]:

$$\vec{J}_s(\vec{r}) = e^{jk_0(\hat{k}_i \cdot \vec{r}')}\left[\frac{1}{Z_0}(\vec{E}_0 \bullet \hat{t})(\hat{n} \bullet \vec{k}_i)(1 - R_{TE})\hat{t} + (\vec{H}_0 \bullet \hat{t})(1 + R_{TM})(\hat{n} \times \hat{t})\right]$$

$$\vec{M}_s(\vec{r}) = -e^{jk_0(\hat{k}_i \cdot \vec{r}')}\left[Z_0(\vec{H}_0 \bullet \hat{t})(\hat{n} \bullet \vec{k}_i)(1 - R_{TM})\hat{t} + (\vec{E}_0 \bullet \hat{t})(1 + R_{TE})(\hat{n} \times \hat{t})\right]$$

(9)

Utilizing these equivalent currents, we calculate the electric field in the far field using the free-space dyadic Green's function as follows:

$$\vec{E}_s(r) = \frac{jk_0 e^{jk_0 r}}{4\pi r}(\overline{\overline{I}} - \hat{k}_s \hat{k}_s) \bullet \iint_S \left[Z_0 \vec{J}_s(\vec{r}') - \hat{k}_s \times \vec{M}_s(\vec{r}')\right]e^{-jk_0 \hat{k}_s \cdot \vec{r}'}ds'$$

(10)

where, $\hat{k}_s$ is the direction of observation.

This method is applicable also in simulating lossy complex targets whose radii of curvature are much larger than a wavelength. In this case one can approximate the surface of complex targets with a number of flat surfaces. The incident field can induce currents on flat surfaces calculated from (9). Therefore, superposing all scattered fields due to the induced currents on flat surfaces yields the scattered field of the complex target

$$\vec{H}_{total} = \sum_{n=1}^{N}\vec{H}_n \qquad \vec{E}_{total} = \sum_{n=1}^{N}\vec{E}_n$$

(11)

When the total scattered field of a complex target is calculated, the scattering amplitude matrix (S) can be determined as:

$$\vec{E}_s(\vec{r}_0) = \frac{e^{jk_0\hat{k}_i\vec{r}}}{r_0} S\vec{E}_i, \text{ where } \vec{E}_s = \begin{bmatrix} E_s^h \\ E_s^v \end{bmatrix}, \vec{E}_i = \begin{bmatrix} E_i^h \\ E_i^v \end{bmatrix}, S = \begin{bmatrix} S_{hh} & S_{hv} \\ S_{vh} & S_{vv} \end{bmatrix}$$

$$S_{hh} = \frac{E_s^h r_0 e^{-jk_0\hat{k}_i\vec{r}}}{E_i^h}, S_{hv} = \frac{E_s^h r_0 e^{-jk_0\hat{k}_i\vec{r}}}{E_i^v}, S_{vh} = \frac{E_s^v r_0 e^{-jk_0\hat{k}_i\vec{r}}}{E_i^h}, S_{vv} = \frac{E_s^v r_0 e^{-jk_0\hat{k}_i\vec{r}}}{E_i^v} \tag{12}$$

Where, r_0 is the distance form target to observation point. The RCS (σ) of the target is also calculated as:

$$\sigma = \frac{r_0^2 \left| \vec{E}_s(r_0) \right|^2}{\left| \vec{E}_i(r_0) \right|^2} \tag{13}$$

2.2.2.   Geometrical Optics (Shadowing Effect)

When the uniform plane wave is incident on a complex target, the areas with normal vectors in the same direction as the wavevector are shadowed. No surface currents are induced on the shadowed facets. To eliminate shadowed facets, Geometrical Optics (GO) approximation is used by applying the criterion $\hat{n} \bullet \hat{k}_i < 0$. This holds for the lit areas, where $\hat{n}$ and $\hat{k}_i$ are normal vector of the facet and wave vector of incident field. We model the lit facets with equivalent surface currents using (9), and then calculate the far electric field from (10) and scattering amplitude (12) or RCS (13).

Model Verification

Based on the aforementioned method, a PO code is generated to calculate the scattering amplitude of a lossy dielectric sphere since its analytical calculation is available to compare with our model. We are provided with a model of sphere with radius of $a = 1\ m$ which consists of 11840 equal-sized triangular facets. For the given value of dielectric constant ($\varepsilon_r = 5 + j10$ [29]), penetration depth is $\dfrac{\delta}{\lambda_0} = \dfrac{1}{\pi}\sqrt{\dfrac{1}{2\,\mathrm{Im}(\varepsilon_r)}} = 0.07$, thus the sphere is sufficiently lossy and it is reasonable to model the target with the equivalent surface currents. After locating the lit facets using $\hat{n} \bullet \hat{k}_i < 0$, we model them with equivalent surface currents using (9), and then calculate the far electric field from (10) and scattering amplitude (12) or RCS (13).
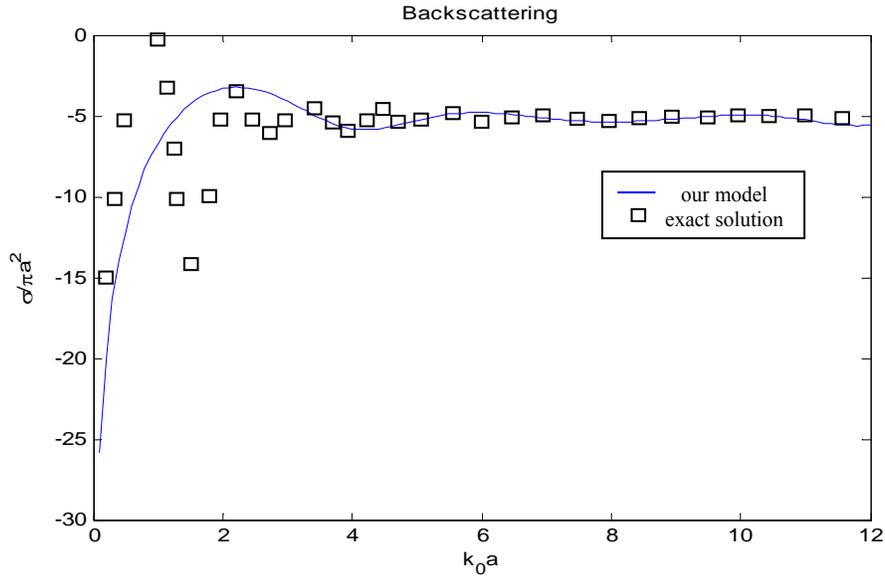
Figure 2.8. Normalized back scattering RCS of a lossy sphere with $\varepsilon_r = 5 + j10$ versus normalized frequency $k_0 a$ compared with exact solution (Figure 3.20 in [29]). It is obvious that by increasing the normalized frequency, the PO approach tends to the exact solution.
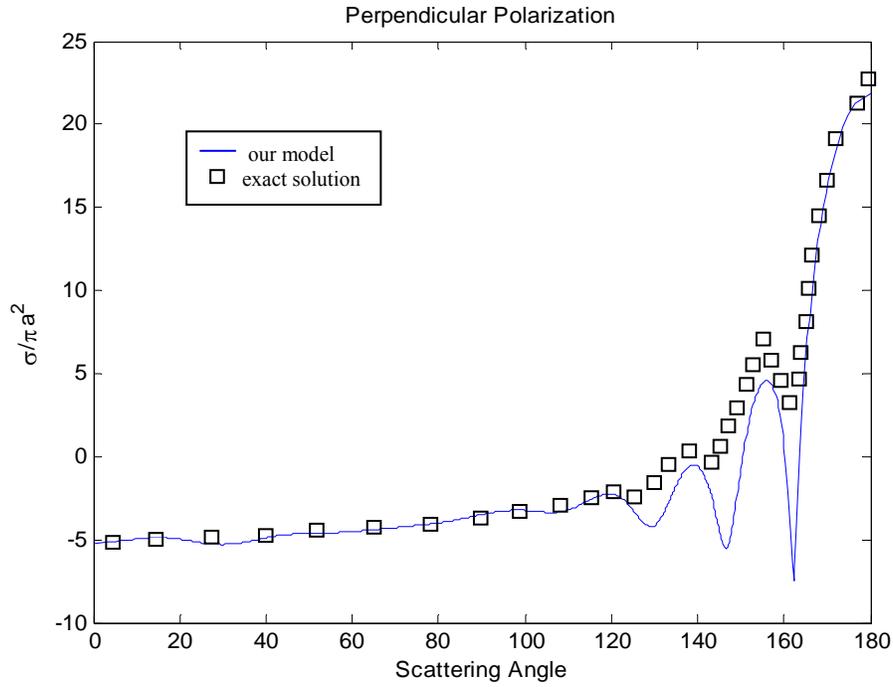
Figure 2.9. Normalized RCS of a lossy sphere with $\varepsilon_r = 5 + j10$ and $a = 2\lambda$ for perpendicularly polarized incident wave compared with exact solution (Figure 3.21 in [29]).
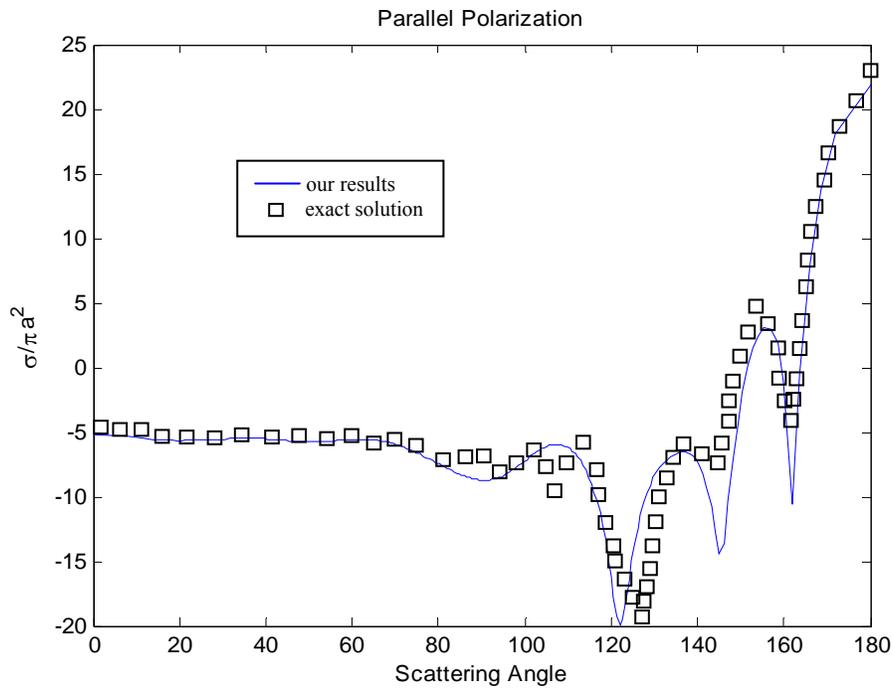
Figure 2.10. Normalized RCS of a lossy sphere with $\varepsilon_r = 5 + j10$ and $a = 2\lambda$ for parallel polarized incident wave compared with exact solution (Figure 3.22 in [29]).

Figure 2.8 to Figure 2.10 show the RCS for different angles of observation and different frequencies. The results are compared with the exact solution presented in [29] and show a very good agreement.

2.2.3. Iterative Physical Optics

The PO approach does not account for the interactions between different body parts and, therefore, does not guarantee the accuracy of the cross-polarized response. To account for the interactions and enhance the accuracy, the iterative physical optics (IPO) method is employed and utilized for human body analysis to calculate the total scattered field and the scattering matrix of the human target.

Since our objects are modeled by a number of flat surfaces, it is rational to explain the IPO method considering two flat surfaces as shown in Figure 2.11. To account for the interaction between two flat surfaces, first we calculate the first order currents using Eq. (6). These currents reradiate and hence induce second order currents on each other. Hence, each surface has two sources of induced currents: from incident field and from other facets reradiating. Consider calculating the interaction of surface 1 with surface 2. The fields induced on surface 2 due to first order currents on surface 1 is calculated as [30]:

$$\vec{H}_{2,1}^{\sec ond}(r,\vec{J}_1^{first}(\vec{r}'),M_1^{first}(\vec{r}')) = \iint_S \vec{J}_1^{first}(\vec{r}') \times \nabla g_0 ds + \frac{1}{jk_0 Z_0}\nabla \times \iint_S \vec{M}_1^{first}(\vec{r}') \times \nabla g_0$$

$$\vec{E}_{2,1}^{\sec ond}(r,\vec{J}_1^{first}(\vec{r}'),M_1^{first}(\vec{r}')) = -\iint_S \vec{M}_1^{first}(\vec{r}') \times \nabla g_0 ds + \frac{1}{jk_0 Y_0}\nabla \times \iint_S \vec{J}_1^{first}(\vec{r}') \times \nabla g_0 ds \qquad (14)$$

33

Where g_0 is the free space Green's function: $g_0 = \dfrac{e^{jk_0 r}}{4\pi r}$, Z_0 and Y_0 are the free space

impedance and admittance and $\vec{r}, \vec{r}'$ are positions of surface 2 and 1, respectively as

shown in Figure 2.11.

Therefore, the induced second order currents on surface 2 are calculated from the

tangential component of second order fields:

$$
\vec{J}_2^{\,second}(\vec{r}) = \hat{n} \times \vec{H}_{2,1}^{\,second}(\vec{r}, \vec{J}_1^{\,first}, \vec{M}_1^{\,first})
$$
$$
\vec{M}_2^{\,first}(\vec{r}) = -\hat{n} \times \vec{E}_{2,1}^{\,second}(\vec{r}, \vec{J}_1^{\,first}, \vec{M}_1^{\,first})
$$

(15)

And the total induced current in the second order scheme is written as:

$$
\vec{J}_s^{\,total}(\vec{r}) = \vec{J}_s^{\,first}(\vec{r}) + \sum_{n=1}^{N} \vec{J}_{sn}^{\,second}(\vec{r})
$$
$$
\vec{M}_s^{\,total}(\vec{r}) = \vec{M}_s^{\,first}(\vec{r}) + \sum_{n=1}^{N} \vec{M}_{sn}^{\,second}(\vec{r})
$$

(16)
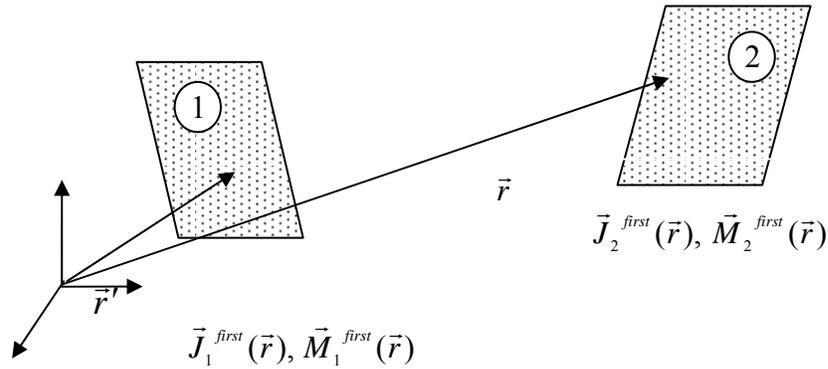
Figure 2.11. The interaction between two flat facets.

The induced fields in one facet are calculated by superposing all the interactions as:

$$\vec{H}_{m,total}^{\,second} = \sum_{n=1,\neq m}^{N} \vec{H}_{m,n}^{\,second} \qquad\qquad \vec{E}_{m,total}^{\,second} = \sum_{n=1,\neq m}^{N} \vec{E}_{m,n}^{\,second} \qquad\qquad (17)$$

Where $\vec{H}_{n}^{\,second}, \vec{E}_{n}^{\,second}$ are the fields on facet m due to currents on facet n which are presented for prototype facets 1 and 2 in Eq (14) and N is the number of facets.

The iterative procedure is continued until the total currents converge. It is shown that due to free space losses during interaction, higher order field components are trivial and currents converge very soon, especially for our object of interest, human body, in which the component sizes are much larger than a wavelength.

Model Verification

In order to verify the above IPO scheme a 90^0 dihedral corner reflector is analyzed and the results are compared with those of [31]. The structure consists of two square PEC surfaces perpendicular to each other. The simulation is done at 9.4 GHz and the results of the second order PO are used to calculate the RCS for the dihedral corner reflector which is shown in Figure 2.12. The results show good agreement with that of UTD presented in [31].
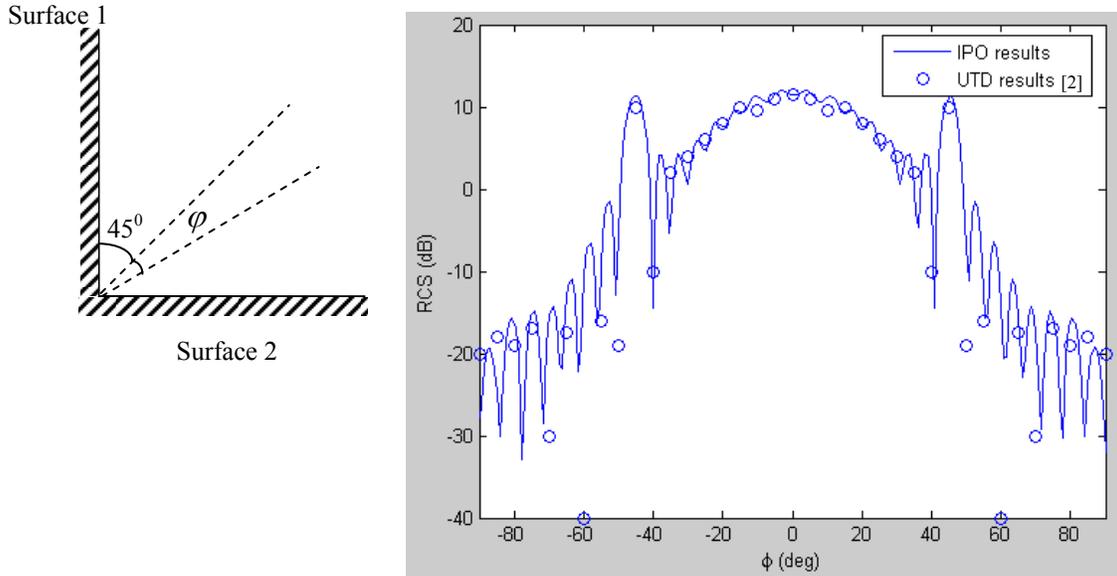
Figure 2.12. RCS of 90^0 PEC dihedral corner reflector with dimensions $5.6988\lambda \times 5.6988\lambda$ at 9.4 GHz in [31] compared to IPO results.

2.2.4. Human Body Analysis

The number of facets on the surface of human bodies range from 700,000 to 1,300,00 for different human body models in order to well accommodate the curvatures of the bodies. According to Eq (17), if N is the number of operation for each facet, calculating all the interactions is in the order of N^2 while for the first order PO we had one operation for each facet and calculation was in the order of N. This number of operations for higher order PO increases the amount of processing time drastically. Basically, if the time needed for each facet's interaction to be completed is 5 seconds on average – which is the limit for the current machine (quad-core AMD CPU 1.25 GHz, 8 GB RAM) – each simulation for any given orientation of incident field will take 75 days for 1,300,00 facets. This huge work load makes us revise the approach and take advantage of some features in human body to make the IPO analysis achievable.

36

2.2.4.a.   Simplifications for the IPO Analysis

Impedance Boundary Condition (IBC)

The lossy nature of human skin introduces a relationship between induced electric and magnetic fields on the surface:

$$\vec{E} = Z_s\, \hat{n} \times \vec{H} \tag{18}$$

Which is called impedance boundary condition (IBC). In this formula, Z_s is the surface impedance of the skin and is given by: $Z_s = \sqrt{\dfrac{j\omega\mu}{\sigma + j\omega\varepsilon}}$ in which the parameters are those of the body skin.

As mentioned, calculating Eqs (14) along with (17) is very time consuming. Eq. (18) which relates electric and magnetic fields on the surface helps us eliminate one of the Eqs (14). We can calculate E field from (14) and find H field simply using (18) or vice versa. This halves the amount of computations we initially needed to perform.

The Distance of Interaction

As the field components attenuate by a factor of $1/k_0 r$ in free space and the wavelength is much smaller than our object sizes, in many cases the fields radiating from a facet vanish even before they reach another facet to begin interacting when they are far from each other. Therefore, those interactions which undergo more than -40dB loss during propagating in free space can be ignored. This criterion yields the maximum distance in with interaction can happen as follows:

$$20\log(1/k_0 r) < -40 \Rightarrow (1/k_0 r) < 0.01 \Rightarrow r > 100/k_0 \tag{19}$$

Which gives $r > 5\,cm$ at 95GHz. This means in $5\,cm$, the field is attenuated around -40dB and is almost trivial; hence if there is a facet in the vicinity above this distance, the interaction is almost zero. This results in eliminating the interaction among facets which are farther than $5\,cm$ from each other

Far- Field Calculation

Eqs. (14) are exact formulations to calculate electric and magnetic fields from currents. Depending on the distance of surfaces compared to wavelength they radiate either in their far- or near- field zones. In case they are far enough, we can use the approximate far-field formula instead of using the exact formula:

$$\vec{E}_2^{first}(r, \vec{J}_1^{first}(\vec{r}'), M_1^{first}(\vec{r}')) = \frac{jk_0 e^{jk_0 r}}{4\pi r}(\bar{\bar{I}} - \hat{k}_s \hat{k}_s) \bullet$$
$$\iint_S \left[Z_0 \vec{J}_1^{first}(\vec{r}') - \hat{k}_s \times \vec{M}_1^{first}(\vec{r}') \right] e^{-jk_0 \hat{k}_s \cdot \vec{r}'} ds' \tag{20}$$

The criterion for the far-field region of a flat surface is given by $2D^2/\lambda$, where D is the maximum length of the surface. The facets' sizes in our model are mostly smaller than $\lambda/2$ and very few facets are longer than $\lambda/2$. These facets are located in areas like thigh and torso. As we know these areas are convex and do not generate second order response in the surrounding areas and are too far from other areas to have any affect. So if we consider $\lambda/2$ as the largest facet size, the far-field criterion will be $\lambda/2$. The upper limit of 2λ is hence considered which is around 6mm and considering the size of human body and distances between components, we conclude that most parts are within

the far-field region of each other which again simplifies the calculation by letting us use far-field approximation instead of Eqs. (14).

Domination of Response in Specular Direction

As it is proved [32], in the specular direction, the coherent component of the scattered field is dominant. This gives rise to criterion for dominant facets as: $\hat{n} \cdot (\hat{k}_i - \hat{k}_s) \approx -1$, where, $\hat{n}$ is facet's normal vector and, $\hat{k}_i$, and $\hat{k}_s$ are the direction of incident (from another facet) and observation. Therefore, only facets which fall in this criterion depending on the direction of incident field are considered for analysis.

Using all the above simplifications, the radar backscatter response of a human body (a thin female model) was calculated. The RCS around the body was calculated by illuminating the object by a uniform plane wave at different orientations and finding the scattered field for each angle as shown in Figure 2.13. Figure 2.14 represents the qualitative first and second order current distribution on human body for illumination from the front side ($\varphi = 90^0$ in Figure 2.13). As expected there are no induced currents in the back part of the body and near the shadow region the surface currents diminish gently. In the second order current distribution in Figure 2.14 (b), all the dark blue parts have zero second order currents, i.e. convex areas like thighs and torso. By investigating the current distribution on the head presented in Figure 2.15, it is observable that second order currents have peaks in some specific areas like lips and around eyes, and almost zero current everywhere else
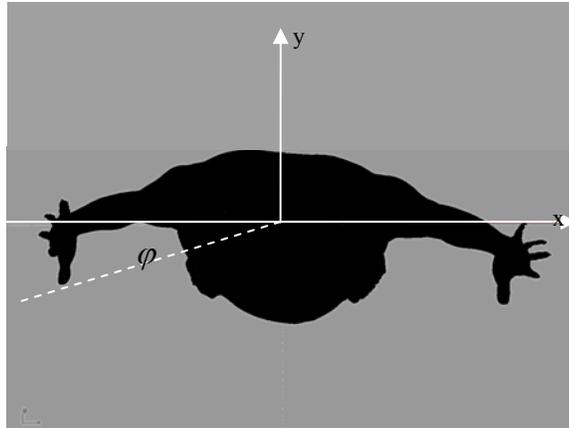
Figure 2.13. Human body is illuminated in different orientation. For each orientation the scattered field and radar cross section are calculated.

side view   front view

(a)   (b)
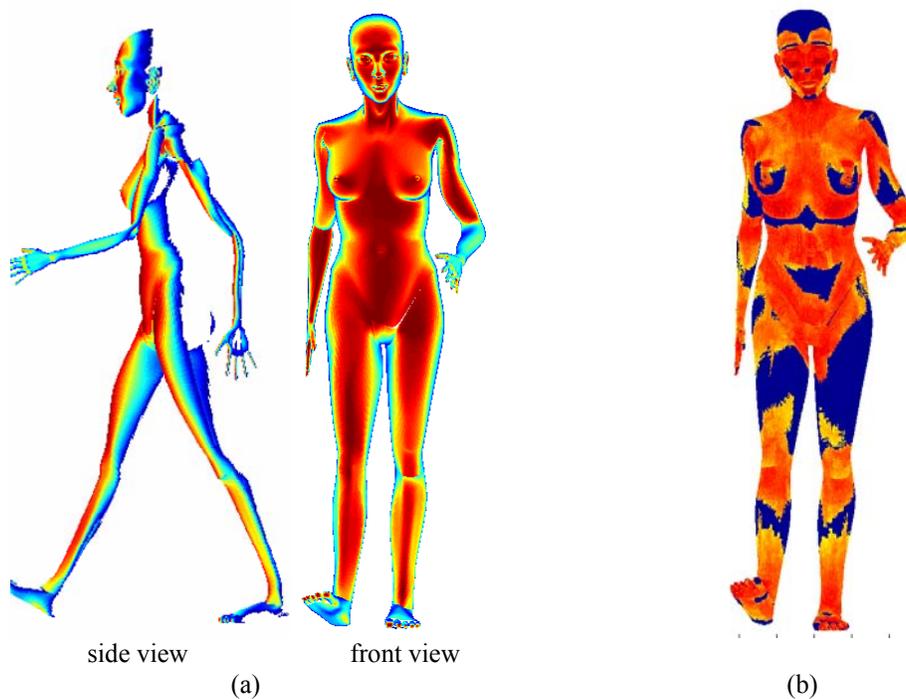
Figure 2.14. (a) First and (b) second order electric current distribution on human body when it is illuminated from the front side. The second order distribution is represented in log-scale.

To have a better understanding of the second order current distribution, we presented it in logarithmic scale in Figure 2.16. These figures show that in convex areas like the top of the head no current is induced which is expected, but in all irregular areas like around nose, eyes, lips and ears they are nontrivial.

40
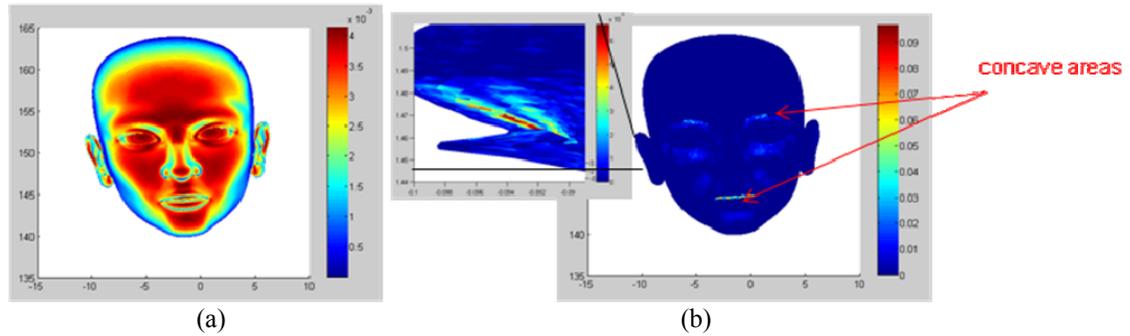
Figure 2.15. (a) first and (b) second order current distribution on human head. First order currents are distributed almost everywhere which in not shadowed and have larger amplitudes in the areas which are more perpendicular to the direction of propagation. Second order currents are concentrated on concave and irregular parts.
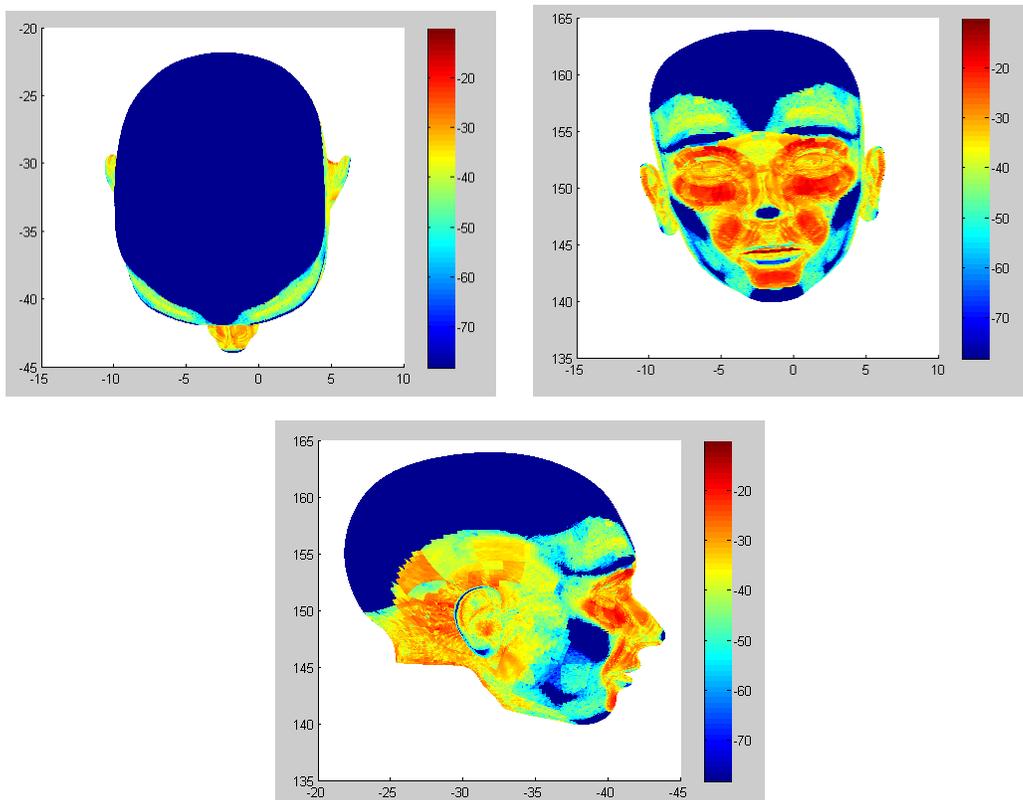
Figure 2.16. Second order electric current distribution in log-scale. It is observable that current is zero in convex areas like head, and is concentrated in irregular areas like around nose, eyes, ears, and upper chin. Convex areas in face like cheeks, chin, forehead and eyebrows have also zero induced currents.

The above current distributions are for the case of normal 90^0 incident angle. However, when the incident angle deviates from 90^0, some parts of body might shadow the other

parts. For example when $\varphi = 0^0$, the right arm shadows the torso and part of the thigh, the torso shadows the left arm, and the right leg shadows the left leg. These shadowed parts are not simply covered by GO method, since that method deals with shadowed part which does not see incident field originally not because they are hidden by other body parts. To find these shadowed parts, first we need to find out the order of the body components with respect to the direction of illumination. All the body components are partially shadowed, hence we need to find the projection of each part on the other considering a specific orientation of the incident wave. Figure 2.17 represents the lit areas of the body for $\varphi = 0^0$ incident angle. As it is shown, the right arm and the head are completely lit (except for their back parts in which the shadowed areas are found using GO method. The right-hand shape hole is observed in torso and in a part of the right leg shows these parts are shadowed by the right hand. The left leg and arm are mostly covered so that only some parts of fingers are shown. Exactly opposite of this happens when illumination angle is $\varphi = 180^0$.
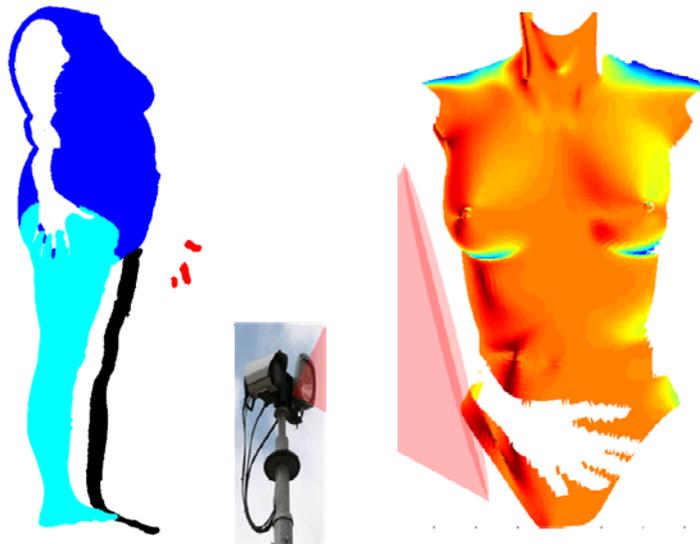
Figure 2.17. Illuminated and shadowed parts of the body for $\varphi = 0^0$ incident angle.

Once the shadowed parts are located, we calculate the current distributions, far fields, scattering amplitude and RCS respectively. The first order PO results are presented in Figure 2.18. The results show the difference between co- and cross-polarized results ranging from -20 to -30 dB.

For the IPO analysis, using all the aforementioned simplifying conditions to expedite the processing time, the second order iteration was computed and is shown in Figure 2.19 for a range of incident angles ($\varphi = 90^0 \sim 140^0$). It is shown that the co-polarized results are almost unchanged and are not affected by the higher order interactions. However, the cross-polarized results are definitely increased for all the angles to up to 5dB. This is mainly due to the fact that most of the cross-polarized response comes from the higher order interactions, since the first order PO is not likely to yield reliable cross-polarized responses. With the increase in cross-polarized response, the ratio of cross- to co-polarized response increases to -15 to -25 dB.
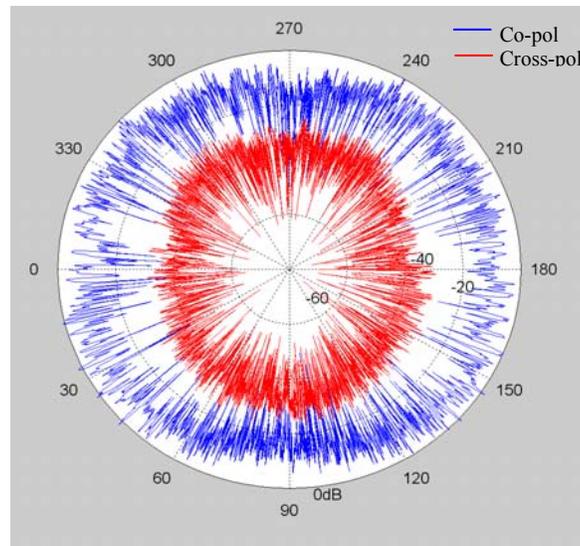
Figure 2.18. Human body RCS, first order results.
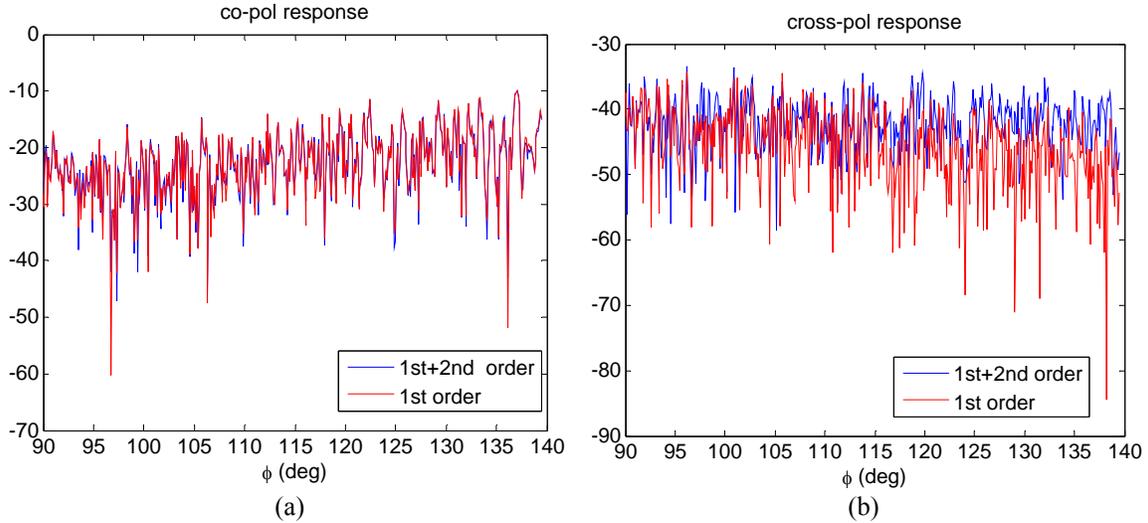
Figure 2.19. Co- and cross-polarized responses from the first and second iterations.

2.2.5.   Identification of Human Bodies with Different Sizes / Genders

In addition to the thin female model, three other human models with different sizes/genders as shown in Figure 2.20 are analyzed. The sizes of models are around the normal human body's for the average oversize and thin women and men.

Figure 2.21 shows the current distribution on the surface of the oversize female body when the plane wave illumination is in the normal incident angle from the front side. The distribution is qualitatively similar to that of the thin body. The IPO simulation results for all four models are presented in Figure 2.22. It is noticeable that for larger targets (oversize man and woman), the level of the response is higher. Table II represents the average value of the responses over the circumference. Male targets have around 1~2 dB higher co-polarized responses compared to the female targets of the same size. For each gender, the responses of the oversize and thin samples have around 3~4 dB amplitude difference.
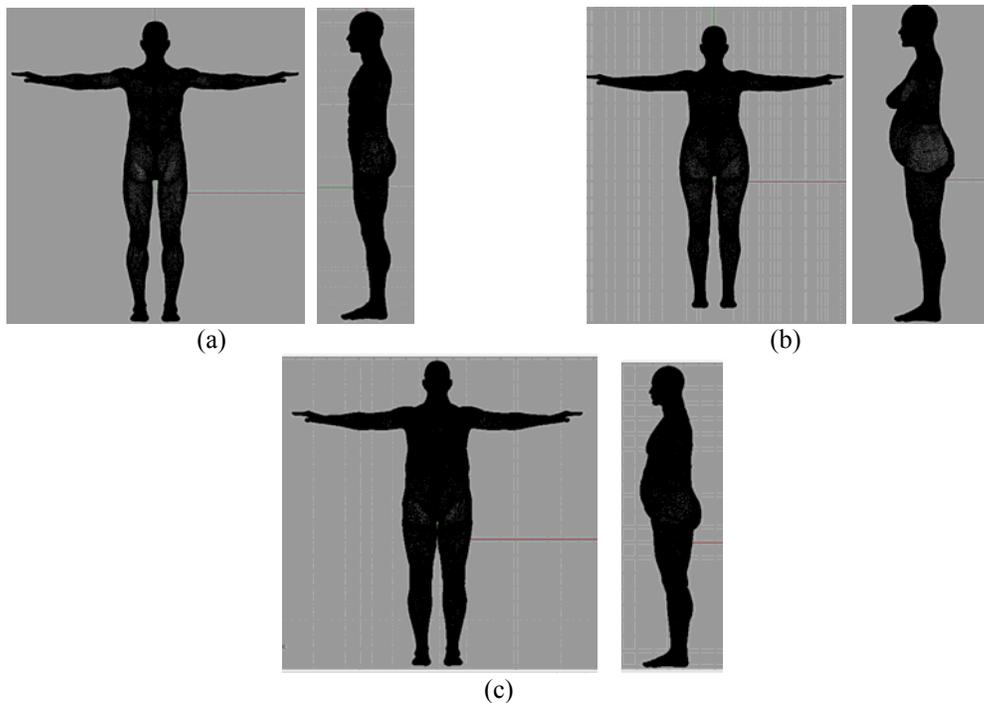
Figure 2.20. (a) thin man (b) oversize woman (c) oversize man models, front and side views.
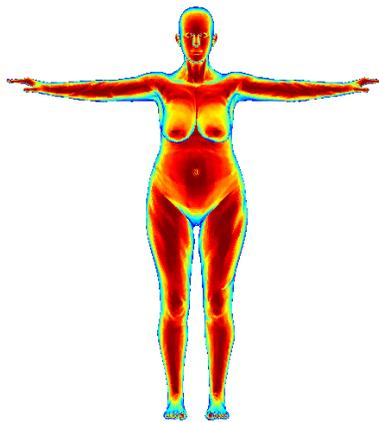
Figure 2.21. The qualitative current distribution on the surface of the oversize woman model

The RCS results for the oblique incident angles ($\theta = 10^0$ and 20^0) have also been calculated by considering the effect of the ground plane. To analyze the effect of ground, we consider a soil surface with the dielectric constant reported in [33]. There different mechanisms are involved in order to evaluate the backscattering response when the ground plane is considered as described in Figure 2.23:
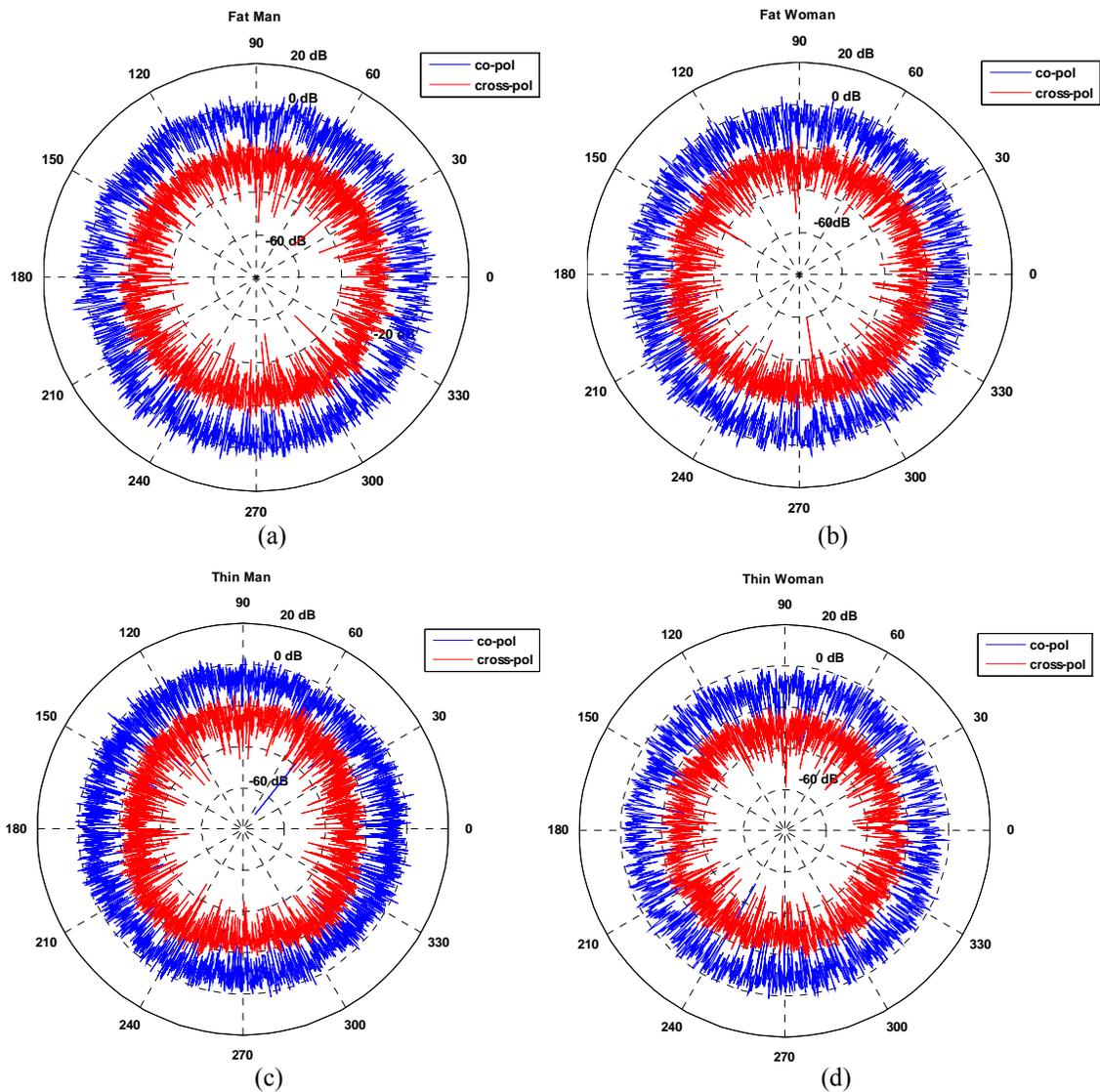
Figure 2.22. The IPO responses for (a) oversize man (b) oversize woman (c) thin man and (d) thin woman targets at $\theta = 0^0$ incident angle. Different amplitude level can be observed for different sizes and genders

	Oversize man	Oversize woman	Thin man	Thin woman
Co-polarized response (dB)	-1.6708	-3.6867	-5.0897	-6.3874
Cross-polarized response (dB)	-21.4106	-22.5764	-22.8746	-25.2444

Table II. The average values of the co- and cross-polarized responses of different human bodies. The higher amplitude for the larger size targets is noticeable.

(a)   (b)   (c)
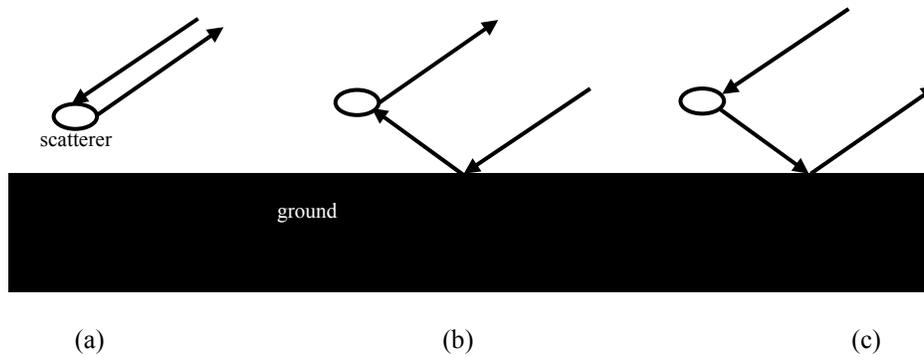
Figure 2.23. backscattering response of the target in the present of the ground plane includes: (a) the backscattering response of the target (b) the response of the target when the incident field is the reflected wave from the ground plane (c) the scattered field of the target is reflected by the ground plane and makes a backscattering response.

- the backscattering response of the target itself as calculated in the previous cases

- the response of the target when the incident field is the reflected wave from the ground plane

- when the scattered field of the target is reflected by the ground plane.

The simulation results for oblique incident angles considering the effect of the ground plane are presented in Figure 2.24 and Figure 2.25. In these cases, the level of the cross-polarized response increases, while the same difference in the level of the amplitude of the co- and cross-polarized responses for different genders and sizes are noticeable as represented by the averages in Table III.
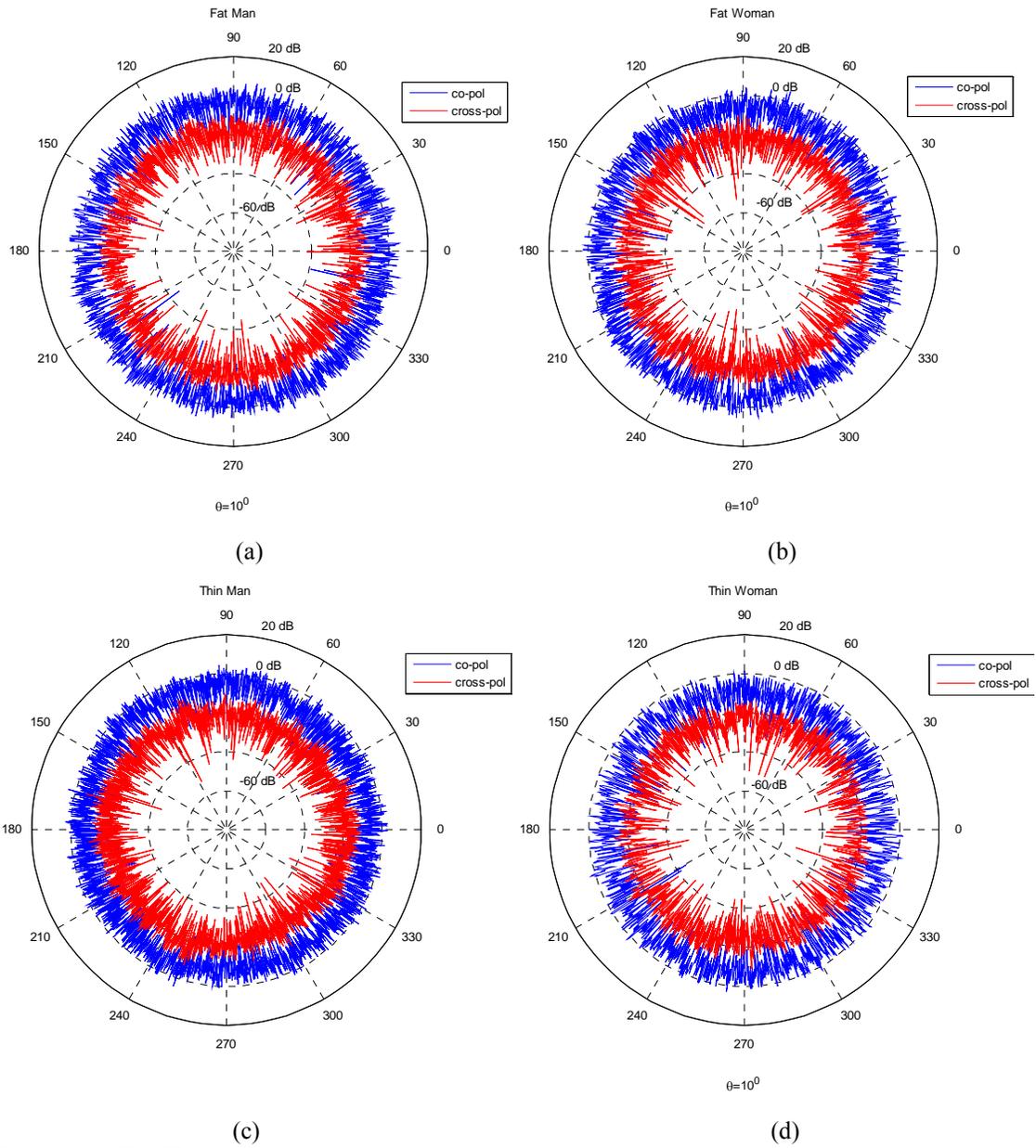
Figure 2.24. The IPO responses for (a) oversize man (b) oversize woman (c) thin man and (d) thin woman targets at $\theta = 10^0$ incident angle. Different amplitude level can be observed for different sizes and genders.
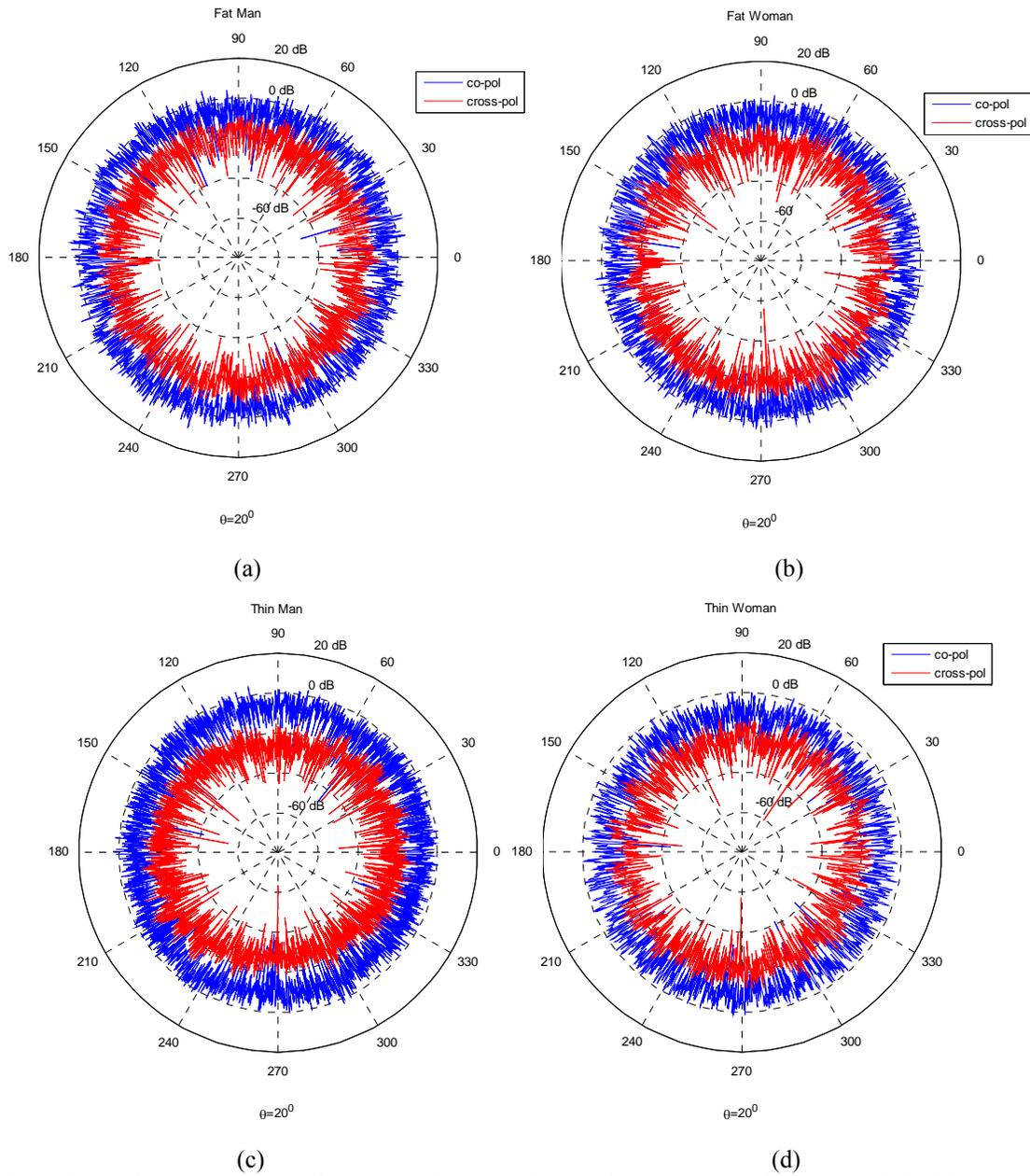
Figure 2.25. The IPO responses for (a) oversize man (b) oversize woman (c) thin man and (d) thin woman targets at $\theta = 20^0$ incident angle. Different amplitude level can be observed for different sizes and genders

	Oversize man	Oversize woman	Thin man	Thin woman
Co-polarized response (dB) $\theta = 10^0$	-1.3710	-3.3538	-4.5742	-5.9942
Cross-polarized response (dB) $\theta = 10^0$	-15.5885	-17.9967	-16.4556	-16.9262
Co-polarized response (dB) $\theta = 20^0$	-2.4570	-4.4897	-5.7288	-5.9926
Co-polarized response (dB) $\theta = 20^0$	-15.0269	-16.9910	-15.8153	-16.9188

Table III. The average values of the co- and cross-polarized responses of different human bodies for $\theta = 10^0$ and $\theta = 20^0$

2.3. Conclusion

In this chapter, the radar backscatter analysis of human bodies at W-band was presented. First the characteristics of human body models and the feasibility of using PO/IPO method for human body analysis were investigated. The formulation of PO/IPO and GO approach and a simplified formulation of IPO approach for human body analysis were presented and discussed. The radar backscatter responses for different human bodies with different sizes/genders were calculated and the feasibility of identifying size/gender was discussed. It was shown that the larger targets (oversize man and woman) have higher level of RCS response and the male targets have around 1~2 dB higher co-polarized responses compared to the female targets of the same size.

Chapter III

Doppler Spectrum / Concealed Object Detection

The human targets in the radar scene are commonly moving when they are under radar interrogation, such as in walking, jogging, or running human subjects or animals, and therefore, their style of motion suggests some means of identification. Doppler radars are employed to capture the motion of the targets and unlike electro-optical measurements; the response of radar cannot be directly visualized and needs to be post-processed. One way is using imaging radars. Another way is investigating the radar signature from different angles or directions. In [34], a method is proposed to extract motion parameters from radar measurement by minimizing the difference between the simulated model and real measurements.

The field scattered from a moving subject undergoes Doppler modulation of a particular signature as a result of the object motion. The index of modulation is proportional to the level of backscatter from different parts of the body in addition to their relative velocity to the body centroid. The overall Doppler spectrum is shifted up/down depending on the radial velocity of the body centroid with respect to the radar platform. Hence the unique features of motion and the radar backscatter contribution of different body parts are rather accurately captured by the Doppler spectrum and can be exploited for target identification.

The Doppler signature can not only be used to distinguish a human from the rest of the radar scene, but it can also be used to isolate the radar backscatter from different parts of

the body. Feature extraction of body movements and human gait recognition based on Doppler radar has been investigated at lower microwave bands [13], [35]- [38] qualitatively where the human body is modeled by a simple uniform dielectric volume or unsophisticated models of homogeneous cylindrical and spherical objects. In [38], the features were extracted using the time-frequency transform of the response measured by a 24 GHz Doppler radar. The possibility of discriminating between human gait and those of other objects based on step rate and mean velocity was investigated as well.

The feasibility of detection of concealed carried objects by human body has also been investigated with different techniques. Traditional detection systems include metal detectors and X-ray systems. The latter has hazardous health effects when used on humans, while the former can only be used in situ for detecting metallic objects. More elaborate systems employ imaging techniques to identify the target and detect contraband. These systems have been very effective, but have a number of shortcomings, such as requiring close proximity to the subject, slow processing, violating the privacy of individuals, and giving low-quality blurred images in a heavily cluttered environment. In [13], detection was investigated at low microwave frequencies and slight decrease in the amplitude of the radar return is used to detect the presence of a rifle against a human body. However, for such techniques to be successful the response of the human must be isolated from its surrounding, the radar needs to be radiometrically calibrated, and the RCS of the human subject at the proper aspect angle and posture without the rifle must be known. Considering the fact that the number of conditions one may encounter (different body and object sizes and shapes) is enormous, algorithms that rely on quantitative RCS values cannot be very reliable. To circumvent these difficulties to some extent the

application of polarimetric radars is proposed for which narrow beams with footprints commensurate to the human body can be generated. Also using radar polarimetry, radiometric calibration will not be required. However, at lower microwave frequencies, the human body can depolarize the backscatter signal considerably and therefore the cross-polarized signature cannot effectively be used. In addition, for narrow beamwidths, very large antennas are required. At high MMW frequencies, the amount of co-polarized backscatter response is dominant for smooth targets and cross-polarized response represents the level of smoothness and symmetry of the target. Uneven and asymmetric targets generate greater cross-polarized response. The geometries of common concealed objects carried by individuals are highly irregular and, once placed near human body, can indeed increase the level of cross-polarized backscatter observed by MMW radars. Therefore, at higher MMW frequencies, a significant increase in the cross-polarized response can be an indication of an external irregular object and can be used for detection.

In this chapter, the radar backscatter responses of walking human bodies as a function of time at W-band are calculated. The Doppler spectra of the bodies are obtained by performing a Fourier transform of the backscatter response and the feasibility of identifying different body sizes/genders and walking dog based on the characteristics of the Doppler spectra are investigated. Then a radar backscatter decomposition algorithm is presented to isolate the response of torso in order to be able to measure the cross-polarized response of the torso. It is verified that the higher cross- to co-polarized response of torso is an indication of the presence of irregular external object. This is also experimentally verified by measuring the RCS of the human torso at the W-band. The

chapter concludes by presenting the radar backscatter analysis of the walking body at Y-band.

3.1. Radar Backscatter Analysis of a Walking Human Body

In order to simulate the radar response of the targets in motion, detailed realistic models are developed by the University of Michigan 3D Animation Laboratory as described before and shown in Figure 3.1. To calculate the scattering amplitude of this model we first select lit facets using GO. Then, the lit facets are modeled by equivalent surface currents using (9) knowing facets' coordinates, normal vectors, and also sizes. Once the surface current distribution for all 7500 frames are calculated, far electric field can be computed from (10) and scattering amplitude from (12).
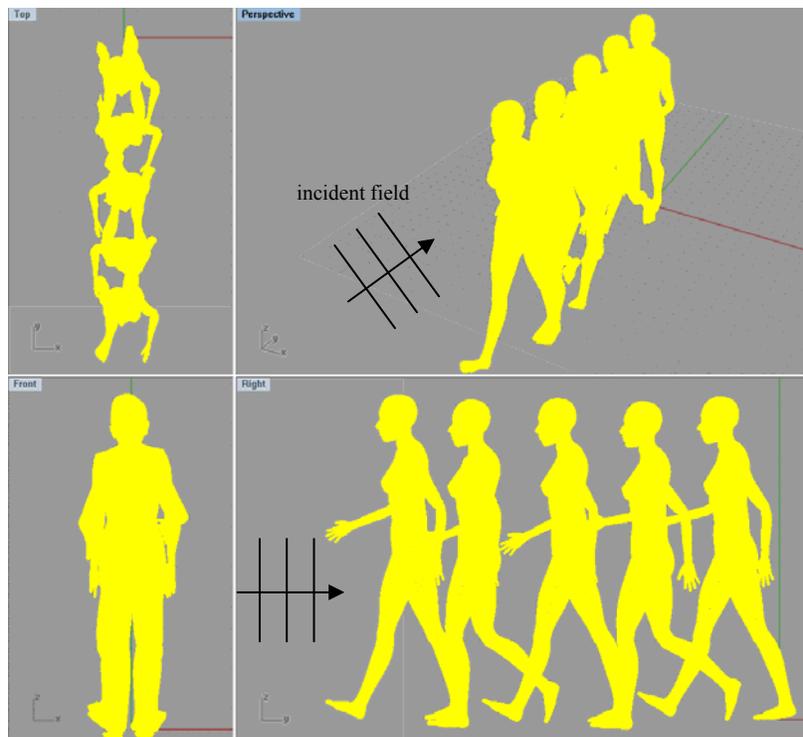
Figure 3.1. Moving human body is illuminated by a monostatic radar in the same direction as walking.

54
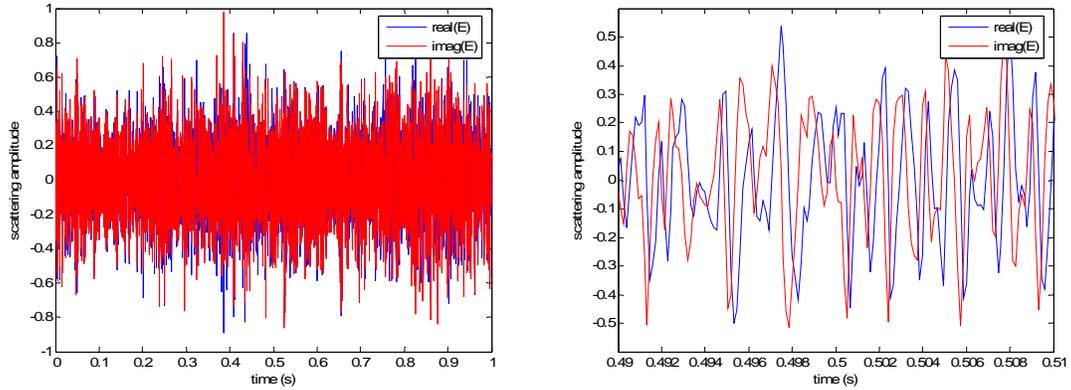
Figure 3.2 Time domain variations of scattering amplitude of the walking human body of Figure 3.1.

(a)

(b)

(c)
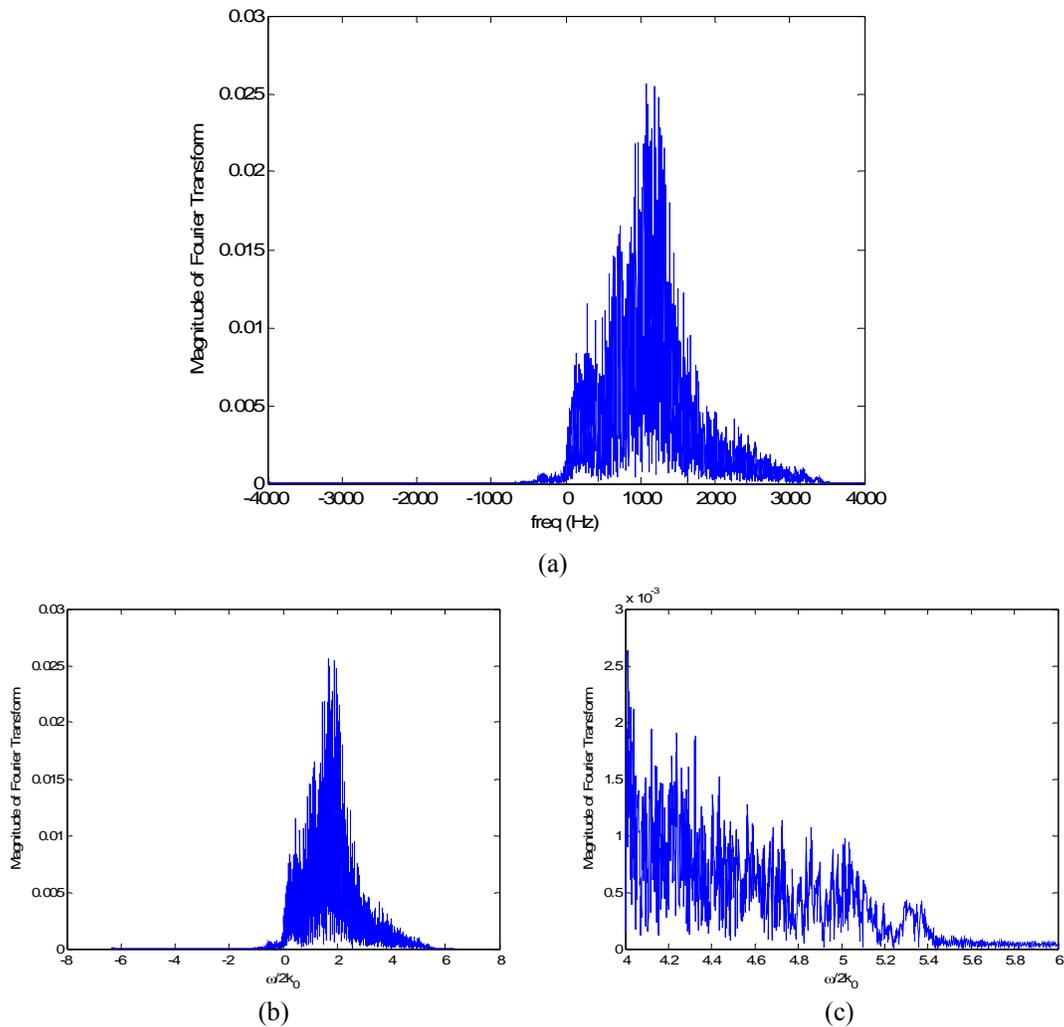
Figure 3.3. (a) Fourier transform of scattering amplitude of human walking. (b) Fourier transform of scattering amplitude of human walking versus $\omega_0/(2k_0)$ to give the velocities. It can be seen that it has peaks around its average velocity (v=1.8 m/s) from 1.4 to 2.1m/s. (c) the extended plot to find maximum velocity which is approximately 5.3m/s.

55

The calculated scattering amplitude versus time (scattering amplitude for a sequence of frames) is represented in Figure 3.2. Performing a Fourier transform on this function yields the Doppler spectrum of a human walking. The Doppler spectrum of a human walking is shown in Figure 3.3 (a) and versus $\omega_0 /(2k_0)$ in Figure 3.3 (b) to represent the velocity content of the human motion. As can be observed, the bandwidth of the spectrum extends from around -630 Hz to +3400 Hz corresponding to a wide range of velocity values from -1 m/s to +5.4 m/s. The negative velocities come from the backward motion of legs and arms which is partly compensated with the average positive velocity. The amplitude is maximized around the average velocity of +1.8 m/s. The power density around the average velocity (mean Doppler shift) is dominated by the torso return. The maximum velocity is about +5.4 m/s. Therefore, the accuracy of the assumed maximum velocity and the resulting sampling rate is confirmed. We have also simulated different parts of the body separately in order to isolate and study the individual responses. The body is separated into six parts based on the difference in the style of motion, including the torso, the head, the left and right legs and arms. The simulation results are presented in Figure 3.4. Investigating the spectra, we realize that the spectra of the head and torso are very similar since the way these components movements are alike except for the fact that the torso response has higher level given its larger cross section. The spectra extend from +1.5 to +2.1 m/s, around the average velocity. To simulate these parts separately, v_{max} is chosen to be +2.1 m/s. This implies that fewer frames are required and processing time is shorter. On the other hand, the limbs contain higher frequency content and hence higher velocity values, as expected from their movement. The hands' and arms' spectra extend from -1 to +4 m/s with lower levels while the spectra of the legs extend from 0 to

56

5.4 m/s with higher backscatter levels. It can be inferred from the results that the fastest motion occurs at the feet.
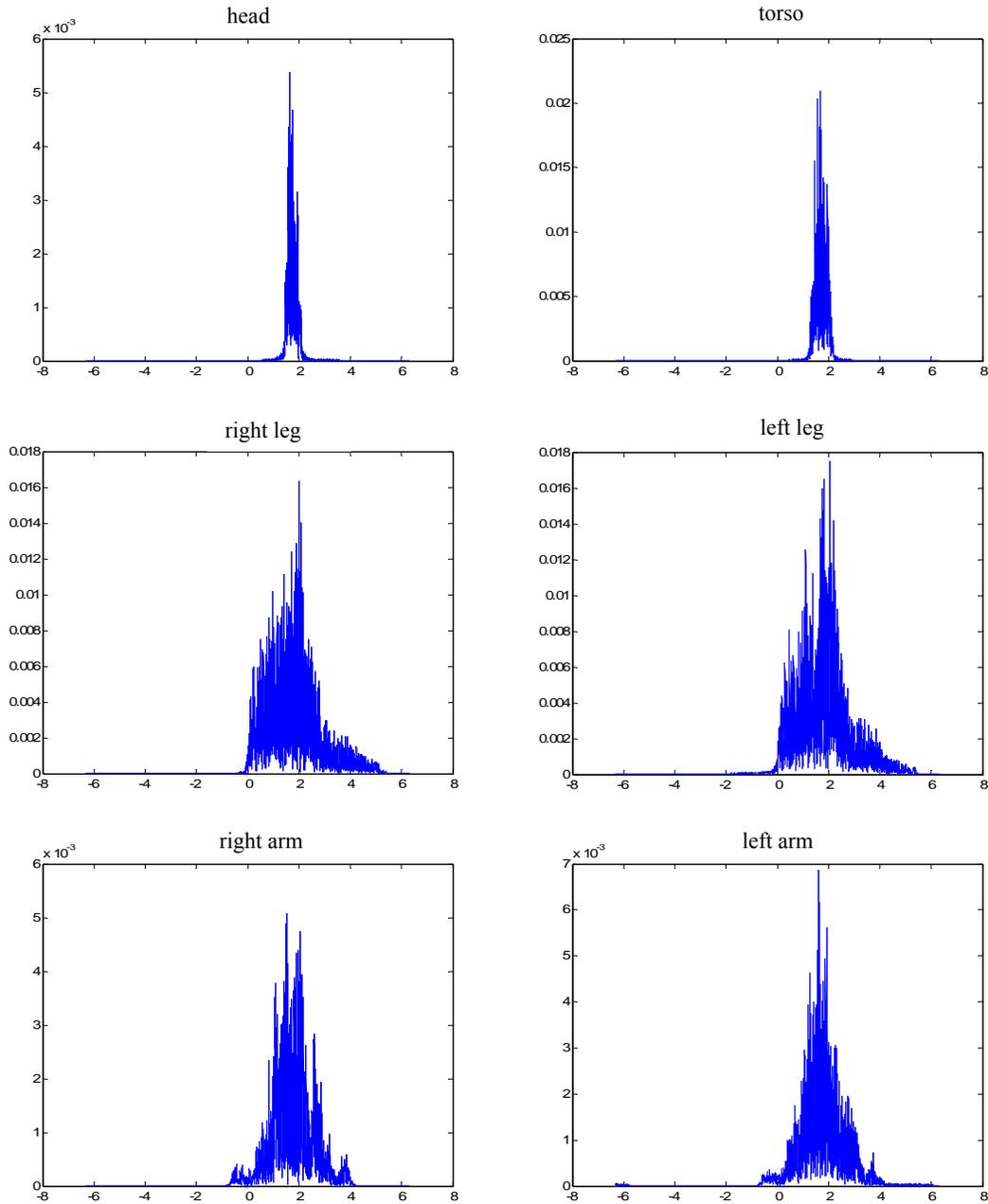
Figure 3.4 (a) Fourier transform of the scattering amplitude of each component of the walking human body versus $\omega_0/(2k_0)$.

3.1.1.   The Effect of Body Size and Gender on the Doppler Spectrum

It is also interesting to investigate how variations in body size and gender affects the Doppler spectrum and whether the measured backscatter Doppler spectrum can be used to distinguish such variations. To study such effects, the other three human bodies were simulated. To make the models extreme cases of their kind, the large size human models are designed to be walking more slowly with limited motions in the limbs and the thin male body follows a similar walking pattern to the female body and is more active and dynamic. The scattering model is run for these human models as before for a two-step motion to capture their Doppler spectra and the results are presented in Figure 3.5. The distinguishing features that separate the female and male bodies can also be recognized by the level of RCS which is higher for the male subjects due to the larger size. The maximum, minimum and average velocities of the thin male body are similar to those of the thin female body, while the RCS level is higher. The Doppler spectra with narrow bandwidth and the energy concentrated mostly around the average velocity belong to oversize and slow bodies whereas a wideband spectrum in which energy is more uniformly distributed in the band belongs to a thin and dynamic person.

Also a scenario in which the direction of motion and radar to target line of sight are not parallel is considered. The Doppler spectrum of the thin woman who is moving in a direction 45^0 with respect to the radar line of sight is presented in Figure 3.6. As observed the spectrum is compressed as the radial velocities of different body components are reduced. Despite the fact that the Doppler bandwidth is smaller at oblique incidence, it is still possible to distinguish the thin bodies from the bigger and slower bodies at normal

incidence, since the backscatter energy is distributed within the band unlike the spectrum of oversize bodies.
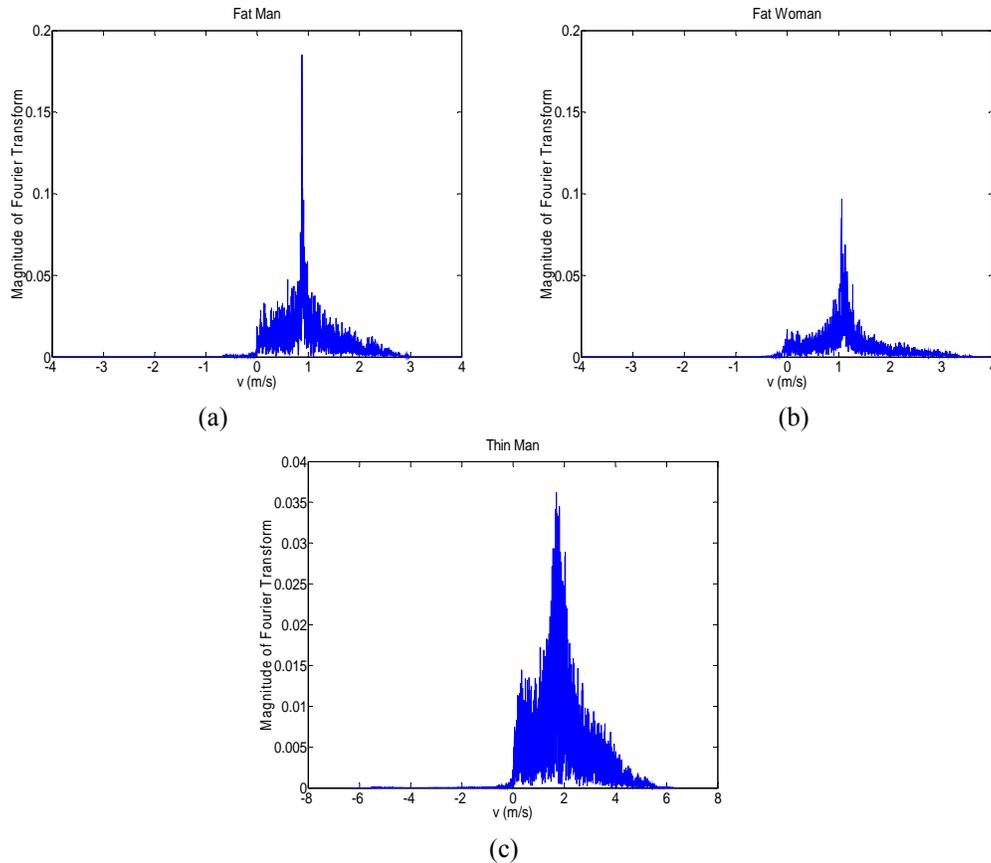
Figure 3.5. Doppler spectra of walking bodies with different sizes and genders. (a) oversize male body (b) oversize female body and (c) thin male body.
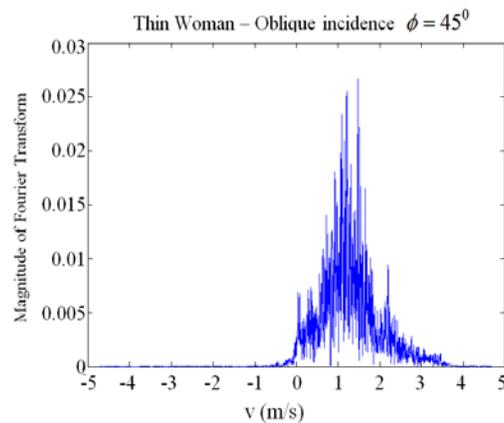
Figure 3.6. Doppler spectrum of a thin woman obliquely walking with respect to the radar with 45^0 angle. It is observable that the velocity content is lower, the maximum velocity is 3.8 (which is $5.4/\sqrt{2}$)as expected). However, it is definitely not a oversize body since the energy is not highly concentrated around the average velocity.

3.1.2. Radar Backscatter Analysis of a Walking Dog

The same procedure is performed for a walking dog to evaluate the Doppler spectrum. The electric permittivity of the skin is approximated to be similar to that of humans, while the effect of a 1 cm layer of thick hair covering the skin can be modeled as a homogeneous anisotropic medium with the effective permittivity ε_{eff}. This effective permittivity can be obtained from a dielectric mixing formula for a medium composed of thin vertical cylinders, representing hair stands, in air background. Using the Polder-van Santen Formula [39] the values of ε_{eff} for TE and TM waves are calculated from

$$TM : \; \varepsilon_{eff} = \varepsilon_{air} + f\left(\varepsilon_{hair} - \varepsilon_{air}\right) \tag{21}$$
$$TE : \; \varepsilon_{eff} = \varepsilon_{air} + f\left(\varepsilon_{hair} - \varepsilon_{air}\right)\frac{2}{\varepsilon_{hair} + \varepsilon_{air}}$$

Where, f is the volume fraction of hair which is approximated by 10%.

By the same token, for this target the radii of body's curvatures is much larger than the wavelength, hence PO method is valid. As the number of frames is not enough like the human case, we interpolate between adjacent frames and generate 6000 frames for the walking dog. The smaller number of frames is mainly because the dog is walking more slowly than the human.

The electric current distribution on the dog's face is shown in Figure 3.7 for the illumination from the front side. Similar to the human body, the current distribution here is maximum on facets which are more perpendicular to the wave vector. Figure 3.8 (a) shows the Doppler spectrum of the walking dog versus velocity ($\omega_0/(2k_0)$). It is observed that velocities spread from -0.2 m/s to 2.5 m/s while the average is around 0.8

m/s. Therefore, the range of periodic motion in dog is smaller than human body as expected. The Doppler spectrum of the walking human body is presented in Figure 3.8 (b) for comparison. Comparing the Doppler spectra of walking human and dog demonstrates major distinctions in maximum, minimum and average velocities as well as the amplitudes. The difference between human and dog's pattern of motion and sizes are adequately accommodated in their Doppler spectra, giving rise to a measure for making distinction between these targets.
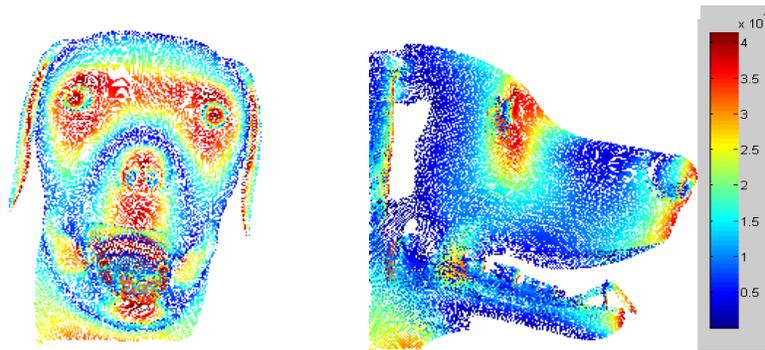
Figure 3.7. Current distribution on some parts of dog's face.

(a)

(b)
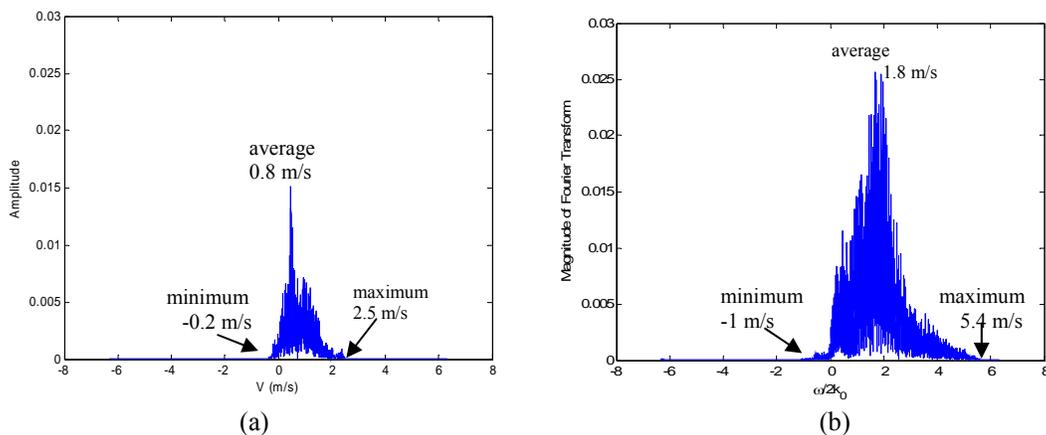
Figure 3.8. (a) Doppler spectrum of scattering amplitude of a walking dog versus velocity $\omega_0/(2k_0)$. It can be seen that it has peaks around its average velocity (v=0.8 m/s) and the maximum and minimum velocities are 2.5 m/s and 0.2 m/s (b) Doppler Spectrum of human body presented in the previous report.

As a result, the identity of a walking body can be estimated to a good extent from its Doppler spectrum. While high RCS determines the size and gender of the body, the bandwidth and the average velocities give a hint about the body weight and the pattern of walking. Hence, a Doppler spectrum is capable of characterizing a target in motion very efficiently.

3.2.   Radar Backscatter Decomposition

The Doppler spectrum was shown to be a good figure of merit to recognize the type of the moving targets. A more challenging question is whether the backscatter data can be used for detecting conceal objects carried by individuals. The concealed carried objects such as handguns and firearms are most commonly carried on the torso and thus it is essential to investigate the response of the torso to investigate the detection of concealed objects. Since the total spectrum of walking human body is a combination of the individual parts' spectra, the goal is to extract the response of torso from the rest of the body.

Here we explore the feasibility of detecting body-attached irregular objects by decomposing the overall backscatter response in terms of its origin from different body parts. As mentioned before, since the shapes of most concealed objects unlike human body are not symmetric and smooth at W-band, they can enhance cross-polarized response. However, when the body is moving, cross-polarized backscatter is increased since concave surfaces are formed and the interactions between different body components are increased. On the other hand, as the concealed objects are commonly

carried near the torso, and noting that torso is convex and does not generate significant cross-polarized backscatter response, the polarimetric signature of torso alone may provide the necessary information for detecting concealed objects.

The backscattering response of the torso is dominated by the single-bounce backscatter mechanism and its polarimetric response resembles that of a sphere. To analyze the polarization response of the torso, first the polarimetric backscattering response is calculated and the responses of S_{hh}, S_{vh}, and S_{hv} are normalized by S_{vv}. Then the Muller matrix is calculated as follows [29]

$$M = [R^T]^{-1} W R^{-1} \tag{22}$$

where,

$$R = \begin{bmatrix} 1 & 1 & 0 & 0 \\ 1 & -1 & 0 & 0 \\ 0 & 0 & 1 & 1 \\ 0 & 0 & -j & j \end{bmatrix} \quad W = \begin{bmatrix} S_{vv}S_{vv}^{*} & S_{vh}S_{vh}^{*} & S_{vh}S_{vv}^{*} & S_{vv}S_{vh}^{*} \\ S_{hv}S_{vh}^{*} & S_{hh}S_{hh}^{*} & S_{hh}S_{hv}^{*} & S_{hv}S_{hh}^{*} \\ S_{hv}S_{vv}^{*} & S_{hh}S_{vh}^{*} & S_{hh}S_{vv}^{*} & S_{hv}S_{vh}^{*} \\ S_{vv}S_{hv}^{*} & S_{vh}S_{hh}^{*} & S_{vh}S_{hv}^{*} & S_{vv}S_{hh}^{*} \end{bmatrix} \tag{23}$$

The elements of Muller matrix are averaged all angles of illumination. To simulate the response of torso for any arbitrary combination of polarizations, the synthesized polarization response $P(\chi, \psi)$ is calculated from

$$P(\chi, \psi) = S M S^T \tag{24}$$

where,

$$S = \begin{bmatrix} 1 & \cos(2\psi)\cos(2\chi) & \sin(2\psi)\cos(2\chi) & \sin(2\chi) \end{bmatrix} \tag{25}$$

and ψ and χ are the orientation angle which ranges from -90 to $+90$ and the ellipticity angle which ranges from -45 for left-hand to $+45$ for right-hand circular polarization. The polarization response of the torso in represented in Figure 3.9 in comparison with that of sphere. It is observable that the co-polarized response is maximum for linear and minimum for the circular polarizations, which is similar to that of a sphere. The only difference is that the response of torso is slightly higher for vertical polarization.

In the presence of an external irregular object the polarimetric backscatter will undergo a change that can be used for detection. The change in the polarimetric backscatter from the torso and the external object results from the direct backscatter of the object and its interaction with the torso (shadowing and multiple scattering). Hence by isolating the polarimetric response of torso, it is possible to detect the existence of concealed irregular objects.

(a)

(b)
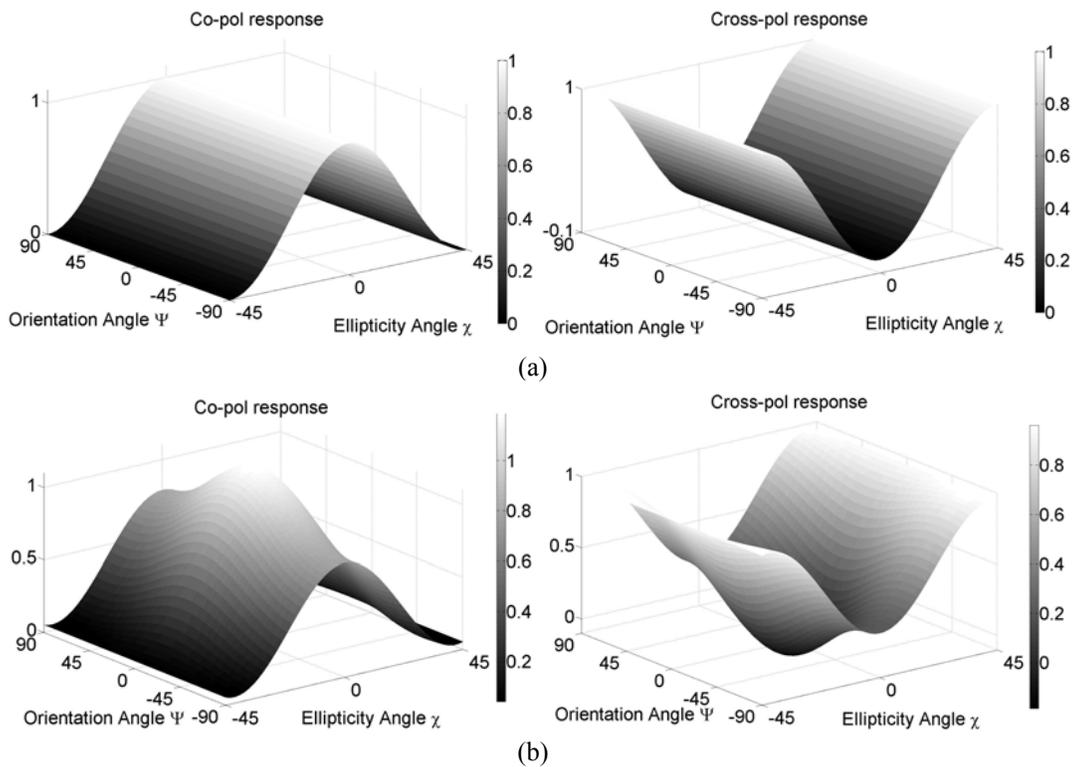
Figure 3.9. (a) Polarization response of sphere and (b) torso.

Since all spectra of body components are overlapping, we cannot isolate the spectrum of the torso by simple filtering. One can attempt to use simple models to create a matched filter for the moving parts, but due to the complex shape and motion of the body parts and their motions, such matched filters are incapable of separating the desired radar responses. We have explored an approach to extract the response of the torso based on the temporal deviations in the RCS response for the body during walking and the time-frequency analysis. In this approach, complex time varying responses from the limbs are removed from the overall backscatter to isolate the response of the torso.

3.2.1. Temporal Variation of Body RCS

To isolate the response of the torso from the full body, we can take advantage of the variations in the response of legs and arms during walking. While the torso response is nearly constant at different instances of walking, the responses of the limbs undergo a major change due to considerable differences in their orientation and position with respect to the radar. At instances when the limbs are spread out a lower backscattering response from the limbs is expected since their projected cross-section in the beam is smaller and, more importantly, the specular reflection from most facets are away from the backscatter direction. On the other hand, when the limbs are aligned with the body, their physical cross-section is higher and there are many facets with their specular reflection in the backscatter direction. Figure 3.10 shows the backscattering response of limbs at different instances of walking positions. As predicted, it is observed that the limbs backscatter is lower at the moments when the limbs are spread out (when the axial orientation is such that the specular component of the scattered field is away from the

backscattering direction) and is higher when they are aligned with the body. Figure 3.11 represents the walking body at different positions. It is shown that at $t = 0.15$ s and $t = 0.65$ s the limbs are spread out and their RCS is lower as shown by Figure 3.10. Similarly, around $t = 0.4$ s and $t = 0.9$ s, the limbs are aligned with the body and their backscatter response is higher.

It is also interesting to compare the backscatter responses of the torso and limbs at different walking positions. Table IV presents the RCS of the torso, RCS of limbs and their ratio at the same walking positions shown in Figure 3.11. It shows that the responses of the limbs are lower at $t = 0.15$ s and $t = 0.65$ s, therefore the ratio of the torso response to the limbs' response is high. Similarly, at $t = 0.4$ s and $t = 0.9$ s, the response of legs and arms are significantly higher, so that the ratio of the response of the torso to the limbs is much lower. The amount of difference in RCS represents a sufficient contrast in motion detection.

The response of the torso does not undergo a significant change during walking due to its minimal motion during walking. This feature can be utilized to isolate the response of limbs from the rest of the body. The response of the body at the moments when the cross-section of legs and arms are small can be mainly attributed to the torso. For example, the response of the body between 0.1s ~ 0.2s and 0.6 s ~ 0.7 s (almost 20 % of the walking time) can be considered the contribution of the torso to a large extent.

	The Torso RCS (dBsm)	The Limbs RCS (dBsm)	Ratio
t = 0.15 s	-6.0208	-18.4051	+12.3843
t = 0.4 s	-7.075	+3.964	-11.0387
t = 0.65 s	-4.5727	-11.6678	+7.0951
t= 0.9 s	-7.2096	+4.1284	-11.3379

Table IV. The RCS of the torso and legs and arms and also their ratio at four sample positions where the legs and arms either aligned with torso or are spread out.
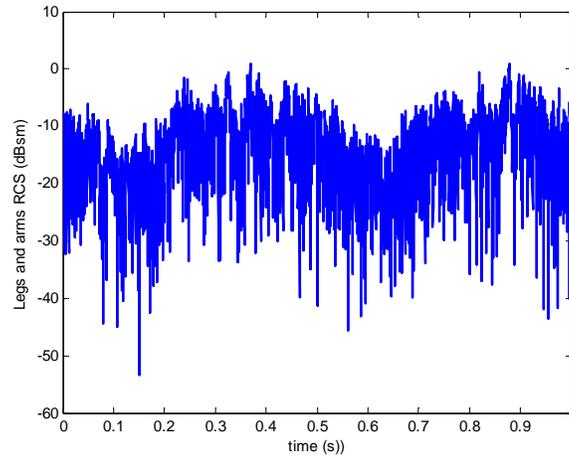
Figure 3.10. Backscattering response of the legs and arms during walking for different walking positions. It is lower when they are spread out ($t = 0.15$ s, $t = 0.65$ s) and higher when they are aligned with the body ($t = 0.4$ s, $t = 0.9$ s).
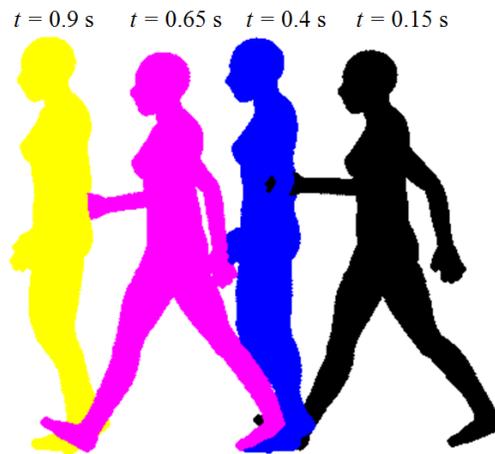
Figure 3.11. The position of human body during walking at different time frames (approaching the radar). It is observable that around t = 0.15 s and t = 0.65 s where the legs and arms are spread out, the RCS of legs and arms are lower as shown by Figure 3.10. Similarly, around t = 0.4 s and t = 0.9 s when the legs and arms are aligned with the body, the response is higher.

3.2.2. Time-Frequency Analysis

During walking, there are moments at which limbs' velocities have the most difference with the velocity of the torso. This of course can also be observed in the radar backscatter Doppler spectra if time-frequency analysis is used. To capture the temporal spectra, the

67

time domain backscatter signal is divided into a number of sub-signals over an appropriate time interval. Each of these signals represents a time frame (with 0.01 s length) during walking. The Fourier transformation is then performed on these sub-signals, yielding a set of spectra in discrete time steps. To avoid spurious response in the frequency domain, the backscatter signal in time domain is multiplied by a series of shifted overlapping Gaussian signals as shown in Figure 3.12. These signals are Fourier transformed and the result is shown in the two-dimensional plots of Figure 3.13 (a) for the thin female model. The observed time domain spectra of backscatter signal reveals detailed features of walking positions. If the selected frames happen to be at the moment where the limbs have their maximum velocities (limbs aligned with the torso), the spectrum is wide and centered around the average velocity for the torso (+1.8 m/s). At another instance, when the legs and arms velocities are minimum, the spectrum is narrower. In this situation, as presented in the previous section, the response of the limbs is about 20 dB lower. In Figure 3.13 (b) and (c) the time-frequency responses of the limbs and torso individually are presented. It is shown that around $t = 0.15$ s and $t = 0.65$ s, the bandwidth of the limbs spectrum is narrow, has lower level, and is centered around the torso's average velocity. On the other hand, when limbs have their maximum velocities, their spectrum is wideband. In this case the total backscatter power is higher, but spread out in the spectrum. Hence there seems to be two approaches to isolate the response of the torso, one is to identify the frame where bandwidth is minimum, and the other one is to identify the frame where the bandwidth is maximum and filter out the high and low frequency components. Figure 3.14 shows two temporal backscatter responses: 1) the response of the body when the spectrum is narrow (around $t = 0.15$s), and 2) the response

of the body when the spectrum is wideband (around $t = 0.4$s). A Gaussian bandpass filter centered at 1140 Hz (corresponding to 1.8m/s) and 3-dB band width of 210 Hz is used to isolate the response of the torso. The filtered responses of the frames closely resemble that of the torso alone at both instances. This method can be used to isolate the response of the torso from the rest of the body for detecting concealed objects around the torso as presented in the next section. It should also be noted that the small differences in the response of the torso in Figure 3.14 (a) and (b) are due to the fact that the posture of the torso itself varies a small amount during walking.
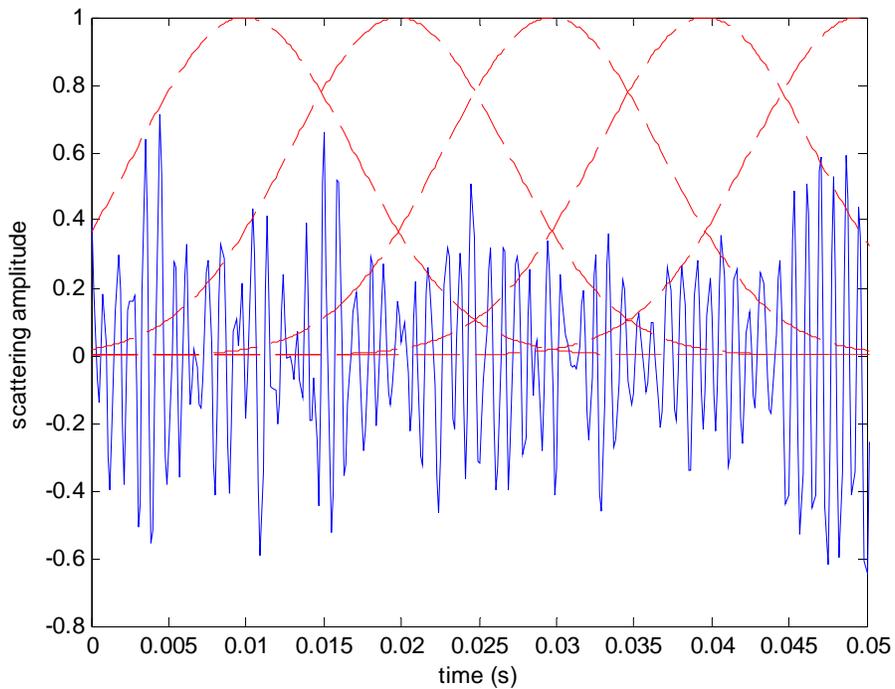
Figure 3.12. The signal is multiplied by a number of shifted Gaussian functions.
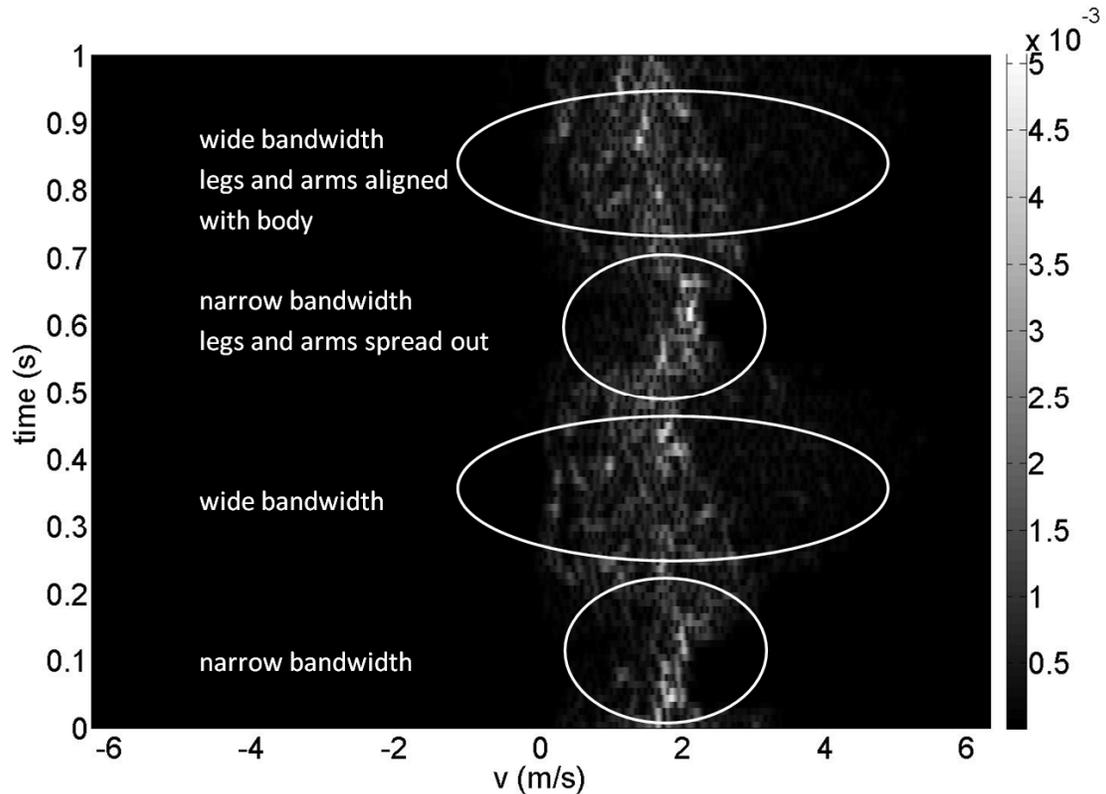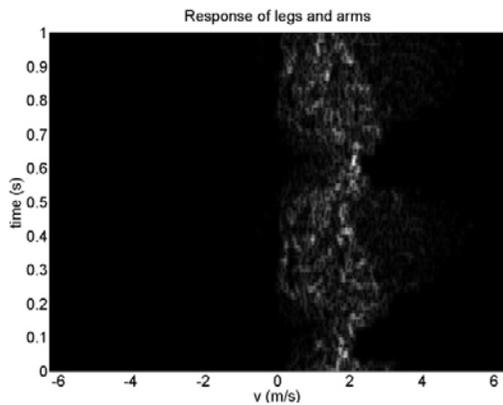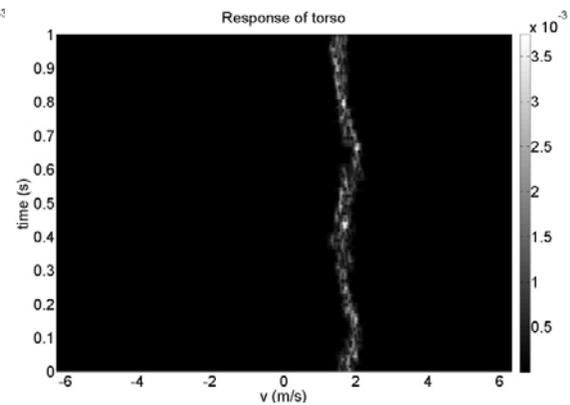
Figure 3.13. The co-polarized response of the human body is Fourier transformed using time-frequency analysis. (a) full body (b) the limbs and (c) the torso. The signal is chopped into a number of sub-signals using a number of shifted Gaussian signals and the Fourier transformed is performed on the resulting sub-signals. The plots show different bandwidths for different frames. For the full body, while there are moments (around $t = 0.4$ s and $t = 0.9$ s) in which the velocity of the legs and arms are maximum and bandwidth is wide, there are some other times (around $t = 0.15$ s and $t = 0.65$ s) that their velocity is minimum and the bandwidth is narrow. The bandwidth of the limbs' spectrum is narrow around $t = 0.15$ s and $t = 0.65$ s and confined around the same velocity as torso is located. At other moments, when legs and arms have higher velocities, their spectrum is wideband and spread out, while the spectrum of torso is narrow around the middle-velocity at all times.

70
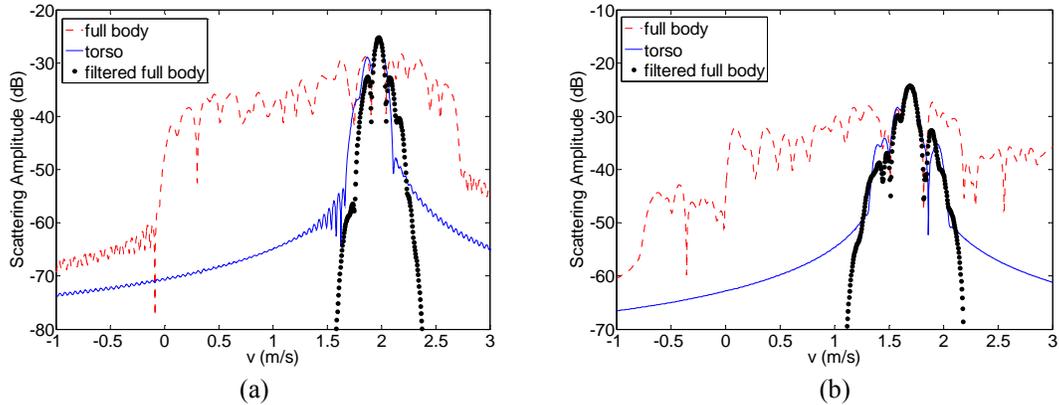
Figure 3.14. Temporal backscattering response of torso and the full body at two instances: (a) the limbs are spread out and the spectrum is narrow. (b) the limbs are aligned with the body and the spectrum is wide. The filtered response of the full body resembles that of the torso at both instances.

3.2.3. Polarimetric Time-Frequency Analysis for Detection of Concealed Objects

As mentioned before, the backscatter response of the torso does not generate any substantial amount of cross-polarized backscatter. On the other hand, the irregular shape of most concealed objects, such as handguns and firearms, can produce a noticeable amount of cross-polarized backscatter response. Also, when a weapon is carried on the torso, the interaction between the torso and the object can generate cross-polarized response as well. This feature can be exploited to detect concealed objects. The procedure for isolating the torso response from the limbs was described in the previous section. We can apply this technique to the fully polarimetric backscatter response and isolate the polarimetric response of the torso alone. The polarimetric radar backscatter analysis is based on examining the ratio of cross-polarized/co-polarized response to explore the presence of objects. To examine the performance of this approach, simulation of a human body with a generic handgun attached is carried out.

71

To begin with, the gun model is incorporated over the human model mesh as shown in Figure 3.15. The gun is moved with the moving body by having it anchored to one of the facets of the waist. Since the handgun is made of metal, a perfect electric conductor boundary condition is used.

The iterative PO model is used to analyze the polarimetric radar backscatter response of the handgun and human body including all interactions up to the third order in the vicinity of the gun. The time-frequency analysis is applied to both co- and cross-polarized responses to isolate the response of the torso. For this purpose, from the time-frequency signal, the instances with maximum and minimum bandwidths are found. Then the signal is filtered around the average velocity of the body in order to isolate the response of the torso. The ratios of cross- to co-polarized responses for the isolated the torso for two cases (with and without the handgun) is investigated. Table V shows the results for the two instances, one where
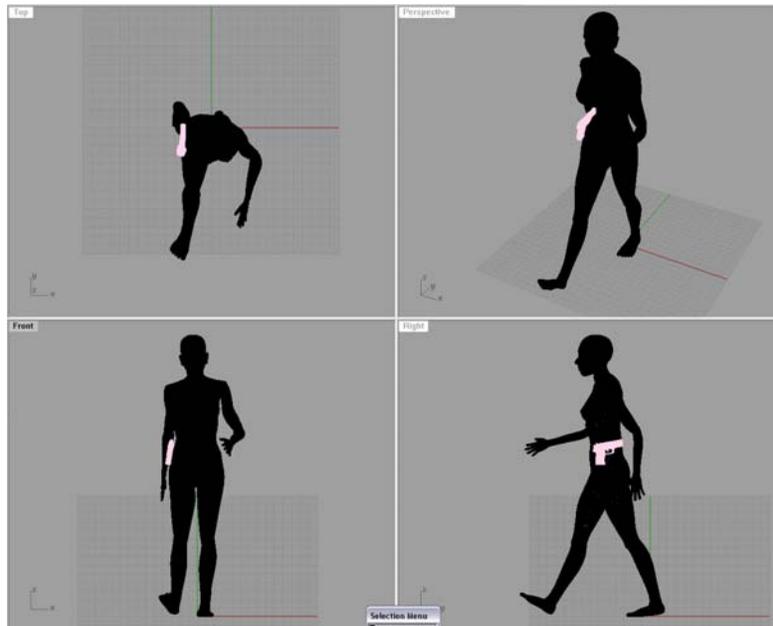
Figure 3.15. the gun is placed on the human waist where a handgun is actually carried.

72

cross- to co-polarized response	Without hand gun (dB)	With handgun (dB)	Ratio (dB)
spread-out position (narrow bandwidth, t = 0.15)	-15.4	-8.23	+7.17
aligned position (wide bandwidth t = 0.4 s	-21.1	-17.58	+3.52
the entire body without using time-frequency analysis	-18.6	-18.11	+0.5

Table V. cross- to co-polarized response of the walking human body at two instances, where the limbs are aligned with the body and where they are spread out. The response is increased when the handgun is present.

the spectrum is narrow and the other where the spectrum is wide. It is shown that the ratio

is increased up to around 7 dB for the case where the limbs are spread out and around 3.5

dB for the case where the limbs are aligned with the body indicating improved detection

for the former case. To demonstrate the overall improvement achieved, the ratio of the

cross- to co-polarized backscatter ratios in the presence and absence of the handgun

without applying time-frequency analysis, is calculated and included in Table V. As

shown in the table, the cross- to co-polarized response of the entire body is only around

0.5 dB higher when the handgun is present which is not high enough to be used as a

means of detection. This highlights the fact that the combination of radar polarimetry in

conjunction with the time-frequency analysis can lead to the detection concealed metallic

objects at a standoff location without the need for high resolution imaging which is the

common practice. It should also be noted that since a Doppler filter is applied to the

backscatter data, all stationary objects that can produce cross-polarized response are also

filtered out. This adds to the robustness of the algorithm and can drastically reduce false

alarm rate.

3.3. W-band RCS Measurement

To verify the increase in the cross- to co-polarized response due to the presence of a handgun, a paper-mache model of upper thigh, torso and head was made with focus on textural smoothness. The surface is covered with a material with skin dielectric constant as shown in Figure 3.16 . The measured polarimetric response of torso with and without a handgun is performed with this dummy. For this purpose, it is mounted atop of a turntable which turns from 0^0 to 360^0 and the radar measures the polarimetric response at each position. The University of Michigan 95 GHz fully polarimetric radar is used to measure polarimetric response of the dummy in the anechoic chamber. The measurement setup is shown in Figure 3.17.

Figure 3.16. Paper-mache model of upper thigh, torso and head.

.

Figure 3.18 shows the polarimetric responses of torso with and without a handgun. It is shown that presence of the gun enhances the amount of cross-polarized response from the torso up to 10 dB. This verifies the fact that the presence of irregular external objects enhances the cross-polarized response of human body.
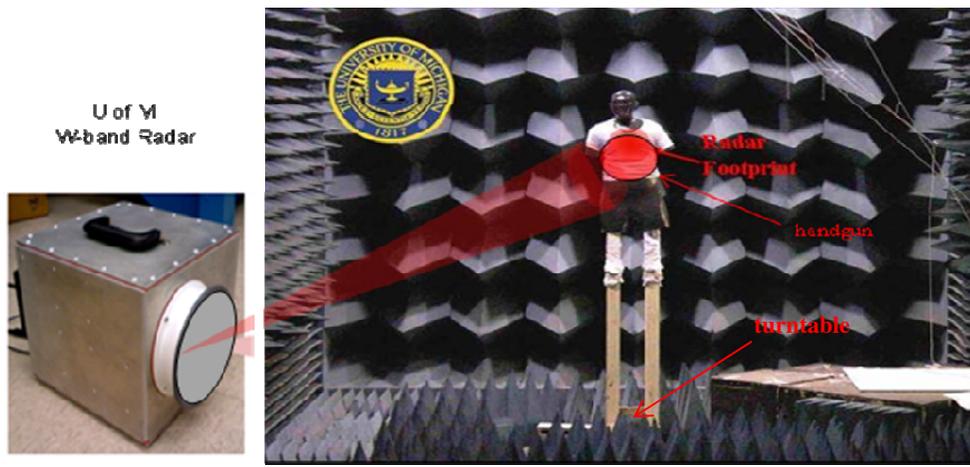
Figure 3.17. W-band RCS measurement setup for human body. It is mounted on top of a turntable.

(a)   (b)
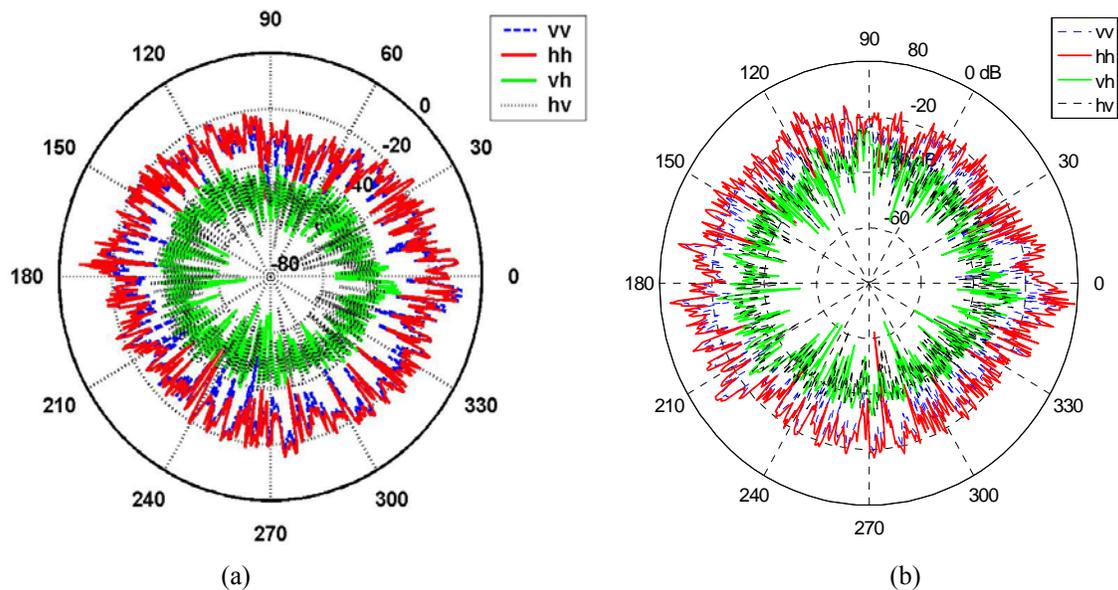
Figure 3.18. Polarimetric response of torso is measured using a 95 GHz radar (a) without and (b) with a handgun. It is observable that the presence of the firearm increases the cross-polarized response

3.4. Radar backscatter Analysis of Human Body at Y-band (220- 325 GHz)

One of the main advantages of radar backscatter analysis of moving objects at MMW frequencies is the higher recognition capability for slowly moving objects. The bandwidth of the Doppler spectra of complex moving targets such as human body becomes wider as the frequency is increased. However, in terms of velocity content it does not changed. In order to fully understand the effect of radar frequency in the Doppler spectrum, the thin female body is analyzed at higher Y-band range (220-325 GHz). The qualitative current distribution on the body is shown in Figure 3.19 (a) and presents variations very similar to those in W-band. The Doppler spectrum shows similar variations with a wider bandwidth from -1600 Hz to 8600 Hz. However, the velocity content remains the same as shown in Figure 3.19 (b). The only obvious difference is the amplitude of the RCS which is around 40% lower compared to the results in W-band. This is due to the fact that skin dielectric constant is lower at Y-band compared to W-band.

| (a) | (b) |
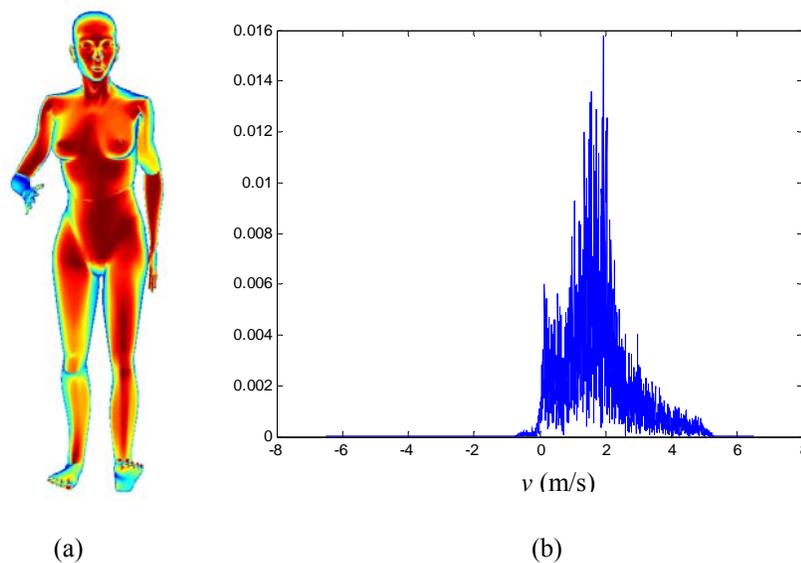
Figure 3.19. (a) The qualitative current distribution on human body and (b) the Doppler spectrum of walking at 240 GHz.
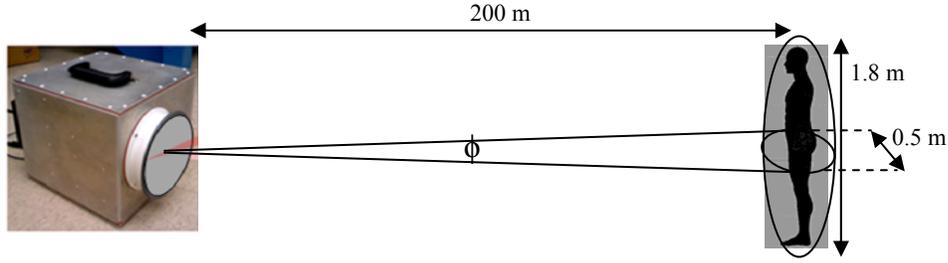
Figure 3.20. The required antenna beamwidth to provide footprints commensurate to human body width.

Y-band frequency range can also be used for the proposed detection algorithm. The chance to have higher co-polarized response for the human body and therefore enhanced cross- to co-polarized response at the presence of irregular objects might be higher, which makes the algorithm more robust. In addition, for standoff detection, antennas with very narrow beamwidth are required to provide footprints commensurate to human body at very large distances. For example, at 200 m range, for an average-size human body width (50 cm width), $\phi = \tan^{-1}(0.5/200) = 0.0025$ rad. At W-band the required antenna aperture to realize such a beamwidth is $\lambda/D = 0.0025 \rightarrow D = \lambda/0.0025 = 3$ mm / 0.0025 = 1.2 m which is large, while at Y-band it becomes three times smaller: $D = \lambda/0.0025 = 1$ mm / 0.0025 = 40 cm. It should be noted that the length of the aperture for the human height is around 3.5 times smaller in each case.

If the antenna aperture length is one third smaller, the aperture area will be 1/9 times smaller and the weight will be 1/27 lighter which results in more compact and light-weight systems. On the other hand, since the wavelength is around 1mm, the dimensions of the waveguide structures are in the order of hundreds of micron. This makes the band suited for micromachining applications. Moreover, Y-band compared to W-band is underutilized and the available bandwidth is much higher. Mature technologies are available at W-band and many technological problems have already been solved, whereas

at Y-band, many concerns regarding sources and amplifiers for MMIC technology should still be addressed and solved. Y-band radars require technological advances to be well-suited for navigation and obstacle detection. These motivate the development of a Y-band radar which can be later enhanced for polarimetric applications and concealed target detection.

3.5.   Conclusion

In this chapter, the radar backscatter responses of walking human bodies at W-band were calculated. This sequence of the backscatter response generates a time domain signal which is Fourier transformed to derive the Doppler spectrum of the target. The feasibility of identifying different body sizes/genders and walking dog based on the characteristics of the Doppler spectra were investigated. Then a radar backscatter decomposition algorithm was presented to isolate the response of torso in order to be able to measure the cross-polarized the response of torso. It was verified that the higher cross- to co-polarized response of torso is an indication of the presence of irregular external object. The RCS measurement of the human torso at the W-band is then presented and verifies the enhancement of the cross- to co-polarized response at the presence of an irregular object. The radar backscatter analysis of the walking human body at Y-band was then presented which motivates the phenomenological studies at Y-band. This necessitates the realization of high resolution radars at Y-band.

Chapter IV

Y-band Radar Design

The frequency ranges of commercial MMW radars are mostly at 77 and 94 GHz for automotive and imaging radars, respectively. With the advances in MMIC technology, the applications in these bands increase and hence the available bandwidth is decreased. In addition, recent demands for very high resolution radars highlighted the need for developing new methods for low-cost and low profile MMW radars at higher MMW frequencies. This requires advances in modern circuitry, digital signal processing techniques and FMCW waveform. There have been several attempts to realize high resolution compact radars at 140 and 220 GHz especially for short range applications with external aperture-type antennas such as a horn or integrated antennas such as planar antennas [40] - [43]. However, in most of these systems, antenna integration is still a challenge mainly because the antennas are bulky and provide simple functionality; while the size, weight and cost of these radars have to decrease in order to be compatible for small moving platforms and mass productions [44]. For this purpose, low-loss, compact, and fully integrated antennas with more sophisticated performance are required.

In this chapter, a compact, light-weight, power-efficient, beam steering MMW imaging and navigation system at Y-band (240 GHz) is introduced for operation in conditions limited by smoke, dust, haze or darkness compatible with Micro-Autonomous System Technologies (MAST). The aim is to provide range resolution of around 40 cm, a field of view $\pm 25^0$ and overall weight below 5 g. The active components of the radar are realized

79

on CMOS and InP, while the passive components are realized on hollow waveguides to reduce weight and loss. The radar antenna is a frequency scanning array using rectangular waveguide structure integrable with the active chips. This motivates the utilization of micromachining to fabricate and integrated the radar component. The technique provides easy fabrication of structures with micron-range dimension control and further reduction of the cost. A basic block diagram of the Y-band radar is presented in Figure 4.1 and the specifications are listed in Table VI.
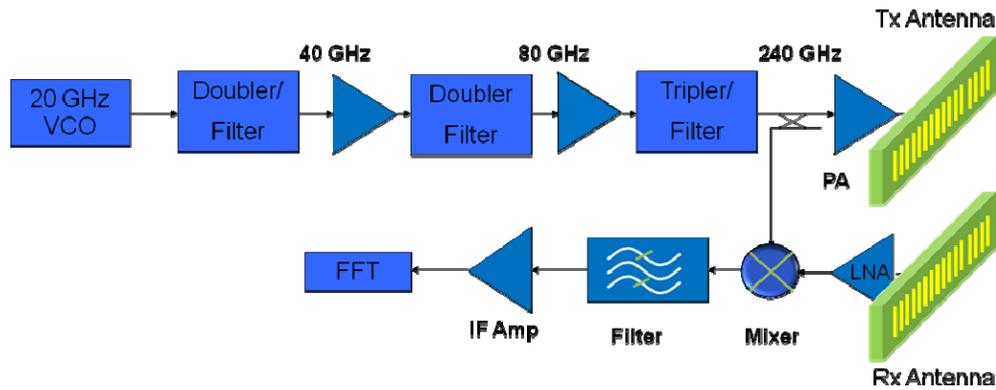
Figure 4.1. Block diagram of the Y-band FMCW radar.

Wavelength	1.2 mm
Peak Tx power	10 dBm
Rx Sensitivity with 5 dB SNR	-135 dBm
Beamwidth	Az: 2^0 El: 8^0
max directivity	27 dB
Polarization	Vertical
Volume	2 cm^3
Weight	5 g
Field of View	±25deg
Range Resolution	37.5 cm

Table VI. Radar specifications.

4.1.   Components

Signal Generator

Depending on the application, the radar transmit signal can be pulse or CW. CW transmissions employ low continuous power compared to the high peak power of the pulsed radars. However, CW radars using unmodulated waveforms cannot measure the target's range [45]. The issue is addressed by frequency or phase modulation of the signal. The frequency modulated CW signal (FMCW) has many advantages over pulse radars. They spread the transmitted energy over a large modulation bandwidth providing good range resolution and their circuitry is well-matched to solid-state transmitters leading to low cost and high reliability systems. The purpose of the radar, and the expected characteristics of the targets, in addition to the demands of moving target indication (MTI) and electromagnetic compatibility (EMC) are some of the factors that determine waveform design. For the Y-band radar, a CMOS digital VCO with 12 bit 50 MS/s ADC is implemented in 65nm CMOS to generate the FMCW signal at 20 GHz. The waveform generated by VCO is a stepped FMCW signal. To design the waveform, first the number of the required frequency steps and bandwidth is calculated. For $\pm\,25^0 = 50^0$ beam steering and 2^0 of beamwidth, 25 frequency steps are required to cover the field of view. The frequency range of 230 ~ 245 GHz is chosen for beam steering. Hence, $\dfrac{15\,\text{GHz}}{25\,\text{steps}} = 600\,\text{MHz/step}$.

The radar is mounted on a moving platform and depending on the application; the platform could be a flyer, rover or crawler. The frame should be updated faster for fast platforms; therefore the VCO should be able to adaptively change the frame update rate

from 2 to 30 per second. For instance, for 30 frames/s for flyers, each frame takes 33 ms
and each frequency step sweep takes 33ms / 25 = 1.33 ms. The ramp signal is shown in
Figure 4.2 (a) where the bandwidth for each sweep is chosen to be 400 MHz. The
receiver bandwidth is calculated as 1 / 1.33 ms = 750 Hz and the range resolution

$$r_{resolution} = \frac{c}{2B} = \frac{300}{2 \times 400} = 37.5\,\text{cm}.$$ The FMCW signal is shown in Figure 4.2 (b) with the

ramp-down segment required for detection of moving targets and Doppler shift.
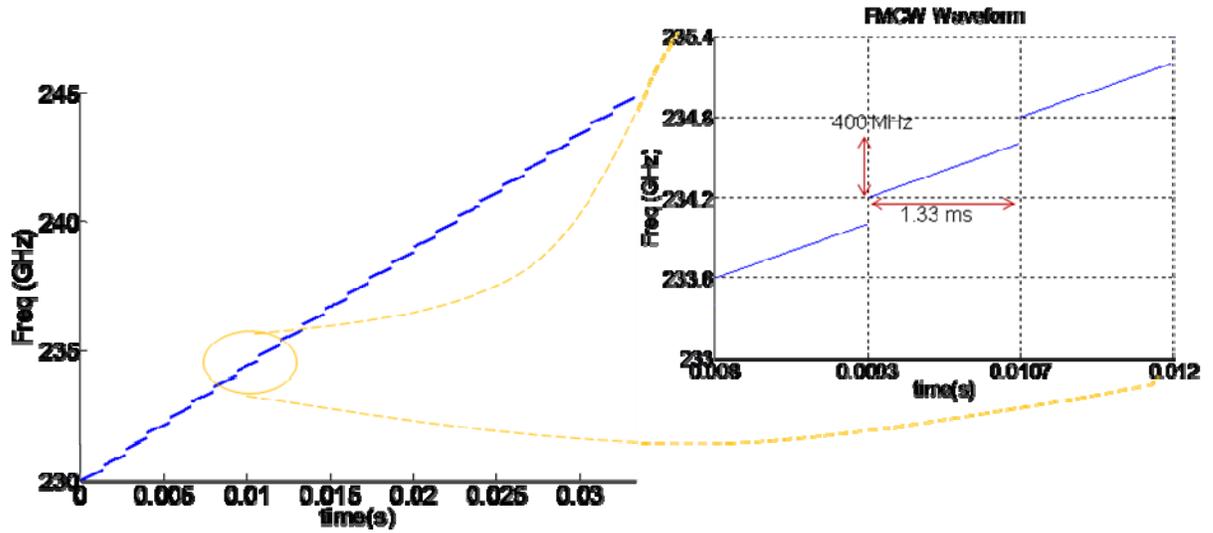
(a)
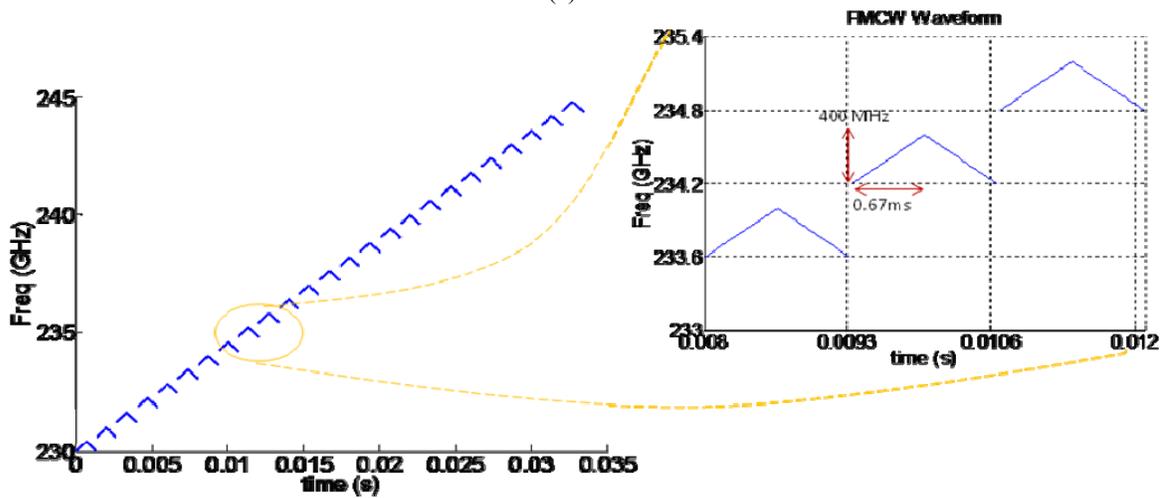
(b)

Figure 4.2. (a) stepped ramp and (b) stepped FMCW signals for moving targets.

82

Transmitter

The main components in transmitters are the up-converting mixer or frequency multiplier, filters and the power amplifier. The IF signal is converted into the RF frequency signal by mixers or frequency multipliers. The undesired harmonics and images are attenuated using bandpass filters. Finally the power amplifier provides amplification for the transmit signal before it excites the antenna. Couplers are commonly used to provide a sample of the transmit signal or the LO for the receiver down-convertor. To provide a 240 GHz signal for the antenna, the VCO signal frequency is first doubled twice using frequency doublers fabricated with non-linear passive or active devices. Schottky diodes on FET can be used as the nonlinear device to generate the second harmonic because of their high cutoff frequency and square-law characteristics. Band-pass filters for harmonic elimination and amplifiers are used after each step of frequency doubling. At the next step a frequency tripler is used to convert the 80 GHz signal to 240 GHz and then amplified with a power amplifier fabricated with high-frequency HEMT transistors.

Receiver

The receiver subsystem takes the signal from the antenna and passes it to the low-noise amplifier (LNA). The system generally consists of LNA, down-converting mixer, filter and IF amplifier. If the transmit and receive antennas are identical, duplexers are used to provide isolation between transmit and receive signal. In addition to the image rejection, filtering in the receiver is used to attenuate interference from other radars or high-powered electrical devices during reception. Receiver noise figure and minimum detectable signal are critical parameters of the receiver subsystem. The minimum

detectable power depends on the signal to noise ratio and thermal noise power and affects the maximum detectable radar range.

The LNA is fabricated with HEMT transistors similar to the PA. A sample of the transmit signal is mixed with the output signal of the LNA and generates the baseband signal. Filter and amplifier are used to remove the higher order harmonics and interferences and to amplify the baseband signal.

Baseband

Almost all modern radars use digital signal processors to perform processing operations such as correlation, Doppler filtering, image rejection, detection processing and tracking. To provide signal for digital processing, A/D converters are placed at the end of the receiver signal path. Data processors are used to convert data produced by the signal processor into a form that is readily interpretable by radar operators.

A low-power processor is used to extract the frequency content of the signal. ADC and FFT modules are important parts of the processor with a developed circuit design techniques to enable high circuit activity and peak energy efficiency during FFT computation.

4.2. Antenna

Most systems employ separate antennas for transmit and receive in order to provide better isolation. According to the radar equation [46], if the maximum radar range r_{max} is defined for the receiver minimum detectable signal S_{min}, according to radar equation

$$r_{\text{max}} = \sqrt[4]{\frac{P_t G_t G_r \sigma \lambda^2}{S_{\text{min}}(4\pi)^3}}$$

(26)

where, P_t is the transmit signal power, G_t and G_r transmit antenna gain, and σ the target RCS. A detectable signal must be larger than the noise (5 to 10 dB higher). S_{min} can be expressed in terms of signal to noise ratio (S/N) required for a reliable detection times to the receiver noise:

$$S_{\text{min}} = \frac{S}{N} P_n = \frac{S}{N} k_0 T_0 B F_n$$

(27)

where k_0 is Boltzman's constant, T is the temperature B is the receiver bandwidth and F_n is the receiver noise figure. If $S/N = 5$ dB, $F_n = 5$ dB and $B = 750$ Hz:

S_{min} (dB$_\text{m}$) $= 5 - 174 + 10 \log (B) + F_n$ (dB) $= -135$ dB$_\text{m}$

To prevent aliasing during RCS measurements the range should be alias-free. The alias-free range is a distance from the radar that a target response appears with the accurate range. Since in FMCW waveform the target range is proportional to the periodicity of baseband signal (T) and to the inverse of pulse repetition frequency, the range function is also periodic and a target outside alias-free range may appear much closer to the radar. If the baseband signal is sampled N times over one period and a chirp bandwidth of ΔF is used, the maximum frequency content is limited to N/T. Noting that for FMCW radar range and frequency shift are linearly dependent, the maximum alias free range is given by

$$R_{max} = \frac{Nc}{2\Delta F} \qquad (28)$$

The range resolution of the radar can be related to the alias range:

$$R = \frac{Nc}{2\Delta F} = Nr_{resolution} \qquad (29)$$

For a known value of alias-free range and range resolution, the number of sampling point can be evaluated.

Antenna maximum directivity can be approximated by $\frac{4\pi}{\Omega_A}$, where Ω_A is the beam solid angle and is defined as the solid angle in which if the antenna radiation intensity is constant (and maximum value), all power would flow through it. In the case of antennas with one narrow major lobe and very negligible minor lobes, the beam solid angle can be approximated as the product of the half-power beamwidths in two perpendicular planes, i. e., azimuth and elevation angles $\frac{4\pi}{\theta_{azimuth} \times \theta_{elevation}}$. The antenna maximum gain is defined as maximum directivity times the antenna efficiency. The radar antenna should provide narrow beams in azimuth and elevation directions (2^0 and 8^0); therefore, the maximum directivity is estimated as $D_{max} = 34$ dB. If the antenna efficiency is 7 dB, the maximum gain of the antenna is 27 dB.

With $S_{min} = -135$ dB$_m$, $P_t = 10$ dB$_m$, $G_t = 27$ dB, and $\lambda = 1.26$ mm, according to Eq. (26), the radar range is represented in Figure 4.3 versus target RCS. The RCS of some know targets such as metal spheres, dry wall, concrete wall, and a human body at that frequency range are presented for comparison.
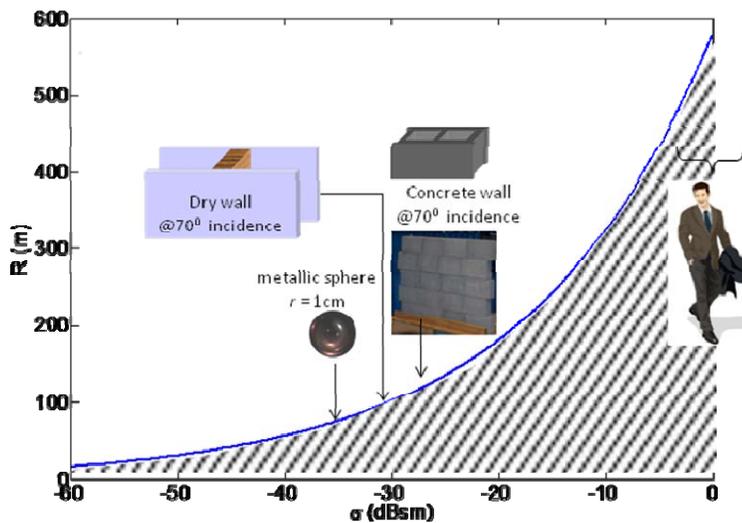
Figure 4.3. Radar range versus RCS is represented for some sample targets. Target that fall under the curve are detectable

The choice of the radar antenna is based on the desired beam dimensions and the area available for the antenna in a typical application. Horns, omnidirectional, lens and reflector antennas are widely used in MMW radar systems. Systems of this kind are large and bulky and not viable for electronic beam scanning. Planar antennas [47], on the other hand, suffer from high losses [48]. Antennas using slotted arrays [49] or dielectric structures [50] mostly exhibit a rather complicated structure and do not easily lend themselves to low-cost mass production. However, planar antennas are compatible with MMIC and can be fabricated on one substrate with the rest of the system, leading to compact-size modules. They are also suitable for electronic beam scanning due to the possibility of the arrays.

In an attempt to reduce size, weight, cost and system complexity, it is desirable to devise a means of providing electronic rather than mechanical beam scanning. It is especially important to eliminate the use of gimbals since they are slow, bulky and

87

susceptible to mechanical failure as they experience strong mechanical forces that sharply limit the scanning speed [51] - [54]. One the other hand, electronic beam steering radars are fast but rather expensive and power inefficient, requiring several Watts of power. In addition, the incorporated phase shifters are lossy, bulky and in most cases not available at higher MMW frequencies [55], [56].

Considering these limitations, a traveling-wave frequency scanning approach is the simplest method of beam steering if enough bandwidth is available for the radar operation [57]. In a traveling-wave frequency scanning antenna array, scanning is achieved as a result of the frequency dependence of the complex propagation constant of the wave propagating inside the waveguide. Principally, elements are fed in series with a transmission line having an appropriate delay line segments between two adjacent elements. As the frequency is swept the delay lines provide different values for the phase difference and cause beam steering. Taking advantage of transmission lines to generate the desired phase shift discharges us from using electronic phase shifters which require additional power to operate, and reduces the cost of the overall system. Moreover, the problem of connecting the miniature MMIC phase shifter chip to the external antenna via a transition is solved since the phase shifters and radiating elements are now in one unit and can be fabricated on a single substrate.

Travelling-wave antennas are designed based on either dielectric materials [58] which result in slow wave radiation or hollow structures [59], [60] which results in fast wave radiation. In upper MMW band, excessive conductor loss in the complex feeding networks is a major problem. In addition, printed transmission lines such as microstrip require very thin substrates to avoid exciting surface waves. Construction of scanning

arrays based on hollow waveguide structures proves to be convenient since they provide enough bandwidth, do not incorporate dielectric materials, yet present high power handling capabilities and lower loss especially at higher frequencies compared to planar transmission lines. In these travelling-wave structures, the length of the waveguide provides the desired phase shift, while the radiation is through slots cut on the walls of the waveguide making it a leaky wave structure. Another advantage of the hollow waveguides is their light weight which makes them attractive when a large structure like an array is required. In addition, manufacturing such a structure at Y-band frequencies with high resolution is feasible using bulk or surface micromachining techniques.

4.3. Fabrication/Assembly

At high MMW and SMMW bands, as the dimensions of the structures shrink, standard machining methods are not suitable because of low fabrication tolerances and high cost in assembly. However, micromachining offers easy fabrication of complex structures with low cost and low mass. Although micromachining can provide the required tolerances for fabrication of small and high precision devices, there are many limitations on what can be fabricated. For example structures that are 2.5D in nature and structures formed by stacking wafers with 2.5D geometries are straightforward to fabricate. Therefore, the structures have to be simple with all its features aligned with the Cartesian coordinate planes in order to be compatible with micromachining processes.

| (a) | (b) |
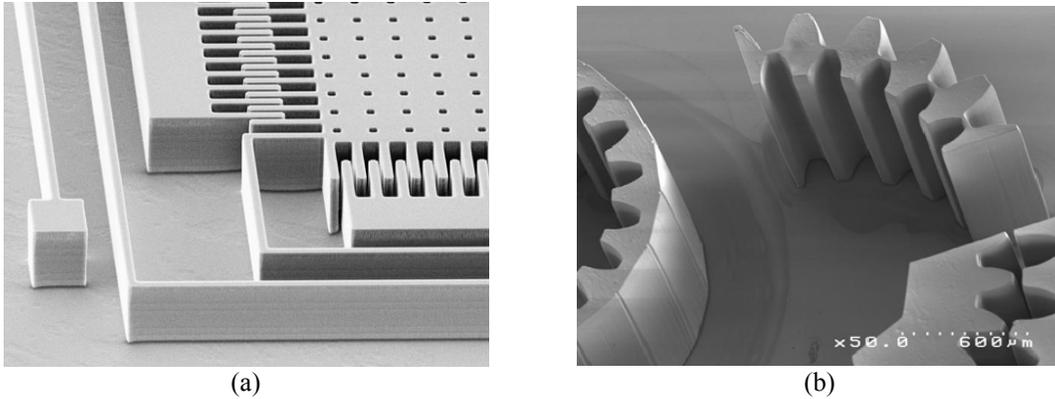
Figure 4.4. (a) Bulk micromachining: the microstructure is fabricated by DRIE etching of silicon substrate [61]. (b) Surface micromachining: the microstructure is fabricated using lithography of a thick SU-8 photoresist layer [62].
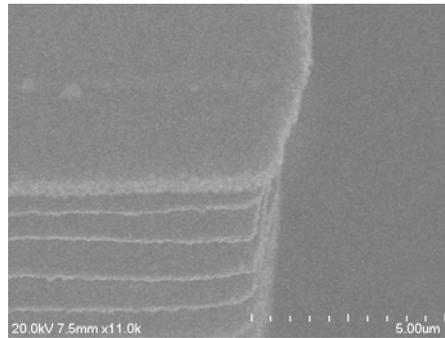
Figure 4.5. Sidewall scalloping of DRIE process

As shown in Figure 4.4, both surface micromachining which creates structures on top of a substrate and bulk micromachining which produces structures inside a substrate are used to create hollow structures. In surface micromachining, the microstructures are fabricated by deposition and etching different structural layers on top of the substrate. For very deep structures such as waveguide trenches, usually thick photoresists are used as structural materials. The material is deposited (spun) on top of the substrate, exposed and developed to form the structure. In bulk micromachining, the substrate itself is the structural material. It is patterned and wet / dry etched to form the microstructure. Bulk micromachining is more expensive and causes sloped sidewalls for wet etching and sidewall scalloping for deep reactive ion etching (DRIE) as shown in Figure 4.5. On the

90

other hand, surface micromachining with thick photoresists is not a consistent process due to issues such as inability to control of the thickness and stress between the thick structural material and substrate.

After forming the waveguide structure by either method, conductive surfaces are eventually built by metal deposition. Lithography techniques or shadow masking can be used to pattern the deposited metal to form array elements if the surface is flat. Shadow masking is not suitable for precise aligning and small exposed areas (below 1000 μm^2). If the surface is not flat such as the case for waveguide trenches which make stepped structures, commonly it is not possible to pattern the thin film layer. Non-contact lithography is one option which results in under-exposure and deviation from the actual dimensions. A feasible method is to selectively deposit metal instead of patterning it. For this purpose, non-standard methods based on shadow masking have been developed to mitigate these problems depending on the application.

When a fully-conductive structure is being microfabricated, dielectric membranes are commonly used for mechanical support for thin metal layers to avoid using dielectric substrates. Depending on the area, thickness, amount of stress and compatibility of the required membrane, silicon, silicon compounds, or organic materials such as polymers and photoresists could be used as membrane. These materials also contribute to bonding wafers to form more complex structures. For silicon compounds and metals, anodic, eutectic and thermocompression bonding are used, while considerably less or no pressure and temperature bonding techniques can be used for organic materials. Fabrication processes commonly used to form complex 2.5 D volumetric structure are summarized in Table VII.

91

Purpose	Techniques	Characteristics/Applications
Bulk/2.5D structure formation	wet/ DRI Etching	Precise depth control, feasibility of multi-step etching, side wall scalloping/ slope, expensive
	thick photoresist patterning	Inconsistency in exposure/developing time
Conductive structure/ element formation	PVD metal deposition	evaporation / sputtering techniques, extremely smooth surfaces
	metal lithography	flat surfaces → conventional lithography stepped surfaces → shadow masking
Dielectric membrane deposition	organic materials	thick, mostly tensile stress, suitable for large area, sensitive to high pressure/temperature
	silicon compounds / metals	thin, high quality, stress controllable, robust to pressure/temperate, suitable for small areas
Stacked layer formation	organic bonding	low/no pressure/temperature low-quality adhesion
	diffusion bonding	high pressure/temperature high quality adhesion

Table VII. Microfabrication processes used for 2.5D stacked structures
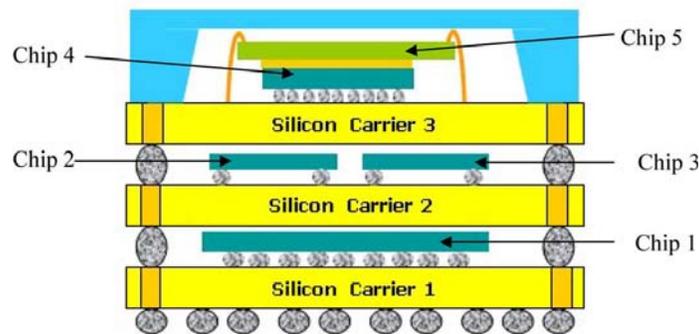
Figure 4.6. Schemetic of 3-D silicon stacked carrier SiP [63]. Chips 1 to 4 are connected with the flip-chip method and chip 5 with wire bonding.

Micromachining also offers feasible approaches for integration of the active chips in the radar substrate. Flip-chip assembly and wire bonding are two well-known methods for interconnecting ICs as shown in Figure 4.6. Based on the application, packaging can be developed using suitable means for interconnection. For the application of the radar, due to the stacked-layer identity of the structure, incorporating the external chips is not straightforward. New methods are developed to meet this goal.

4.3.1.　　　Microfabrication of Rectangular Waveguide

Microfabrication of a simple WR-3 waveguide trench as a basic component of the radar is investigated to explore and find the most efficient techniques suitable for radar fabrication. Most of the early work in waveguide micromachining involved creating the waveguide height by stacking layers of etched silicon wafers. However, this technique needs high-quality wafer-to-wafer metallic bonds in order to prevent interruption of the current flow. There have been several attempts to fabricate W-band waveguides with low-cost microfabrication techniques such as lithography [64], [65]. However, in these techniques, the height of the waveguide is limited by the maximum thickness of the spun photoresist, limiting the fabrication to the reduced-height waveguides which suffer from high attenuation. Taking advantage of the "snap-together" technique, a rectangular waveguide was fabricated in two halves and then the halves were put together to form a complete waveguide ([66] - [68]). Therefore, low-cost lithography methods are first used to fabricate a simple deep channel with vertical sidewalls.

The photoresist SU-8 from Microchem© [69] is a widely used photoresist which can be spun up to 1 ~ 2 mm. The thickness versus spin speed of SU-8 series 2100 is shown in Figure 4.7 (a). To achieve a WR-3 waveguide depth (approximately 432 μm), multi-step spinning is required. A soft-bake step after each spin is necessary to help remove all the cross-links of the polymer which might cause cracking or non-uniformity. To avoid underexposure problems, the thickness of photoresist should be first measured precisely using the Nano-spec (a non-contact spectroscopic-reflectometry tool used for transparent film thickness measurements). After lithography and post-exposure bake, it is developed in Microchem SU-8 Developer. Figure 4.7 (b) shows a meander-line waveguide trench

after gold sputtering. It is observed that some sidewalls are not stiff enough and broke during development or blow dry. This can be attributed to the under-exposure or over-development of the material or high stress between the silicon wafer and thick SU-8 layer. The thickness of the SU-8 layer is comparable to the thickness of the standard 500 μm wafers and hence the amount of stress cannot be neglected. In addition to all these problems, with SU-8 it is not feasible to fabricate a multi-step structure needed for waveguide transition for active component assembly. Moreover, unlike deposition methods the thickness of the spun photoresist cannot be precisely controlled and there is always an error in the thickness (up to 10% for multi-step spinning) involved with spinning. The investigations showed a variety of different thicknesses (380 μm ~ 460 μm) for different spinning conditions.

Due to all these issues, an alternative silicon DRIE approach is used to fabricate the radar substrate. The advantages of this method compared to lithography are:

- Uniformity and flatness of the surface of the substrate

- Controlling the etch depth precisely by time-etching

- Feasibility of consistent etch in different instances

- Feasibility of fabricating multi-step structures using multiple mask layers

- Robustness of the material to high pressure/temperature of bonding

- CMOS-clean processing

- Compatibility with non-standard packaging techniques

- Diverse and selective options for etchants (wet/dry, isotropic/anisotropic)

- Backside process capability needed for packaging

94
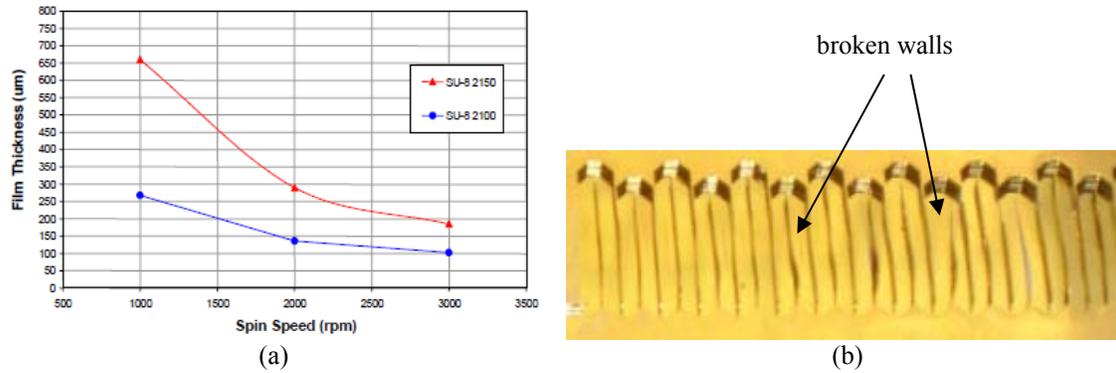
Figure 4.7. (a) Thickness versus spin speed of SU-8 series 2100. (b) meander-line structure fabricated by spinning SU-8 2100 in two steps. The structure is gold-sputtered after developing and hard-bake.

4.4.   Conclusion

In this chapter, a Y-band beam steering MMW imaging and navigation radar system was introduced for operation in conditions limited by smoke, dust, haze or darkness. Different components of the radar and their development technology were described. The radar antenna is a frequency scanning array using rectangular waveguide structure. Manufacturing such a structure at Y-band frequencies with high resolution is feasible using micromachining techniques. The compatible techniques were then introduced and the microfabrication process of a rectangular waveguide was discussed in order to find the most efficient method to fabricate the structure.

Chapter V

MMW Frequency Scanning Antenna Design

The design details of the MMW frequency scanning antenna are presented and discussed in this chapter. This includes introducing the waveguide slot array and hybrid-coupled patch array antennas, loss and reflection minimization required for a very long array, narrowing the beamwidth and all the limitations that should be considered to make the structure compatible with micromachining techniques.

5.1. Design Overview

The frequency scanning array is designed using hollow rectangular waveguides where the length of the waveguide provides the desired phase shift, while the radiation is through slots cut on the walls of the waveguide. This one-dimensional array in the azimuth direction makes a wide beam in the elevation direction which is not desirable. Therefore, in order to confine the beam in the elevation direction, widening the antenna aperture is performed using slot-coupled patch arrays as suggested in Figure 5.1. This two-dimensional structure provides a two-dimensional confined beam.

To design a frequency scanning array based on hollow rectangular waveguides, different configurations of slots - transverse, diagonal and longitudinal -on the narrow and broad walls of the waveguide can be considered as represented in Figure 5.2 (a). The frequency scanning antenna is designed for comparatively large scanning angles ($\pm 25^0$)

around the broadside angle. Since rectangular waveguide is a fast wave structure and its propagation constant is smaller than that of the free space ($\beta < \beta_0$), with spacing smaller than half a wavelength in free space - to avoid generating grating lobes- phase shift between radiating elements is calculated as:

$$\varphi = \beta l < \beta_0 l \xrightarrow{l < \lambda_0/2} \varphi < \beta_0 \lambda_0/2 \rightarrow \varphi < \pi \tag{30}$$

where β is the propagation constant of the TE_{10} mode in the waveguide and l is the distance between array elements. To achieve broadside radiation it is required that the phase shift between elements is $2n\pi$ which is not feasible with this configuration. To resolve this problem, slots can be positioned with spacing larger than half a wavelength and the grating lobes can be suppressed using spatial filters [70]. Another alternative is to have longitudinal or diagonal slots and take advantage of the "phase reversal" phenomenon. However, these methods are not suitable for frequency scanning applications since with a limited bandwidth, none of them can provide a sufficient amount of phase shift between slots along the waveguide to generate large scanning angles. According to array factor formula

$$AF = \frac{\sin(N\psi/2)}{\sin(\psi/2)} \tag{31}$$
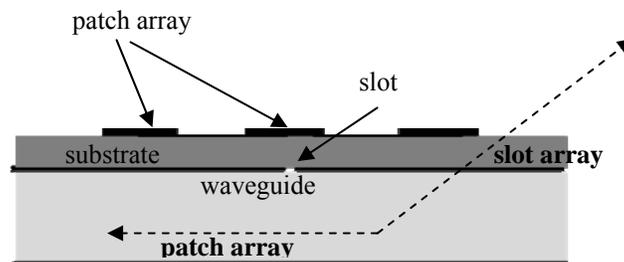
Figure 5.1. The two-dimensional structure of the antenna
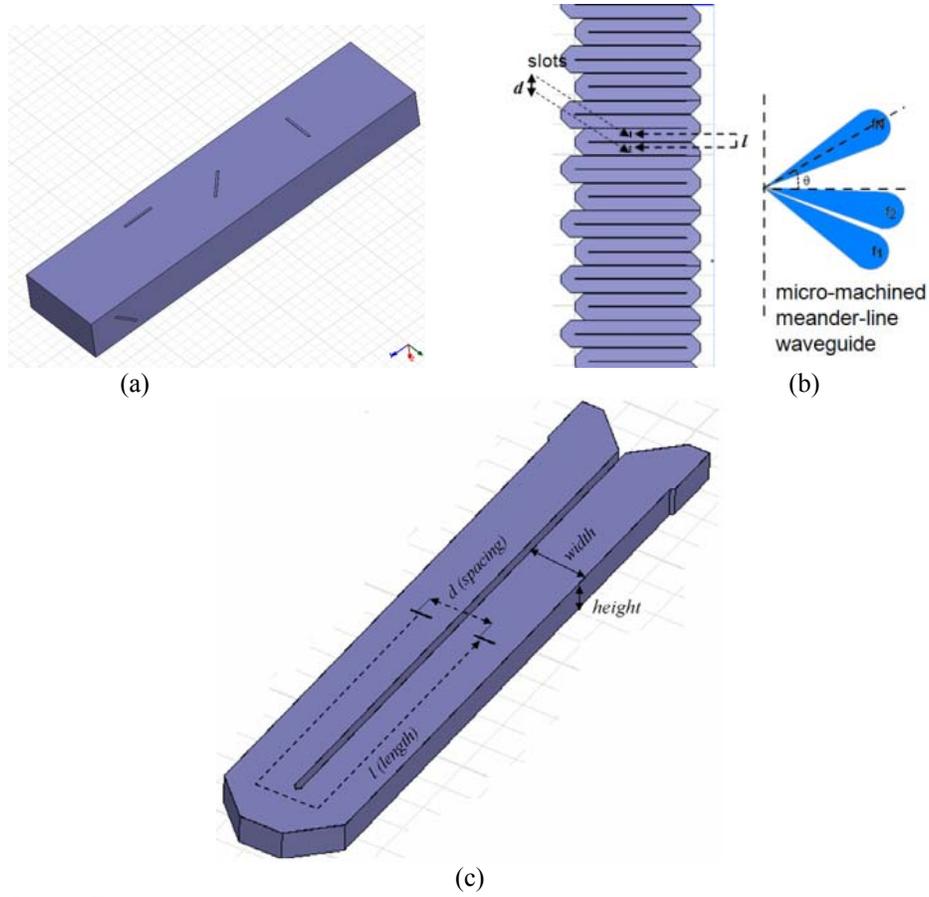
Figure 5.2. (a) Different configuration of slots cut on the walls of a rectangular waveguide. (b) Planer meander-line waveguide slot antenna (d) unit cell of the proposed structure.

where, $\psi = kd\sin(\theta) + \varphi$, k is the wavenumber, d is the spacing between array elements and, φ is the phase shift between elements which is equal to $\varphi = \beta d$. The maximum available scanning angle is then independent of the spacing between slots as

$$\theta_1 = \sin^{-1}\left(\lambda_1 (\frac{1}{\lambda_{g0}} - \frac{1}{\lambda_{g1}}) \right) \tag{32}$$

where, λ_{g0} and λ_{g1} are guiding wavelengths at the center and maximum frequencies. At Y-band, considering the dimensions of the WR-3 standard waveguide ($a = 864$ μm, and $b = 432$ μm), we need to provide approximately 130 GHz bandwidth around 230 GHz (

185 ~ 315 GHz) to achieve $\pm 25^0$ scanning angle around an off-broadside angle (43^0) which is not practical. In order to achieve broadside radiation and a satisfactory amount of phase shift between elements without the need for a large bandwidth, we are required to meander the waveguide which results in the increase in phase shift, while maintaining the spacing between them a smaller quantity in order to avoid generating grating lobes as shown in Figure 5.2 (b) and (c). In this design, the waveguide is bent around the H-plane to have the transverse slots cut on the broad wall as the radiating elements so that microfabrication techniques are able to manage etching the height of the waveguide which is more achievable than etching the thick width of the waveguide. In this structure, $\psi = kd \sin(\theta) + \beta l$ where d is the spacing between elements which is the sum of the waveguide width and the separating wall, while l is the length between them in each turn as shown in the unit cell of the structure in Figure 5.2 (c). Hence, it is feasible to realize broadside radiation at any desired frequency with $\beta l = 2n\pi$ since l is flexible amd the maximum scanning angle can also be calculated as

$$\theta_1 = \sin^{-1}\left(\frac{l\lambda_1}{d} (\frac{1}{\lambda_{g0}} - \frac{1}{\lambda_{g1}}) \right) \tag{33}$$

To have the broadside radiation at the center frequency, l is chosen to be a modulus of λ_{g0} in order to generate $2n\pi$ phase shift between the elements at the center frequency. Table VIII shows the range of scanning angle assuming 15 GHz available bandwidth (230 ~ 245 GHz) around the broadside radiation at 237.5 GHz for different values of wall thicknesses and length between elements. The structure of the meander-line waveguide requires the current distribution on the broad wall of waveguide to reverse after a turn as

shown in Figure 5.3. Therefore, the length between slots must be corrected by adding a $\lambda_{g0}/2$ segment so that the magnetic current on the slots are in phase at the center frequency. The additional segment increases the scanning angle as shown in Table VIII. For the current design, $t = 250\mu m \rightarrow l = 5.5 \lambda_{g0} = 1.02$ cm is chosen.

To achieve a very narrow beamwidth (i.e. $\alpha = 2^0$), the length of the antenna should be extended by using a number of the unit cells. Considering $\alpha = \dfrac{\lambda}{L}$ where, L is the aperture length, at 230 GHz, $L = 37.4$ mm to achieve 2^0 beamwidth, which gives around 36 turns. Since the overall waveguide length is quite large ($\sim 36\times l = 36$ cm), and a large number of slots are involved, sources of loss and reflection from the finite conductivity of metals, waveguide turns, and slots must be managed very carefully.

out of phase   in phase

(a)   (b)
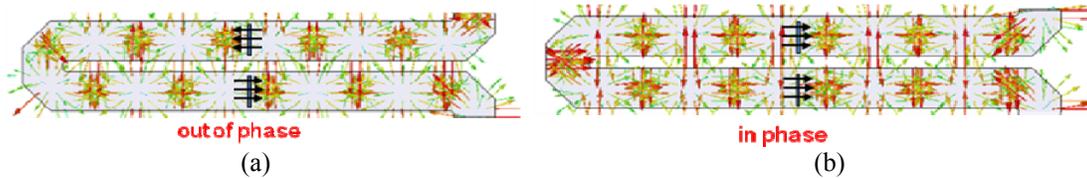
Figure 5.3. The current distribution on the broad wall of the rectangular waveguide. (a) For $l = n\lambda_{g0}$ it is noticeable that the direction of the electric field on the slot is reversed. (b) The reverse is compensated by adding adding a $\lambda_{g0}/2$ waveguide segment.

Thickness of the separating wall $d = a + t$	Length between the elements	Range of the scanning angle
$t = 50$ μm	$l = 4 \lambda_{g0}$	23.30 ~ -21
$t = 150\mu m$	$l = 5 \lambda_{g0}$	26.4 ~ -23.70
$t = 250\mu m$	$l = 5 \lambda_{g0}$	240 ~ -21.80
$t = 50$ μm	$l = 4.5 \lambda_{g0}$	26.40 ~ -23. 70
$t = 250\mu m$	$l = 5.5 \lambda_{g0}$	26.50 ~ 23.80

Table VIII. The scanning angle of the antenna for different wall thicknesses and lengths between elements.

100

5.2.   Reflection Minimization

There are two sources of reflection in the meander-line structure: the bends and the slots. To minimize the reflection from the bends, their profile should be designed for a minimum reflection. This can be performed by optimizing the shape of the bends using Ansoft HFSS. Simulations results show that a diagonal cut around the edges provides a better transmission compared to a curved turn as shown in Figure 5.4 (a) and (b). However, even though the reflection from bends is minimized, a number of successive small reflections from all bends add up to a considerable amount. One way to minimize total reflection from bends is to make the distance between bends an odd modulus of $\lambda_g/4$ at the center frequency to make a destructive interference– the two-way distance should be a modulus of $\lambda_g/2$ - so that the total reflection is cancelled. A unit cell of such a structure is presented in Figure 5.5 (a) consisting of four waveguide sections. In this structure, in order to have the slots in phase while having $\lambda_g/4$ spacing between the elements, the length of one of cells should be λ_g smaller. Figure 5.5 (b) shows the reflection coefficient of this structure. It is observed that although the reflection is minimized at the center frequency, it is a considerable amount at other frequencies and might cause a constructive interference and large reflection in the final structure. Figure 5.5 (c) represents the reflection coefficient for the total of nine unit cells which shows a very high return loss around 233 and 243 GHz. Another way to minimize the total reflection is to have constructive interference for the center frequency, since the reflection of the bend is already minimized by optimizing the diagonal cut shown in Figure 5.4.
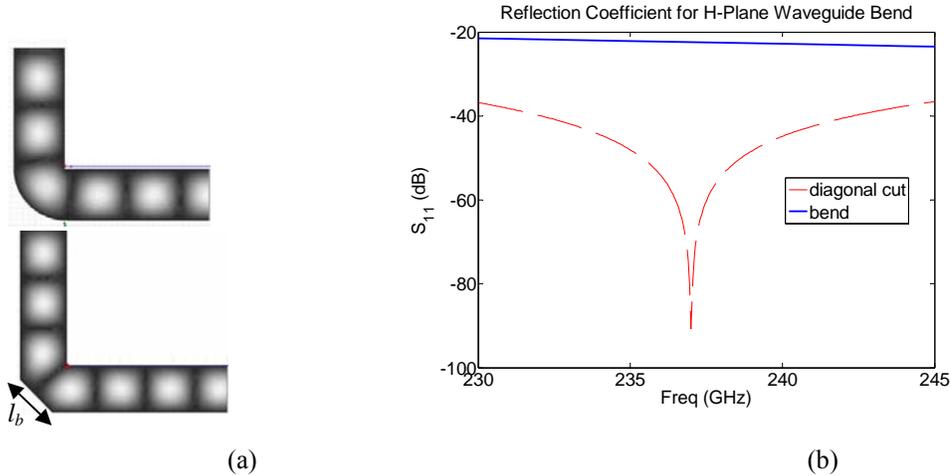
Figure 5.4. (a) Electric field distribution inside the waveguide for curved and diagonal cut bends. (b) Reflection coefficient from the bends. The diagonal cut bend is 45^0 and $l_b = 0.85$ mm.

In this case, the reflection in the beginning and the end of the band is minimized by changing the thickness of separating walls (t) to make the destructive interference. The reflection coefficient of the structure is shown in Figure 5.5 (e) and (f) for one and nine unit cells. The maximum reflection is below -18 dB as opposed to -2 dB reflection for the former structure, while the reflection at the center frequency is maintained around -60 dB. This structure has thicker separating walls which makes it stiffer and suitable for microfabrication.

To minimize the reflection of the slots, having cut one slot in each turn, the two-way distance between two successive slots is an integer multiple of λ_g ($2 \times 5.5 = 11 \lambda_g$ in this design). Therefore, their successive reflections add up coherently and causes scan blindness at the center frequency. To mitigate this problem we need a reflection canceling pair for each slot positioned at $\lambda_g / 4$. A unit cell of the proposed geometry is shown in Figure 5.6 (a). In this case, the array factor can be written as:
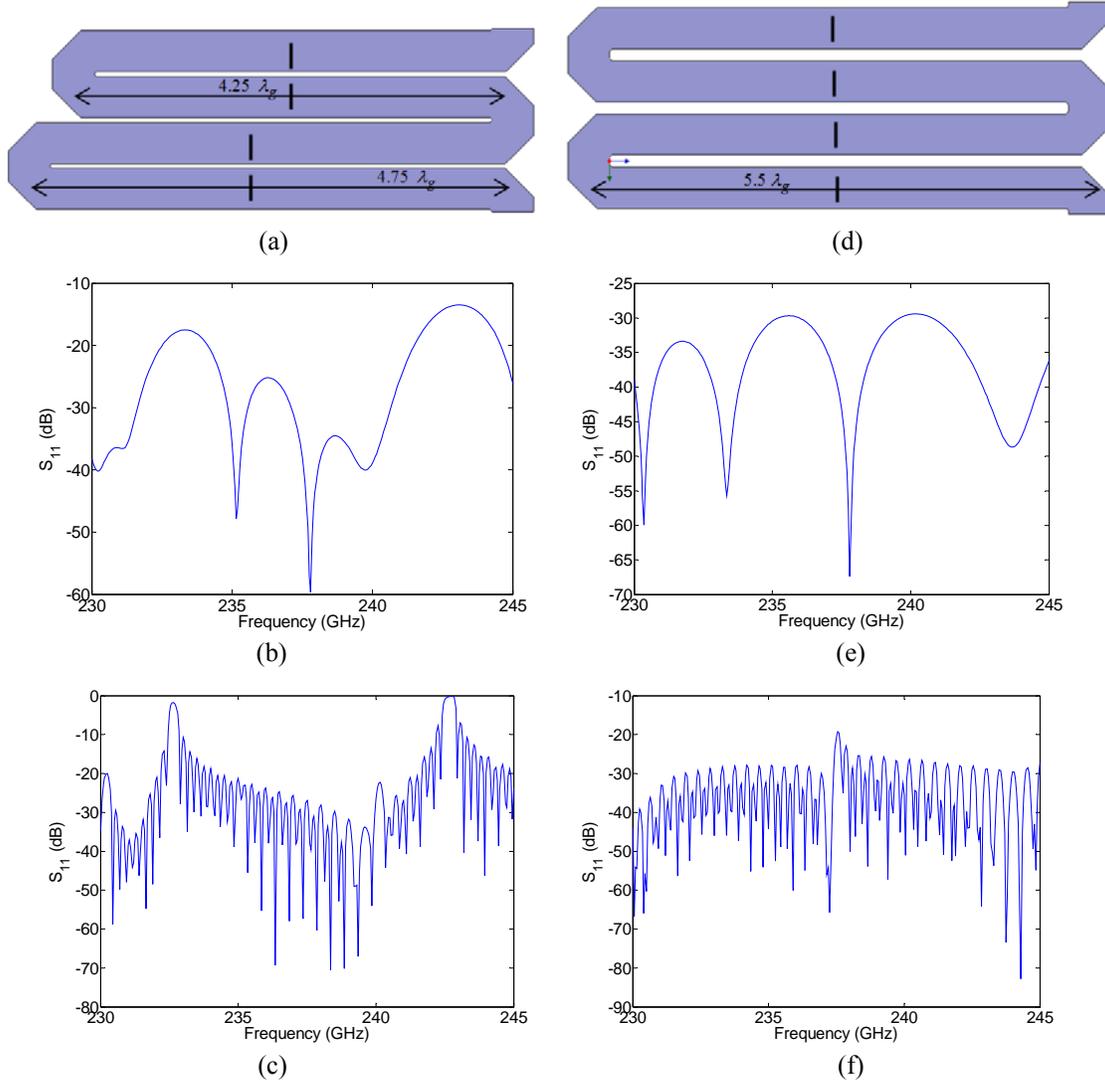
Figure 5.5. (a) The unit cell of the meander-line structure optimized for minimum reflection at the center frequency with 50 μm separating walls. (b) Reflection coefficient for the unit cell. It is minimized for the center frequency. (c) Reflection coefficient for nine unit cells. The constructive interference at some other frequencies causes a high reflection. (d) The unit cell of the meander-line structure with 250 μm separating walls optimized for minimum reflection at the beginning and end of the band. (e) Reflection coefficient for the unit cell. (f) Reflection coefficient for nine unit cells

$$AF = 1 + e^{-jk_0 d_y \sin(\theta)\sin(\varphi)+j\phi_1} + e^{jk_0 d_x \sin(\theta)\cos(\varphi)+j\phi_0} \tag{34}$$
$$+ e^{jk_0(d_x \sin(\theta)\cos(\varphi)+d_y \sin(\theta)\sin(\varphi))+j(\phi_0+\phi_1)}$$

where $\phi_0 = \beta_g l$ and $\phi_1 = \beta_g d_y$, $d_y = \lambda_g / 4$, $l = 5.5\lambda_g$. The array factor represented in

Figure 5.6 (a) for the whole array for the actual value of $d_x = a + 250$ μm $= 1114$ μm.

103
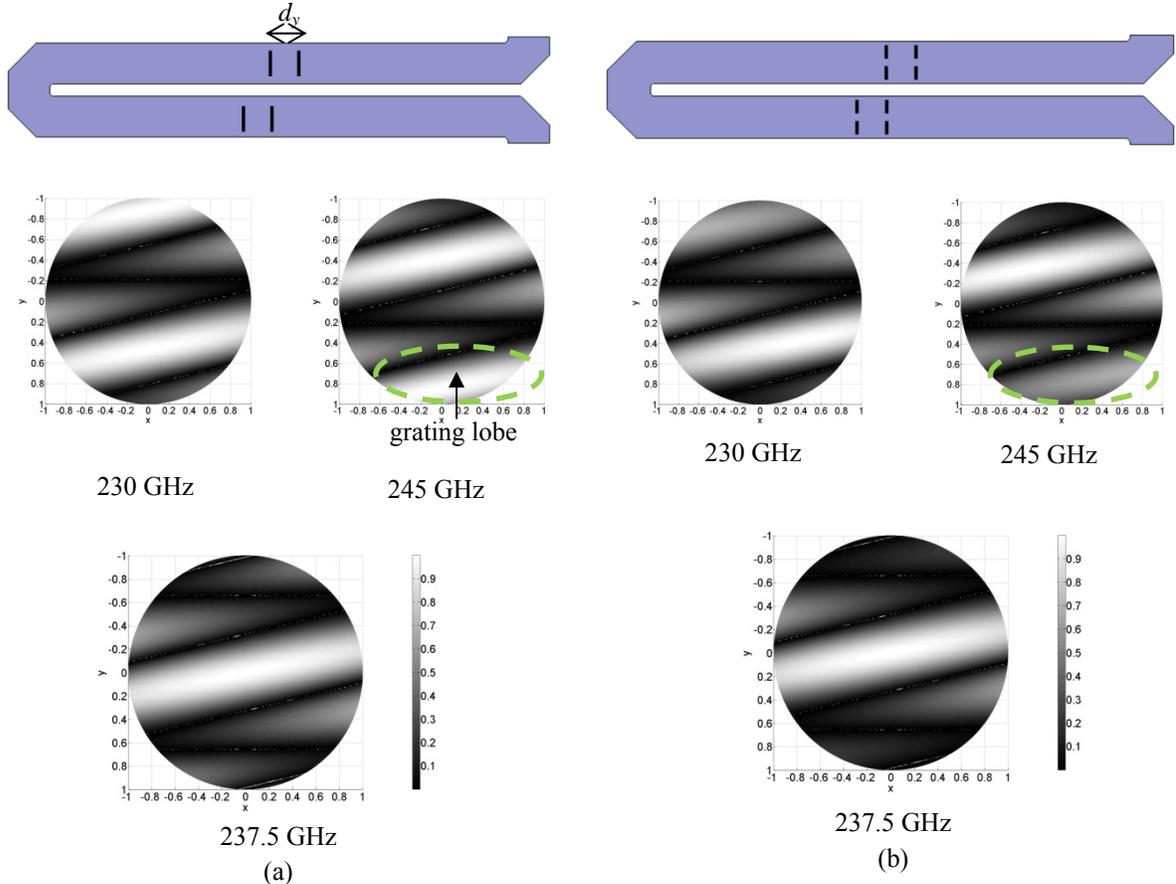
Figure 5.6. (a) Unit cell with reflection cancelling slot and the analytical far-field pattern of the array at the beginning, center and end of the band. (b).The final proposed structure with additional slot across the broad wall of the waveguide and the analytical far-field pattern of the array at the beginning, center and end of the band. It is observable that the grating lobe is around -8 dB lower.

It is observable that the grating lobes are generated due to the fact that the spacing is larger than half a free space wavelength ($\lambda_0 = 1.2$ mm) which is mostly imposed by the width of WR-3 waveguide. To overcome this problem, we assign two slots along the width of the waveguide to make the spacing half as shown in Figure 5.6 (b). The array factor of this structure can now be written as:

$$AF = 1 + e^{jk_0 d_x \sin(\theta)\cos(\varphi)} + e^{-jk_0 d_y \sin(\theta)\sin(\varphi) + j\phi_1} + e^{jk_0(d_x \sin(\theta)\cos(\varphi) - d_y \sin(\theta)\sin(\varphi)) + j\phi_1}$$
$$+ e^{jk_0(2d_x \sin(\theta)\cos(\varphi) + d_y \sin(\theta)\sin(\varphi)) + j(\phi_0 + \phi_1)} + e^{jk_0(3d_x \sin(\theta)\cos(\varphi) + d_y \sin(\theta)\sin(\varphi)) + j(\phi_0 + \phi_1)} \tag{35}$$

104

As it is shown, the grating lobes have much lower amplitude (-8 dB lower) in the azimuth direction and have been removed. This is mainly due to the fact that the antenna physical size is increased which results in a narrower beam.

5.3. Conductor Loss

In a rectangular waveguide, the conductor loss is calculated from [71]

$$\alpha = \frac{R_m(2bk_c^2 + ak_0^2)}{ab\beta_{TE_{10}}k_0 Z_0} \tag{36}$$

where $R_m = \sqrt{\frac{\omega\mu_0}{2\sigma}}$, is σ the electrical conductivity, k_c the cut-off frequency of the waveguide, k_0 wavenumber, Z_0 free space characteristic impedance, a and b are width and height of the waveguide. In 230~245 GHz band for the standard WR-3 waveguide size, $\alpha \approx 18$ dB/m for gold and 16 dB/m for copper and the total loss for the meander-line structure is around 6.6 dB for gold and 5.9 dB for copper which mean around 20% of the power reaches the end of the waveguide. The amount of radiated power from slots should be managed accordingly in order to have a uniform power distribution for each element.

5.4. Slot Positioning and Shape

Although transverse slots are not commonly used in array applications for broadside radiation mainly because the spacing is twice as much the longitudinal slots which results in grating lobes, they are successfully used in traveling-wave arrays for off-broadside

radiation [72] and are suitable for the application of this work since the length required to generate the desired phase shift is provided by the length of the meander-line structure. In addition, since these slots are used to excite patch arrays later and the patch arrays should be oriented along the elevation direction, they should be positioned along the waveguide. For the array positioned along the waveguide, transverse slots are the only options for excitation.
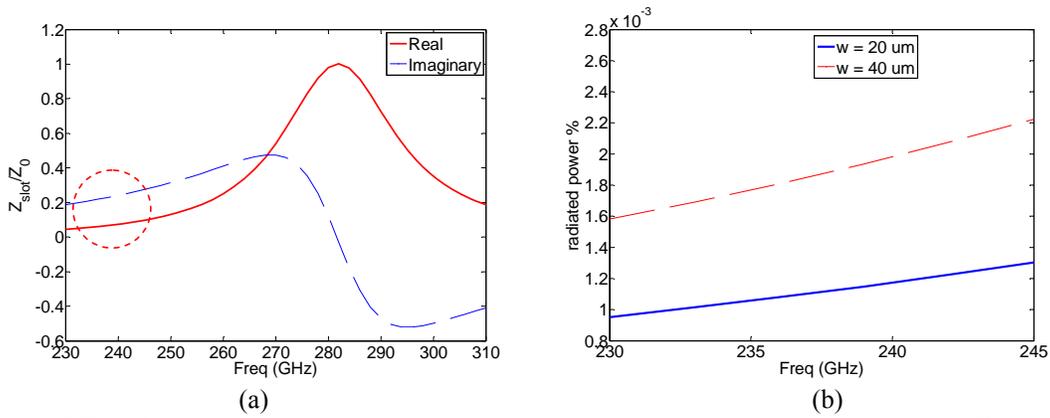
Figure 5.7. (a) Normalized slot impedance versus frequency. A resonance happened at 282 GHz. (b) The total power associated with a non-resonant slot for two different widths.

At the resonant frequency, the amount of radiated power and thus the radiation resistance of a slot are maximized as shown in Figure 5.7 (a). However, since in a large array it is mostly desirable to distribute the power evenly among the elements, a small amount of power is apportioned to each slot and thus the slots should be non-resonant. In addition, the width of the waveguide does not allow two resonant ($\lambda_0 / 2$) slots. Therefore, the dimensions of the slots are chosen to be much smaller than $\lambda_0 / 2$. By changing the dimensions of the slots, we can control the amount of radiated power off each slot. Figure 5.7 (b) shows the total power associated with a non-resonant slot (radiated plus stored) for slots with around $\lambda_0 / 4$ length at two different widths. Since

the amount of propagating energy is decreased along the waveguide as it is partly radiated and stored around each slot, and lost due to the finite conductivity of metal, the dimensions of the slots should be increased gradually so that the radiated power remains constant throughout the length of the waveguide even though the input power is decreased. To design the slot dimensions, first we assume that the radiated power from the four adjacent slots in each turn is constant. Therefore, considering the conductive loss, in each turn

$$P_2 = P_1 - 4\alpha_s P_1 - \alpha_c P_1 \tag{37}$$

where, P_1 and P_2 are the input and output powers in the waveguide, α_c is the percentage of the conductive loss and α_s the percentage of the radiated power off of each slot. For the next turn, the amount of the input power is decreased to P_2 hence α_s for each slot should be increased so that the total power $\alpha_s P$ remains constant. This recursive formula is used to assign power for radiating slots in each turn considering the fact that only 20% of the power is radiated. Ansoft HFSS is used to estimate the radiated power from slots with different widths and the simulation results show that increasing the width of the slots gradually from 5 μm to 60 μm guarantees uniform radiated power. The widths of each set of the slots are shown in Figure 5.8

| 5 μm | 10 μm | 15 μm | 21 μm | 28 μm | 35 μm | 43 μm | 52 μm | 60 μm |
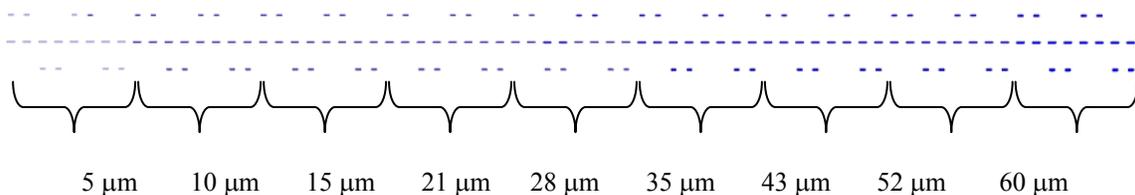
Figure 5.8. The slot width for each four turns so that nine different widths are used for the 36 turn waveguide. The length of the slots is 380 μm.

5.5. Hybrid-Coupled Patch Array

As mentioned, the one-dimensional array of slots generates a very wide beam in the elevation direction. For many applications ranging from collision avoidance to indoor mapping, wide beamwidth is not desirable due to the possibility of the interference caused by other targets. In order to confine the beam, we need to provide a long aperture in that direction as well. One method to achieve this is to design patch arrays which are fed by these slots. Figure 5.9 shows a hybrid-coupled patch array proposed to provide a narrow beam in the elevation direction. In these arrays, the patches are positioned on top of the slots separated by a dielectric substrate. The center patch is fed by the slot on the bottom layer of the substrate, while the rest are series-fed through the center one [73]. The feeding is a combination of both planar and non-planar methods. The main advantage of this coupling method is the ability to control the illumination function separately in both array directions in order to produce a specified radiation pattern so that while the pattern is scanning in the azimuth direction, it is fixed in the elevation direction.
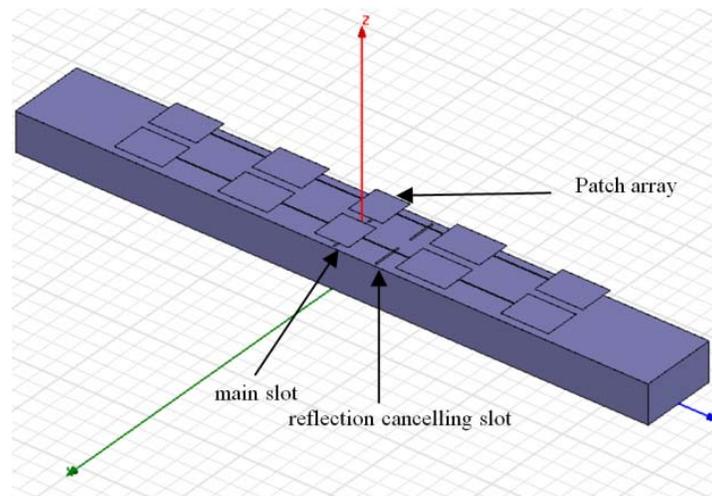
Figure 5.9. Hybrid-coupled patch array fed by the main slot

108

However, the main issue associated with designing patch antennas at high frequencies is that in order to suppress the propagation of the surface waves, very thin substrates are required. For example, at 240 GHz, 50 μm glass or 20 μm silicon substrates are only around one tenth of the guiding wavelength and they are almost impossible to handle. Yet at the same time, they are thicker than what can be spun or deposited specifically for most commonly used low-loss materials (such as spin-on glass [74] which can be spun up to 5 μm). In addition, dielectric materials add to the size and loss of the structure. Hence, using a dielectric substrate for the patch array is not desired. Instead, an air substrate can be used where the patch array is suspended on a thin layer of a thin dielectric membrane. With an air substrate, no surface waves are excited, bandwidth is improved and the efficiency is greatly enhanced.

In general, the design procedure can be organized in two parts: the series-fed patch array and the aperture-coupled patch. The series-fed array consists of patches and high impedance transmission lines. Quarter-wave transmission-line sections can be used to minimize the return loss. To design a broadside standing wave patch array, all the patches must be in phase so that both the patches and the connecting lines are approximated to be half a guiding wavelength long. To obtain nearly uniform illumination for all the patches, the widths are chosen to be identical. For maximum radiation, the patch width is approximated as [75]

$$W = \frac{\lambda_0}{2} \sqrt{\frac{2}{\varepsilon_r + 1}}$$

(38)

At 240 GHz for an air substrate $W = 652$ μm. The width of the waveguide plus the

109

thickness of the separating walls ($t = a + 250$ μm $= 1114$ μm) should be able to accommodate the width of two patch arrays (given that there are two slots along the width). Since $W > 1114$ μm / 2, we are required to decrease the width. This will also increase the gap and help decrease the mutual coupling between the adjacent arrays. On the other hand, wider patch provides narrower beamwidth in the azimuth direction which helps lower the side lobe level. Therefore, an optimized width is required to provide a narrow enough beamwidth in the azimuth direction with a minimized mutual coupling

A three-element series-fed patch array is designed with the help of the equivalent circuit model of the patch antenna and shown in Figure 5.10 (a) and (b). The equivalent conductance and susceptance of the patch antenna for $h / \lambda_0 < 0.1$ are calculated as

$$G_r = \frac{W}{120\lambda_0} \left(1 - \frac{1}{24} (k_0 h)^2 \right)$$

(39)

$$B_r = \frac{W}{120\lambda_0} \left(1 - 0.636 \ln(k_0 h) \right)$$
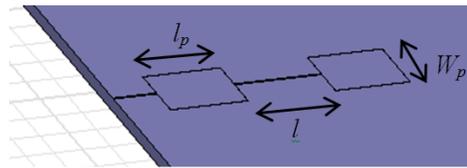
(a)
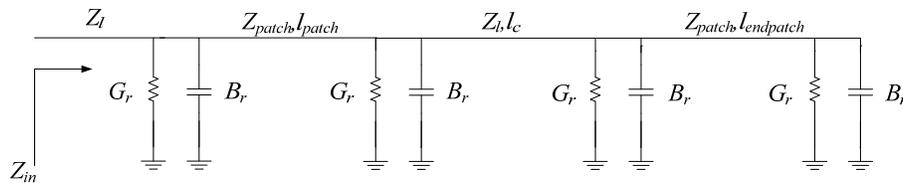
(b)

Figure 5.10. (a) series-fed patch array, (b) equivalent circuit model of the series-fed patch array.

110

where *h* is the thickness of the substrate. This model is used to approximate the lengths of patches and transmission lines which are slightly shorter than half a wavelength due the presence of the slot admittance $G_r + jB_r$. The end patch is slightly shorter than the other patches in order to match the open-circuit end to the rest of the array. The final optimization of the dimension is carried out by Ansoft HFSS to achieve the minimized return loss at the center frequency.

As for the aperture-coupled (center) patch, the length of the patch and the connecting transmission lines to the series-fed patch array are estimated using the circuit model shown in Figure 5.11 (a) and then optimized by using Ansoft HFSS so that that the S-parameters are resonant and the directivity of the antenna is maximized at the center frequency as shown in Figure 5.11 (b). The radiation pattern of the hybrid-coupled patch array for a total of seven elements (two three-element series fed each side of the center patch) is presented in Figure 5.11 (c) and provides 8^0 of beamwidth.

To provide efficient slot-patch coupling, the thickness of the air substrate should be kept below 100 μm. For thicker substrates, the coupling is weakened as shown in Figure 5.12. As mentioned before, hollow structures including a patch substrate are fabricated using silicon bulk micromachining. The proposed substrate will include patches and slots on either side of the substrate which is a custom-made, non-standard ultra-thin wafer with the precise thickness of the substrate. These substrates are costly and hard to handle. To make the structure more robust for fabrication, the feasibility of using thick standard substrate was investigated. As shown in Figure 5.13 incorporating dielectric walls confine the field under the patch. The idea stems from the fact that the vertical field component of the slot adjacent to the dielectric wall with a higher dielectric constant is

enhanced; since the tangential component of the electric field remains the same while the normal component is decreased by the ratio of dielectric constant of the two media. Therefore, the electric field is bent toward the boundary.

(a)

(b)

f = 230 GHz   f = 237.5 GHz

(c)
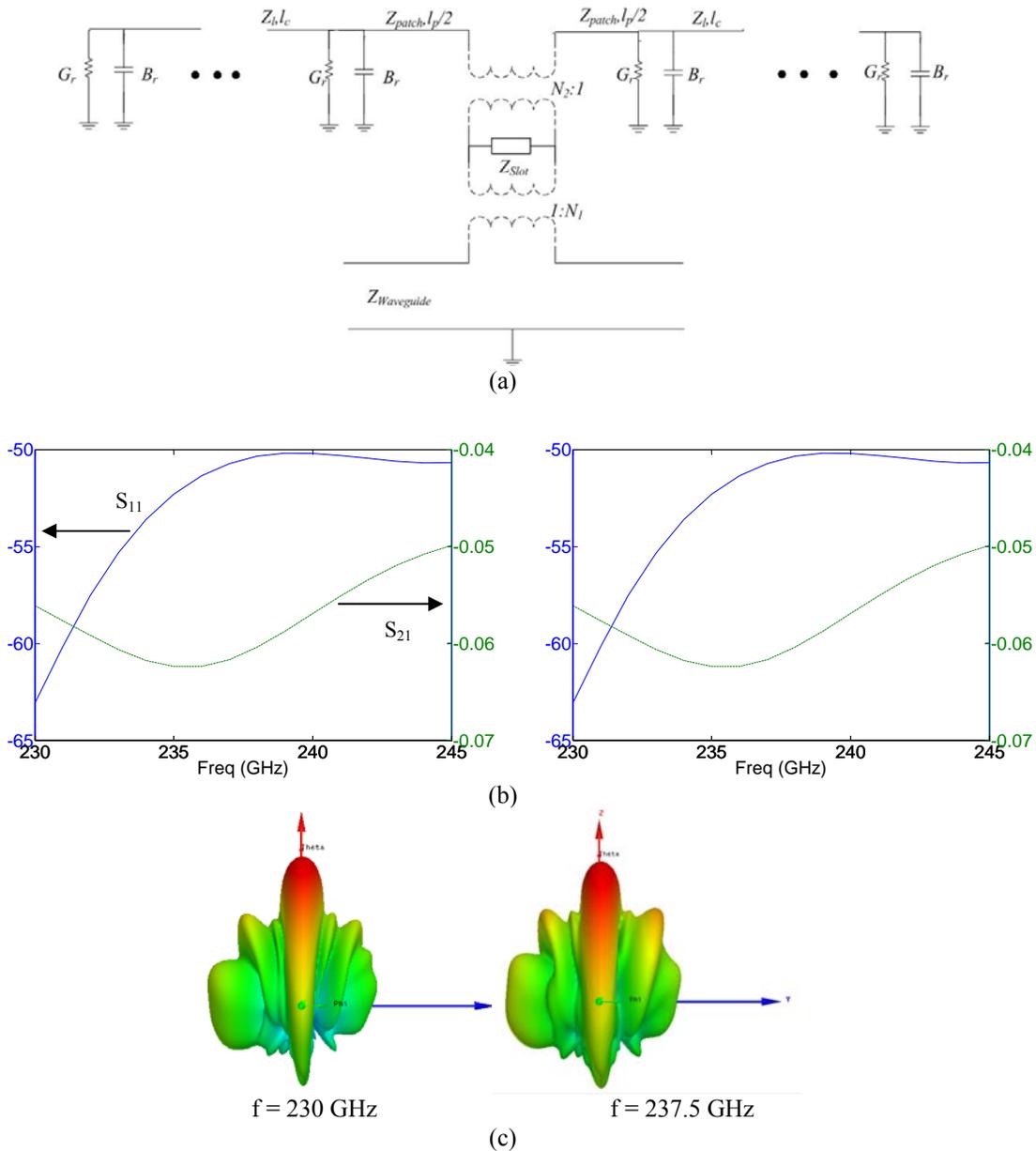
Figure 5.11. (a) equivalent circuit model of the hybrid-coupled patch array, (b) directivity of the hybrid-coupled patch array and the S-parameters of the waveguide for the center patch length of 380 um. The lengths of the center patch and connecting line to the series-fed array are optimized in such a way that the directivity is maximized and the S-parameters show resonance and (c) far-field radiation pattern of the antenna.
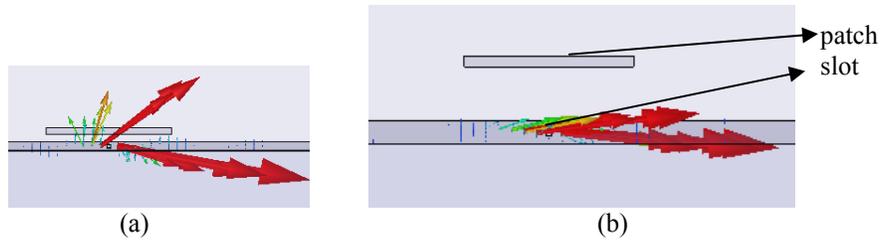
Figure 5.12. Electric field distribution for air substrate at 230 GHz (a) 80 um substrate (b) 250 um substrate (c) 250 um substrate with silicon walls
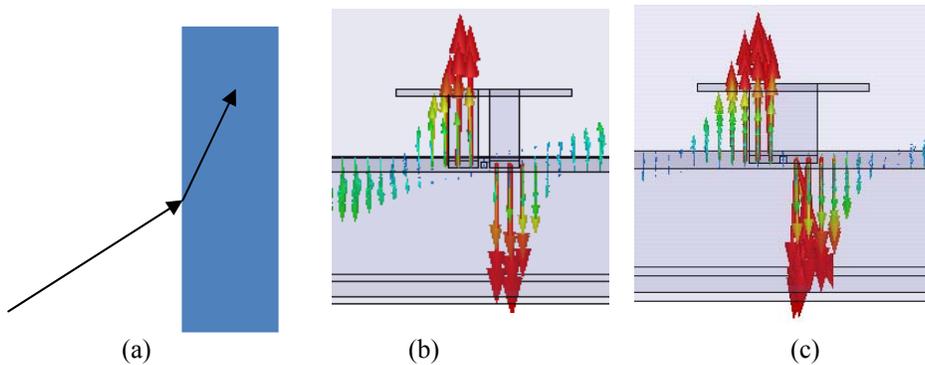
Figure 5.13. (a) Electric field at the boundary of two dielectric materials. The electric field distribution under a patch element excited from a very thin slot far from the patch element assisted by (b) high dielectric vertical walls (c) dielectric block.

Although a single patch may now be excited on thick substrate, the rest of the array can take advantage of a thin substrate as suggested by the structure shown in Figure 5.14 (a), in which the center patch is fed through the slot with the thick air substrate and dielectric block, while the rest of the patches are series-fed with the original thin substrate making a multi-step structure. This structure can be fabricated on a thick standard wafer which is more robust. The dimensions of the center patch and silicon block are optimized using Ansoft HFSS. The simulation results show low side-lobe level and acceptable directivity over the band shown in Figure 5.14. (b) and (c).

(a)

(b)

(c)

(d)
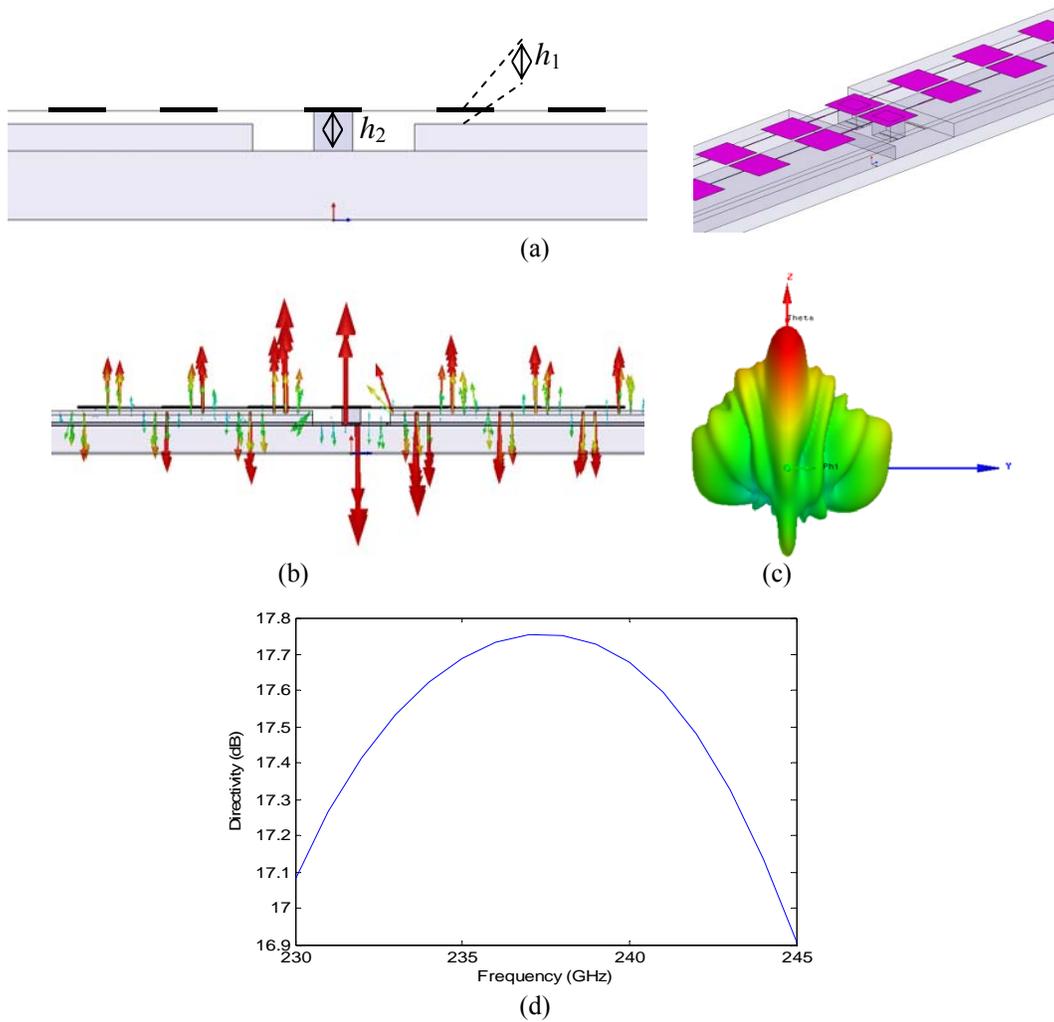
Figure 5.14. (a) The proposed hybrid-coupled patch array with silicon block to enhance slot-patch coupling. (b) The electric field distribution (c) the radiation pattern at the center frequency 237.5 GHz and (d) the directivity over the frequency band.
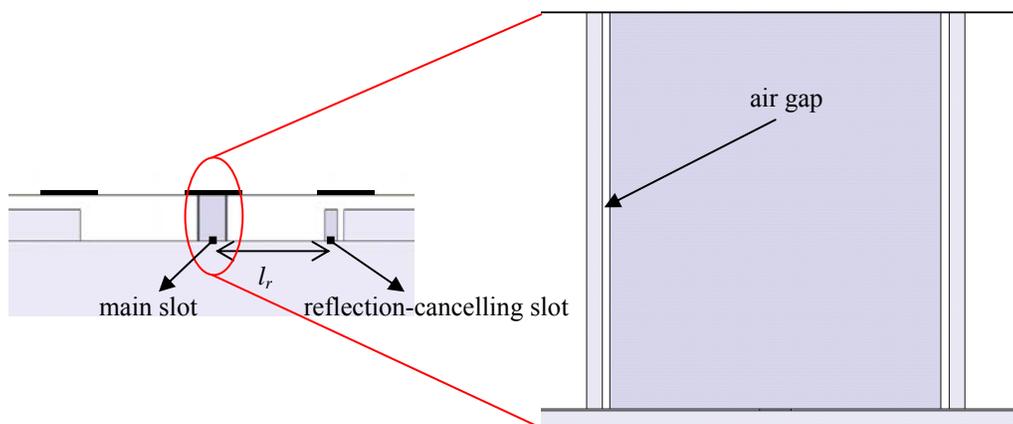
Figure 5.15. A developed version of hybrid-coupled patch array compatible with microfabrication.

114

As a part of fabrication process, this multi-step structure is metal-coated to provide a ground for the patch array. However, as mentioned it is not possible to selectively deposit metal on multi-step substrates. The sidewalls of the silicon block and the reflection cancelling slots will be coated as a result which is not desirable. To be more compatible with microfabrication limitations, the altered design in Figure 5.15 is proposed where all the sensitive areas are protected and selective coating is not required. In this design, two sets of silicon walls are added to the structure to prevent gold deposition on the main silicon block and the reflection-cancelling slot. As shown in the figure, since the air gap is very thin ($< 3 \sim 5$ μm) and the aspect ratio is high, the walls are not metal-coated during metal deposition. In addition, the reflection cancelling slot is covered with a block which will be metal-coated later and makes it capacitive. Since the radiating slot is inductive, the distance between the two (l_r) should now be a modulus $\lambda_{g0}/2$ to cancel the reflection. The dimensions of the slot and the blocks are optimized in Ansoft HFSS to minimize the reflection loss at the center frequency.
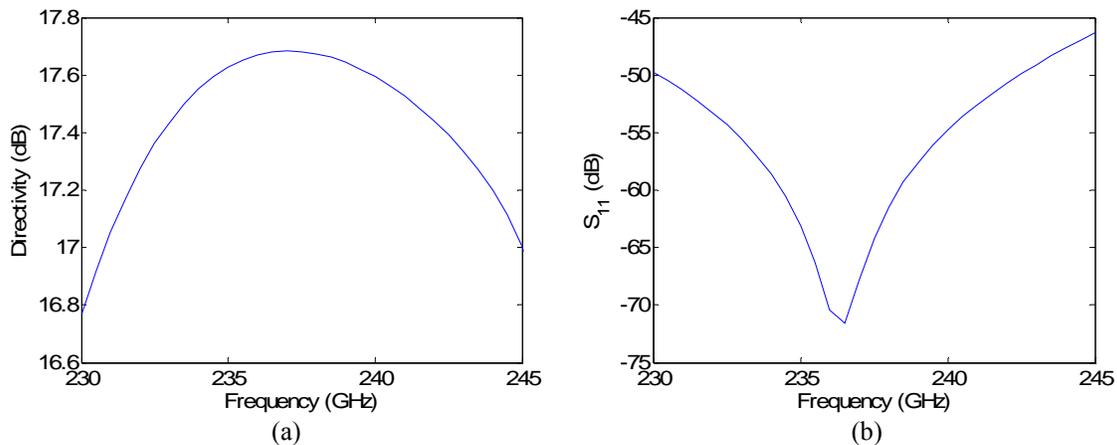
Figure 5.16. (a) The directivity and (b) return loss versus frequency of the patch array of Figure 5.15. $l_r =$ 950 μm

5.6. The Final Design

The final antenna structure and its radiation pattern in the azimuth direction are shown in Figure 5.17 (a) and (b). The presented results are from the analysis of half of the structure with the current computer resources. It is noticeable that the main beam is steering from -24^0 to $+26^0$ by changing the frequency from 230 GHz to 245 GHz. The scan angle for different frequencies is listed in Table IX.
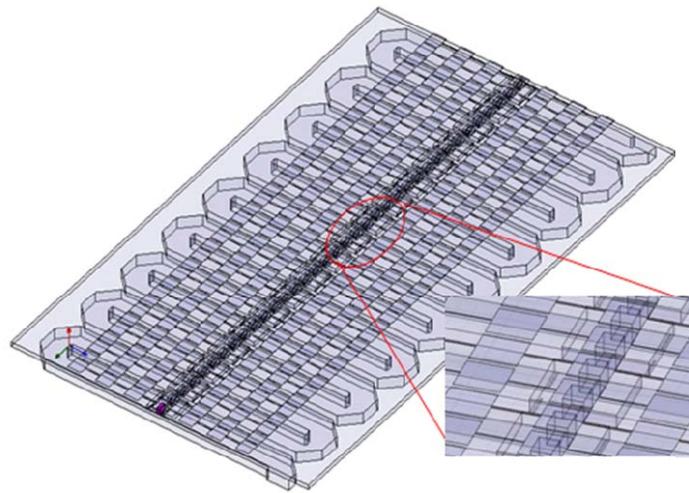
(a)
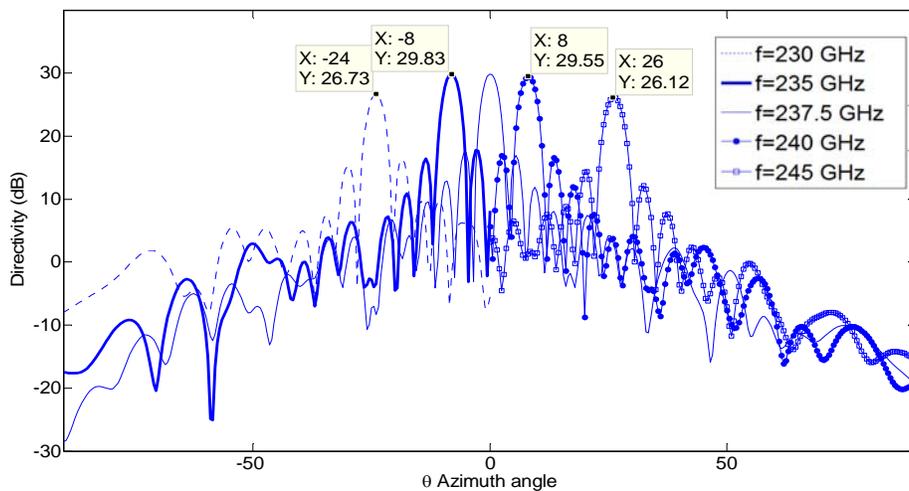
(b)

Figure 5.17. (a) The final structure (b) the radiation pattern in azimuth direction to verify the frequency scanning.

116

Frequency (GHz)	Scan Angle	Directivity
230	-24 deg	26.73 dB
235	-8 deg	29.83
237.5	0 deg	29.87
240	8 deg	29.55
245	26 deg	26.12

Table IX. The scan angle and directivity versus frequency.

5.6.1.   Sensitivity Analysis

Despite high level of accuracy, micromachining with multiple fabrication processes is prone to errors caused by small misalignments, as well as geometrical distortions resulted from lithography and etching. Etching silicon very deep (~432 μm) with uniformity and high precision over large areas is rather difficult. The etch rate might vary depending on the temperature, the position of the feature on the wafer, RIE lag effects, loading effects, etc. One of the very common errors in DRIE etching is the non-uniformity in large open areas. Basically, the edges of the wafer are etched faster than the center resulting in bowed surface structure as shown in Figure (a). This effect could be further increased in structure such as meander-line waveguide due to the loading effect cause by the adjacent channels. The non-uniformity in not trivial and can be up to 15%. However, since it only affects the height of the waveguide, it does not change the propagation constant and dispersion characteristics of TE_{10} mode of the waveguide which is only the function of waveguide width. However, for a reduced-height waveguide, loss increases as shown in Figure (b). It is noticeable that 70 μm error in height causes around 10% increase in waveguide loss.

In addition, since the etched area for the meander-line structure is very long (~ 36 cm) and multi-step patterning and etching are required for this large area, a spotless pattering

cannot be guaranteed everywhere due to the possible residues or contamination of processing. Specifically, oxide and photoresist masks cannot be totally spotless. Experimental results show that the residues might cause bumps with up to 20 μm height after etching. This is about 5% of the waveguide height. Therefore, it is essential that a structure with randomly-distributed etching defects as shown Figure 5.19 be also simulated to test the effect of these spots on the performance of the structure. The simulation results does not show a noticeable effect on the antenna pattern and return loss, mainly due to the small height and area of the residues. It should be noted that the presented figure is the extreme case. One average, there is one smaller bump per two/three turns.

h_{WR-3} 80%~ 85% h_{WR-3}

(a)

(b)
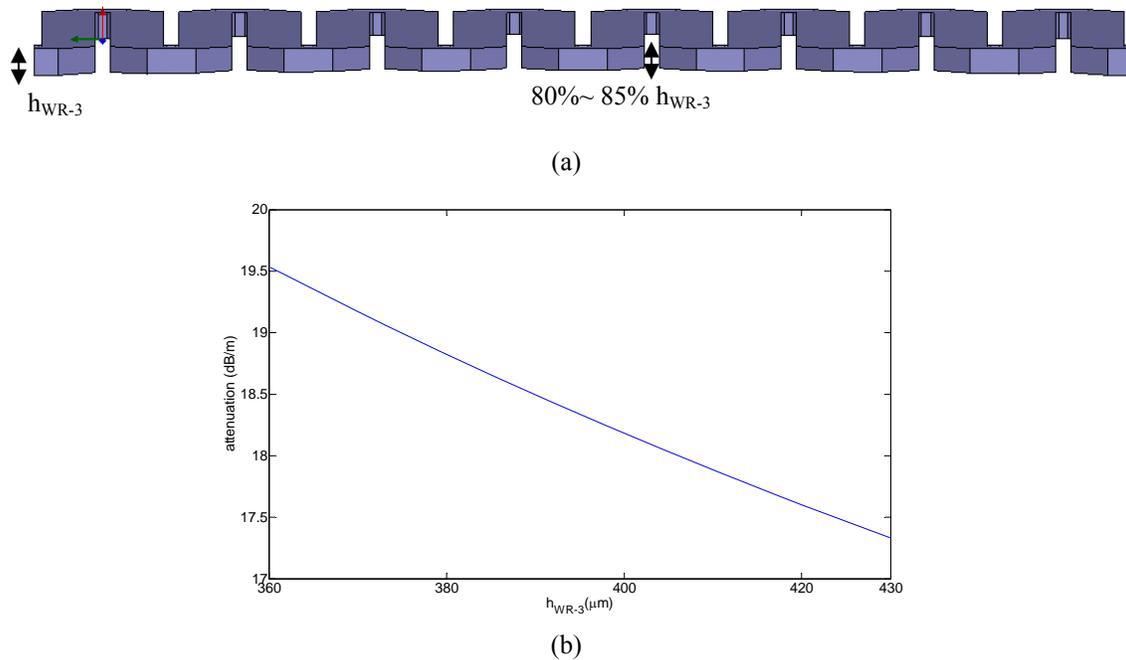
Figure 5.18. (a) Non-uniformity in the etched surfaces caused by DRIE. (b) Waveguide loss versus height. It is shown that by decreasing the height, loss increases.

Figure 5.19. Two cells of the antenna structure are simulated with randomly-distributed defects with 20 µm height and 50 µm × 100 µm area (corresponding to the largest bump experimentally measured)

5.7.   Modified Design for Reduced Loss

As shown in section 5.3, the conductor loss for WR-3 standard waveguide is around 18 dB/m and therefore causes around 7 dB loss in the antenna structure which above 80 % of the power. This fact requires us to design very narrow slots (as narrow as 5 µm) in order to distribute the power evenly among all the elements. This has two drawbacks: first, 80% power loss makes the antenna very inefficient and second, an extremely highly sensitive system is required to measure the radiated power off of the tiny slots.

In general, standard waveguides are designed for 2:1 operation bandwidth and that justifies the 2:1 ratio of the width to the height. The dimensions are determined based on limited dispersion and evanescent-wave coupling of the higher order modes throughout the whole band (which is 220 – 325 GHz for the WR-3 waveguide). However, loss is not necessarily optimized. As we use a very small fraction of the band, the loss of the waveguide can be optimized considering all the above facts and microfabrication limitations.

Figure 5.20 shows the waveguide conductor loss for different widths and heights at the end of the band. As expected, it is observable that loss is decreased as the dimensions are

119

increased. Based on limitations on microfabrication, antenna design and the possibility of the excitation of higher order modes, very wide and deep waveguides cannot be chosen. With some intermediated dimensions such as $a = 1100$ μm and $b = 700$ μm the waveguide loss is reduced to half while many of the other design parameters can be maintained.
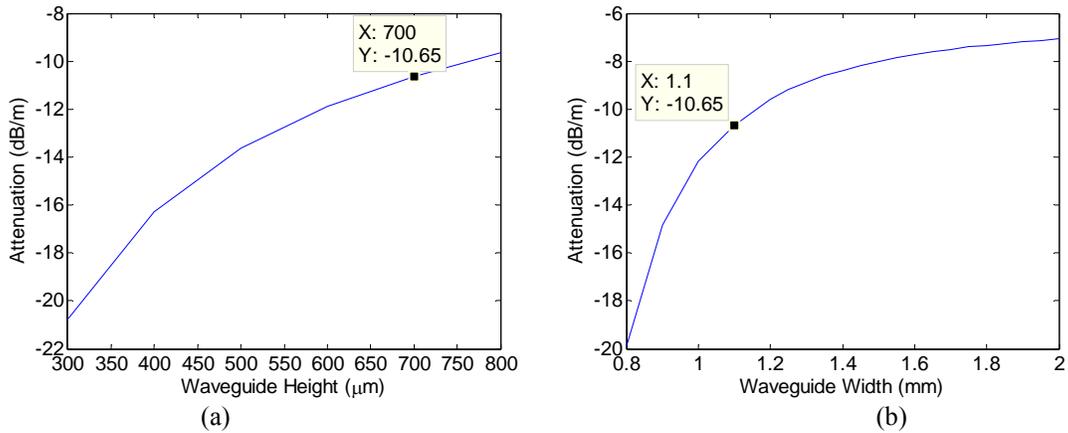
Figure 5.20. Waveguide loss (a) versus waveguide height for width = 1100 μm (b) versus waveguide width for height = 700 μm
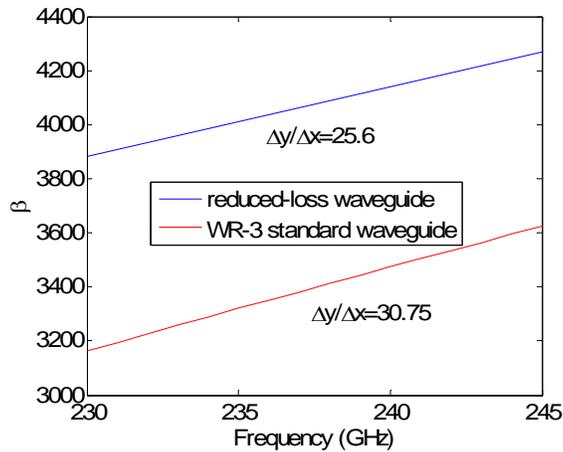
Figure 5.21. The dispersion diagram: propagation constant (β) versus frequency. The slope is decreased for the reduced-loss waveguide

120

However, the dispersion characteristics of such a waveguide are slightly different from the WR-3 standard waveguide. As shown in the dispersion diagram of Figure 5.21, the slope of propagation constant is lower and thus the longer waveguide length are required to provide the desired phase shift. For $\pm 25^0$ scan range, l is chosen to be $8.5 \lambda_{g0} = 1.3$ cm. In order to further reduce the loss, waveguide length is decreased to around 3 cm so that the number of radiating element is decreased and the amount of power assigned to the slots can be increased. It is noticeable that 0.5 cm reduction in waveguide length increased the beamwidth by only 0.5^0 and the design beamwidth is now 2.5^0.

Now that the overall waveguide loss has decreased, more power can be assigned to each slot. As will be shown later, the low input power and dynamic range of the system limit the capability to measure the radiated power off the narrow slots. Therefore, in this design the dimensions of the slots have increased as well as shown in Figure 5.22 . Also, the reflection cancelling slots are eliminated since as the slots are non-resonant, the reflection from each is a very trivial amount. Therefore, most of the power is now assigned to the radiating slots.

60 μm   70 μm   80 μm   100 μm   120   140   160   200   200   200   200
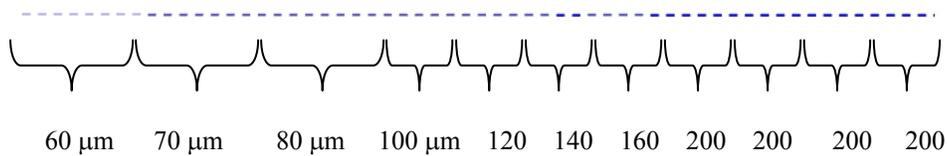
Figure 5.22. The slot width for each four/two turns so that eight different widths are used for the 28 turn waveguide. The length of the slots is 400 μm.

5.8.   Conclusion

In this chapter, the design details of MMW frequency scanning antenna were discussed. The design of meander-line waveguide for minimized reflection, slots dimensions and orientation and hybrid-coupled patch array were studied. The chapter finishes with a modified design with lower overall conductor loss and higher efficiency.

Chapter VI

Radar Integration

In this chapter, major issues regarding the radar integration are addressed. As shown in the radar block diagram (Figure 4.1), the antenna is connected to the output of the power amplifier and the input of the low-noise amplifier in transmit and receive parts. Active components and devices such as amplifiers, mixers, multiplier, etc, are most conveniently fabricated and integrated using MMIC due to the compact geometry and ease of integration of shunt and series elements. Since the antenna structure is based on rectangular waveguides, appropriate transitions from these transmission lines to waveguides are required to connect such devices. In addition, since the active components are originally fabricated on a different substrate, they should be integrated with the antenna substrate. The integration can be resolved by developing an approach to embed the chip inside the substrate connected to a planar transmission line and then transitioning the planar transmission line to the waveguide.

Some other passive devices such as filters have better loss performance when designed based on rectangular waveguides. These bandpass filters can also help eliminate the unwanted signals from the active chips. Taking advantage of waveguide structures to design integrated filters, their fabrication and integration are also investigated.

The required components in the RF front-end are highlighted in the radar block diagram shown in Figure 6.1. Y-band CPW to rectangular waveguide transitions, integration of active chip with such a system, and Y-band rectangular waveguide filters,

all compatible with micromachining methods are studied and novel approaches are proposed and verified.
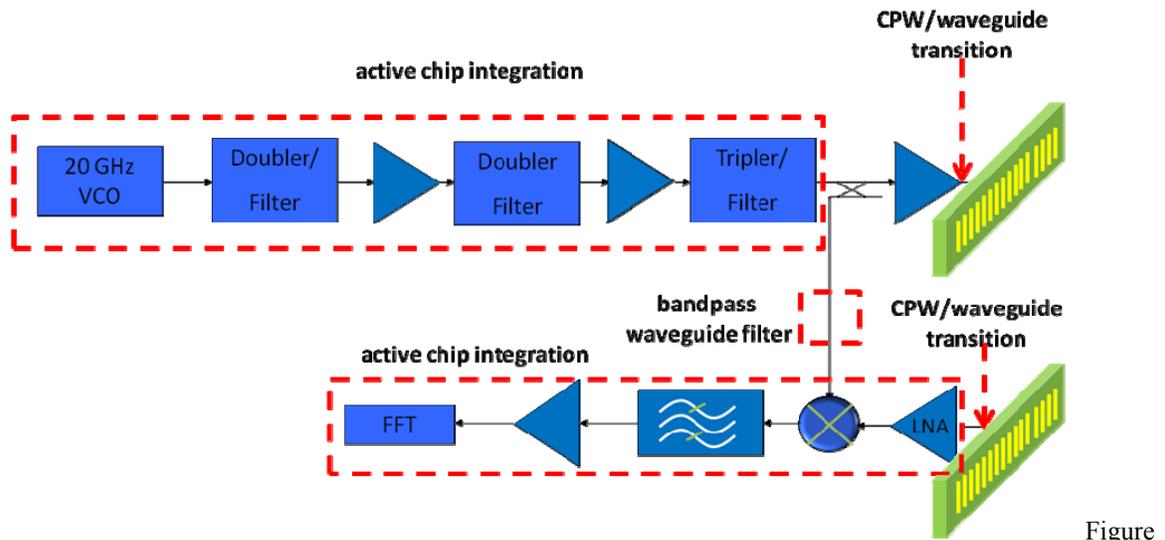
6.1. The passive components for radar integration are highlighted in the radar block diagram. These components include CPW/waveguide transition, bandpass waveguide filters and active chip packaging.

6.1.   CBCPW to Rectangular Waveguide Transition

Traditional CPW to rectangular waveguide transitions based on E-plane probe excitation involve attaching a suspended resonant probe to the center conductor of a CPW lines from broad wall of the waveguide ([76], [77]) as shown in Figure 6.2 (a). This transition covers the waveguide band and is easy to fabricate at microwave and low MMW frequencies using the standard fabrication and assembly methods. At high MMW and SMMW frequencies fabrication of very small suspended probe within a waveguide with micromachining techniques becomes challenging. In [78] - [80], using non-contact lithography, the CPW line is patterned after etching the suspended probe. However, since photoresist cannot be spun uniformly in the presence of the probe and the wafer and the

124

mask cannot be in contact during lithography, the quality of patterning deteriorates. Alternatively, if the CPW is patterned first, the surface cannot be etched to form the probe. Attaching a suspended probe to wafer eventually is not practical, either.

The microfabrication of a transition can be performed conveniently using two stacked wafers, if a short-circuited probe extending the entire height of the waveguide can be used. The waveguide trench and the probe are patterned and etched on one substrate while the CPW line is patterned on another substrate which is bonded to the trench later to form a waveguide as shown in Figure 6.2 (b). Nonetheless, a short-circuited probe acts purely reactive and cannot be matched to the CPW line. To properly excite a waveguide with this probe, a resonant condition must be achieved to eliminate the probe reactance. It is well-known that a pin terminated by the broad wall of a rectangular waveguide acts as an inductive element whose inductance is inversely proportional to its diameter and the waveguide dimensions [81]. The geometry and the equivalent circuit model of a shorting pin are shown in Figure 6.3 (a). For this case the transformer turn ratio can be calculated from [82]

$$n = \sqrt{\frac{2a}{b}\left(\frac{\tan ka}{ka}\right)^2} \tag{40}$$

where, a and b are the width and height of the rectangular waveguide and k is the free space wavenumber. To compensate for the inductance of the shorting pin X_p, a capacitive element is needed. Since a step discontinuity in the E-plane of the waveguide acts as a capacitive element, it can compensate for the inductive behavior of the pin.

125

(a)

(b)
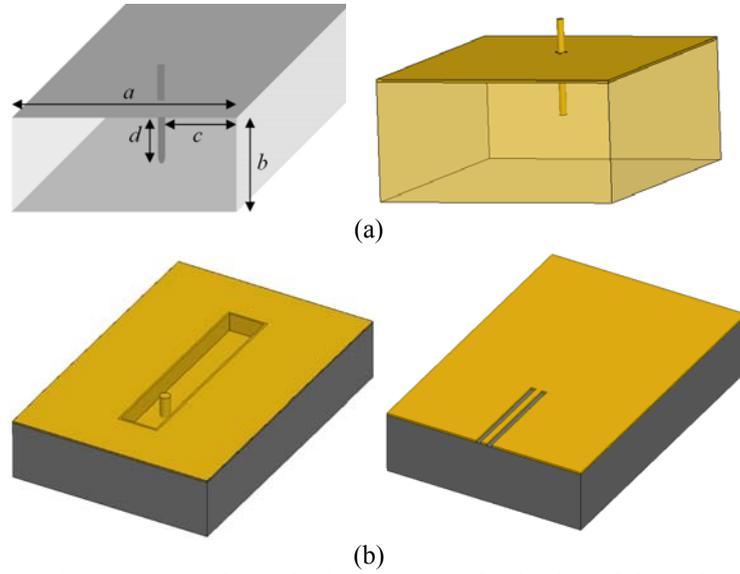
Figure 6.2. (a) Suspended E-plane probe excitation. (b) Microfabrication of short-circuited probe for in-plane CPW is performed on two wafers: one for waveguide trench and the probe, the other for CPW line. The two wafers are bonded to form the transition.

(a)

(b)
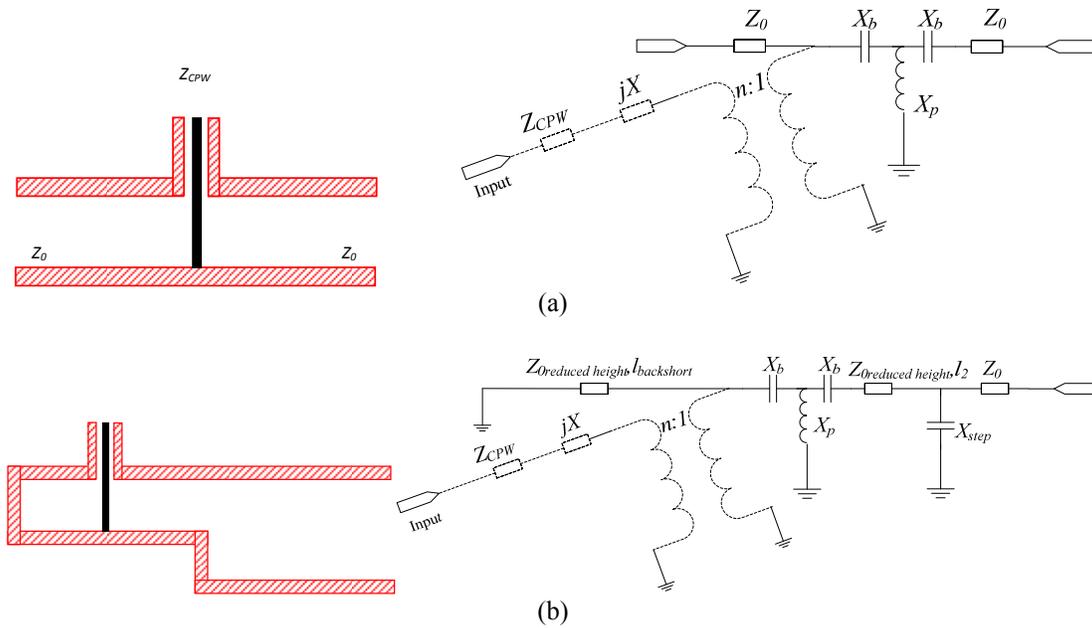
Figure 6.3. (a) A short-circuited pin in a reduced height rectangular waveguide and its equivalent circuit. In the circuit model, L_p is the equivalent inductance and C_b is the series capacitance of the short-circuited probe [80] and Z_0 is the characteristic impedance of the waveguide. (b) E-plane step discontinuity generates a shunt capacitance (X_{step}) required to achieve a resonance needed for the mode conversion and the equivalent circuit model for the proposed transition.

That is, a resonant condition can be realized by terminating a short-circuited pin in a reduced-height waveguide with a step transition from the reduced-height waveguide to

126

the standard-size waveguide as shown in Figure 6.3 (b). The length of the waveguide between the pin and the step transition can be used to control the capacitance seen by the inductance. Also, the waveguide height can be used to control the capacitance at the step transition point. This structure eliminates the use of suspended probe for the transition and is simple to fabricate.

The transition is designed for a CBCPW (Cavity-back CPW) to rectangular waveguide. CBCPW lines are preferred at very high frequencies for mounting active components due to their low-loss characteristics. A novel low-loss membrane supported CBCPW ([83], Figure 2) has been designed for this application in which the dielectric substrate is removed and the line is suspended over a hollow trench in order to eliminate dielectric loss. In addition the conductor loss is decreased (compared to traditional CPW lines) substantially by reducing the current density near the edges and distributing it more uniformly over the metallic strip and the ground around it. For fabrication purposes, a dielectric membrane on top of the line supports the suspended line over the trench. This line can be easily incorporated with hollow rectangular waveguides [83].

The proposed structure is presented in Figure 6.4. Unlike the previously microfabricated transitions, the CBCPW line is positioned in-plane with the waveguide top wall and can be easily fabricated using two stacked silicon wafers. For this transition, three conversion steps are required: from CBCPW to CPW inside the waveguide, CPW to reduced-height waveguide, and reduced-height waveguide to standard waveguide. The CPW line printed over the top waveguide wall is given a different characteristic impedance in order to create a transmission line resonator including the pin. This second resonator that is coupled to the pin and step resonator inside the waveguide provides

127

another impedance match. The center conductor of the CPW line is open-circuited at the location of the pin and the pin is connected to the lower wall of a reduced-height waveguide. On the other side of the pin, the reduced-height waveguide is short-circuited at a distance to appear as another reactance parallel to the pin inductance. The discontinuity from CBCPW line to CPW line inside the waveguide is also modeled by a shunt capacitance. To design the transition, first the dimensions of waveguide and CBCPW line are chosen based on the desired frequency range. The initial values of elements of the circuit model are selected using the analytical formulas and measurement results reported in [81] and [82]. These values along with the length of waveguide and CPW line sections are optimized using transmission line analysis of the circuit model to obtain the resonant behavior. A structure based on these values is designed and then optimized using the full-wave simulator Ansoft HFSS.
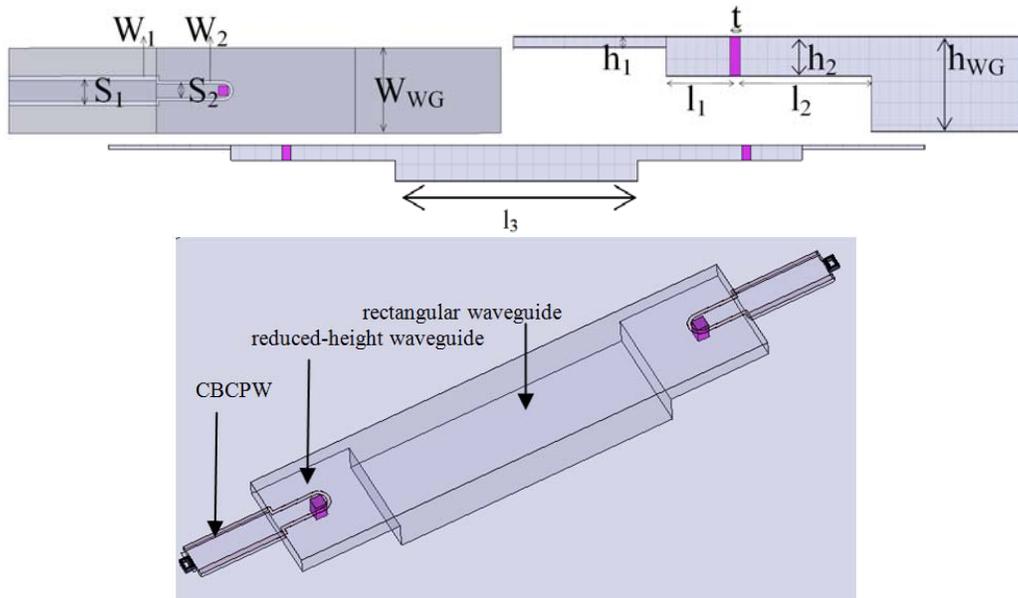
Figure 6.4. CBCPW to rectangular waveguide transition, top view, side view and the perspective of a back-to-back configuration which includes a transition from CBCPW to CPW, CPW to reduced-height waveguide and reduced-height waveguide to the standardWR-3 rectangular waveguide.

128

To verify the performance, two sets of transitions for different frequency ranges were designed and fabricated: one at the lower MMW band (Ka-band) with standard machining techniques and another at our desired frequency band (240 GHz).

6.1.1.   Ka-band Transition

A prototype at Ka-band for WR-28 waveguides was designed and the reflection coefficient of the optimized structure is compared to that of the circuit model for the back-to-back transition in Figure 6.5 to verify the performance of the transition. As shown, a good agreement is obtained while the physical structure provides a better performance than the one predicted by the circuit model. The electric field distribution of the optimized structure is shown in Figure 6.6 (a) and well represents the conversion of the CPW mode to the waveguide mode using the terminated pin. Figure 6.6 (b) shows the reflection and transmission coefficients of this transition. It is observed that a transmission above -1 dB and reflection below -10 dB for more than 9% of the bandwidth can be achieved. An enlarged plot of the transmission coefficient over the passband is also shown in Figure 6.6 (c).

The bandwidth of the transition is sufficient for most application at these very high frequencies. However, in situations where more bandwidth is needed, the number of shorting pins and step discontinuities can be increased accordingly. To add one more resonance, another shorting pin and step discontinuity can be introduced. The geometry of a three-pole structure is shown in Figure 6.7 (a). The simulated transition and reflection coefficients of the structure are presented in Figure 6.7 (b). It is shown that the

additional resonance increases the bandwidth up to about 15%. This can be further increased by adding more resonant elements.

As mentioned before, for fabrication a dielectric membrane is used to support the top suspended thin metal layer of the CBCPW and prevent it from collapsing. The membrane covers the conductor and the structure cannot be fed by probes from the top. The top layer and the membrane are protecting the active components that excite or receive the waveguide signal. In order to test the transition and be able to make contact to the probe, the top layer of the membrane is also patterned with a CPW line and is connected

(a)

(b)
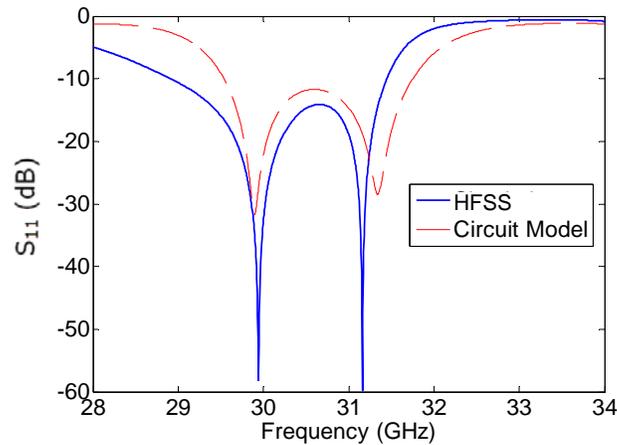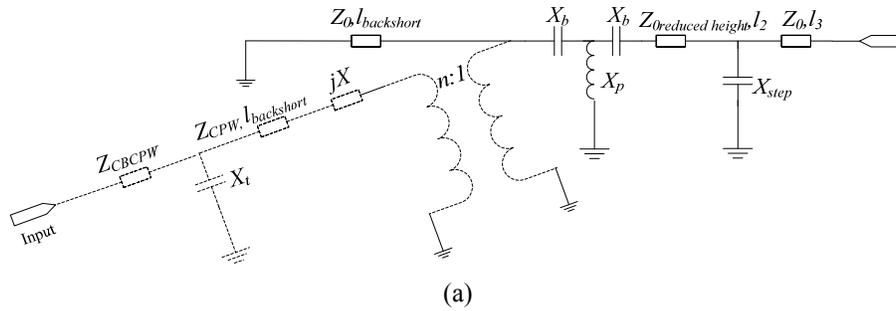
Figure 6.5. (a) Equivalent circuit model for the transition. (b) Reflection coefficient of the circuit model of the back-to-back structure for the initial values of Z_{CBCPW}=50 Ω, Z_{CPW}=85 Ω, $X_t = -j$ 140 Ω, $X = -j$ 110 Ω, $n = 1$, $X_b = -j$ 8 Ω, $X_p = +j$ 58 Ω, $X_{step} = -j$ 1000 Ω, $l_{backshort} = 5$ mm $= \lambda_g/3$, $l_2 = 10$ mm $= 2\lambda_g/3$, $l_3 = 17$ mm compared to the coefficient of the full wave analysis for optimized values of $S_1 = 1.46$ mm, $W_1 = 0.37$ mm, $S_2 = 0.972$ mm, $W_2 = 0.247$ mm, $W_{WG} = 7.112$ mm, $h_{WG} = 3.556$ mm, $h_1 = 0.379$ mm, $h_2 = 1.65$ mm, $t = 0.49$ mm, $l_1 = 5.024$ mm, $l_2 = 9.97$ mm, and $l_3 = 16.8$ mm . The waveguide dimensions are set as the standard dimensions of WR-28 Ka-band waveguides.

130
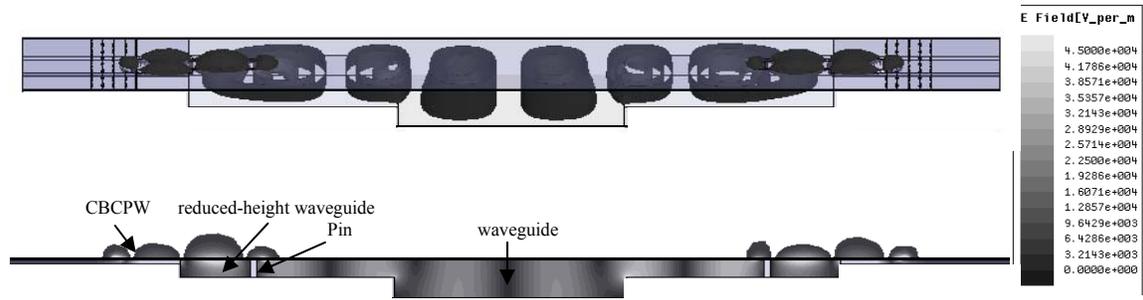
(a)
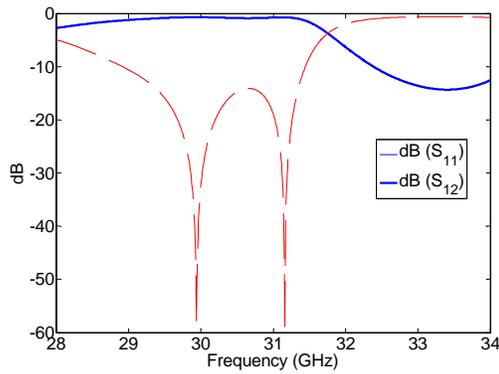
(b)
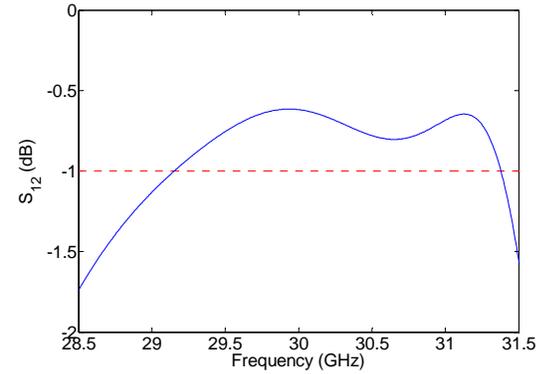
(c)

Figure 6.6. (a) Electric field distribution at 30GHz for a back-to-back transition with the optimized values (b) Reflection and transmission coefficients for the back-to-back transition at Ka-band. (c) transmission coefficient at the passband.
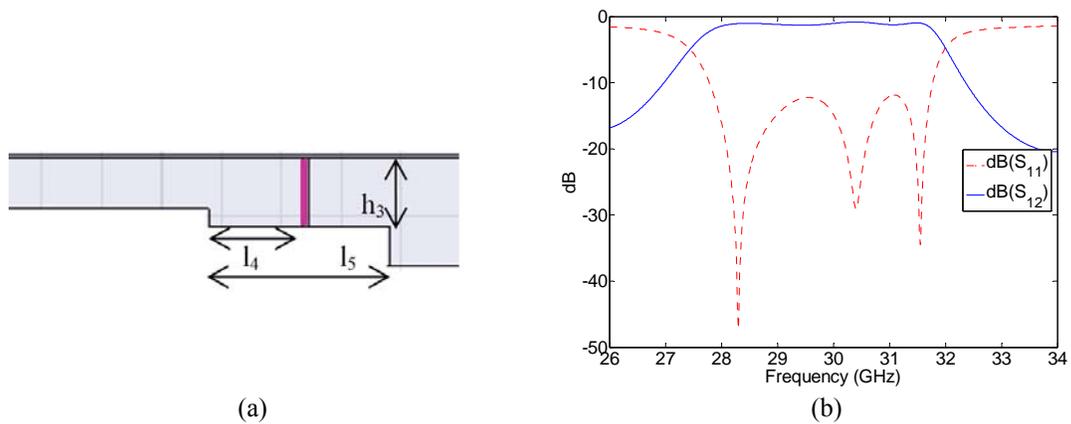
(a)

(b)

Figure 6.7. The bandwidth of the transition is increased to about 15% as a result of having a three-pole structure by adding one resonance, a shorting pin and a step discontinuity with $h_3 = 2.26$ mm, $l_1 = 5$ mm, $l_2 = 10$ mm, $l_4 = 3.3$ mm, $l_5 = 6$ mm,. Additional resonances can be introduced for further enhancement.

(a)   (b)
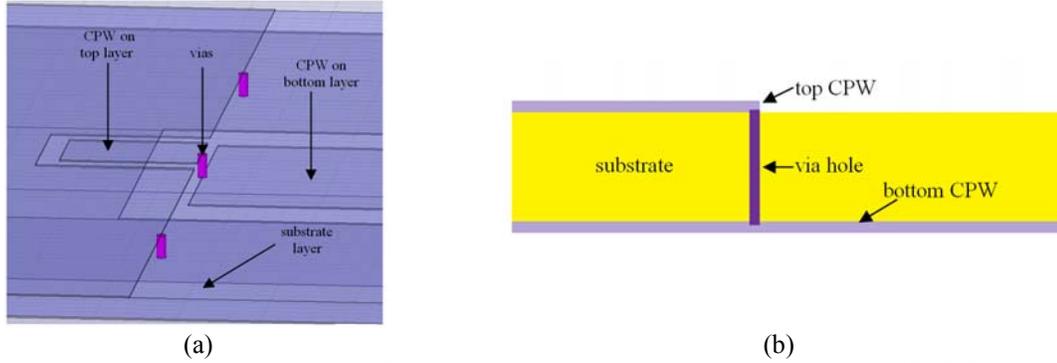
Figure 6.8. A transition from a 50 ohm CPW line patterned on top of the substrate to the CBCPW line patterned on the bottom layer. The lines are connected through electroplated via holes. (b) side view.

(a)   (b)
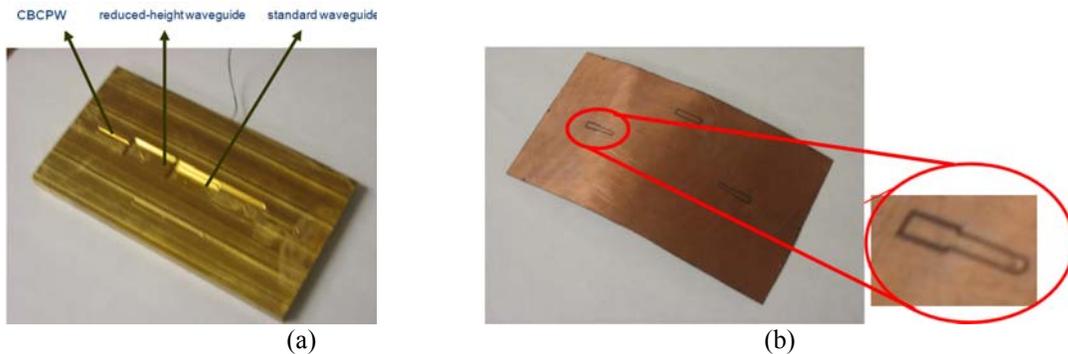
Figure 6.9. (a) The CBCPW trench, reduced-height waveguide and the standard waveguide are machined on a brass plate. (b) the top cover includes the lines is a substrate whose both sides are etched with CPW patterns.

to the bottom layer through via holes as shown in Figure 6.8. With this transition, the structure can be fed from the top by 50 ohm GSG probes. To fabricate this structure, the lower parts including the CBCPW, reduced-height waveguide and standard-height waveguide are machined on an ultra-machinable Alloy 360 brass plate and gold-plated to prevent oxidation. Rogers Duroid 5880 with ¼ oz. (8 μm) electrodeposited copper foil is used as the top cover of the waveguide as well as the membrane for CBCPW. The thickness of the substrate is chosen to be 0.127 mm (5 mil), thin enough to serve as a membrane. Both sides of the substrate are patterned and connected by metalized via holes as shown in Figure 6.8. Additional vias are drilled in the substrate in order to suppress the substrate mode. The fabricated parts are shown in Figure 6.9.

132

Different techniques were tested to bond the substrate to the brass unit. Initially solder paste and silver epoxy were used. However, since a high temperature is needed for pastes and epoxies, the substrate was warped and damaged, and the brass unit oxidized. Also, the results were not satisfactory due to misalignments and air gaps around the edges. In addition, the solder reflow caused short circuits in the substrate during the bonding process. Moreover, many times the thin pins were bent and easily broke during bonding at high temperatures. The best results were obtained by screwing the two units together. Since the substrate is very thin, a thick metal plate is used on top of it to ensure sufficient pressure is applied to the substrate and brass unit to prevent possible air gaps. The silver-plated long rigid steel wires are snapped into holes drilled on the bottom of the reduced-height waveguide and soldered. The pins pass through holes cut on the substrate to facilitate alignment of the substrate and the unit. After bonding, the structure is fed by GSG probes connected to the network analyzer using Ka-band flexible cables. Prior to measurement it is essential that the probes and cables be calibrated. For this purpose, on-substrate TRL calibration lines were simulated and designed. For TRL calibration, three calibration standards were fabricated on the same substrate. These include two line segments with known phase shifts for thru measurements and an open-ended line with a known electrical length for a reflection measurement. After calibration, S-parameters of the transition are measured and presented in Figure 6.10. The measurement results show a good agreement with the simulation, around 9% bandwidth with below -10 dB return loss and over -1 dB for insertion loss. The observed deviations from the simulation are attributed to misalignment, especially near the pin positions and possible air gaps between the substrate and the brass unit. The air gap should be of lesser concern since

screws connecting the substrate to the brass unit should apply enough pressure to make good metal-to-metal contact. Since alignment is done by hand, a small misalignment can lead to small deviations from the ideal response. To examine this hypothesis, a simulation was carried out where the top substrate was shifted to one side by a very small amount to produce about 300μm translational displacement at the pin position. This is a typical length that might be misaligned by manually aligning. Figure 6.11 shows the simulation results for the misaligned structure where it is shown that the transmission has decreased specifically for frequencies lower than 29 GHz. Also, the impedance match near 31 GHz is not as good as what the structure is capable of producing. This is very similar to the measured results indicating that even careful hand alignment is not good enough to achieve the best performance this transition can produce at Ka-band. To achieve better results a better alignment approach will be needed. For the ultimate application of this transition at Y-band wafer alignment approaches with micromachining are available for achieving alignment accuracy of around 1μm.

(a)   (b)
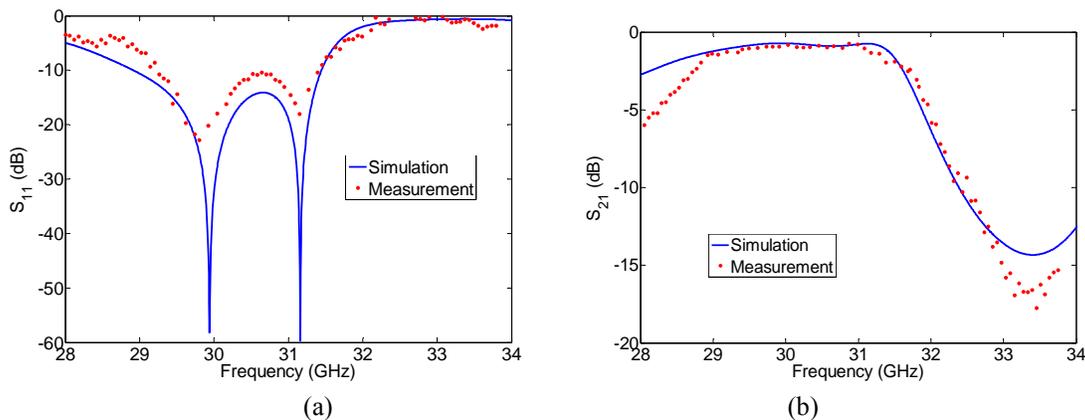
Figure 6.10. Simulation compared to measurement results for reflection and transmission coefficients which show a good agreement with the simulation. The observed deviations from the simulation are attributed to misalignment, especially near the pin positions and possible air gaps between the substrate and the brass unit

134
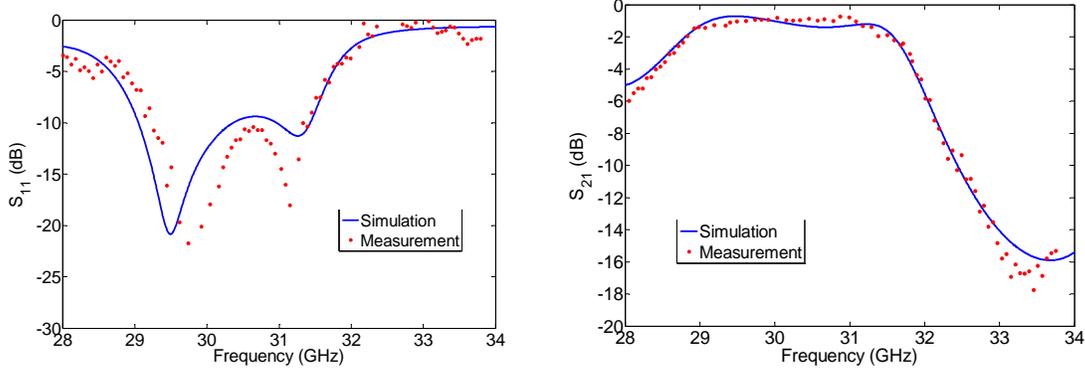
Figure 6.11. Simulation results of a structure with misalignments (300 μm translational displacement) between the top substrate and the brass unit compared to the measured results. The transmission is decreased for frequencies lower than 29 GHz and the impedance match near 31 GHz is not as good as that of the optimized

| (a) | (b) |
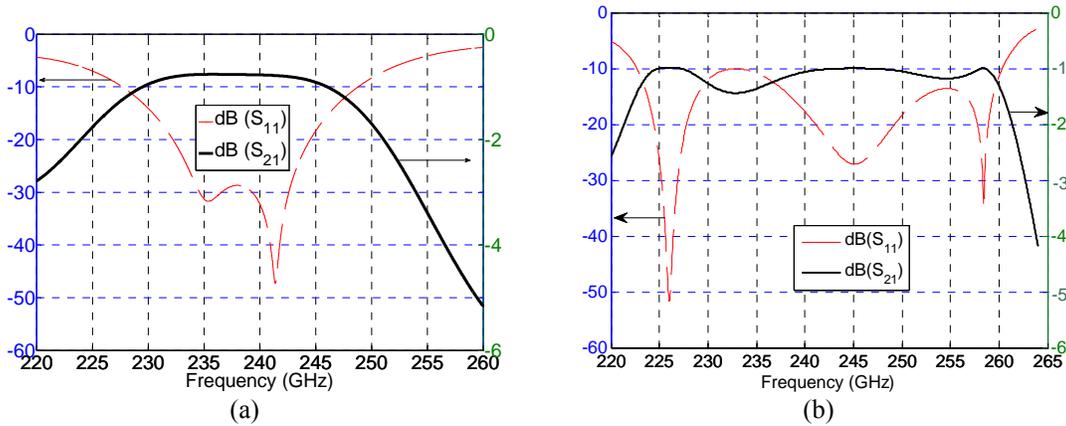
Figure 6.12. Transmission and reflection coefficient of the back-to-back structure (a) S_1 = 210 μm, g_1 = 45 μm, S_2 = 140 μm, g_2 = 30 μm, h_1 = 46 μm, l_1=330μm, l_2=450μm, t =100μm, h_2=159 μm, W_{WG}=864 μm, h_{WG}=432 μm l_3 = 2.44 μm, showing insertion loss less than 1 dB. (b) same values except for h_2=143 μm, l_3 = 5.24 μm, showing higher bandwidth and insertion loss of lower than 1.5 dB for the back-to-back structure.

6.1.2.   Y-band Transition

After verifying the performance of the transition at Ka-band, a Y-band transition version was designed for the radar. The reflection coefficient of the optimized structure is shown in Figure 6.12 for the back-to-back transition. Figure 6.12 (a) shows a transition with transmission above -1 dB and reflection below -10 dB for more than 9% of the

bandwidth around 238 GHz. Figure 6.12 (b) shows another transition with transmission above -1.5 dB while the bandwidth is enhanced to 17% by only changing the height of the step discontinuity and the length of the waveguide by which we can take advantage of a third resonance. By changing these parameters, transmission at the desired bandwidth can be achieved.

6.1.2.a. Sensitivity Analysis

Since the DRIE etch rate might vary depending on the parameters mentioned before, it is most likely that the required etch depth values are not very precise. Hence it is essential to examine the sensitivity of the structure to the fabrication tolerances. For the nominal values of the WR-3 and reduced height waveguide depths (h_{WG} = 432 μm and h_2 =159 μm as shown in Figure 6.4), a maximum error of about around ± 20 μm might be expected for different DRIE runs for depths larger than 400 μm. Figure 6.13 (a) and (b) shows the simulated S-parameters for different values of h_{WG} and h_2. The simulation results show that errors as high as 20μm (5 %) in h_{WG} do not perturb the bandwidth and insertion loss of the transition from it nominal values considerably. For h_2 however, we need to maintain the error within ± 5 μm which is quite achievable. Experimental results on over 10 wafers etched with this method show that the error always remained less than 5 μm.

One other critical issue is the quality of top to bottom wafer bonding. One of these critical areas is the point where the shorting pin on the bottom wafer is connected to the center conductor of the CPW line on the top wafer. Fortunately a relatively good electric

contact can be established between the pin and the CPW center conductors. This is verified by measuring the ohmic resistance between signal and ground. To investigate performance degradation in case of weak gold bonding over the pin, simulations are carried out allowing a small gap between the pin and the center conductor. Figure 6.13 (c) and (d) represents how much the transmission and reflection coefficients are affected in case the pin is not electrically connected to the top wafer. The results show that a gap size values below 3 μm, does not affect the S-parameters significantly. For the actual structure, since the membrane does not have a large stress and does not buckle, a gap larger than a micron is not expected.
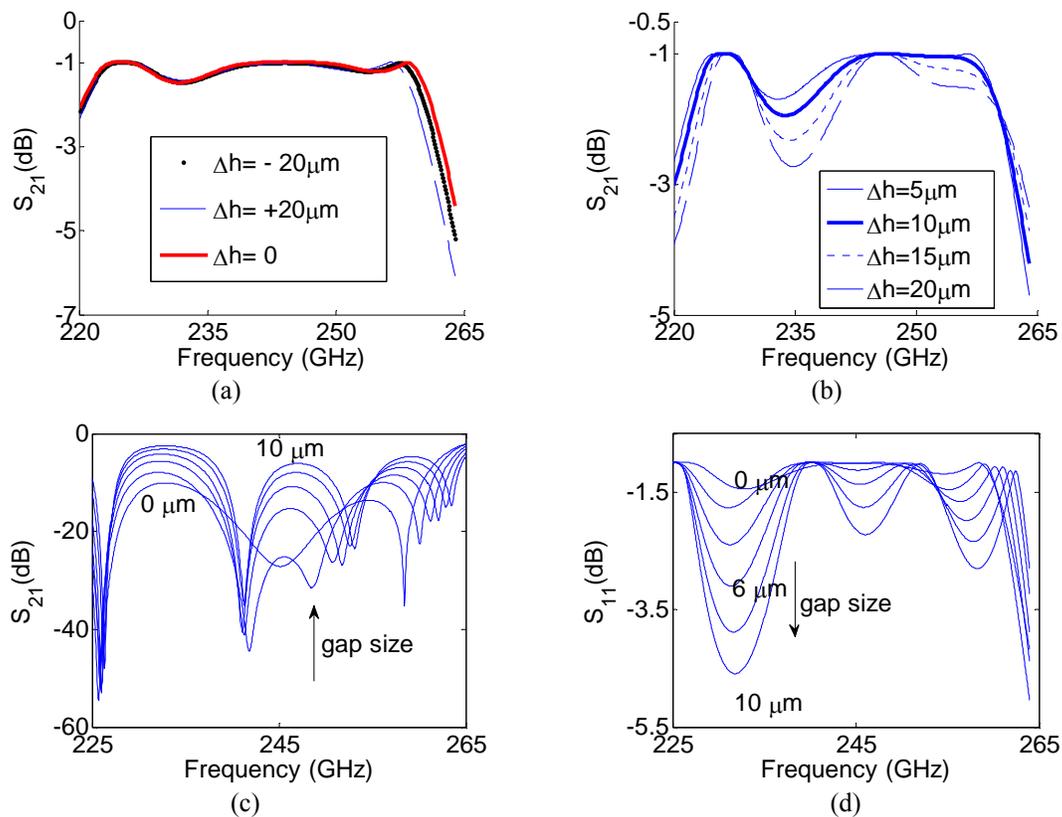
Figure 6.13. Transmission coefficient of the transition when (a) h_{WG} is varied ± 20 μm (~5%) showing the response of the transition is insensitive to variations in waveguide height, b) the response is shown to be more sensitive to the reduced waveguide height h_2 for $\Delta h > 5$ μm . (c) The transmission and (d) the reflection coefficients when a gap is assigned between the top of the pin on the bottom wafer and the top wafer. The response degrades for gaps above 3 μm.

137

6.2. Integration of the External Active Chips

The active components such as the VCO, frequency multipliers and amplifiers are being fabricated on separate chips. However, since the RF front-end of the antenna is designed and fabricated using silicon micromachining, integration of the chips in the silicon substrate must be investigated. Two types of chips for the multiplier chain and VCO were considered and fabricated. As shown in Figure 6.14, they have to be integrated in the silicon substrate of meander-line waveguide. The integration of VCO may be simpler due to lower frequency of operation and can be done with wirebonding. Our focus here is on high frequency integration of external chips.
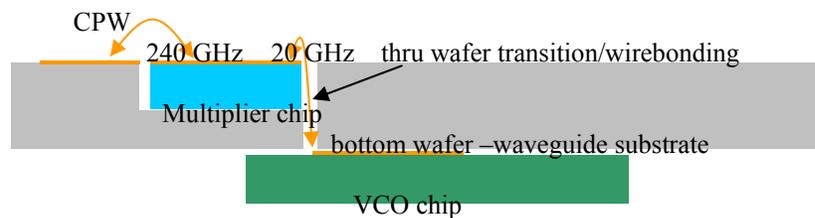
Figure 6.14. The proposed configuration for integration of the multiplier and VCO

A number of methods have been considered to integrate the multiplier chain chips in the radar structure. Most methods are based on integrating from the top side, i.e. etching an area with the same dimensions of the chip on the top side of the wafer and then dropping the chip. However, connecting the center conductors and grounds of the CPW lines is a challenging process. Among the well-known integration methods, wirebonding and flip-chip have been initially investigated. Wirebonding fails due to the long length of the wire which is compared to the wavelength at 240 GHz. It generates an inductance which cannot be easily compensated. Flip-chip adds to the fabrication complexity and puts the transmission lines on the opposite side of the wafer and out of access; therefore

direct DC connection for bias with wireboding is not possible. In addition, in both methods the high temperature and pressure of bonding will damage the electronic components.

A method based on capacitive coupling that provides access to the DC lines and requires the external chip to be embedded after the bonding, was developed and is shown in Figure 6.15. In this design, the area required for the chip is etched all the way through the substrate to make a hole. This allows the chip to be inserted from the backside of the substrate in the final stage of the fabrication. Figure 6.16 shows the structure of the thru-wafer transition for packaging. The chip has to be connected to the CBCPW line on the wafer (which is connected to the rectangular waveguide using the aforementioned transition). Since the width of the CBCPW is quite different from those of grounded CPW on the chip, the CPCPW is connected to a $\lambda/2$ line with a narrower center conductor with similar dimensions of the chip center conductor and gap to smoothen the transition. The characteristic impedance of this line is not 50 ohm, but it is not critical since the length is $\lambda/2$. The line is extended on top of the chip to cover the CPW part and if the chip is well-inserted, creates a connection between the line and the chip. However, the chip might have gaps from the sides and the top in case the pressure is not enough or the surfaces are not uniform and flat. The transition is optimized for practical sizes of gaps. The insertion and return loss of such a transition (back-to-back) is shown in Figure 6.17 for different values of gaps between the chip and the wafer. The length of the $\lambda/2$ line was optimized to get the minimum insertion loss for cases when we have gaps of 5 μm to 10 μm between the chip and the transmission line on the top wafer. These cases are more realistic as we cannot guarantee the connection under any pressure.

139

(a)

(b)

(c)
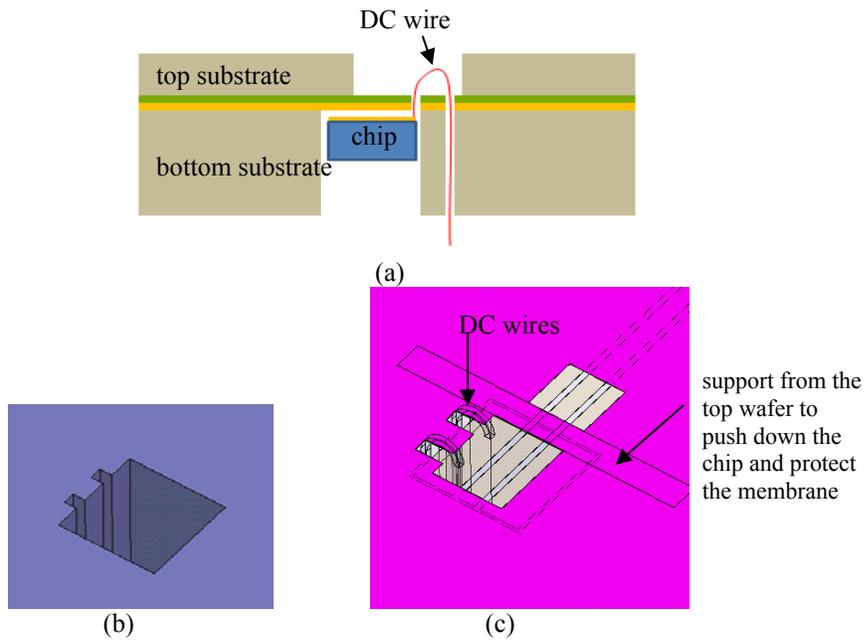
Figure 6.15. (a) Schematic of the thru-wafer transition for chip packaging. (b) a hole is etched on the bottom wafer for the chip and for the DC line transfer. (b) The structure of the packaging after bonding and embedding the external chip.

top view

side view
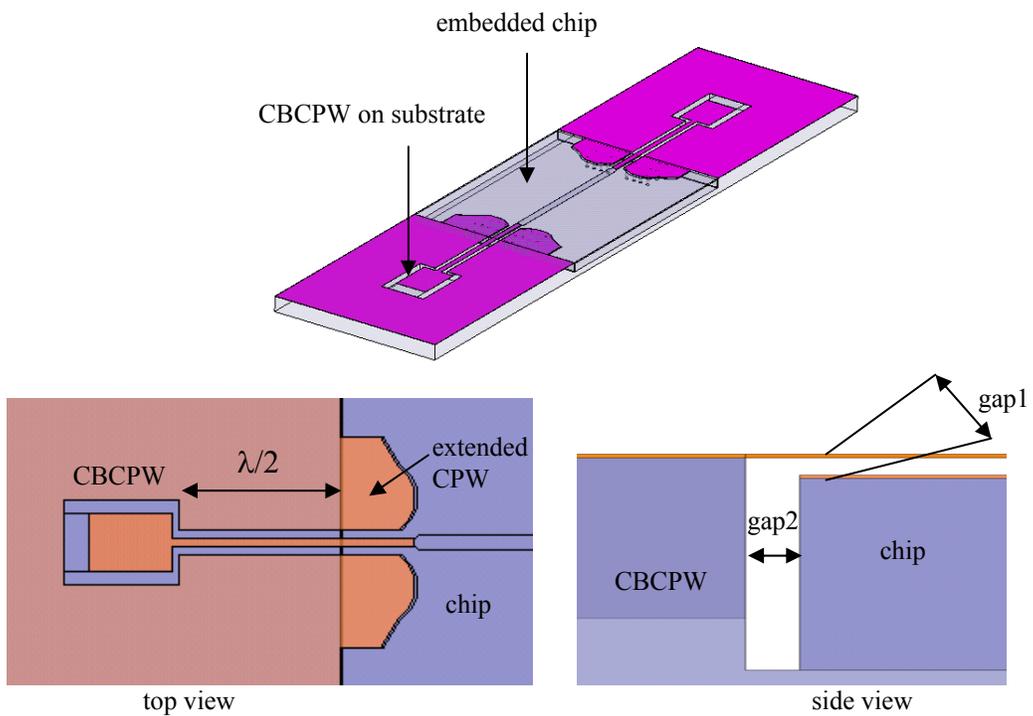
Figure 6.16. The transition between the chip and CBCPW. It includes an intermediate step of narrow transmission line with $\lambda/2$ length

The simulation results show that the loss of a back-to-back transition is below -1 dB in general and around -0.5 dB if the gap is not greater than 5 µm. It should be noted that the actual chip is 240 GHz in one side and 20 GHz on the other side which is connected to the VCO. Therefore, this transition is only required on one end and the transmission loss is below -0.5 dB in general and around -0.25 if the gap is not greater than 5 µm. It should be noted that the test chip for this design is a simple microstrip line with grounded CPW input and output shown in Figure 6.18 (a). The microstrip-CPW transition is optimized to get the maximum insertion for the line.
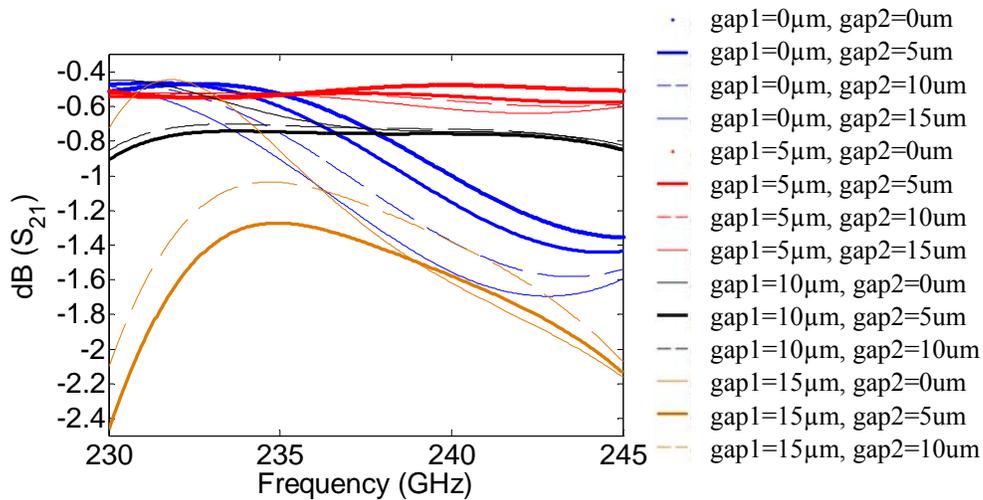
Figure 6.17. The transmission coefficient of the back-to-back transition in Figure 5 (a) for different gap values.
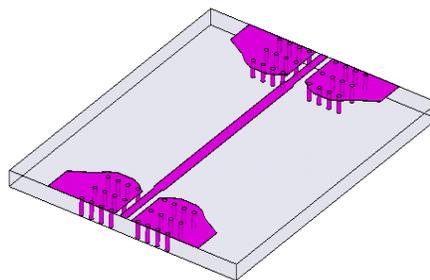
Figure 6.18. The transmission line chip designed to test the packaging.

6.3.   E-plane Rectangular Waveguide Filter

Waveguide filters, like ordinary filters are designed using reactive elements. These reactive components are usually realized by inserting discontinuities or obstacles such as rods or diaphragms along the length of the host waveguide. At microwave and low MMW frequencies, these filters are fabricated by cutting slits in the cross-section of the waveguide, inserting the element inside and finally soldering the edges. The structure of the E-plane rod filter is very much compatible with silicon micromachining. In this structure, the required susceptance for filter is obtained by metal rods in the E-plane which extend all the way across the cross section of the waveguide, separated by the lengths of the waveguide as the impedance transformers as shown in Figure 6.19 (a). Depending on the number of poles, it consists of a number of rods serving as inductances separated by lengths of the waveguide. This structure is simpler than iris, since the inserts are rod shape and do not deform along the cross-section of waveguide. Therefore, they can be easily fabricated using single-step etching of silicon. The standard WR-3 waveguide along with rods with h = 432 μm and cross-sections larger than 50 μm × 50 μm – to provide mechanical rigidity - were used to design filters with various passbands. This filter can be modeled by an equivalent circuit model shown Figure 6.19 (b). It is well-known that a rod terminated by the broad wall of a rectangular waveguide acts as an inductive element whose inductance is inversely proportional to its cross-section size and the waveguide dimensions. By changing the dimensions of the cross-sections of the rods the desired inductance values can be designed. The spacing between the rods is an impedance transformer whose length is a quarter of a guiding wavelength of the fundamental TE_{10} mode of the waveguide. Figure 6.20 (a) shows the response of the full-

wave analysis of a two-pole filter (with three rods) shown in Figure 6.19 (a) compared to the response of the circuit model. It is designed to have the passband between 230~245 GHz and the nulls around 235 and 240 GHz. In this structure, the length of the impedance transformer is considered (2+1/4) λ in order to limit the bandwidth to 230~245 GHz. For wider band applications, the length could be decreased to (1+1/4) λ or λ /4 as shown in Figure 6.20 (b).
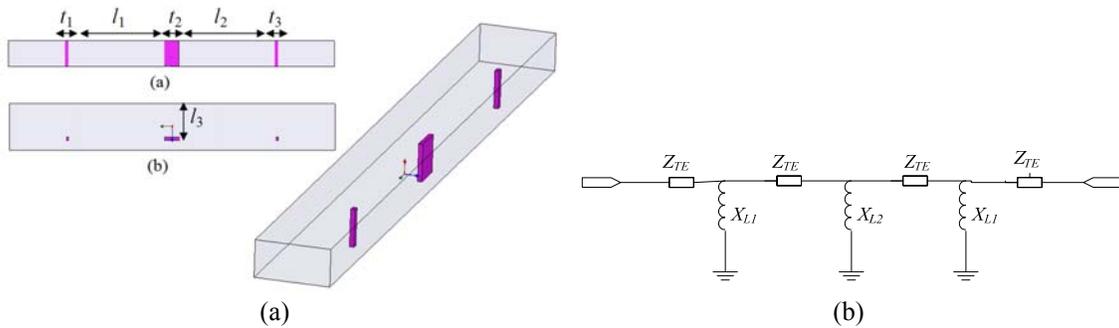
Figure 6.19. (a) The structure of E-plane two-pole filter. (b) The equivalent circuit model.
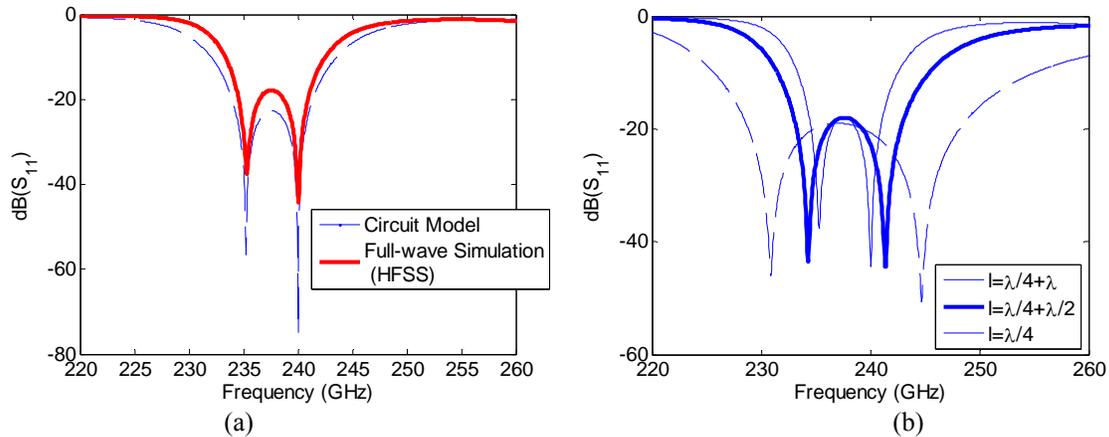
Figure 6.20. (a) The reflection coefficient of the filter presented in Figure 1 with t_1=75 μm, l_1=2.344 mm, t_2=365 μm, l_2= l_1, t_3= t_1, l_3= 638.6 μm. (b) The response of the same filter with various values for l= l_2= l_1 maintaining λ /4 difference.

(a)   (b)
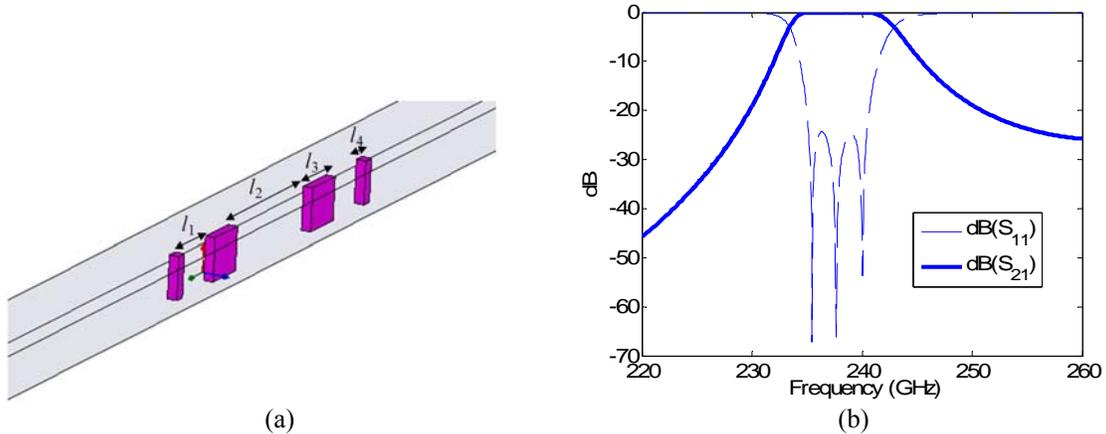
Figure 6.21. (a) The structure of the three-pole filter. (b) The response of the filter for with t_1=117 μm, l_1= 636 μm, t_2=466 μm, l_2=1.562 mm, t_3= t_1, t_4= t_2, l_3= l_1, l_4= l_2

Another filter with three-pole (four rods and three connecting lines) was also designed for the same frequency band. The total length of this filter is shorter since the spacing is kept at λ /4 and the roll-off is higher since one more pole is added. The response of the filter is shown in Figure 6.21. Higher order filters can also be realized with this method depending on the application.

6.4.   Conclusion

In this chapter, components and techniques required for radar integration were presented and discussed. These include a transition from CPW to rectangular waveguide, a transition for embedding external chips and waveguide filters. The components are designed compatible with micromachining techniques using novel approaches developed for antenna fabrication.

144

Chapter VII

Microfabrication Processes

In this chapter, microfabrication processes for the radar antenna and other components are presented. As discussed in chapter 4.3, silicon DRIE is a viable approach for fabrication of high-performance micromachined waveguide structures. In [84] and [85], both diamond and rectangular waveguide were fabricated by bonding two halves of the waveguide. A high-precision silicon micromachined waveguide transition with a capability to integrate filters has been proposed in [86] and shows wideband characteristics at the same frequency range. However, for higher frequency applications, these structures show a high degree of fabrication complexity due to error in alignment, air gaps between conductive parts, poor metal contact, inaccuracy in patterning because of non-contact lithography, complex assemblies of various parts, and high number of steps needed for construction which cannot be easily adopted for microfabrication. Therefore, a novel micromachining process was developed to fabricate the radar structure.

The proposed structures include the WR-3 waveguide trench and a top cover for lines and slots for the waveguide slot array antenna and for non-radiating components such as waveguide transitions and filters. For the final antenna, the patch array which is suspended on a membrane on top of the waveguide configuration adds one more step to the fabrication. Therefore, the complete structure is fabricated in three parts as shown in Figure 7.1; the meander-line waveguide is etched on a wafer, the slots are etched on

another wafer and bonded to the first wafer, and finally the patch arrays are patterned on a third wafer and then bonded to the structure.
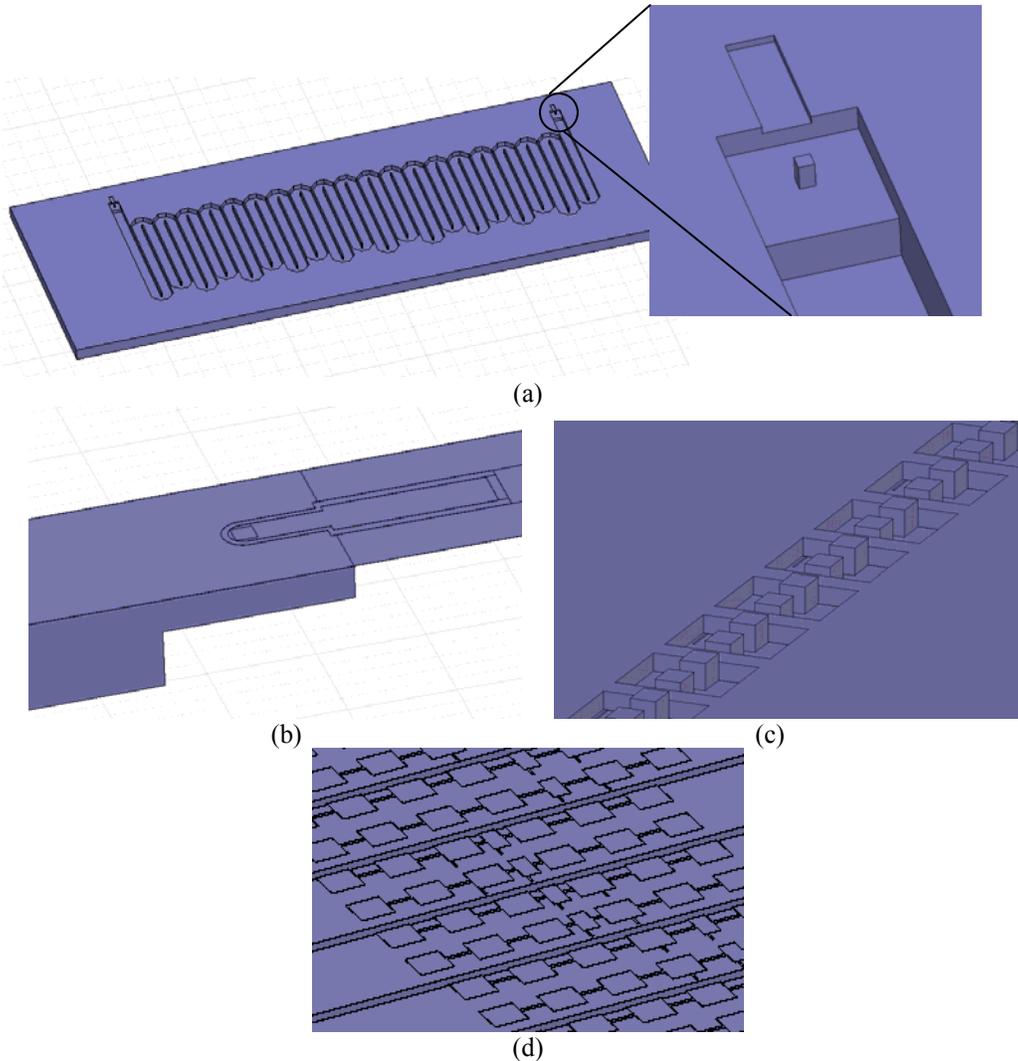
Figure 7.1. The radar structure fabrication steps. (a) First wafer includes waveguide trench and multi-step structure of the waveguide transition (b) Second wafer includes slots and CPW line patterns with the patch substrate on the other side (c) Third wafer includes the patch arrays. The wafers are connected using wafer bonding processes.

7.1.   First Wafer - Meander-line Structure

To fabricate the waveguide structure trench, the silicon wafer is patterned and then etched using DRIE. This method is a highly anisotropic etch process used to create deep,

steep-sided holes and trenches in wafers, with aspect ratios of 20:1 or more. The Bosch DRIE process contains successive cycles of passivation and etching with the flow of SF_6 and C_4F_8 gases.
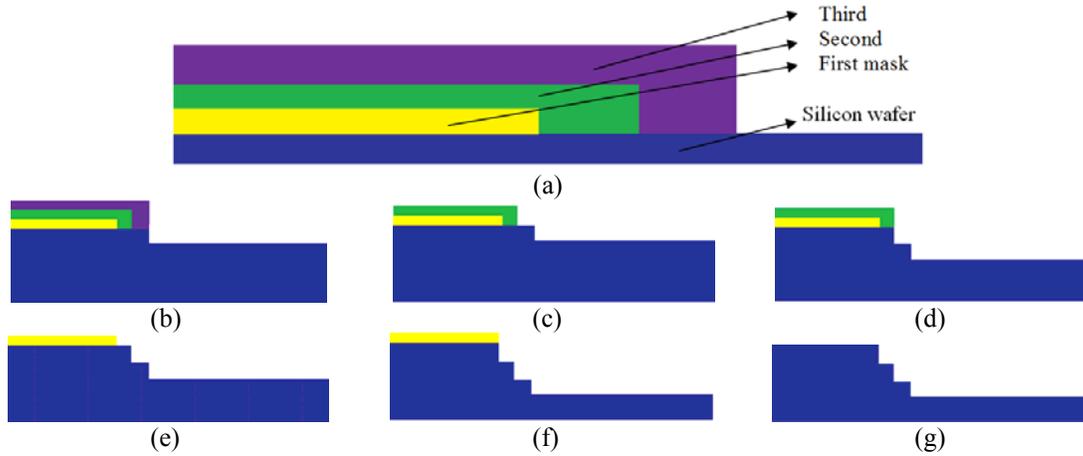
Figure 7.2. Multi-step etching process for the First wafer. (a) Three different mask layers are deposited and patterned. (b) The wafer is etched with the last mask layer down to the desired thickness. (c) The mask layer is removed. (d) The wafer is etched with the next mask layer. (e) The mask layer is removed. (f) The wafer is etched with the final mask layer. (g) The mask layer is removed. The process can be carried on for more number of steps as long as the appropriate mask layer is chosen.

To create a multi-step structure required for waveguide transitions on a silicon wafer, the wafer is patterned successively with different mask materials. It is etched with the last mask to the desired depth. Then the mask is removed and etching is continued with the next mask to the desired depth for the next step. This process can be carried on to achieve different steps of different depth within the silicon wafer. The fabrication process is illustrated in Figure 7.2. By carefully managing etching time and thickness of the mask layers, a consistent process can be achieved. This method can be extended for other materials and more layers as well as wet etching processes.

After the wafer is etched, a layer of silicon dioxide is deposited as a diffusion barrier before metalizing the surface with gold. This layer is needed for next step of wafer-to-

wafer gold bonding to stop diffusion of silicon through the gold layer at high temperature and pressure and to prevent eutectic bonding. Since our last mask layer is silicon oxide, we keep it to be used as the diffusion barrier to simplify the process and to avoid adding one more step. For gold deposition, a sputtering tool with sidewall coverage capability is used which guarantees coverage of around 50% of the value on the exposed surfaces. In order to deposit gold, it is necessary to deposit an adhesion layer first. Experiments showed that a chrome layer alone does not prevent silicon diffusion through gold at high temperature and pressure. Either titanium or a combination of chrome and titanium with thicknesses of 300 ~ 500 A^o provides a superior diffusion barrier layer between gold and silicon. The minimum gold thickness of 1.2 μm is needed in order to ensure at least 0.5 μm of gold is deposited on the sidewalls.

7.1.1. Requirements for Measurement

7.1.1.a. CPW to CBCPW Transition

The designed low-loss CBCPW line is suspended on a membrane and hence, measurement probes cannot be placed on it since even a small amount of pressure applied by the probes might break the membrane. On the other hand, conventional CPW has substrate and is stiff enough for the probe pressure. Therefore, it is more convenient to have conventional CPW for measurement purposes so a transition from a conventional CPW to CBCPW is required to characterize the performance of the transition as shown in Figure 7.3 (a). For the ease of fabrication and lower loss, a grooved CPW is designed. The substrate is made of silicon and loss tangent is calculated based on the resistivity of

the silicon wafer. It should be noted that the response of the CPW to CBCPW transition is eventually de-embedded from the final measured results.

There is a difficulty in the fabrication of the grooved CPW and the CBCPW on the same wafer. The lower wafer on which the cavity of CBCPW and the grooved CPW are to be fabricated must be metalized, however, the grooves and the backwall of the CPW cannot be metalized or the CPW will be short-circuited shown in Figure 7.3 (b). In order to protect these areas from gold deposition, patterning was found to be practically impossible as was initially envisioned. Spinning photoresist evenly for patterning is not possible over the grooves. To overcome this problem, we develop a technique based on the limitation of gold deposition in high aspect ratio features. We have experimentally shown that when the width of a trench is less than 5 μm and the aspect ratio is higher than 10, gold is not deposited on the bottom and lower portion of the side walls of the trench. Figure 7.3 (c) shows the desired short segment of grooved CPW, which is fabricated with the so called "shadow walls" as shown in Figure 7.3 (d). In this structure the thin protecting walls shadow gold deposition because of the high aspect ratio of the channels. After gold deposition, since the bottom the sides of the shadow walls are not covered with gold, they can be removed using isotropic silicon etchants like xenon difluoride (XeF_2) or sulfur hexafluoride (SF_6). The etch time depends on the gap width between the walls and is longer for thinner and deeper gaps as it is hard for the gas to penetrate inside these areas. However, in order to reduce damage to other areas, the wafer is exposed to the etchant over a relatively short period of time to make the walls frail. Ultrasonic vibration is then used to remove the fragile walls completely. Figure 7.4 (a) and (b) show the structure before and after etching the shadow walls. The walls are completely

149

removed after 5 min of exposure to XeF_2 and 2 minutes of ultrasonic vibration. Figure 7.4 (c) shows a SEM image of the end wall of the grooved CPW (tilted 20^0 for a better view of the backwall) which verifies that the shadow walls prevented gold deposition over the vertical walls of the middle silicon block.
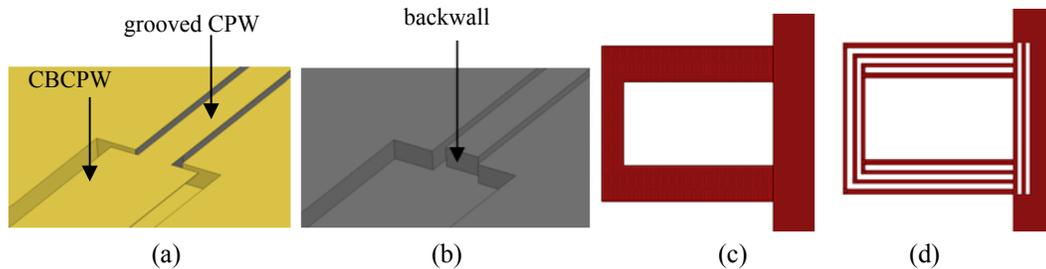
Figure 7.3. (a) The schematic of the transition from grooved CPW to the CBCPW (b) Bottom substrate with top layer removed. The backwall shown in (b) should not be covered with gold (c) Top view of very short section of grooved CPW (d) the proposed structure for fabrication to avoid gold deposition on the sidewalls.
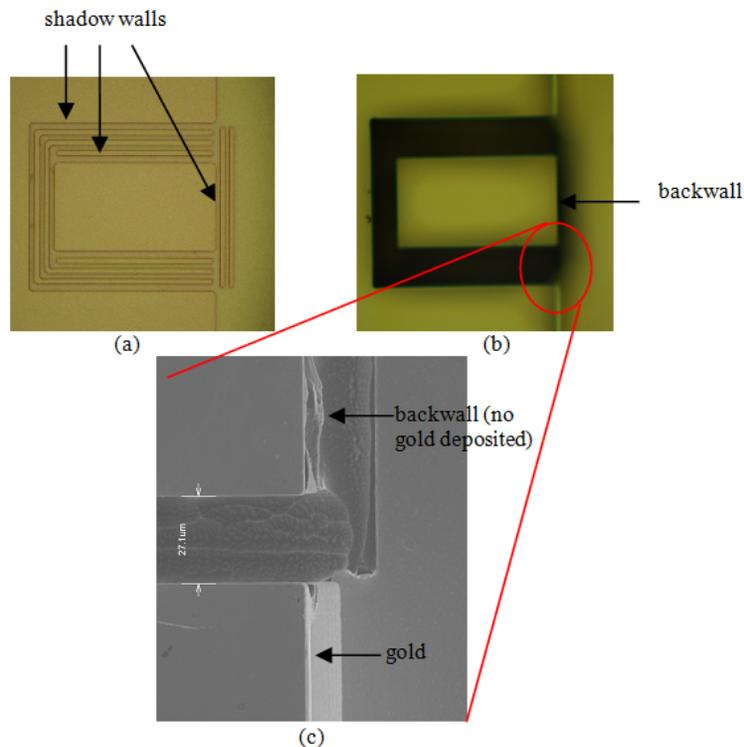
Figure 7.4. The grooved CPW (a) before (b) after removing the shadow walls. (c) SEM photo of the backwall (tilted 200) which verifies that the shadow walls prevented gold deposition effectively.

150

7.1.1.b.   Calibration Set

In order to de-embed the effect of the grooved CPW line on the measured S-parameters, calibration standards for the designed CBCPW lines are required. Since it is not feasible to design matched loads for the line, the TRL (through-line-reflect) technique is chosen to calibrate the system. A set of through and half wavelength lines along with a shorted line is used. These lines include the grooved CPW to CBCPW transition which will be de-embedded in the final measured results.

Figure 7.5 shows the microscopic image of the fabricated three-step meander-line waveguide, back-to-back transition and the waveguide filter.

(a)   (b)

(c)

(d)
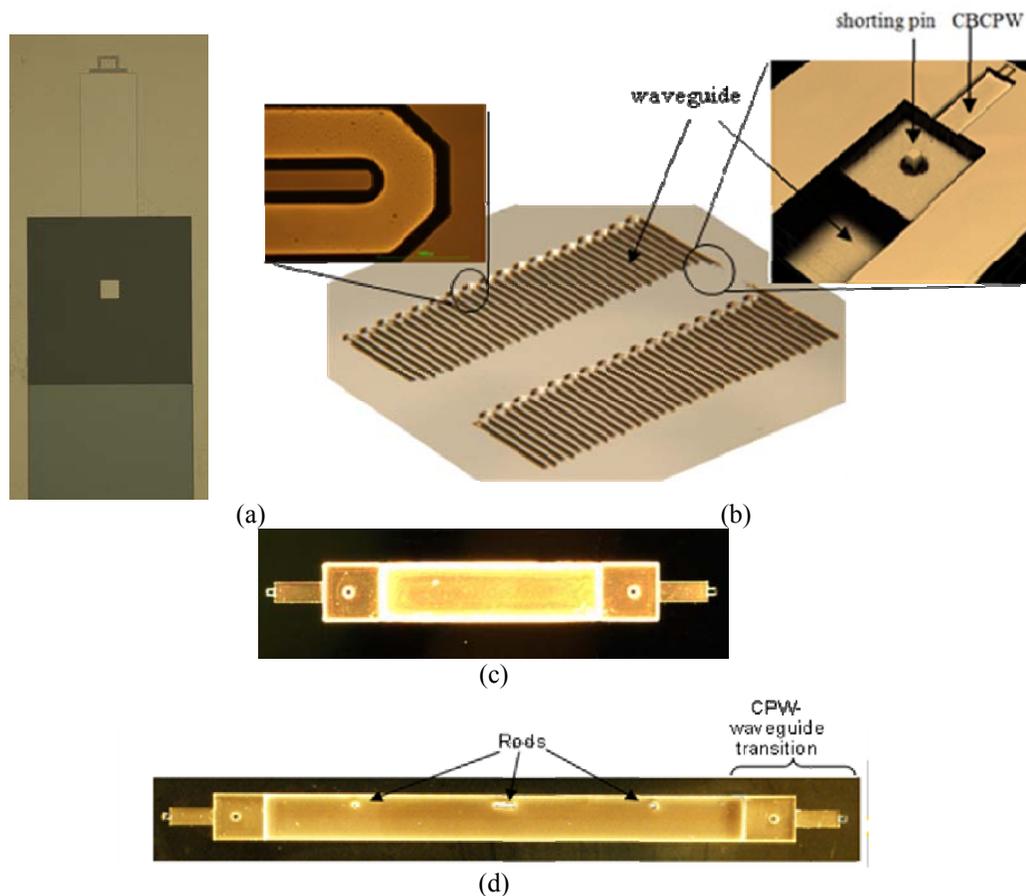
Figure 7.5. (a) Three-step patterning the waveguide. (b) Meander-line waveguide. (c) back-to-back CBCPW to waveguide transition. (d) waveguide filter with the transition

151

7.2. Second Wafer –Slots / Patch Array Substrate

A second wafer is used to cover the top part of the meander-line structure, which includes the CPW lines and slots. This wafer also serves as the substrate of the patch arrays. Two variations of the structure were fabricated at this stage. A simpler process was developed to fabricate the transition, filters and slot-waveguide antenna. A second process is proposed to fabricate the hybrid-coupled patch array which needs a third wafer.

Since the CBCPWs are suspended on a thin membrane layer, a stacked layer of LPCVD $SiO_2/Si_3N_4/SiO_2$ (ONO) is first deposited on top of the second wafer. This layer provides a small amount of tensile stress so that the membrane does not buckle after the wafer release. The wafer is then gold-coated with an adhesion layer, and then patterned and etched to form the CPW lines as well as the slots. Then it is flipped over and the backside is etched to form openings on top of the CBCPW and the slots. The structure is suspended on a membrane around the open areas of the wafer and should be carefully handled. Figure 7.6 illustrates the fabrication process of this wafer and Figure 7.7 shows the fabricated CPW lines and slots on the gold side of the wafer.

At this stage, the first and second wafers should be bonded. Since the wafers are gold covered, we have to perform gold-to-gold thermocompression bonding. This bonding technique provides a hermetic of the surfaces and guarantees the continuity of the current flow. One concern however, is diffusion of silicon through gold, introducing impurities and failure in bonding. To overcome this problem, as mentioned before, a SiO_2 diffusion barrier layer before gold deposition is necessary [87]. The stacked membrane layer already serves as the diffusion barrier on the second wafer

152

The wafer alignment can be performed using backside processing of alignment marks or top side alignment through the transparent membrane. After aligning and clamping the wafers, they are placed inside the bonding chamber and a pressure of 3000 ~ 4000 torr and temperature of 375^0 ~ 400^0c is applied for 40 minutes [88], [89]. Mechanical robustness of gold bonding has been verified by dicing and examining the bonded wafers at multiple locations. Visual inspections and mechanical tests to separate the segments of bonded wafers all indicated very high quality gold-to-gold bonding. The process is shown in Figure 7.8 and the fabricated slot-waveguide array, CBCPW to waveguide transition and CPW and CBCPW lines for calibration are presented in Figure 7.9.

| (a) | (b) | (c) |
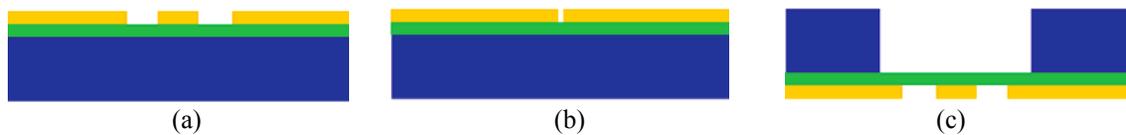
Figure 7.6. Second wafer fabrication process. A stacked layer of LPCVD SiO_2/Si_3N_4/SiO_2 (ONO) as a membrane followed by gold is deposited. Then gold is patterned with the mask of (a) CPW and CBCPW lines. (b) the slots. (c) The wafer is flipped over and the backside is etched from the top of the areas around CBCPW and slots.

| (a) | (b) |

Figure 7.7. Fabricated second wafer. (a) top side- CPW/CBCPW lines (b) top side - slots

| (a) | (b) |
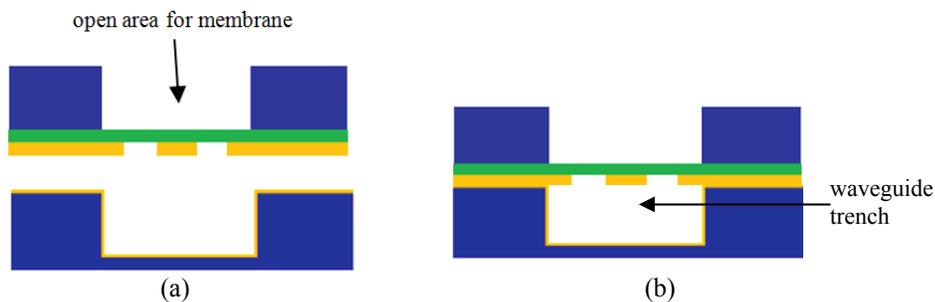
Figure 7.8. First and second wafers. (a) before gold-gold thermocompression bonding (b) after bonding

153
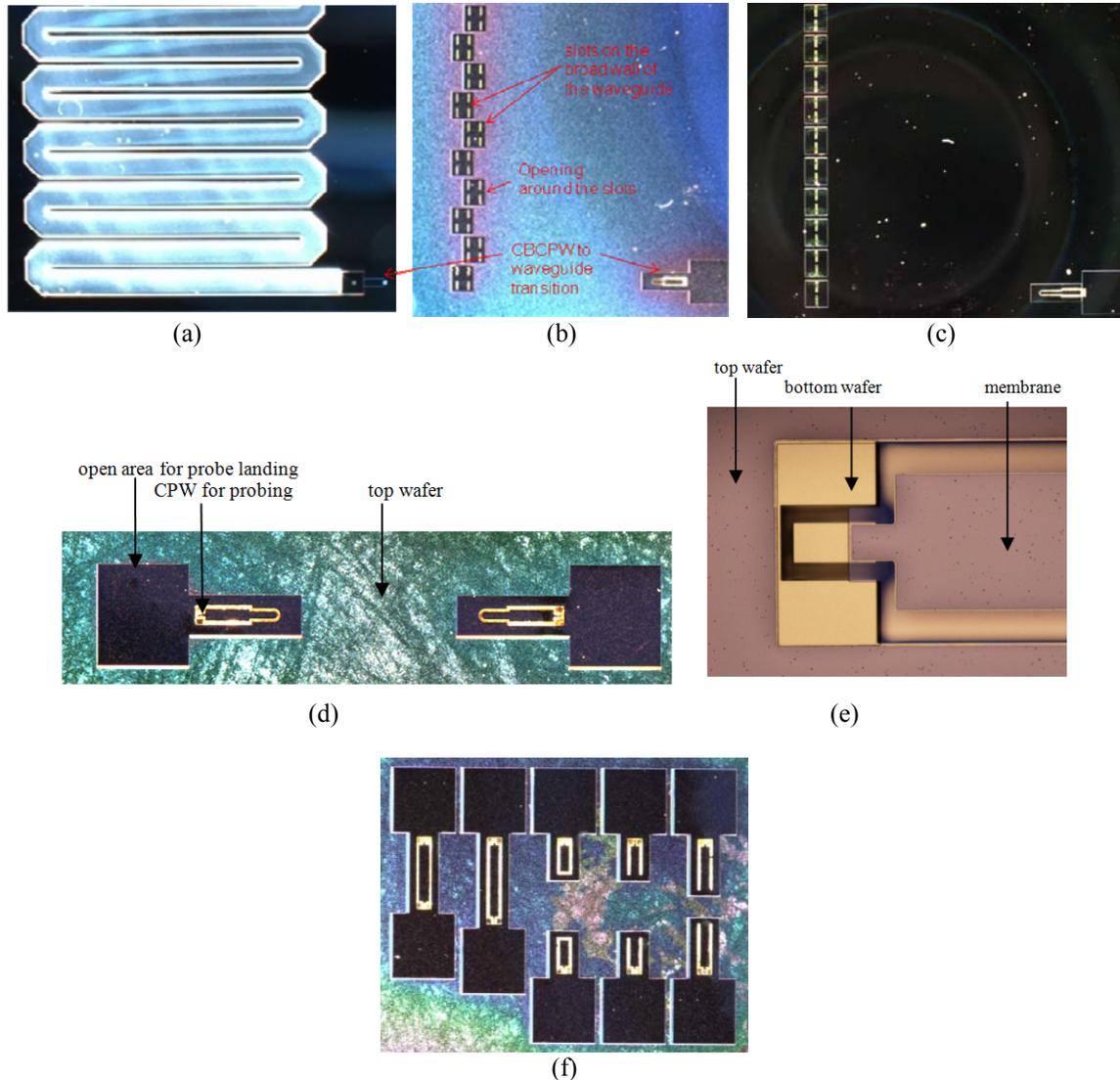
Figure 7.9. (a) First wafer before bonding. (b) the meander-line slot antenna after bonding, (c) the low-loss design (d) the CBCPW/waveguide transition, (e) the CPW/CBCPW transition, (f) calibration standards, from left to right: thru, line, open, short, offset short.

To fabricate the patch array version of the antenna structure, after CPW/slot patterning on the second wafer, the backside is etched with a different pattern. While silicon is still completely removed from the areas around the CBCPW membrane, the pattern of the patch substrate is etched around the slots with the pattern shown in Figure 7.10 (a). We perform a multi-step etching for the substrate with a similar process mentioned for the first wafer with the membrane as the etch stop of the process. Then the substrate is gold-

coated as shown in Figure 7.10 (b). Due to the RIE lag effect, the etch depth is dependent on the etched area, i. e., it is deeper for larger areas. Figure 7.10 (c) shows a more realistic figure of what is realized after etching. This issue is addressed by simulating such a structure. The results show a similar performance for etches deeper than 60% which indicates the steps do not cause a noteworthy change in the antenna pattern and the reflection loss.

The wafer is then bonded to the first wafer as shown in Figure 7.11 with the same gold-gold bonding process. Figure 7.12 shows the fabricated patch array substrate.

(a)   (b)

deeper   shallower

(c)
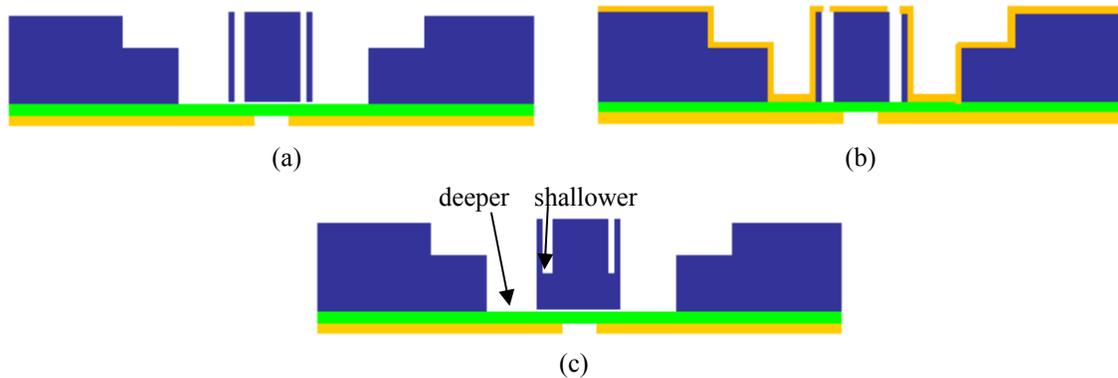
Figure 7.10. (a) multi-step etching for the patch array substrate. Thin shadow walls are also formed to protect the sidewalls of the silicon block from gold-deposition. (b) gold-coating the substrate. (c) the realistic version of the structure.

(a)   (b)
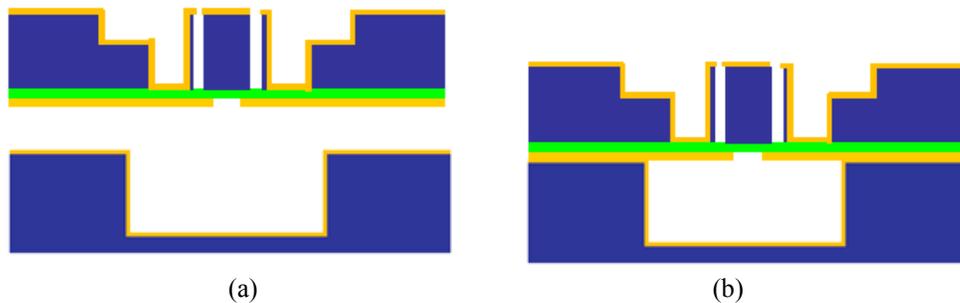
Figure 7.11. First and second wafers. (a) before gold-gold thermocompression bonding (b) after bonding
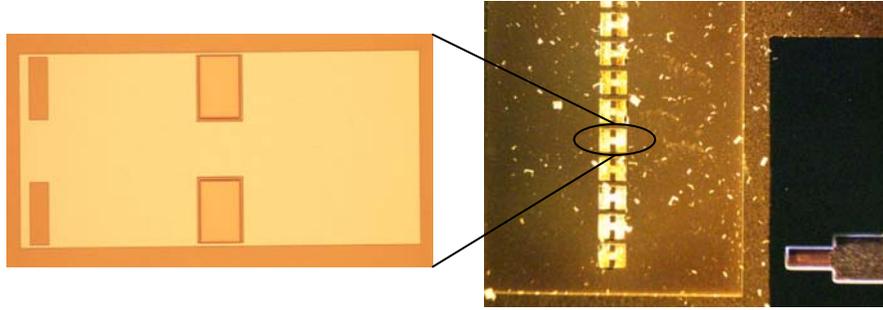
Figure 7.12. Fabricated patch array substrate

7.3.   Third Wafer –Patch Array

The patch array structure consists of $36 \times 2 = 72$ (two in each turn) seven-element patch sub-arrays (total of 504 patches). The array has to be suspended over a membrane on top of the air substrate. Initially, stacked layers of ONO, SU-8 and PDMS (a polymeric organosilicon compound) were tested to serve as membranes. In these processes, the membrane layer is first deposited on a silicon wafer. Then gold is deposited and etched to form patch arrays. This wafer had to be bonded to the bonded pair of first and second wafer. After bonding, the silicon of the third wafer should be removed to have the patches suspended on the membrane. For this purpose, both wafer release and wafer etching techniques can be used. For the wafer release, a release layer such as photoresist should be used before the membrane layer. However, releasing a wafer involves a wet etching process after bonding which cannot be used due to penetration of the solvent to the bottom layers. Dry etching of the whole wafer did not work either since etching is not uniform. It attacks the edges and areas around the circumference of the wafer strongly. The only other way is removing the top wafer locally only around patch areas using DRIE.

The choice of bonding method is flexible since here no high quality adhesion is needed. If the membrane is ONO, diffusion or anodic bonding can be used. However, the main issue with the ONO layer is that it cannot be suspended over a large area. SU-8 cracks at temperatures above 150^0C, so a low temperature bonding method should be used. One way is to use a photo-patternable glue applied on the wafers. Unfortunately, such a material was not available. Photoresist is the only known choice but it outgases and losses its adhesive properties when it is placed inside the DRIE chamber. Crystalbond LT which is used for temporarily mounting in microfabrication was another option. The material can be diluted with acetone and spun, but cannot be not patterned, it has to be applied manually and therefore the thickness cannot be controlled which causes gap between patches and substrate. However, since the adhesive properties are very good, it was used to test the SU-8 membrane. Nevertheless, during the wafer removal process, the membrane collapses around the edges, while silicon is still left around the center. SU-8 layer can be more efficient if the wafer removal process is improved.

Using polymer bonding techniques with a polymer membrane is another option. In order to avoid all the above problems a membrane transfer technique with Parylene [90] was used. The fabrication process is illustrated in Figure 7.13. First, to make a membrane layer with a low adhesion with the wafer, a layer of a photoresist (as a release layer) is spun on the unpolished side of a silicon wafer and baked. Using the unpolished side of the wafer helps decrease the adhesion of the Parylene layer to silicon after removing the release layer. Then, a layer of Parylene with 5 ~ 15 um thickness and then gold is deposited and patterned to form the patch arrays. At the last step, we make some cuts on the Parylene around the circumference of the wafer to provide access to the bottom

157

photoresist layer. The wafer is soaked in acetone and then IPA (isopropyl alcohol) solutions for several days to dissolve the photoresist completely as shown in Figure 7.13 (b). The fabricated third wafer is shown in Figure 7.14.

Since Parylene, like other polymers, very efficiently bonds to itself, the gold-bonded pair should also be covered with Parylene first as shown in Figure 7.15 (a). This layer could be very thin (< 5 μm) in order not to affect the patch array loss. Parylene bonding is performed under vacuum in order to avoid Parylene interaction with oxygen and nitrogen at $150+$ ^{0}C and 800 N force over a 4 inch wafer for 30~40 minutes. For this very structure, bonding pressure should be much higher (5000 ~ 7000 N) than usual since the gold-bonded pair is bowed by a small amount and we have to compensate for it to make sure the Parylene layers are in contact everywhere on the wafer.

The patch array membrane is transferred after bonding. A razor blade can used to cut the Parylene from the circumference of the third wafer so that the wafer is debonded and released as shown in Figure 7.15 (d). Since the Parylene from the patch wafer is connected to the bottom Parylene wafer, this method is called the Parylene transfer method [90]. Figure 7.14 shows the fabricated Parylene membrane.
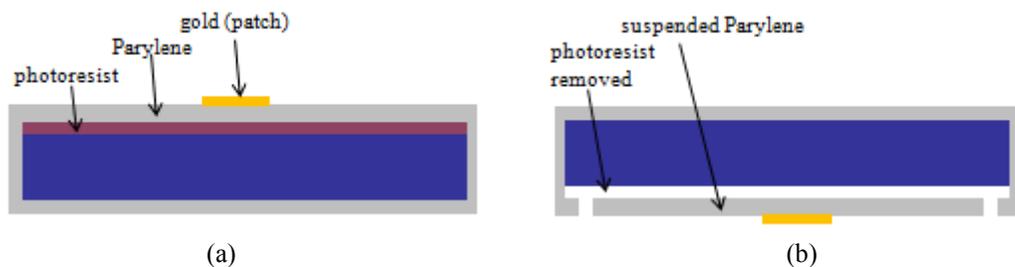
Figure 7.13. Third wafer fabrication process. (a) photoresist, Parylene and patterned gold are deposited on a silicon wafer. (b) photoresist is dissolved by soaking the wafer in acetone and IPA.

158
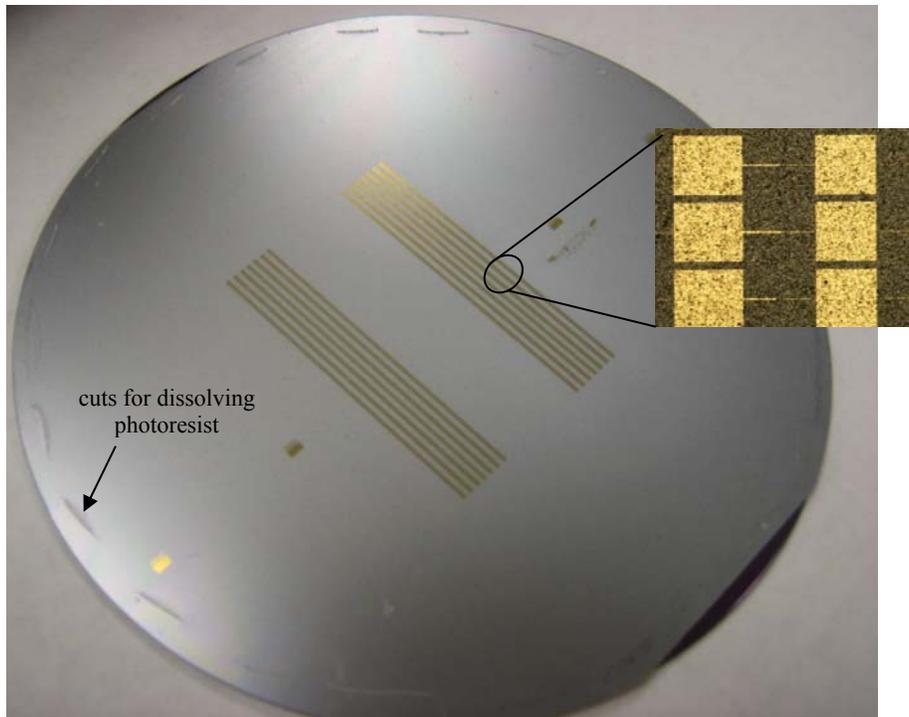
Figure 7.14. Fabricated third wafer after dissolving the photoresist release layer.

(a)

(b)

(c)

(d)
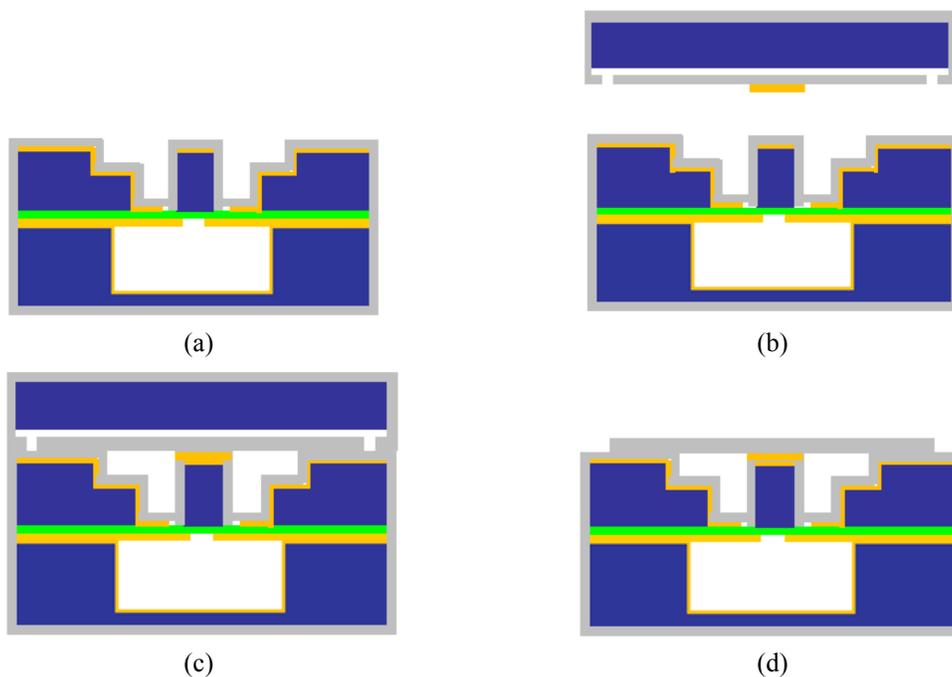
Figure 7.15. Last step of the fabrication process. (a) The gold-bonded pair is Parylene-coated. (b) The wafers are aligned and (c) bonded. (d) The third wafer is de-bonded with a razor blade through the edges.
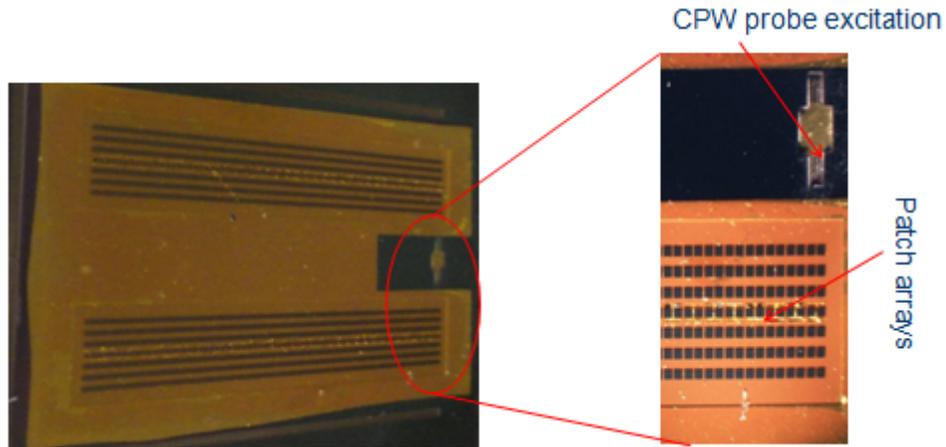
Figure 7.16. Final fabricated structure.

7.4. Chip Packaging

The fabrication process for the chip integration is shown in Figure 7.17. A two step etching is required on the first wafer to fabricate the hole as well as the cavities for CBCPW. Also, the open area on the top wafer should be designed in such a way that it blocks the chip partly on the areas which are not covered by lines or lumped elements so that the chip cannot press on the membrane and break it. The test chips are fabricated on a standard-thickness silicon wafer as shown in the process in Figure 7.18. The chips on the wafer are diced at the end of the process. Figure 7.19 shows a photograph of the fabricated chips after dicing and Figure 7.20 shows the fabricated transition. The holes on the bottom wafer are etched to insert the chips inside while the top wafer covers the hole partially in order to have the chip held in place. The chip can be fixed inside the hole using glue or a block of silicon with dimensions with the same size as the hole.
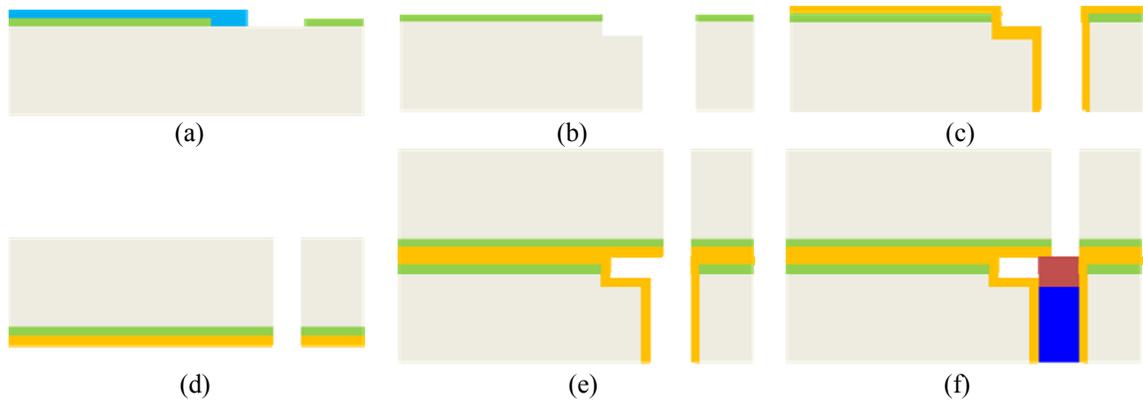
Figure 7.17 Fabrication process of the transition between the chip and the CBCPW. (a) two-step pattering (b) two step etching (c) gold sputtering for the first wafer. (d) top wafer (membrane, line patterns and etching the open areas). (e) top-bottom wafers gold bonding. (f) inserting the chip inside.
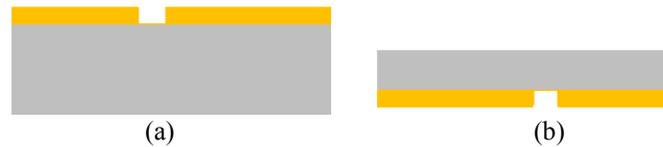
Figure 7.18. Fabrication process of a test chip (a) pattering gold on a silicon wafer (b) etching the backside of the wafer to thin down to the desired chip thickness.
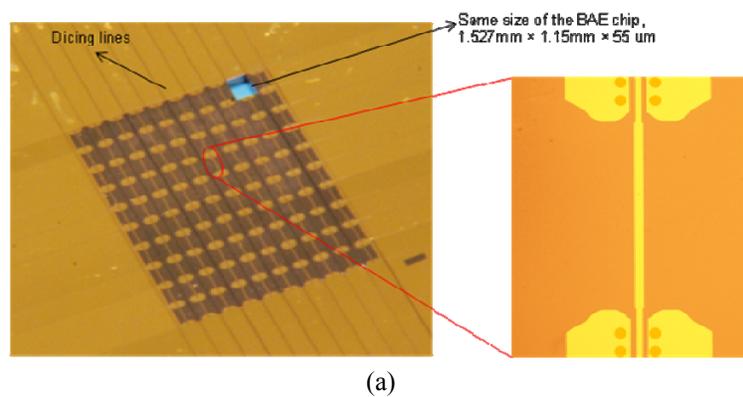
Figure 7.19. (a) the chip is fabricated on a silicon wafer with a simple CPW to microstrip transtion optimized for maximum insertion.

CBCPW line   the hole for DC wires   the hole for the chip   CBCPW line

Bottom wafer   top wafer-top side   top wafer-bottom side

the hole for the chip

Extended CPW for capacitive coupling

the hole for DC wires
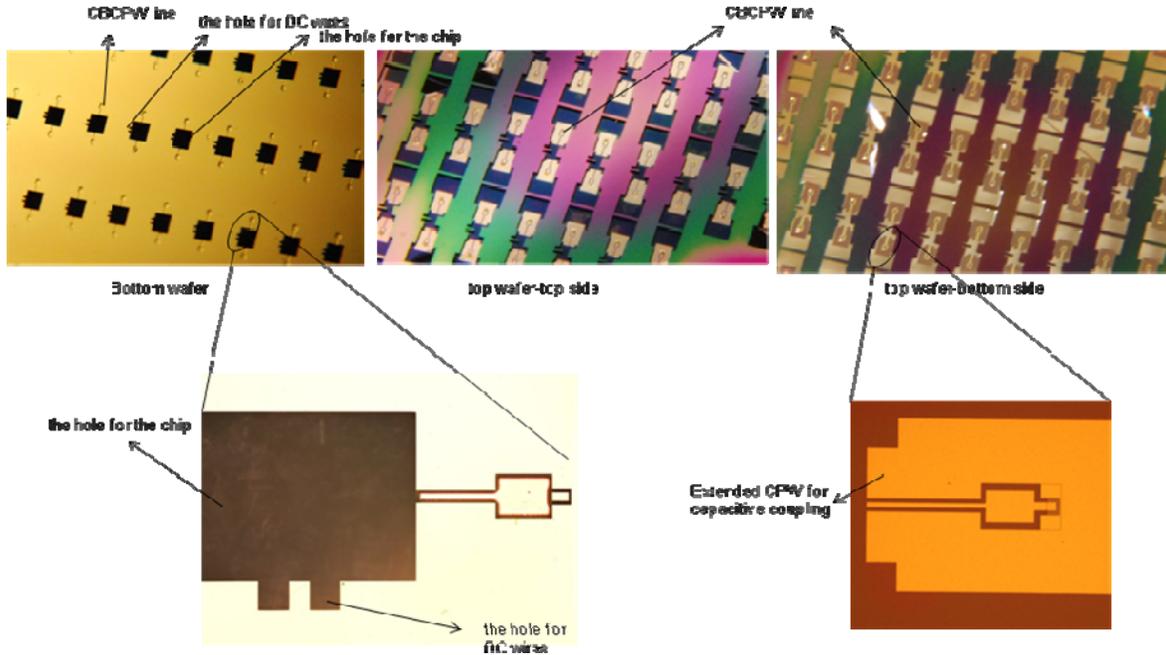
(b)

Figure 7.20. The bottom and the top wafer of the fabricated transition. It is observed that the holes on the bottom wafers are partially covered by the top wafer.

7.5.   Estimation of the Cost

Microfabrication is low-cost because many of the processes can be performed in parallel with multiple components on a single wafer. This includes most of the depositions and wet etchings. In addition, the cost of fabrication on a 6 inch or larger wafers is commonly equal to that on a 4 inch wafer, but since the yield is higher with larger wafers, cost can be considerably decreased. Figure 7.21 shows the yield of the radar structure with 4 inch and 6 inch wafers. The cost of process remains the same, yet the yield with 6 inch wafers is 4 times higher. Table X lists the estimated cost and time of microfabrication for different processes on a 6 inch wafer. Processes such as PVD and LPCVD depositions, although long and costly, have the same wafer process cost and time so the components cost much lower due to wafer parallel processing.

162
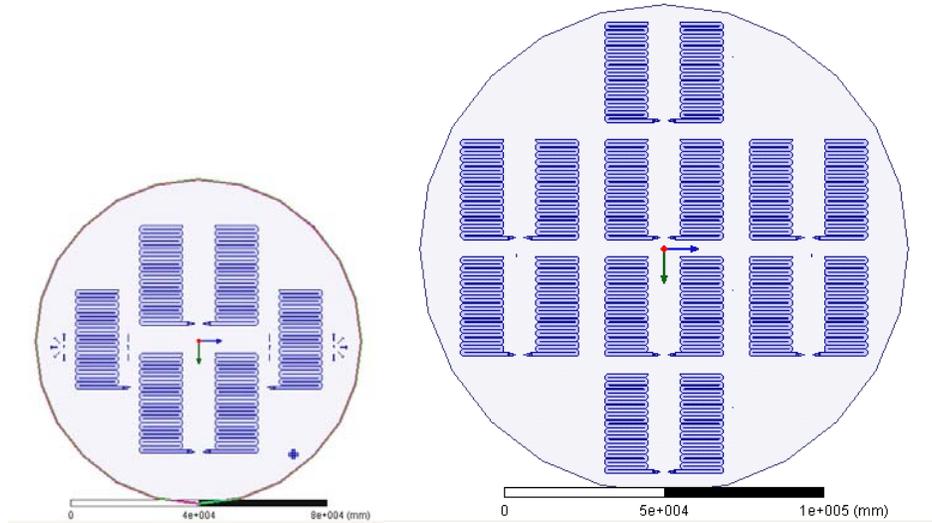
Figure 7.21. Yield of the radar structure with 4 inch and 6 inch wafers. It can be observed that while only two radars (including one transmitter and one receiver antennas) can be fabricated on a 4 inch wafer, eight radars (one pair of antennas) can be fabricated on a 6 inch wafer.

	Lithography	DRIE	PVD Deposition	LPCVD Deposition	PECVD Deposition
Cost ($)	33	60	60 (gold) + 3 (Parylene)	63	14
Time (min)	7 steps = 105	5 steps = 90	3 steps = 120 (gold) 2 steps = 180 (Parylene)	13 hrs	2 steps = 30

	Wet Etching Processes	Dry Etching Processes (except DRIE)	Gold Bonding	Parylene Bonding
Cost ($)	20	35	70	70
Time (min)	15 steps = 75	4 steps = 75	60	60

Table X. The estimated cost and time of microfabrication for different processes on a 6 inch wafer. The estimated total cost is 428 $/ 6 inch wafer which results in 428 $ / 8= 53$ for each radar including a pair of transmitter and receiver antenna.

The total microfabrication cost for a pair of transmitter and receiver antennas is estimated to be 53$. The final costs of the other radar components including all the active chips are estimated to be below 1$ each. Therefore, the final cost of the radar can be estimated to be below 60$.

7.6.   Conclusion

In this chapter, the details of microfabrication processes of the proposed structures were discussed. The process is performed on three separate silicon wafers each of which include a part of the antenna and other passive devices which are bonded together at the final step. Various microfabrication procedures such as silicon DRIE, gold deposition, multi-step mask deposition, silicon-dioxide deposition, low-stress silicon-dioxide/silicon nitride deposition, XeF_2 silicon etching, gold-gold thermocompression bonding, topside and backside wafer alignment, polymer deposition, polymer bonding, etc. are employed and optimized for the fabrication of the radar components.

Chapter VIII

On-Wafer Y-band Measurements

Making accurate and reliable measurements at high MMW frequencies is a challenging task and demands high quality instrumentation. MMW frequency extenders are used along with vector network analyzers to provide the signal at the desired frequency band. The measurement at the high MMW frequencies especially Y-band have been more focused on WR-3 rectangular waveguide devices [91] - [94]. Although there are some difficulties associated with waveguide measurement such as poor interconnectability between the DUT and the waveguide flange at the test port, it has been shown to be more convenient and reliable than on-wafer measurements. The first full two-port on-wafer measurement capability up to 220 GHz was reported in 1999 [95]. Since then further developments have enabled full two-port on-wafer VNA measurements up to higher frequencies [96]. The Y-band measurements have been recently facilitated using OML [97] and VDI [98] frequency extenders connected to the PNA-X. The on-wafer measurements are conducted using ground-signal-ground (GSG) picoprobes used to excite the CPW lines on the DUT.

In this chapter, the measurement setup for full two-port S-parameter measurements of waveguide transitions and filters is first introduced and the results of the measurement are presented. The antenna radiation pattern measurement setup is then described and the radiation pattern of a standard E-plane horn antenna and the waveguide slot array are measured with this system and discussed.

8.1.   S-parameter Measurement

On-wafer S-parameter measurements of the fabricated waveguide transitions and filters are performed using the dual source PNA-X with OML frequency extenders shown in Figure 8.1. The setup includes:

1.   Agilent PNA-X N5245A

2.   OML frequency extending modules

3.   GGB 220-325 GHz GSG probes with 80 μm pitch size

4.   WR-3 bent waveguides

5.   Cascade MMW probe station and micropositioners

6.   Leica S8APO stereomicroscope

The configuration is assembled in such a way as to provide a system with high reliability and capability to easily move and control the GSG probe location. The devices under test are fed through the probes connected to the frequency extending modules using WR-3 bent waveguides controlled by Cascade Microtech MMW micropositioners. The On-substrate TRL calibration set as shown in Figure 8.2 is measured first to de-embed the effect of the CPW line. In addition, the response of a back-to-back transition is also de-embedded from the final response of the structures by measuring the fabricated calibration lines shown in Figure 7.9. (e). After calibration, the S-parameters of the devices were measured and are presented in Figure 8.3 and Figure 8.4 for the CBCPW to waveguide transition and waveguide filters. The measurement results show good agreements with the simulation. The deviation can be mainly attributed to the error in the probe placement and establishing good contacts on the pads. In addition, the quality of gold bonding and high quality ohmic contact as well as the deviation of the dimensions

(especially depth) of the fabricated structures from the designed ones cause differences
between the measured and simulated results.
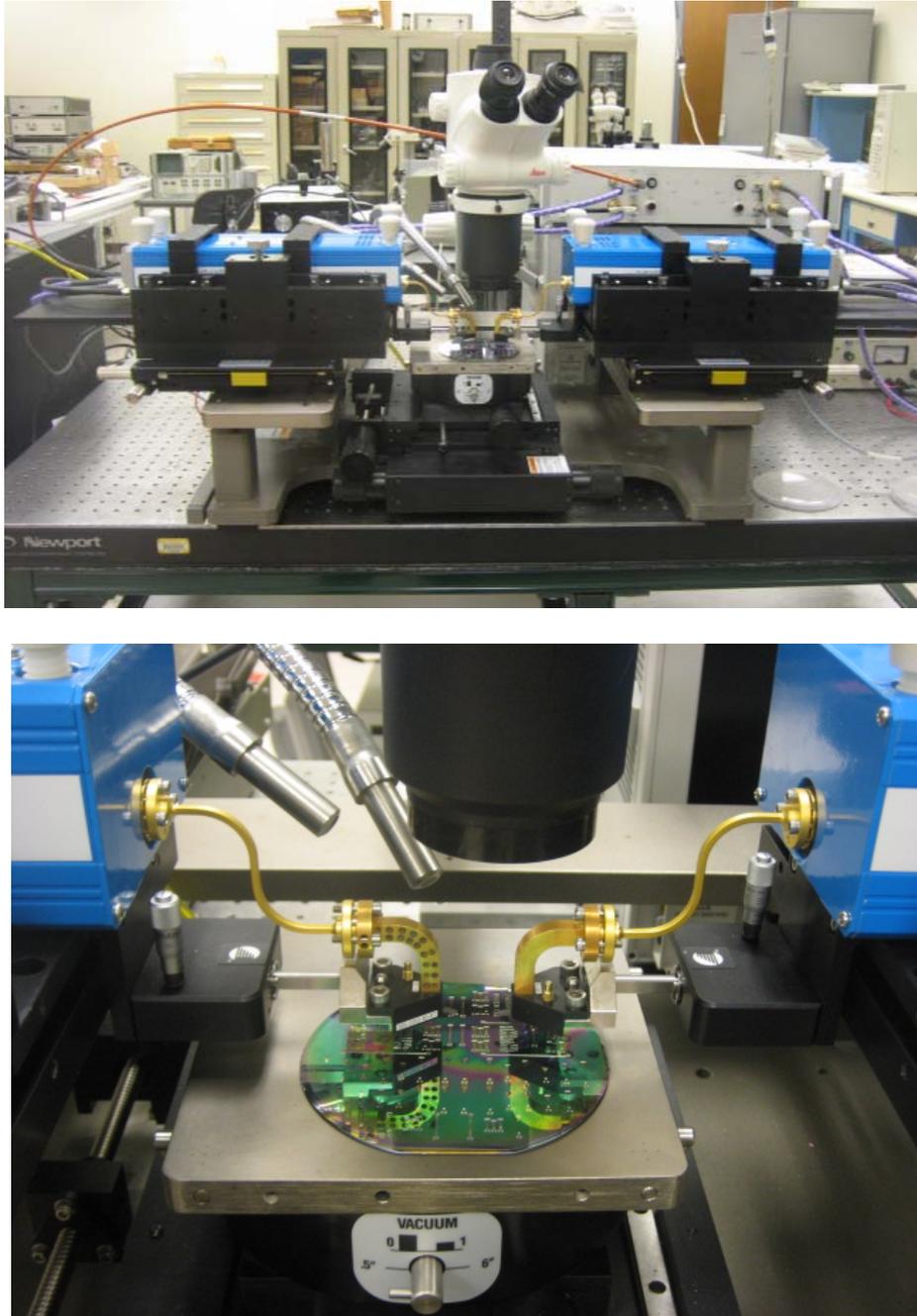
Figure 8.1. WR-3 (220-325 GHz) measurement setup.
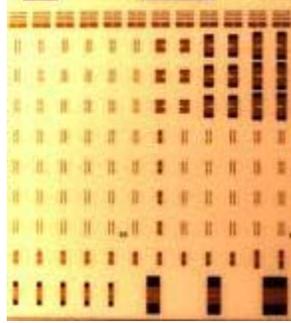
Figure 8.2. GGB CS-15 calibration substrate with line, thru, matched load, short and open.

(a)　　　　　　　　　　　　　　　(b)
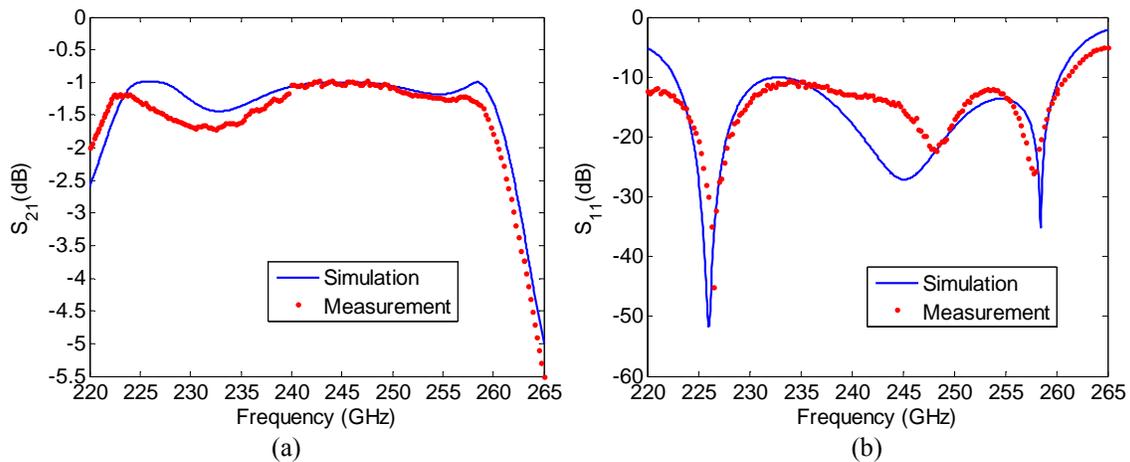
Figure 8.3. The measured transmission and reflection coefficients of the back-to-back transition structure of Figure 6.4. The results are in good agreement with the simulation. The transmission coefficient is below -1.5 dB for the two series transitions and the waveguide section in between**.**

(a)　　　　　　　　　　　　　　　(b)
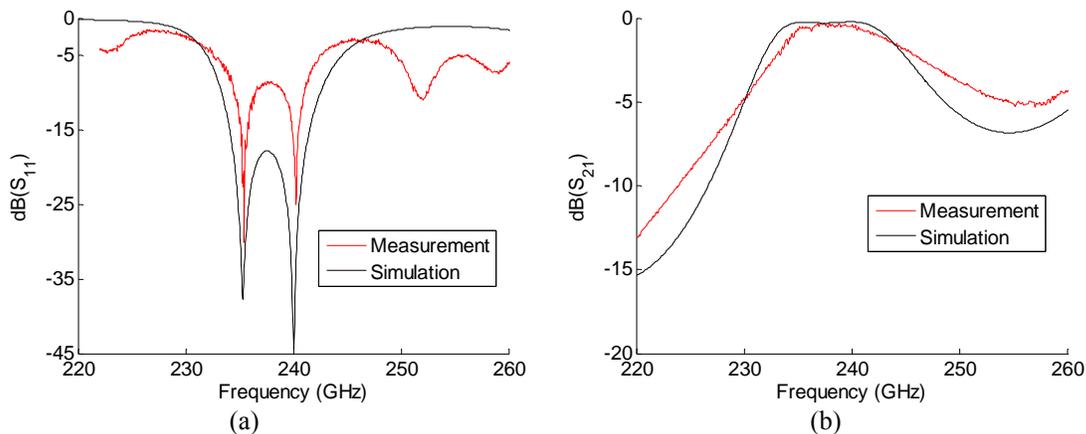
Figure 8.4. The measured (a) reflection and (b) transmission coefficient of the filter shown in Figure 6.19 compared to the full-wave simulation. The nulls of the filter are precisely detected and the results are in good agreement with the simulation.

8.2. Antenna Radiation Pattern Measurement

At Y-band frequencies - due to the large free space path loss (80 dB + 20 log(d)) – the received far-field signals commonly fall below the dynamic range of the measurement system. In particular, this is the case when the apertures of the antennas are large compared to the wavelength so that their far-field distance is more than a meter away. For this antenna with 4.5 cm aperture length, $2D^2/\lambda > 3$ m. Since the dynamic range of the system is around 75 dB, measuring the far field of the antenna is not practical.

In the recent years, the near-field antenna pattern measurement technique has become a popular alternative to the standard far-field measurement method. Characterization of radiation properties of antennas using a near-field technique is based on the measurement of both magnitude and phase of the electric field in the vicinity of the antenna. Based on the uniqueness theorem, using the tangential electric field over a closed surface, the field everywhere outside the source region can be uniquely evaluated. Therefore, first the near-field of the antenna should be measured over an area. A probe is moved on a near-field rectangular area above the antenna and by scanning the field at each point generates a grid. Spatial resolution and the extent of the scanned area, the probe distance from the antenna and the precision in positioning the probe are critical parameters for accurate measurement. The extent of the scanned area is determined by the truncation spatial frequency $f_x = \dfrac{1}{2\Delta x}$, where $\Delta x = \beta \lambda_0 / 2 \, (\beta < 1)$ is the spatial resolution. The attenuation of the non-propagating wave can be obtained from: $\alpha_z = \sqrt{k_x^2 - k_0^2} = k_0 \sqrt{\left(\dfrac{1}{\beta}\right)^2 - 1}$, therefore the loss factor is calculated as $L = dB(e^{-\alpha_z d})$, where $d = \gamma \lambda_0$ is the distance from

the antenna to the probe. Upon substituting d and α_z, $L = 54.58\gamma\sqrt{\left(\dfrac{1}{\beta}\right)^2 - 1}$ dB which

establishes a relationship between spatial resolution and the probe distance to the antenna

for a chosen loss factor.

The setup shown in Figure 8.5 was used to measure the antenna near-field. The antenna

is fed through the CPW to waveguide transition using GSG probes connected to a

frequency extender. To measure both x- and y-directed radiated electric fields, two WR3

open-ended waveguides with thinned walls to minimize reflection from the waveguide

probe, one straight and one twisted, for both E_x and E_y measurements as shown in Figure

8.6 are used. They are placed at the near-field region on top of the antenna while their

other end is connected to the other frequency multiplier which is mounted on top of an

XY stage as shown in Figure 8.7. The high-resolution XY linear stage is utilized to move

the waveguide probe in a grid and collect the data. The stage consists of two orthogonal

ballscrew linear stages with brushless servomotor and line encoders mounted atop of each

other and are separately controlled by two PWM digital controllers. A Matlab code was

developed to simultaneously control the stage and collect S_{21} data from the PNA-X. In

order to have maximum dynamic range and stable measured data, the PNA-X is set to

have 300 Hz IF bandwidth and averaging factor of 8.
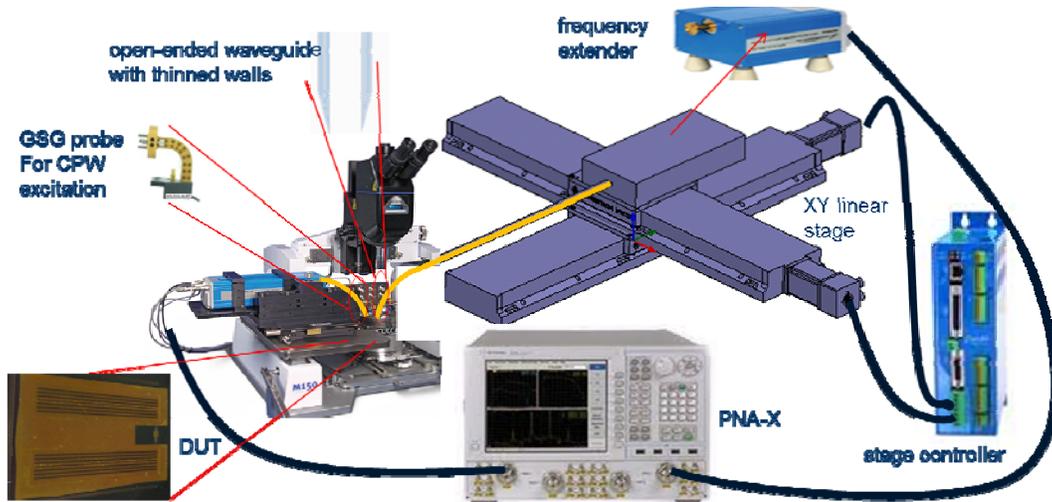
Figure 8.5. The proposed setup to measure the antenna near-field.

(a)

(b)
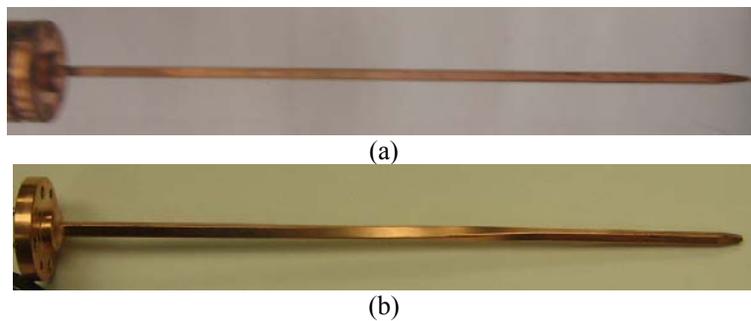
Figure 8.6. (a) Straight and (b) twisted waveguide probes to measure co- and cross-polarized field components.
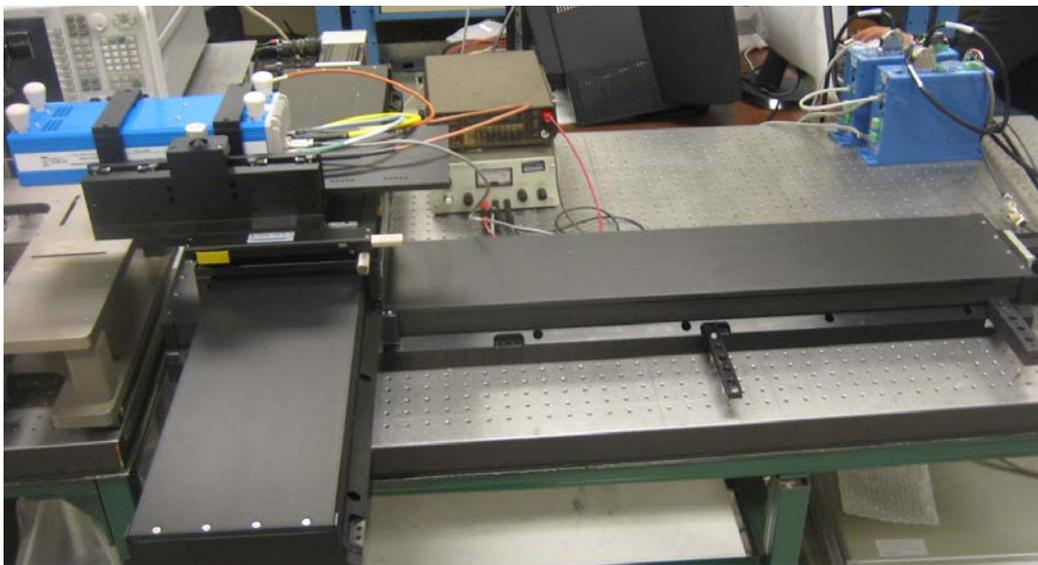
Figure 8.7. The XY stage used to move the near-field waveguide probe.

171

8.3. E-plane Horn Antenna

The near-field pattern of a standard Y-band E-plane horn antenna was measured in order to examine the performance of measurement setup. Since the XY stage is positioned horizontally and the horn is positioned vertically as shown in Figure 8.8, the near field is measured in only one-dimension. The E-plane horn antenna has dimensions of 8.2 mm × 5.2 mm and tapered length of 13.5 mm. The far field of the WR-3 waveguide probe (a = 864 μm, and b = 432 μm) is , $2D^2/\lambda \sim 1.2$ mm, so the near field can be scanned with any length above 1.2 mm. The area is 3 cm with 300 μm (around $\lambda_0/4$) spacing and the S_{21} at each point is measured and stored at f_0 = 237.5 GHz with Δf = 15 GHz.
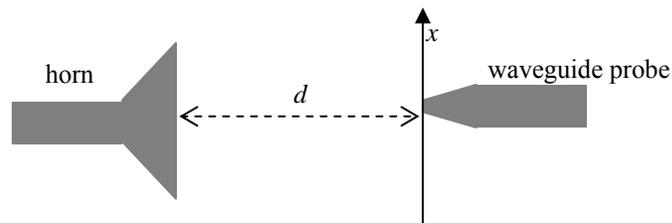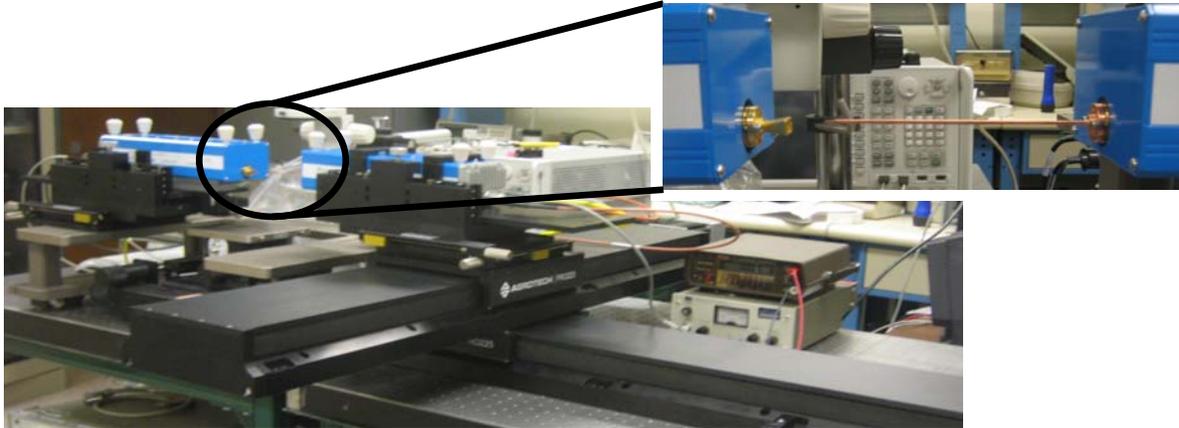
Figure 8.8. Measurement setup for the near-field measurement of the E-plane horn.
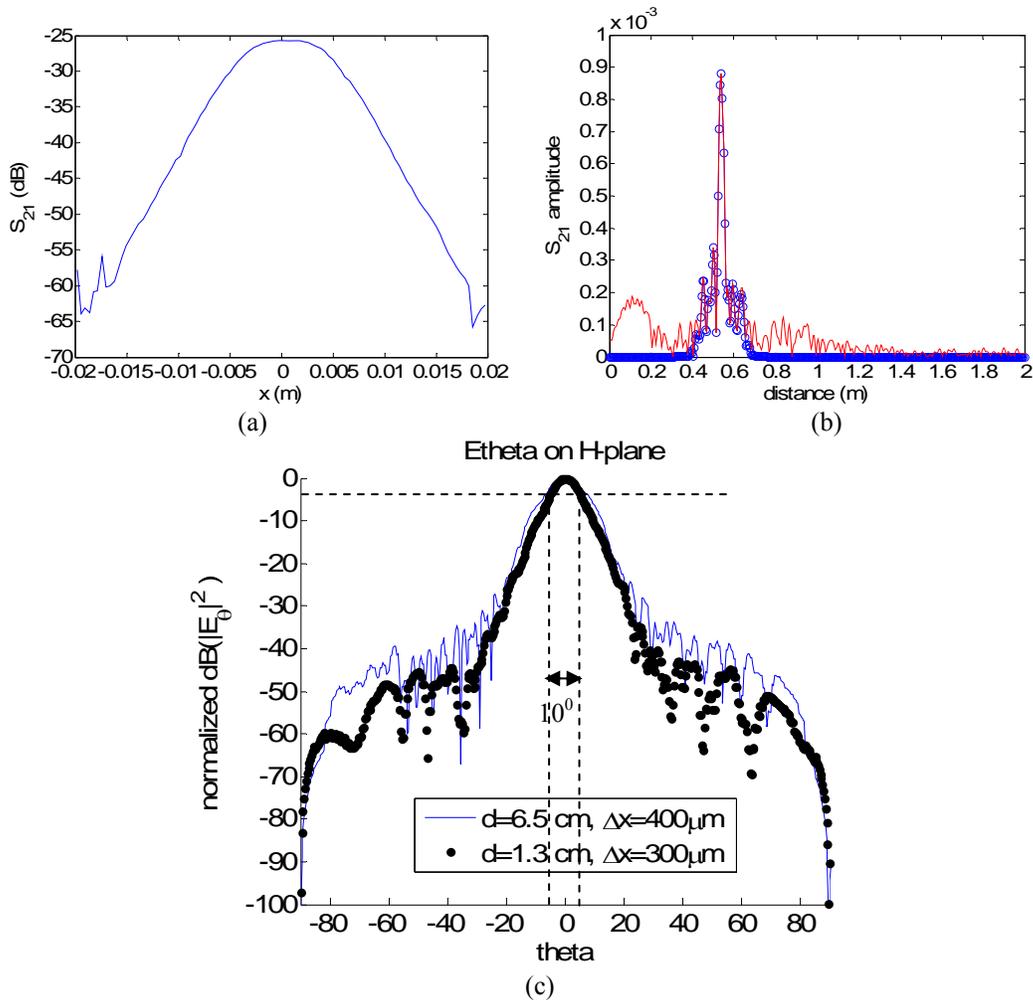
Figure 8.9. (a) S_{21} magnitude versus the scanned area at $f = 237.5$ GHz. (b) The time-domain and the gated response with Kaiser filter for the received signal at x = 0. (c) The normalized far-field radiation pattern verifies 10^0 HPBW.

Figure 8.9 (a) shows the S_{21} magnitude at the center frequency for the co-polarized component versus the scanned area and shows it has dropped around -40 dB at the beginning and the end of the area. With 15 GHz bandwidth, the resolution of the time domain signal is 67 ps, so if the distance between the antenna and the probe is larger than $c / 2 \times 67$ ps ~ 1 cm, the higher order scattered signals can be gated out. A code was developed to calculate the time-domain signal using an inverse Fourier transform algorithm and the gated response with a Kaiser filter and the results are shown in Figure 8.9 (b). The measurement was performed at two different distances (1.3 cm and 6.5 cm)

and two different spatial resolutions (300 μm and 400 μm) for comparison. The far-field signal is calculated using the Fourier transform code and the spatial frequencies are mapped to the angles. The normalized far-field radiation pattern is shown in Figure 8.9 (c) for both distances. The measurement results match and the reported half-power beamwidth (HPBW) of the horn (10^0 in the H-plane) is verified.

8.4. Waveguide Slot Array

The near-field of the Y-band quasi one-dimensional waveguide slot array shown in Figure 7.9 (a) and (b) was measured using the near-field setup shown in Figure 8.10. In this setup the waveguide probe is connected to the frequency extender through a waveguide section with a bend and is controlled by the XY stage. Since the waveguide section is light-weight, the weight of the suspended waveguide probe might cause the lengthy waveguide to bend. In addition, the waveguides are prone to shake each time the stage moves and hence need relaxation time. To minimize such vibrations which impose additional scan time and cause error in the stability of the system, the stage is clamped to the optical table. Furthermore, Styrofoam is used to firmly attach the waveguides to the frequency extenders.

After exciting the waveguide with the GSG probe, the waveguide probe is moved on top of the openings around the slots as shown in Figure 8.11 at different distances from 2mm to 5 mm. The distance should not be farther because of power loss due to the free space path loss and radiation from the GSG probe which is minimized when the probe is sitting on the wafer as shown in Figure 8.12. However, it is observed that the radiated power off the slots could not be sensed and measured by the waveguide probe even for

the co-polarized field element. This can be attributed to the very narrow initial slots (5 μm as represented in the inset) and low dynamic range and high loss in the system imposed by long waveguide sections and GSG probes.
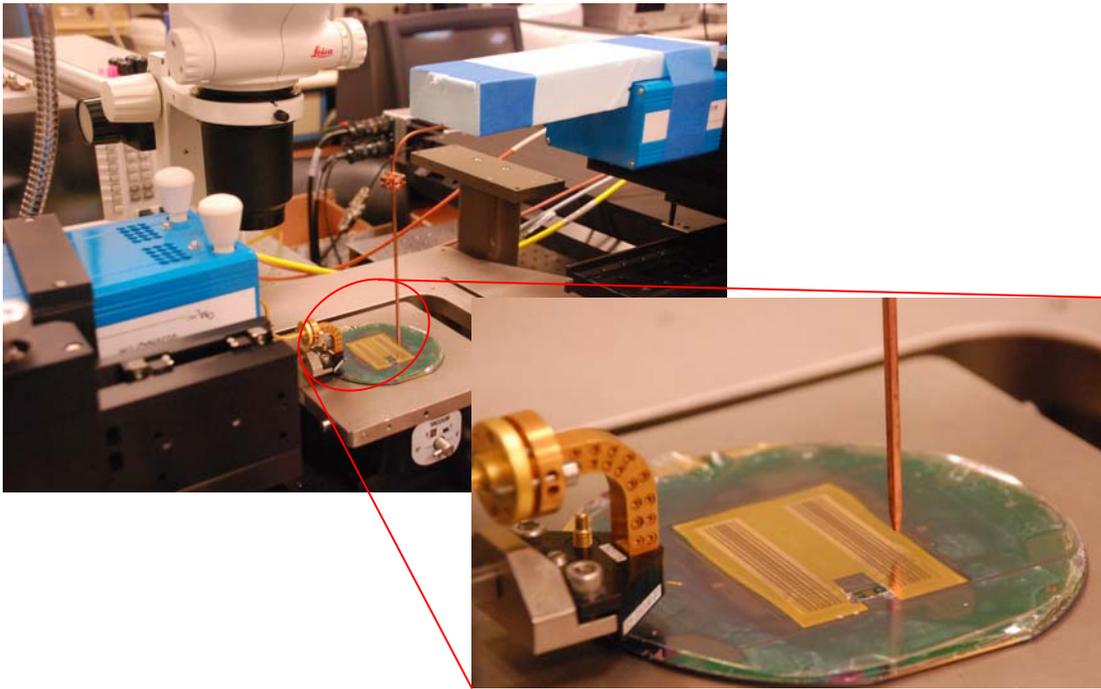
Figure 8.10. The setup proposed for the antenna measurement. The antenna is excited through the GSG probes and the radiated power is measured with a waveguide probe. The waveguide probe is connected to the frequency extender through a waveguide bend and its position is controlled by the XY stage.
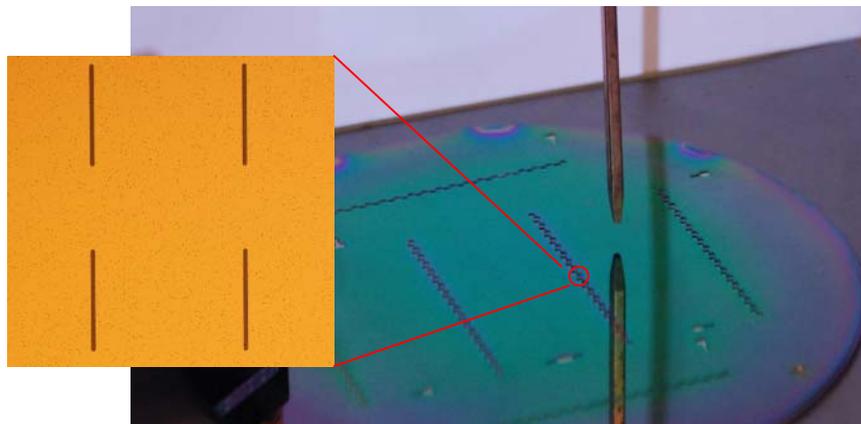
Figure 8.11. The waveguide probe moving on top of the slot openings.
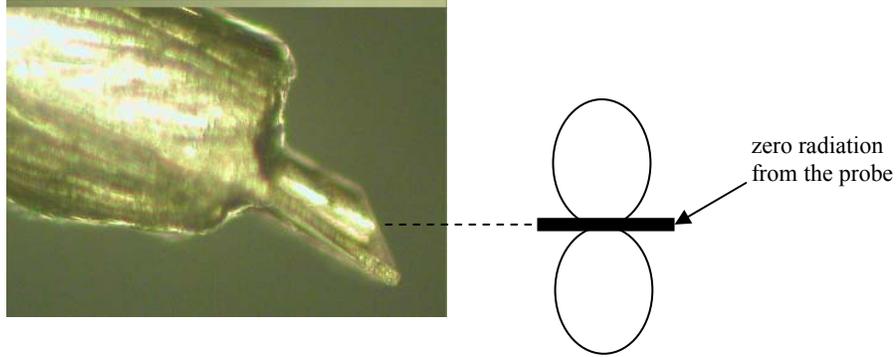
Figure 8.12. Radiation pattern of the GSG probe.

(a)

(b)
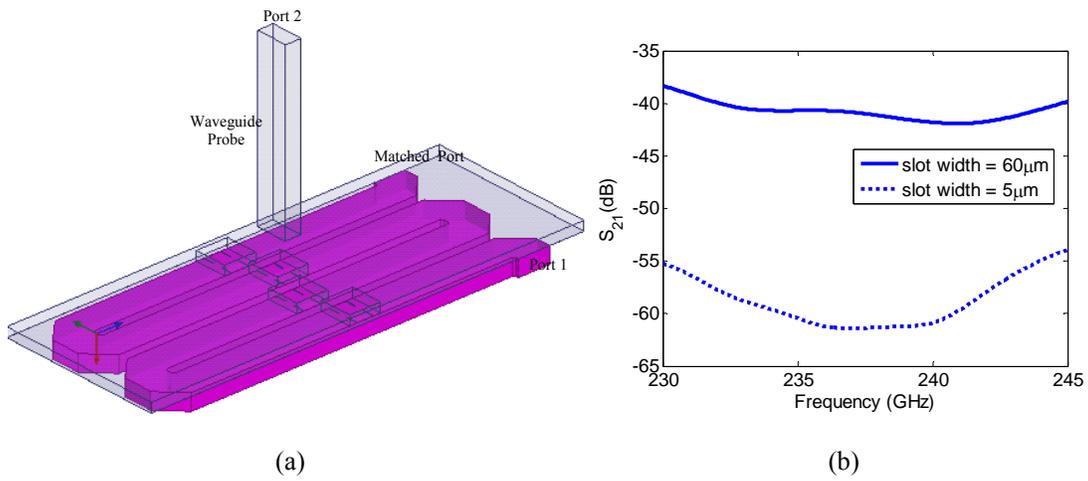
Figure 8.13. The structure simulated to calculate the power radiated from the slots
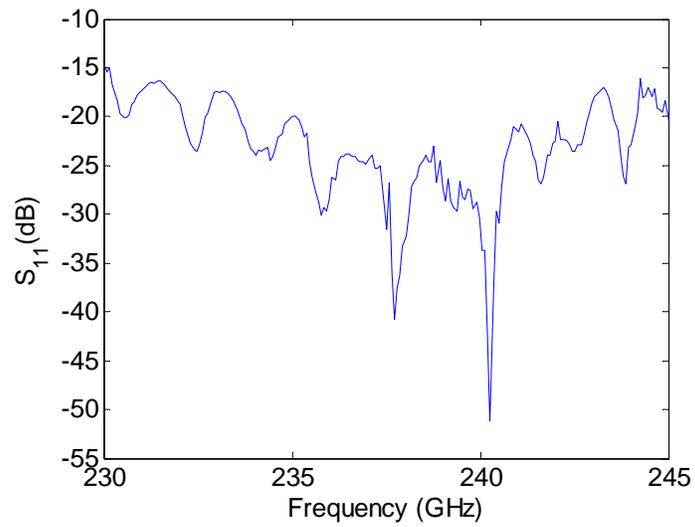
Figure 8.14. The reflection loss of the waveguide slot array.

The measured power radiated from the slots could be characterized by simulating structure such as the one shown in Figure 8.13 (a). In this structure, the waveguide probe is modeled by an open-ended waveguide and the S_{21} of the two waveguide ports for the narrowest and widest slots are shown in Figure 8.13 (b). It is observed that the received signal of the widest slot is 18 dB higher than that of the narrowest slot for the same input signal. Therefore, to explore the minimum measurable power from the slots, the structure is excited from the other end where the widest slots (60 μm) are present. The S_{11} of the antenna is shown in Figure 8.14. It is observed that it is below -20 dB for most of the band. The field is scanned over a ~ 1 cm × ~ 3 mm on top of the opening for slots at a 2 mm distance. The S_{21} magnitude at the center frequency for the co-polarized component is shown in Figure 8.15. It is observaed that the intensity of the signal is higher around the slot areas but it rapidly drops after the first two / three turns. This is mainly because the width of the slots decrease and the so does the radiated power. This test demonstrates that due to high loss, low input power and low dynamic range, we cannot expect to be able to measure the radiated power off the narrow slots. Therefore, the waveguide loss must be decreased and the dimensions of the slots must be increased.
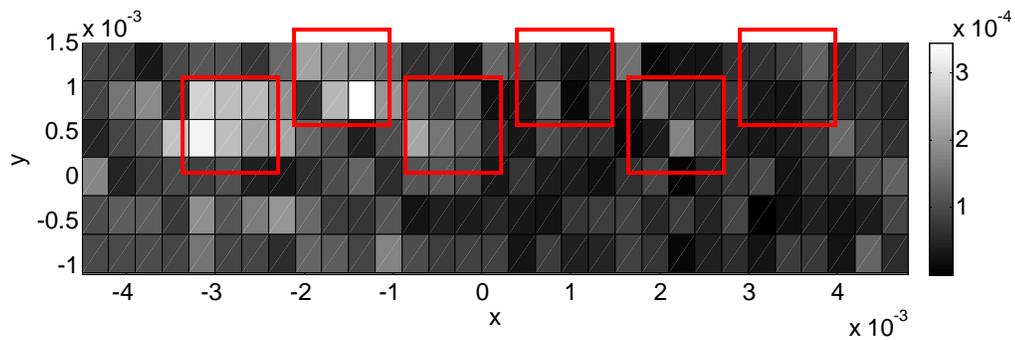
Figure 8.15. (a) The S_{21} intensity measured over the slot openings.

The reduced-loss waveguide with larger slots proposed in section 5.7 (Figure 7.9) was then measured with the same setup. The field is scanned over ~ 1.2 cm × ~ 3 mm on top of the opening for slots at 1.5 mm distance. The S_{21} magnitude at the center frequency for the co-polarized component is shown in Figure 8.16 (a). It is observed that the intensity of the radiated signal is decayed along the length of the antenna. Figure 8.16 (b) plots the intensity on top of the first 10 slots area along the line shown in Figure 8.16 (a) and shows around a 20 dB loss which is much higher than expected. The time-domain signal using inverse Fourier Transform algorithm at two different spots is shown in Figure 8.17. Since the amplitude of the main signal is higher than any other interference, we do not use time gating to evaluate the far-field. An advantage of not using time-gating is the ability to keep the information from the whole band and verify the frequency scanning behavior of the antenna.

(a)

(b)
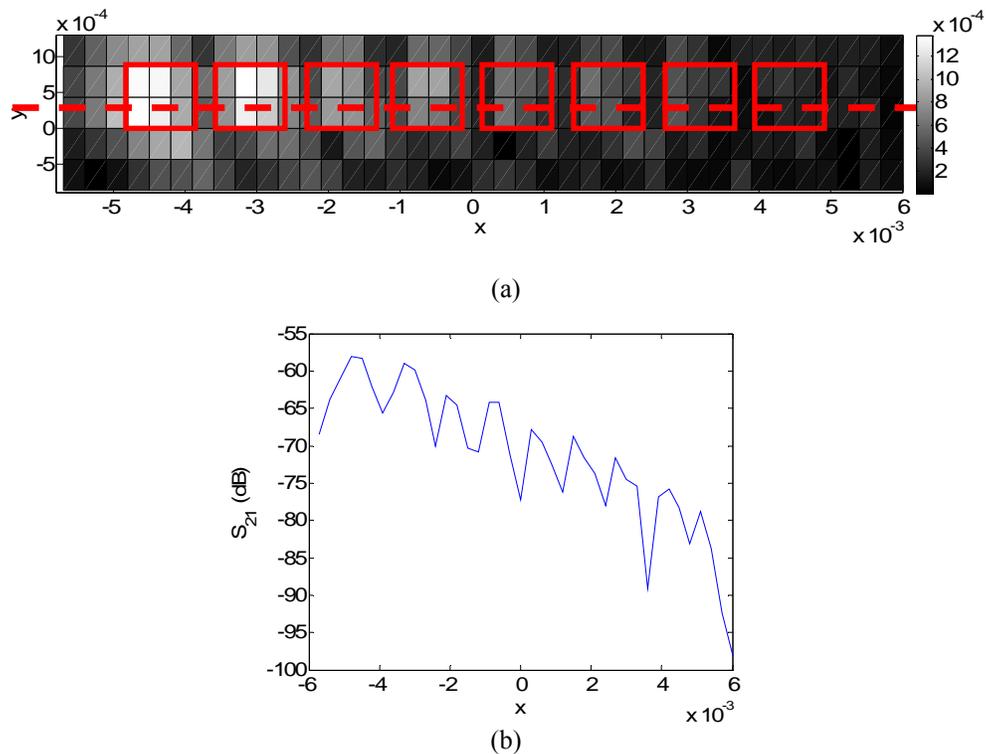
Figure 8.16. (a) S_{21} intensity measured over the slot openings of the reduced-loss design. (b) S_{21} intensity over the cells shown in part (a).
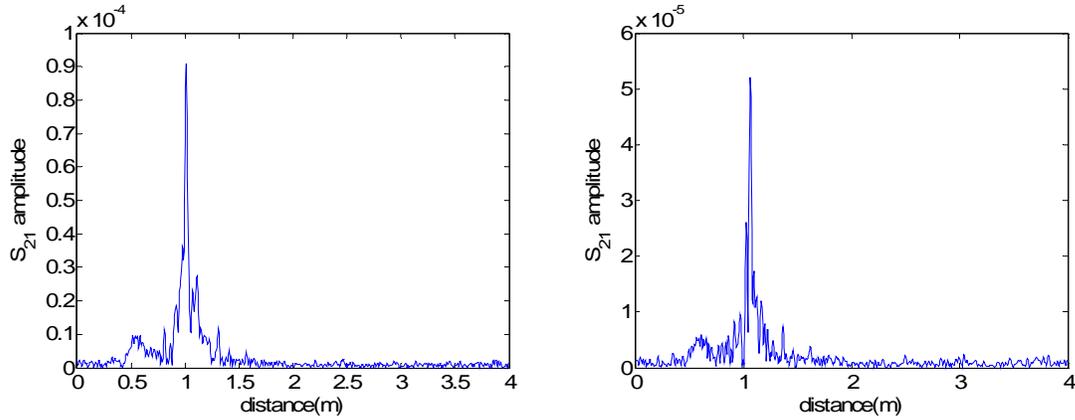
Figure 8.17. The time domain response at two different spots on top of the slots.

The far-field signal is calculated using the Fourier transform code and the spatial frequencies are mapped to the angles. The normalized far-field radiation patterns for different frequencies are shown in Figure 8.18. The measurement results verify the frequency scanning behavior of the antenna by showing beam steering from -23.4^0 to 28.5^0 in 230~245 GHz range. Table XI lists the scan angle versus frequency.

However, the beamwidth of the antenna is 8.5^0 which is much wider than what was initially designed. This is mainly due to the high loss which results in a shorter effective aperture. It is anticipated that degradation in gold conductivity may cause this higher loss. This was investigated by breaking the bond of the two wafers. It was observed that the mechanical robustness of the bond is very good and the gold quality around bonded areas is high. However, the quality is degraded on the etched areas where no pressure is applied. Figure 8.19 shows the bottom surface of the bottom wafer before and after gold bonding. The roughness and impurity of the surface can be attributed to the gold-silicon eutectic bonding which happens around gold bonding temperature (363^0c) without the need to apply pressure.

(a)   (b)   (c)   (d)   (e)
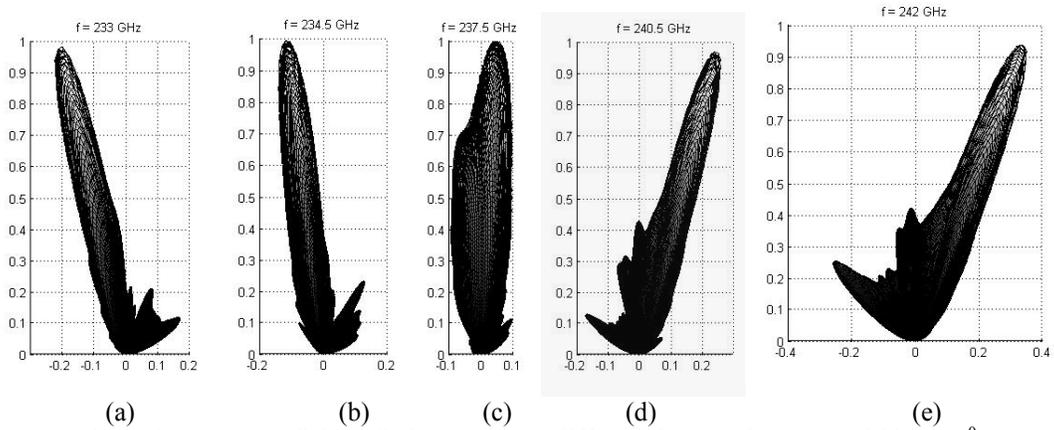
Figure 8.18. (a) Far-field radiation pattern at different frequencies, beamwidth = 8.5^0.

Frequency (GHz)	Scan Angle (deg)
230	-23.4053
231.5	-17.5268
233	-11.6482
234.5	-5.7124
236	-1.1459
237.5	2.8762
239	8.7032
240.5	14.7422
242	19.3431
245.	28.5448

Table XI. The scan angle versus frequency for the waveguide slot array.

(a)   (b)
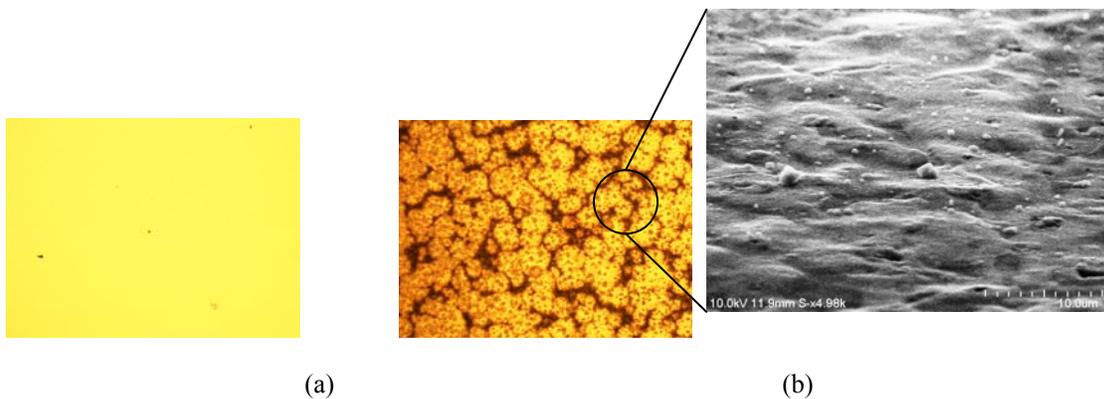
Figure 8.19. Etched area of the bottom wafer (a) before and (b) after bonding. The SEM photo in the inset shows around 5~10 µm roughness.

In order to resolve this issue, an extra layer of a diffusion barrier material (SiO_2) is deposited on the bottom wafer right before gold deposition. Figure 8.20 shows the transition area after the bonding for both cases. The microscope is focused on the bottom wafer through the transparent membrane. The gold on the bottom wafer remains spotless even after the bonding when a diffusion barrier layer is used.

The near-field of the antenna with the improved gold bonding process is then scanned over ~ 3 cm × ~ 4 mm on top of the opening for slots at 1.5 mm distance. The S_{21} magnitude at the center frequency for the co-polarized component is shown in Figure 8.21 (a). The intensity of the radiated signal decays along the length of the antenna. Figure 8.21 (b) plots the intensity on top of the slots along the line shown in Figure 8.21 (a). It shows that the signal level has decayed with a much lower rate compared to the previous antenna. The far-field signal is calculated using the Fourier transform code and the spatial frequencies are mapped to the angles. The normalized far-field radiation patterns for different frequencies are shown in Figure 8.22. The measurement results verify the frequency scanning behavior of the antenna by showing beam steering from -21.2^0 to 29.8^0 in 230~245 GHz range. Table XII lists the scan angle versus frequency.

(a) (b)
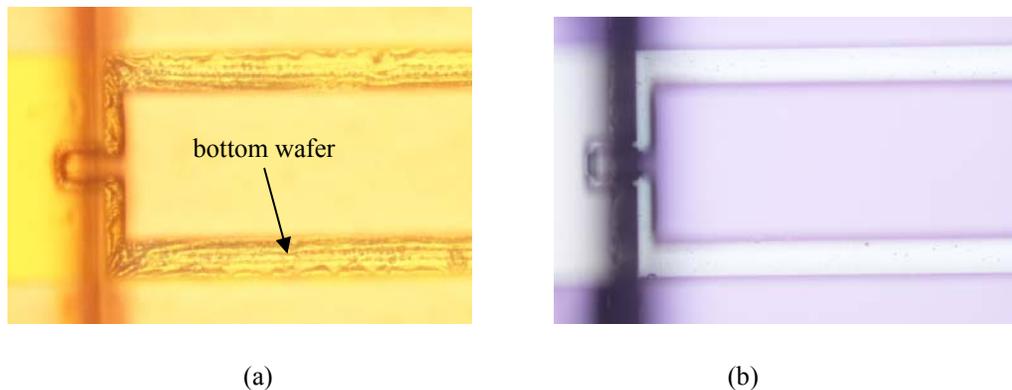
Figure 8.20. Gold quality on the bottom wafer after bonding (a) without and (b) with a diffusion barrier layer.
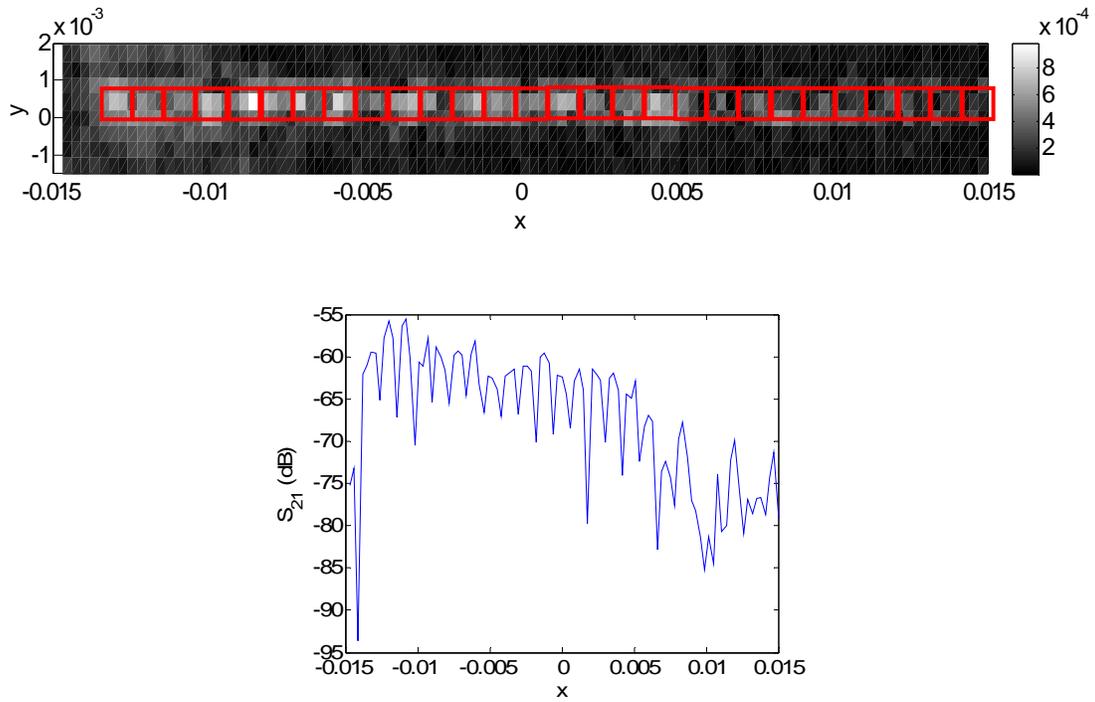
Figure 8.21. (a) S_{21} intensity measured over the slot openings of the reduced-loss design with the diffusion barrier layer. (b) S_{21} intensity over the cells shown in part (a).
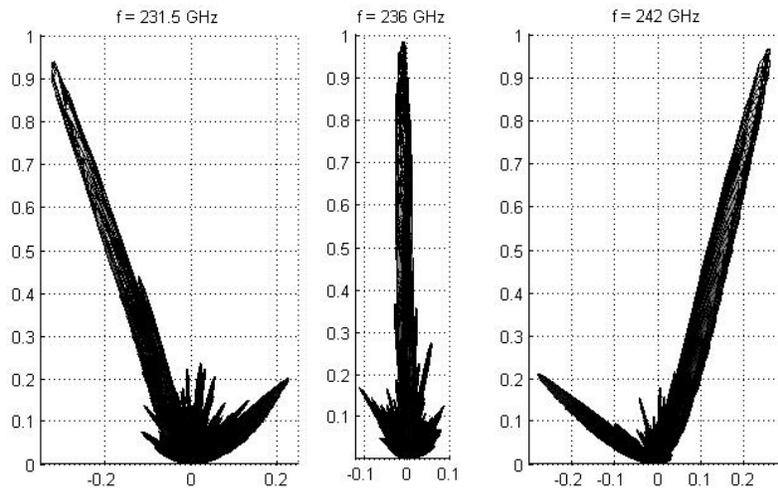
Figure 8.22. Far-field radiation pattern of the reduced-loss design with the diffusion barrier layer at different frequencies, beamwidth = 3.5^0.

Frequency (GHz)	Scan Angle (deg)
230	-21.2
231.5	-16.1
233	-11
234.5	-5.9
236	-0.8
237.5	4.3
239	9.4
240.5	14.5
242	19.65
243.5	24.7
245.	29.8

Table XII. The scan angle versus frequency for the waveguide slot array (reduced-loss design with the diffusion barrier layer)

The scanning range is a bit off-centered which could be due to over-etching the depth of the waveguide and the non-uniform etching which causes deviations in the dispersion characteristics. The beam width is now 3.5^0, still wider than the design (2.5^0) and shows the fabricated structure is still more lossy compared to the design. This can be further improved by using a thicker and more conformal (to cover the sidewalls) diffusion barrier layer, performing bonding at lower temperature, smoother etching and using SoI (silicon on insulator) wafers to have a more uniform etching.

8.5. Conclusion

In this chapter, the Y-band on-wafer measurement setup for the full two-port S-parameter measurements of waveguide antenna, transitions and filters is introduced and the results of the measurements are presented. The initial results on the first fabricated antenna showed problems with the slot size which reduced the radiated power from small slots. A second antenna design was fabricated with an improved slot design. This antenna

shows improved performance. However, there were still problems due to loss in the feed waveguide. This loss was found to be due to conductor loss associated with poor gold quality. This problem was addressed with a modified fabrication process. A third antenna was fabricated and tested. This antenna showed the desired beam scanning. The beam width was improved compared with the earlier results but is still high due to los in the structure. Suggestions to reduce this loss will be discussed in Chapter 9.

Chapter IX

Conclusion and Future Work

9.1.   Summary and Conclusion

This thesis presented novel techniques to enhance human target identification at heavily cluttered environment and detection of concealed carried irregular objects at high MMW band as well as developing compact and light-weight frequency scanning radar at Y-band for navigation and obstacle detection. It began with radar backscatter analysis human body at W-band in Chapter 2. The PO/IPO and GO approaches were introduced and developed based on the characteristics of human body such as size, surface smoothness, skin dielectric constant and loss. The results of the RCS analysis showed that the larger targets (oversize man and woman) have higher level of RCS response. The radar backscatter analysis of walking human bodies and a dog was discussed in Chapter 3. The Doppler spectra of human body and dog were derived by performing a Fourier transform from the received signal in time domain (which was stored as a sequence) and were compared to find a means of identification of the target. It was shown that the spectra of different body size/gender and dog are different in many aspects such as shape, magnitude and bandwidth. This feature can be used to identify these targets. The polarimetric responses of the walking bodies were then studied and the feasibility of detecting body-attached irregular objects by decomposing the overall backscatter response from different body parts was investigated. It was shown that the level of cross- to co-polarized response of torso increases when an external irregular object is present. This makes the approach viable for the detection of external objects carried on the torso.

185

Human Doppler Analysis at Y-band was performed using the same method. It was shown that the RCS magnitude and bandwidth of the Doppler spectrum was changed, which motivated us pursuing similar studies at higher MMW bands.

Chapter 4 introduced a new generation of MMW radars at Y- band in an attempt to have low-profile, low-cost systems with higher range resolution for navigation and obstacle detection. The specifications of the radar components were discussed. The radar antenna is a waveguide slot frequency scanning array with ±25deg steering capability with narrow (2^0) beamwidth. The feasibility of manufacturing and integrating this structure using micromachining techniques with the emphasis on the advantages of silicon DRIE was also studied. In Chapter 5, the design details of a two-dimensional micromachined meander-line frequency scanning antenna array were presented. The antenna was designed based on WR-3 rectangular waveguides with the slots cut on the broad wall of the waveguide as the radiating elements. Since this structure makes a narrow beam one-dimensional array, slot-coupled patch arrays were used to confine the beam in the other direction. The limitations in microfabrication were considered in the design of the antenna structure.

Chapter 6 presented the methods and components developed for radar integration, compatible with microfabrication techniques. These include a) a CPW to rectangular waveguide transition which is needed since the antenna structure is excited with frequency multipliers which are fabricated on planar transmission lines, b) wafer transition for embedding external VCO and frequency multiplier chips, c) waveguide bandpass filters are also designed to be incorporated with the system mainly in order to remove the DC component of the signal received by the antenna. All these components

and integration techniques should be compatible with micromachining processes used to fabricate the antenna substrate.

The microfabrication processes of these structures were discussed in Chapter 7. The process used three separate silicon wafers each of which include a part of the antenna and other passive devices which are bonded together at the final step. Various microfabrication procedures such as silicon DRIE, multi-step mask deposition, gold deposition silicon-oxide deposition, low-stress silicon-oxide/silicon nitride deposition, XeF_2 silicon etching, gold-gold thermocompression bonding, topside and backside wafer alignment, polymer deposition, polymer bonding, etc. were employed to fabricate the radar components. The measurement results for the Y-band devices were presented in Chapter 8. The reflection and insertion loss of the waveguide transition and filter were in a good agreement with the simulation. The initial results from antenna showed a high loss which were improved by changing the design of the waveguide and the microfabrication technique. The antenna was able to scan the field of view from -21^0 to 29^0 with 3.5^0 beamwidth.

9.2. Future Work

9.2.1. MMW Phenomenology

The radar backscatter analysis of human body can be continued in various directions:

- Investigating the effect of clothing on the RCS and cross-polarized response: Although clothings have minimal effect on the radar backscatter, heavy clothings might change the level of RCS. In addition, large wrinkles on the

clothings can cause considerable effect on the cross-polarized response if they make corner reflectors or cause additional multipath as represented in Figure 9.1.

- Parallel processing: The PO/IPO code can be enhaced using parallel computing methods to save time/memory in the current algorithm and to be able to solve more complex scenarios.

- Analysis at higher frequency bands: This can be achieved using the Y-band radar and has the advantages of achieving smaller beamwidth and more compact radars.

Figure 9.1. The effect of heavy clothings with wrinkles on the radar backscatter.

9.2.2.   MMW Technology

The future work of this project mainly involves the integration of the Y-band radar. This includes verification of the performance of the thru-wafer transition for packaging and the hybrid-coupled patch arrays as well as the performance of the active components of the radar. Moreover, the technologies empowered by the contribution of this work are numerous. These include improvement in microfabrication processes and enhancing the antenna performance.

9.2.2.a.   Microfabrication Improvement

The performance of the radar antenna was enhanced using lower-loss waveguide structure (with larger dimensions) and larger slot dimension. This could be further optimized considering limitations in microfabrication such as the maximum achievable etch depth and optimization of the parameters of gold thermocompression bonding such as bonding pressure and temperature to maintain the quality. It was experimentally shown that by using mask layers with high selectivity, the etch depth for the current process can be as deep as 1 mm. Also, gold bonding can be performed in lower temperatures and pressures by forfeiting the mechanical bonding quality. In addition, the non-uniform etching of silicon caused by loading effect in DRIE can be completely compensated using etch-stop layers. These layers are commonly thin high quality silicon oxide layers which are very selective to DRIE and are very efficiently used as etch-stop.

Due to the lack of fast and selective Parylene etchants, it is not selectively etched in the current radar. This might cause some additional loss due to the presence of a lossy dielectric. Hence, selective Parylene etching should also be investigated.

h_{WG} 80%~ 85% h_{WG}
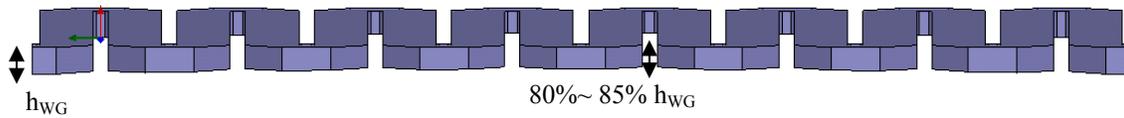
Figure 9.2. Etch non-uniformity of long structure caused by DRIE

9.2.2.b.   Polarimetric Radar

The radar performance can be enhanced for applications in obstacle detection especially walking human body identification and the detection of concealed carried object by making it polarimetric. As suggested by the algorithm presented for human body analysis, the polarimetric response of the radar backscatter is the main parameter in the detection algorithm. The current antenna can only provide v-polarized signal as a result of the v-polarized patch arrays. The arrangement of the patch array is suggested in Figure 9.3 for an h-polarized antenna. With such a configuration, the radiating edge of the patch can be rotated 90^0 in order to generate h-polarized radiation. Instead of having two identical antennas, the radar can be designed with one v-polarized and one h-polarized antennas, both as transmitting and receiving antennas.

190
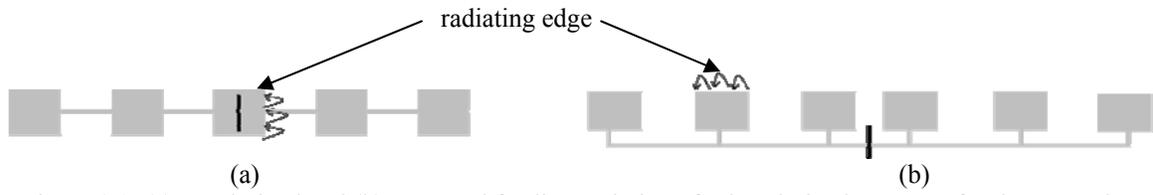
Figure 9.3. (a) v-polarized and (b) proposed feeding technique for h-polarized antennas for the same slot.

BIBLIOGRAPHY

[1] P. Bhartia and I. J. Bahl, *Millimeter Wave Engineering and Applications*, New York: John Wiley, 1984.

[2] URL:http://www.rfcafe.com/references/electrical/ew-radar-handbook/rf-atmospheric-absorption-ducting.htm

[3] H. J. Liebe, T. Manabe, G. A. Hufford. "Millimeter-wave attenuation and delay rates due to fog/cloud conditions", *IEEE Trans. Antennas Propagat.*, vol. 37, pp. 1617–1623, Dec. 1989.

[4] D. M. Sheen, D. L. McMakin, and T. E. Hall, "Three-dimensional millimeter-wave imaging for concealed weapon detection," *IEEE Trans. Microwave Theory Tech.*, vol. 49, pp.1581–1592, Sep. 2001.

[5] K. B. Cooper, R. J. Dengler, G. Chattopadhyay, E. Schlecht, J. Gill, A. Skalare, I. Mehdi, and P. H. Siegel, "A high-resolution imaging radar at 580 GHz," *IEEE Microw. Wireless Compon. Lett.*, vol. 18, no. 1, pp. 64–66, Jan. 2008.

[6] A. B. del Campo, A. A. Lopez, B. P. D. Naranjo, J. G. Menoyo, D. R. Moran, and C. C. Duarte, "CWLFM millimeter-wave radar for ISAR imaging with range coverage," in *Proc. IEEE Int. Radar Conf.*, May 9–12, 2005, pp. 933–938.

[7] H. D. Collins, D. L. McMakin, T. E. Hall, and R. P. Gribble, "Real-time holographic surveillance system," U.S. Patent 5 455 590, Oct. 3, 1995.

[8] R. W. McMillan, N. C. Currie, D. D. Ferris, and Jr. M. C. Wicks, "Concealed weapon detection using microwave and millimeter wave sensors," *Microwave and Millimeter Wave Technology Proceedings,* pp. 1-4, 1998.

[9] V. B. Shteinshleinger, et. al., "A new type of device to locate objects hidden under the clothes of people," 2001 CIE International Conference on, Proceedings, pp. 227-230.

[10]   R. W. McMillan, "Terahertz Imaging, Millimeter-Wave Radar," Advances in Sensing with Security Applications Digest, NATO Advanced Study Institute, Il Ciocco, Italy, pp. 1-26, July 17-30, 2005.

[11]   Automatic two-stage IR and MMW image registration algorithm for concealed weapons detection. Chen, H.-M. Varshney, P.K. Vision, *IEE Proceedings Image and Signal Processing*, Aug 2001, vol. 148, number 4, pp 209-216.

[12]   P. F. Goldsmith, C.-T. Hsieh, G. R. Huguenin, J. Kapitzky, and E. L. Moore. "Focal Plane Imaging Systems for Millimeter Wavelengths", IEEE Trans. Microwave Theory and Techniques, Vol. 41, pp. 1664–1675, October 1993.

[13]   T. Dogaru, C. Le, and G. Kirose, "Time-Frequency Analysis of a Moving Human Doppler Signature," Army research lab technical report, ARL-TR-4728, Feb 2009.

[14]   W. H. Haydl, M. Neumann, L. Venveyen, A. Bangert, S. Kudszus, M. Schlechtweg, A. Hulsmann, A. Tessmann, W. Reinert, and T. Krems, "Single-chip coplanar 94-GHz FMCW radar sensors," *IEEE Microw. Guided Wave Lett.*, vol. 9, no. 2, pp. 73–75, Feb. 1999.

[15]   A. Tessmann, S. Kudszus, T. Feltgen, M. Riessle, C. Sklarczyk, and W. H. Haydl, "Compact single-chip W-band FMCW radar modules for commercial high-resolution

sensor applications," *IEEE Trans. Microw. Theory Tech.*, vol. 50, no. 12, pp. 2995–3001, Dec. 2002.

[16]   I. D. Robertson and S. Lucyszyn , *RFIC and MMIC Design and Technology*, 1st ed. The Institution of Electrical Engineers, London, 2001.

[17]   G. D. Morgan, P. D. Beasley, C. L. Murray, and C. Koh, "Design considerations for a millimetric front-end for FMCW radar," in *Inst. Eng. Technol. Millimeter-Wave Products Technol. Seminar*, Nov. 16, 2006, pp. 7–12.

[18]   P. Uhlig, C. Günner, S. Holzwarth, J. Kassner, R. Kulke, A. Lauer, and M. Rittweger, "LTCC short range radar sensor for automotive application at 24 GHz," in *Proc. 37th Int. Microelectron. Symp.*, Nov. 14–18, 2004.

[19]   C. Wang, R. Qian, and X.-W. Sun, "Low cost _-band FMCW radar modules for automobile application," in *Proc. IEEE Int. RF Integration Technol.: Integrated Circuits for Wideband Commun. Wireless Sensor Networks Workshop*, Nov. 30–Dec. 2 2005, pp. 153–156.

[20]   R. Kulke, C. Günner, S. Holzwarth, J. Kassner, A. Lauer,M. Rittweger, P. Uhlig, and P. Weigand, "24 GHz radar sensor integrates patch antenna and frontend module in single multilayer LTCC substrate," in *Eur. Microelectron. Packag. conf.*, Jun. 12–15, 2005, pp. 239–242.

[21]   S. Raman and G. M. Rebeiz, "A 94 GHz unipolar subharmonic mixer," in *IEEE MTT-S Int. Microwave Symp. Dig.*, vol. 1, Jun. 1996, pp. 385–388.

[22]   H. F. Cook, "Dielectric Behavior of Some Types of Human Tissues at Microwave Frequencies", *J. Appl. Phys.*, Vol. 2, pp. 295-300, 1951.

[23]   C.M. Alabaster, 'Permittivity of human skin in millimetre wave band," Electronics Lett. ,16th October 2003 Vol. 39 No. 21

[24]   Walters, T., *et. al*, "Heating and pain sensation produced in human skin by millimeter waves: comparison to a simple thermal model', *Health Physics*, Mar. 2000, 78, 3, pp 259 – 267

[25]   Gabriel, C. and Gabriel, S.: 'Compilation of the dielectric properties of body tissue at RF and microwave frequencies', Final report for AFOSR/NL Bolling AFB DC 20332-0001, June 1996.

[26]   URL: http://www.makehuman.org/

[27]   K. M. Robinette, H. Daanen, and E. Paquet, "The CAESAR project: a 3-D surface anthropometry survey," in *Proc. 3-D Digital Imaging and Modelling*, pp. 380-386, Oct., 1999, Ottawa, Canada

[28]   URL: http://um3d.dc.umich.edu

[29]   F. T. Ulaby, C. Elachi, *Radar Polarimetry for Geoscience Applications*. Artech House, Norwood, MA, 1990.

[30]   F. Obelleiro, M. G. Araujo, J. L. Rodriguez, "Iterative physical-optics formulation for analyzing large waveguide with lossy walls," *Microwave Opt. Tech. Lett.,* vol. 28, pp. 21-26, Jan. 2001.

[31]   T. Griesser and C. A. Balanis, "Dihedral corner reflector backscatter using higher order reflections and diffractions," *IEEE Trans. Antennas Propagat.,* vol. 35, pp.1235-1247 Nov. 1987.

[32]   R. D. De Roo and F. T. Ulaby, "Bistatic specular scattering from rough dielectric surfaces," *IEEE Trans. Antennas and Propagat.*, vol. 42, pp. 220-231, Feb. 1994

[33]   Nashashibi A., Ulaby F., and Sarabandi K., "Measurement and modeling of the millimeter wave backscatter response of soil surfaces," *IEEE Trans. Geosci. Remote Sensing*, vol. 34, no. 2, pp. 561-572, Jan. 1996

[34]   P. van Dorp and F. C. A. Groen, "Human walking estimation with radar," *IEE Proc. –Radar Sonar Navig.,* vol. 150, No. 5, Oct. 2003

[35]   G. E. Smith, K. Woodbridge, and C. J. Baker, "Multistatic micro-doppler signature of personnel," *IEEE Radar Conference*, pp. 1–6, 2008.

[36]   Y. Kim and H. Ling, "Human activity classification based on microdoppler signatures using a support vector machine," *IEEE Trans. Geosci. Remote Sensing*, vol. 47, no. 5, pp. 1328–1337, 2009.

[37]   B. G. Mobasseri and M. Amin, "A time-frequency classifier for human gait recognition," in *SPIE Defense, Security and Sensing*, vol. 7306, 2009.

[38]   C. Hornsteiner, and J. Detlefsen," Characterisation of human gait using a continuous-wave radar at 24 GHz," *Advances in Radio Science* 2008, Vol. 6, p. 67-70

[39]   D. Polder and J. H. van Santen, "The effective permeability of mixtures of solids," *Physica*, vol. 12, no. 5, pp. 257-271, 1946.

[40]   Helmut Essen, et. al. "A High Performance 220-GHz Broadband Experimental Radar", IRMMW-THz 2008, Pasadena, USA, September 2008.

[41]   G.P. Gauthier, J.P. Raskin, *and* G.M. Rebeiz, A 140–170-GHz low-noise uniplanar subharmonic Schottky receiver, *IEEE Trans Microwave Theory Tech,* vol. 48, 2000, 1416–1419.

[42]   Abbasi, M., Gunnarsson, S.E., Wadefalk, N., Kozhuharov, R., Svedin, J., Cherednichenko, S., Angelov, I., Kallfass, I., Leuther, A., Zirath, H., "Single-Chip 220-GHz Active Heterodyne Receiver and Transmitter MMICs With On-Chip Integrated Antenna", *IEEE Trans. Microwave Theory Tech,* pp: 466 - 478, Volume: 59 Issue: 2, Feb. 2011

[43]   S. Gunnarsson , N. Wadefalk , J. Svedin , S. Cherednichenko , I. Angelov , H. Zirath , I. Kallfass and A. Leuther "A 220 GHz single-chip receiver MMIC with integrated antenna", *IEEE Microw. Wireless Compon. Lett.,* vol. 18, no. 4, pp.284 - 286 , 2008.

[44]   B. Pan, Y. Li, G.E. Ponchak, J. Papapolymerou, *and* M.M. Tentzeris, A 60-GHz CPW-fed high-gain and broadband integrated horn antenna, *IEEE Trans Antennas Propagat* 57 (2009), pp. 1050–1056.

[45]   M. Jankiraman, Design of Multi-Frequency CW Radars, Scitech Publishing, Inc., 2007.

[46]   Skolnik, M. I. (ed.), Radar Handbook, McGraw-Hill (1970)

[47]   W. Menzel, D. Pilz, and R. Leberer, "A 77-GHz FM/CW radar front-end with a low-profile low-loss printed antenna," *IEEE Trans. Microw. Theory Tech.*, vol. 47, no. 12, pp. 2237–2241, Dec. 1999.

[48] M. E. Russell *et al.*, "Millimeter-wave radar sensor for automotive intelligent cruise control (ICC)," *IEEE Trans. Microwave Theory Tech.*, vol. 45, pp. 2444–2453, Dec. 1997.

[49] Y. Kimura, H. Shinoda, J. Hirokawa, and M. Ando, "Sidelobe suppression of two-beam single-layer slotted waveguide array," in *Asia–Pacific Microwave Conf.*, Yokohama, Japan, 1998, pp. WE2D-1.

[50] T. Tanizaki *et al.*, "Multi-beam automotive radar front end using noncontact cylindrical NRD switch," in *IEEE Int. Microwave Symp. Dig.*, Baltimore, MD, 1998, pp. 521–524.

[51] K. L. Klohn, R. E. Horn, H. Jacobs, and E. Freibergs, "Silicon waveguide frequency scanning linear array antenna," *IEEE Trans. Microwave Theory Tech.*, vol. MTT-26, pp. 764–773, Oct. 1978.

[52] Manasson, *et. al.*, "MMW scanning antenna," *IEEE Aerospace and Electronic Systems Magazine*, vol. 11, no. 10, pp. 29-33, Oct. 1996

[53] V. Fusco, "Mechanical beam scanning reflect array," *IEEE Trans. Antennas Propag.*, vol. 53, no. 11, pp. 3842–3844, Nov. 2005.

[54] Metamaterial based steerable antenna for millimeter wave radar applications

[55] K. V. Caekenberghe, T. Vaha-Heikkila, G. Rebeiz, and K. Sarabandi, "Ka-band MEMS TTD passive electronically scanned array (ESA)," in *Proc. IEEE APS/URSI Symp.*, Albuquerque, NM, Jul. 2006, pp. 513–516.

[56] B. Schoenlinner, X. Wu, J. Ebling, G. Eleftheriades, and G. Rebeiz, "Wide-scan spherical-lens antennas for automotive radars," *IEEE Trans. Microw. Theory Tech.*, vol. 50, no. 9, pp. 2166–2175, Sep. 2002.

[57] A. Ishimaru and H. S. Tuan, "Theory of frequency scanning antennas," *IRE Trans. Antennas Propagat.*, vol. 10, Mar. 1962

[58] J. Bahl and K. C. Gupta, "Frequency scanning by leaky-wave antennas using artificial dielectrics,", IEEE lEEE TRANSACnONS ON A i i W A S *k?4D* PROPAGATIoEi, JULY 1975 584-589

[59] H. Y. Yee, "The design of large waveguide arrays of shunt slots," *IEEE Trans. Antennas Propag.*, vol. 40, pp. 775–781, 1992

[60] A. Patrovsky, and K. Wu, "Substrate integrated image guide array antenna for the upper millimeter-wave spectrum," *IEEE Trans Antennas Propagat.*, vol. 55, pp. 2994-3001, Nov. 2007.

[61] URL: http://www.qudostechnology.co.uk/etching.php

[62] URL: http://memscyclopedia.org/su8.html

[63] S. W. Yoon, V. P. Ganesh, et. al., "Packaging and assembly of 3-D silicon stacked module for image sensor application," IEEE Trans. Advanced Packaging, vol. 31, pp. 519-526, Aug. 2008.

[64] J. W. Digby, *et. al.* "Fabrication and characterization of micromachined rectangular waveguide components for use at millimeter-wave and terahertz frequencies," *IEEE Trans. Microwave Theory Tech.*, vol. 48, pp. 1293–1302, Aug. 2000.

[65]   C. E. Collins, *et. al.* "A new micro-machined millimeter-wave and terahertz snaptogether rectangular waveguide technology," *IEEE Microw. Guided Wave Lett.*, vol. 9, pp. 63–65, Feb. 1999.

[66]   J. L. Hesler, K. Jui, R. K. Dahlstrom, R. M.Weikle, T. W. Crowe, C. M. Mann, and H. B. Wallace, "Analysis of an octagonal micromachined horn antenna for submillimeter-wave applications," *IEEE Trans. Antennas Propagat.*, vol. 49, pp. 997–1001, June 2001.

[67]   W. R. McGrath, C. Walker, M. Yap, and Y.-C. Tai, "Silion micromachined waveguides for millimeter-wave and submillimeter-wave frequencies," *IEEE Microw. Guided Wave Lett.*, vol. 3, pp. 61–63, Mar. 1993.

[68]   R. N. Simons and S. R. Taub, "New coplanar waveguide to rectangular waveguide end launcher," *Electron. Lett.*, pp. 1138–1139, June 1992.

[69]   URL: http://www.microchem.com/products/su_eight.htm

[70]   L. Josefesson, "A waveguide transverse slot for array applications*", IEEE Trans. Antennas Propagat.*, vol. 41, pp. 845-850, July 1993

[71]   R. E. Collin, Foundations for *Microwave Engineering*. New York: McGraw-Hill, 1966.

[72]   R. S. Elliott, Antenna Theory and Design, Englewood Cliffs, Prentice-Hall, 1981, page 90

[73]   F. P. Van Der Wilt and J. H. M. Strijbos, "A 40 GHz planar array antenna using hybrid coupling," *Perspectives Radio Astron. Technol. Large Antenna Arrays*, pp. 129–134, 1999

[74]   URL:https://www51.honeywell.com/sm/em/products-applications/ dielectrics/spin-on-glass.html?c=21

[75]   F. J. Goebels and T. S. Fong, "Four independent beams from a single linear array," *IEEE Trans. Antennas Propagat.*, vol. AP-13, pp. 683–691, Sept. 1965.

[76]   M. Vahidpour, and K. Sarabandi, "Cavity-backed coplanar waveguide to rectangular waveguide transition for micromachining applications," *IEEE Trans. Microwave Theory Tech.*,

[77]   T. Q. HO and Y. Shih, "Spectral-domain analysis of E-plane waveguide to microstrip transitions," *IEEE Trans. Microwave Theory Tech.*, vol. 37, pp. 388-392, Feb. 1989.

[78]   Y. Lee, J. P. Becker, J. East, L. P. B. Katehi, "Fully micromachined finite-ground coplanar line-to-waveguide transitions for w-band applications," *IEEE Trans. Microwave Theory Tech.*, vol. 52, pp. 1001-1007, Mar. 2004

[79]   Y. Li, B. Pan, M. M. Tentzeris and J. Papapolymerou, "A fully micromachined W-band coplanar waveguide to rectangular waveguide transition", *in Proc. of 2007 IEEE-IMS Symposium,* Honolulu, Hi, June 2007

[80]   Y. Li, B. Pan, C. Lugo, M. M. Tentzeris, and J. Papapolymerou, "Design and characterization of a W-band micromachined cavity filter including a novel integrated transition from CPW feeding lines," *IEEE Trans. Microwave Theory Tech.,* vol. 55, pp. 2902-2910, Dec. 2007

[81]   N. Marcuvitz, *Waveguide Handbook*, McGraw-Hill, New York, 1951, pp. 271-273

[82]   R. F. Harrington, *Time-Harmonic Electromagnetic Fields*, McGraw-Hill, New York, 1961, pp. 177-179 and 425-428

[83]   M. Moallem, J. East, and K. Sarabandi, "Optimally designed membrane-supported grounded CPW structure for submillimeter-wave applications," *Int. Symp. Antennas Propagat.* Charleston, NC. 2009.

[84]   J. P. Becker, Y. Lee, J. R. East, and L. P. B. Katehi, "A finite ground coplanar line-to-silicon micromachined waveguide transition," *IEEE Trans. Microwave Theory Tech.*, vol. 49, p. 2001, Oct. 2001.

[85]   Y. Lee, J. P. Becker, J. East, L. P. B. Katehi, "Fully micromachined finite-ground coplanar line-to-waveguide transitions for w-band applications," *IEEE Trans. Microwave Theory Tech.*, vol. 52, pp. 1001-1007, Mar. 2004

[86]   Y. Li, B. Pan, M. M. Tentzeris and J. Papapolymerou, "A fully micromachined W-band coplanar waveguide to rectangular waveguide transition", *in Proc. of 2007 IEEE-IMS Symposium,* Honolulu, Hi, June 2007.

[87]   URL: www.mnf.umich.edu/ToolDocs/doc00088.pdf

[88]   Tsau, C.H. Spearing, S.M. Schmidt, M.A., "Characterization of wafer-level thermocompression bonds", *Microelectromechanical Systems, Journal of* , vol. 13, pp. 963 - 971, Dec. 2004.

[89]   J. Wu, et al., "Study on the Gold-Gold Thermocompression Bonding for Wafer-level Packaging," *Advanced Materials Research* Vols. 60-61, pp 325-329, 2009.

[90]   Hensup Kim, Dissertation, *An Integrated Electrostatic Peristaltic Micropump with Active Microvalves*, University of Michigan, 2006

[91]   Measurements of Micromachined Waveguide Devices at WR-3 Band using a T/R-T Module Based Network Analyzer

[92]   W. H. Chow, A. Champion, and D. P. Steenson, "Measurements to 320 GHz of millimetre-wave waveguide components made by high precision and economic micro-machining techniques," in *Proc. 8th High Freq. Postgrad. Stud. Colloq.*, 2003, pp. 90–93.

[93]   C. H. Smith, A Sklavonuos, and N. S. Barker, "SU-8 Micromachining of Millimeter and Submillimeter Waveguide Circuits," *IEEE MTT-S International Microwave Symposium*, Vol. 1-3, pp. 961-964, 2009.

[94]   T. Skaik, Y. Wang, M. Ke, S. Qian, and M. Lancaster, "A Micromachined WR-3 Waveguide with Embedded Bends for Direct Flange Connections," *Proc. 40th European Microwave Conference*, Paris, Sep. 2010, pp. 1225-1228.

[95]   T. Gaier, L. Samoska, C. Oleson, G. Boll, "On-Wafer Testing of Circuits Through 220 GHz," *Ultrafast Optics and Electronics Conference*, Snowmass, CO, April, 1999. *OSA Trends in Optics and Photonics Series* Vol. 28, pp. 20-26.

[96]   On-Wafer Vector Network Analyzer Measurements in the 220-325 GHz Frequency Band

[97]   OML, Inc. URL: http://www.omlinc.com/

[98]   Virginia Diodes, Inc. URL: http://vadiodes.com/